Imogolite nanotubes : order-disorder transition and dynamics of nanoconfined water

Arianna d'Angelo

université PARIS-SACLAY

Imogolite nanotubes: order-disorder transition and dynamics of nanoconfined water

Nanotubes d'imogolite : transition ordre-désordre et dynamique de l'eau nanoconfinée

Thèse de doctorat de l'université Paris-Saclay

École doctorale n° 564 physique de l'Ile-de-France (PIF)
Spécialité de doctorat: Physique
Graduate School : Physique. Référent : Faculté des sciences d'Orsay

Thèse préparée au Laboratoire de Physique des Solides (Université Paris-Saclay, CNRS) et à l'Institut Laue-Langevin, sous la direction de Pascale LAUNOIS, Directrice de recherche, le co-encadrement de Stéphane ROLS, chercheur, et Erwan PAINEAU, chargé de recherche

Thèse soutenue à Paris-Saclay, le 13 décembre 2022, par

Arianna D'Angelo

Composition du jury

Eric FERRAGE Directeur de recherche, Institut de Chimie des Milieux et Matériaux de Poitiers	Président
Livia BOVE Directrice de recherche, Institut de Minéralogie et Physique des Milieux Condensés, Sorbonne Université	Rapporteure & Examinatrice
Denis MORINEAU Directeur de recherche, Université de Rennes 1	Rapporteur & Examinateur
Jean-Marc ZANOTTI Directeur de recherche, CEA - Laboratoire Léon Brillouin	Examinateur
Andrey KALINICHEV Directeur de recherche, IMT Atlantique - SUBATECH, Univ. Nantes	Examinateur
Pascale LAUNOIS Directrice de recherche, Université Paris-Saclay	Directrice de thèse

THESE DE DOCTORAT
NNT : 2022UPASP143

université PARIS-SACLAY

ÉCOLE DOCTORALE
Physique en Île-de-France (PIF)

Titre: Nanotubes d'imogolite: transition ordre-désordre et dynamique de l'eau nanoconfinée
Mots clés: dynamique, nanoconfinement, imogolite

Résumé: Ce travail de thèse est dédié à l'étude des nanotubes d'imogolite et des propriétés structurales et dynamiques de l'eau confinée dans leur cavité. La stœchiométrie de ces tubes hydrophiles est $SiAl_2O_7H_4$ et leur diamètre interne est d'environ 1,5 nm. Dans le premier chapitre du manuscrit, l'état de l'art concernant les nanotubes d'imogolite est développé, avec un accent particulier sur le confinement de l'eau. Dans le second chapitre, les techniques expérimentales utilisées dans la thèse sont présentées. Ce chapitre comprend aussi des sections qui détaillent les formalismes de diffusion des rayons X et des neutrons. Le chapitre trois est consacré à la théorie des simulations de dynamique moléculaire, avec les potentiels atomiques utilisés et la procédure employée pour obtenir, à partir de trajectoires simulées, les observables de rayons X et de neutrons. Les chapitres quatre et cinq présentent les résultats obtenus au cours de la thèse. Dans le chapitre quatre, la structure du nanotube sec est déterminée et une transition ordre-désordre du sous-réseau formé par les hydroxyles internes du tube, prédite par les simulations de dynamique moléculaire, est observée expérimentalement. La transition est d'abord caractérisée par les simulations, en définissant un paramètre d'ordre et en le corrélant à des quantités expérimentales. L'existence de la transition est démontrée par diffusion élastique des neutrons, et elle est ensuite étudiée plus en détail par diffusion quasi-élastique et inélastique des neutrons, qui mettent en évidence son caractère complexe. Le chapitre cinq étudie la structure et la dynamique de l'eau à l'intérieur des nanotubes. L'arrangement périodique selon la direction de l'axe du tube des molécules d'eau à l'intérieur des imogolites est d'abord illustré grâce aux simulations de dynamique moléculaire. Cette périodicité est ensuite confirmée expérimentalement par diffusion des rayons X *in situ*. La dynamique de l'eau confinée est étudiée en divisant les molécules d'eau en deux catégories, à savoir l'eau "lente" et l'eau "rapide", en fonction de leurs coefficients de diffusion déduits de la dynamique moléculaire. Les expériences de diffusion quasi-élastique des neutrons sont expliquées en ces termes, avec deux composantes associées à ces deux catégories. Enfin, la présence d'un mode de vibration caractéristique de l'eau adsorbée sur la paroi est mise en évidence par diffusion inélastique des neutrons.

Title: Imogolite nanotubes: order-disorder transition and dynamics of nanoconfined water
Keywords: dynamics, nanoconfinement, imogolite

Abstract: This thesis work is dedicated to the study of imogolite clay nanotubes and to the structural and dynamical properties of water confined in their cavity. The stoichiometry of these hydrophilic nanostructures is $SiAl_2O_7H_4$ and their inner diameter is about 1.5 nm. In the first chapter of the manuscript, the state of the art regarding imogolite nanotubes is developed, with a special focus on water confinement. In the second chapter, the experimental techniques used in the thesis are presented. This chapter also includes sections presenting the X-ray and neutron scattering formalisms. Chapter three is dedicated to the theory of Molecular Dynamics simulations, detailing the atomic potential used and the procedure employed to obtain, from simulated trajectories, the X-ray and neutron observables. Chapter four and five present the results obtained during the thesis. In chapter four, the structure of the dry nanotube is determined and an order-disorder transition of the tube's inner hydroxyl sublattice, predicted by Molecular Dynamics simulations, is shown to be observed experimentally. The transition is first characterized by simulations, by defining an order parameter and correlating it to experimental quantities. The occurrence of the transition is proved experimentally by means of elastic neutron scattering experiments. It is further investigated by means of quasi-elastic and inelastic neutron scattering experiments, which highlight its complex character. Chapter five investigates the structure and the dynamics of water inside imogolite nanotubes. It starts by illustrating, by means of Molecular Dynamics simulations, the periodic arrangement of water molecules inside imogolites, along their long axis. This periodicity is then confirmed experimentally thanks to in-situ X-ray scattering experiments. The dynamics of confined water is investigated by dividing water molecules into two categories, *i.e.* "slow" and "fast" water, according to their diffusion coefficients deduced from molecular dynamics simulations. The experimental quasi-elastic measurements are explained in these terms, by finding two components associated to these two categories. Finally, the presence of a vibration mode characteristic of water adsorbed on the wall is evidenced by inelastic neutron scattering.

Contents

Acronyms

H_{in} Internal hydrogens of the tube.

H_{out} External hydrogens of the tube.

BET Brunauer–Emmett–Teller theory.

CHC Controlled Humidity Cell.

CNT Carbon Nanotube.

DFT Density Functional Theory.

DOS Density of States.

EINS Elastic Incoherent Neutron Scattering.

EISF Elastic Incoherent Structure Factor.

FTIR Fourier-Transform Infrared Spectroscopy.

FWHM Full Width Half Maximum.

GDOS Generalized Density of States.

Ge-INT Nanotube having chemical formula $(OH)_3Al_2O_3GeOH$.

HWHM Half Width Half Maximum.

INS Inelastic Neutron Scattering.

IR Infrared Spectroscopy.

LJ Lennard-Jones.

MD Molecular Dynamics.

MSD Mean Squared Displacement.

NSE Neutron Spin Echo.

ODT Order-disorder transition.

OH Hydroxyl group.

OP Order Parameter.

QENS Quasielastic Neutron Scattering.

RH Relative Humidity.

Si-INT Nanotube having chemical formula $(OH)_3Al_2O_3SiOH$.

SSA Specific Surface Area.

SW Single-Walled Nanotube.

TEM Transmission Electron Microscopy.

TGA Thermogravimetric Analysis.

TOF Time-Of-Flight Spectrometer.

vdW van der Waals.

WAXS Wide Angle X-ray Scattering.

XRD X-ray Diffraction.

XRS X-ray Scattering.

Acknowledgements

The thesis work presented in this manuscript was carried out in the Laboratoire de Physique des Solides (CNRS, Orsay) of the University Paris-Saclay (Ecole Doctorale Physique en Ile de France) and in the Institut Laue-Langevin (Grenoble), thanks to the financial support given by the ANR and the Institut Laue-Langevin.

First of all, I would like to thank the members of the jury: Livia Bove, Denis Morineau, Jean-Marc Zanotti, Andrey Kalinichev, Eric Ferrage and Laurence Noirez (invited member) for having accepted to evaluate my research work, and for the stimulating discussions we had at the defense.

I sincerely would like to express my deepest gratitude to my three supervisors, Pascale, Stéphane and Erwan, for dedicating so much time and energy to my project. I have collected an enormous amount of knowledge from you.

I thank Pascale for teaching me the rigor and critical thinking necessary to conduct scientific research, and for always being available for fruitful discussions even when incredibly busy. I learnt everything I know about X-ray diffraction from you. I thank Erwan for introducing me to the dreadful realm of chemistry and for being always helpful and available when needed. Your ability in creating connections between present results and previous papers is undeniable and you were of great help during the last hectic weeks of thesis writing. I thank Stéphane for his constant support and his contagious positive mindset. You were a great leader, not only by giving effective help when I was stuck on a problem, but most importantly demonstrating trust in me and allowing me the freedom to follow my own ideas. This project was successful due to your guidance and you still are a constant source of inspiration for me.

As I spent my first year in the LPS, I had the chance to be collaborating with the people in the MATRIX group. In particular, Stéphan Rouzière deserves a special thank you for the support during the X-ray experiments and the data treatment. A thank you to all the other members of the MATRIX group I interacted with: Pierre-Antoine Albouy, Pascale Foury, Denis Petermann, Stéphane Cabaret, Gilles Guillier, Claire Goldmann, Victor Baledent. I am also very grateful to Geoffrey Monet that kindly allowed me to use his exemplary scripts for visualization and neu-

tron analysis. I also cannot express how grateful I am to Marie-France Mariotto, for being the most efficient bureaucratic problem-solver that I ever met.

Next, I would especially would like to thank the people at the ILL for making it the incredible workplace that hosted me during my second and third year. First of all, the CS group: Miguel Gonzalez, Elisa Rebolini, Cinthya Herrera, Eric Pellegrini, Dominik Arominski, Mathieu Tillet, Guillaume Communie, Shervin Nourbakhsh and Tobias Weber. Special thanks go to Remi Perenon for enlightening me, during my very first month of PhD, about the workings of a neutron software infamous for its obscure mode d'emploi (no names mentioned). At the ILL, I had the chance to perform many neutron experiments, and I need to thank all the instrument scientists that I had on my side during beamtime: Francesca Natali, Markus Appel, Fernando Formisano, Jean-Marc Zanotti, Quentin Berrod, Viviana Cristiglio, Peter Fouquet. I've learnt something from all of you. A thank you for all the technicians, Olivier Meulien, Yann Berlemont and Olivier Aguettaz, without whom no experiment would have ever taken place. I really have to thank the ILL for allocating me a disproportionate amount of neutron beamtime: if Grenoble is known for being astoundingly surrounded by mountains, the mountain of data that I collected and analyzed (or, more accurately said, still in the process of being analyzed...) is even more astounding. This allowed me to have a thesis very rich and diverse in experimental data and I'm very grateful for it.

I would also like to thank Maguy Jaber for the TGA measurements, Valerie Magnin for welcoming more than once in IsTerre for the adsorption isotherms, and Erik Elkaim for the precious synchrotron measurements at SOLEIL.

I would like to thank my thesis mentor, Emmanuelle Rio, and my thesis tutor, Laura Bocher, for being part of my Comité de Suivi Individuel, participating in discussions on my progress and giving me critical advice.

Finally, I would like to say a big thank you to my close friends in Italy: Costanza, Maria Vittoria, Benedetta, Agnese, Francesca and Benedetta, for always making me feel like I never left home.

A huge thank you goes to the great PhD community of the ILL. To Bettina, Mohamed and Chen, with whom I shared all the ups and downs

of the PhD journey, for being the nicest and most fun officemates I could possibly hope for. To Rasmus, Jennifer, Maddie, Madeleine, Carmen, Milos, Edmond, Himanshu, Fernanda, Ronja, Daniela and Lucas, thank you for forming a brilliant PhD crew, made of bright and stimulating people: each of you has taught me something different and I cherish plenty of wonderful memories. It was a pleasure to share this journey with you!

Thank you to my housemates, Lucrezia and Blandine, for making our apartment with no living room such a homey place where I always happily returned after a bad (or good!) day at work.

A final thank you to my family, for always putting my education first, and for their constant support and presence.

Résumé en français

Bien qu'elle constitue les deux-tiers de la surface de la Terre, l'eau reste toujours mal comprise. En effet, un grand nombre de ses propriétés sont anormales par rapport à d'autres liquides. À ce jour, un modèle moléculaire complet de l'eau qui reproduise toutes ses propriétés manque encore. De plus, dans la nature, l'eau est confinée dans des environnements géologiques ou biologiques – la taille des cavités de confinement étant de l'ordre du nanomètre. Les argiles dans les sols ou les protéines dans les systèmes biologiques en sont des exemples. Dans ce cas, les anomalies se multiplient : les propriétés thermodynamiques changent tandis que de nouvelles configurations géométriques et de nouveaux régimes dynamiques apparaissent.

Dans cette perspective, les nanocanaux unidimensionnels sont des systèmes d'intérêt fondamental. Parmi ces systèmes unidimensionnels, nous considérerons les nanotubes d'imogolite. Ce sont des minéraux argileux naturels, découverts pour la première fois en 1962 dans des sols volcaniques japonais. Leur stœchiométrie est $SiAl_2O_7H_4$, et ils peuvent également être synthétisés par chimie douce. D'un diamètre de l'ordre du nanomètre, les nanotubes d'imogolite sont des systèmes idéaux pour étudier le nano-confinement de l'eau.

Une compréhension complète de la structure et de la dynamique d'une espèce confinée requiert la compréhension de la dynamique du "conteneur". Pour cette raison, le présent travail a un double objectif : il se concentre sur la structure et la dynamique du tube lui-même et sur l'étude des propriétés de l'eau confinée.

Étude du nanotube d'imogolite sec : transition ordre-désordre des groupes hydroxyles internes

La première partie de cette thèse est dédiée à l'étude du nanotube sec. La caractérisation de l'échantillon a été effectuée par microscopie électronique en transmission, spectroscopie infra-rouge, des expériences d'isothermes d'adsorption, ainsi que par diffraction des rayons X et simulations de dynamique moléculaire.

Les surfaces interne et externe du tube sont couvertes de groupes hydroxyle -OH. Grâce aux simulations de dynamique moléculaire, nous

avons constaté que les -OH internes sont orientés, c'est-à-dire tous alignés dans la même direction, la liaison hydrogène étant située dans un plan perpendiculaire à l'axe du tube (Fig.1a). Cette configuration est stable de 50 à 300 K, et par la suite nous appellerons cet état l'"état ordonné". Repérons l'orientation d'un hydroxyle par rapport au rayon qui relie l'oxygène au centre du tube dans le plan perpendiculaire à l'axe du tube. Des retournements des -OH, c'est-à-dire le changement d'orientation des liaisons -OH commencent à être observés à T = 400 K.

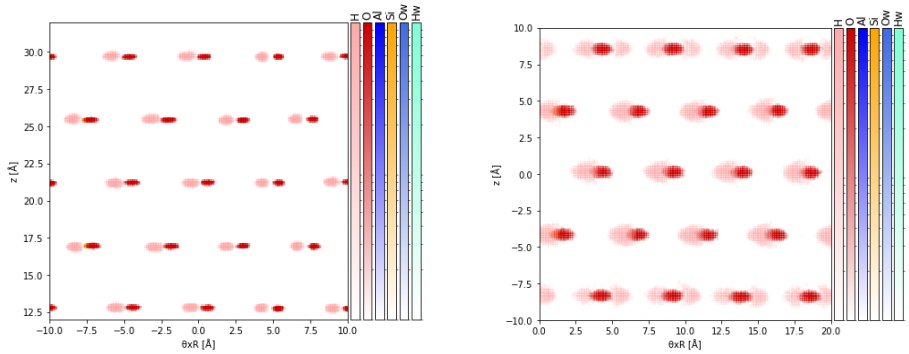

a) T=50 K b) T=400 K

Figure 1: Configuration des hydroxyles internes à faible T (en rouge les oxygènes, en rose les hydrogènes). En a), l'état ordonné; en b), la transition vers l'état désordonné.

À des températures encore plus élevées, la distribution angulaire des -OH tend à s'équilibrer, pour atteindre une configuration très symétrique – dans laquelle il y a autant de OH orientés d'un côté que de l'autre – que nous définissons comme l'"état désordonné". Le mécanisme de diffusion quasi-élastique associé peut être modélisé comme une diffusion par saut entre deux sites. De plus, l'inversion complète de toutes les liaisons -OH dans une chaîne perpendiculaire à l'axe du tube peut être associée à une propagation de parois de domaine. Ces modes de diffusion, pilotés par l'entropie, sont appelés solitons.

Les simulations de dynamique moléculaire prédisent que cette transition ordre-désordre peut être mesurée par la diffusion des neutrons et notamment qu'elle peut être caractérisée expérimentalement par l'apparition d'un signal quasiélastique, avec une énergie d'activation $E_a \sim 280$ meV.

Nous avons introduit un pseudo-spin pour caractériser l'orientation de l'hydroxyle, ayant une valeur $+1$ ou -1. Le paramètre d'ordre est la somme des pseudo-spins et il vaut 0 dans la phase désordonnée. En utilisant un modèle d'Ising unidimensionnel, nous avons évalué la constante d'interaction entre les pseudo-spins : elle est d'environ 50 meV. La petite

valeur de J par rapport à E_a est typique d'une transition ordre-désordre, par opposition à une transition displacive.

Par la suite, l'existence de cette transition est étudiée expérimentalement. L'intensité élastique mesurée (EISF) sur le spectromètre IN13 présente une diminution nette entre 300 K et 350 K, que nous pouvons attribuer à la transition attendue car la baisse d'intensité correspond à la contribution des H internes. Néanmoins, la diminution d'intensité se produit sur un domaine de température plus réduit dans les données experimentales que dans les simulations, montrant un premier désaccord entre les deux. La dépendance en vecteur d'onde Q de l'EISF a été mesurée sur le spectromètre à écho de spin WASP. Nous avons observé que la forme globale de la courbe diffère significativement de l'EISF simulé, ce qui suggère que la dynamique observée ne correspond pas à une simple diffusion par saut entre deux sites. De plus, le signal quasielastique, étudié sur le spectromètre à temps de vol IN6-SHARP, met en évidence une différence supplémentaire entre les données et les simulations : nous observons expérimentalement que les largeurs des deux lorentziennes fittées sont presque constantes avec la température, l'intensité du signal étant le seul paramètre sensible à la température. Ceci est en désaccord avec un modèle classique de saut entre deux sites, alors qu'une diffusion de type soliton pourrait être invoquée pour éclairer les données.

Structure et dynamique de l'eau dans les nanotubes d'imogolite

Après avoir étudié les propriétés structurales des Si-INT, nous nous sommes concentrés sur le comportement de l'eau confinée dans ces structures nanoporeuses, tout d'abord avec la dynamique moléculaire. Les simulations permettent de mettre en évidence comment l'eau confinée à l'intérieur des Si-INTs se structure en couches concentriques (fig. 2a). En fonction de leur géométrie, les molécules d'eau peuvent être classées en trois populations différentes : première et deuxième couche, et eau dans le cylindre interne. De plus, cinq types de configuration d'adsorption sont identifiés, les deux configurations les plus probables étant : une molécule adsorbée à plat dans le site d'adsorption triangulaire (type 1, fig. 2c), et une molécule adsorbée perpendiculairement (type 2, fig. 2d).

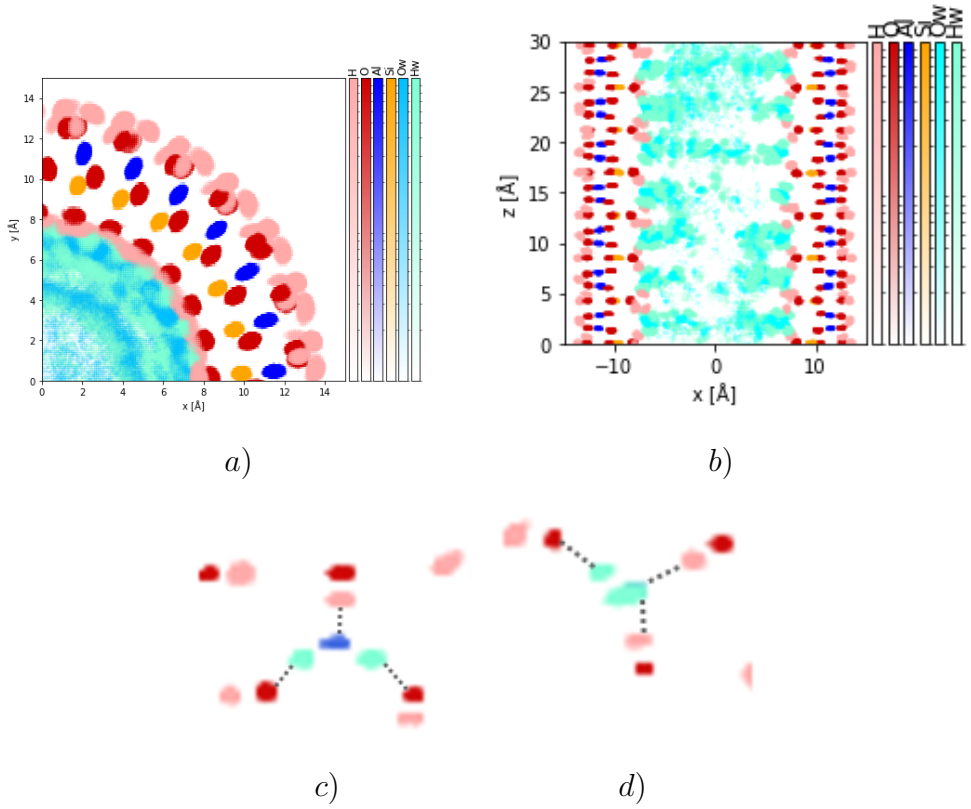

Figure 2: *a*) Structuration radiale de l'eau (oxygènes en bleu clair, hydrogènes en bleu turquoise). *b*) Structuration longitudinale de l'eau. *c*) Configuration d'adsorption : type 1. *d*) Configuration d'adsorption : type 2.

L'eau se structure également le long de la direction z (fig. 2*b*), en raison d'une surface interne périodiquement "rugueuse". En effet, les nanotubes d'imogolite présentent un ordre périodique le long de l'axe du nanotube, dont la période est égale à T = 8.45 Å. Les silanols forment des protubérances avec une période T/2. À faible hydratation - de 0 à 6 wt% - les molécules d'eau ont tendance à remplir les espaces entre les groupes silanol. Lorsque le tube est rempli avec plus de 6-8wt% d'eau, les molécules d'eau sont également distribuées dans la partie centrale des nanotubes et occupent toutes les positions disponibles en z, car la distance à la paroi est suffisamment grande pour ne plus induire une organisation des molecules selon z.

Cette structuration périodique en z a été étudiée par diffraction de rayons X. En effet, la structuration de l'eau a un impact important sur l'intensité de la réflexion (002) du diffractogramme. Les simulations de dynamique moléculaire montrent que si la distribution de l'eau à

l'intérieur de la cavité du nanotube est homogène en z, l'intensité de la réflexion (002) ne change pas. Au contraire, si l'eau se structure en z, son intensité est modifiée. Par conséquent, l'intensité de la réflexion (002) caractérise la portion de l'eau adsorbée organisée périodiquement en z. Un ensemble de données obtenues in-situ, avec une cellule à humidité contrôlée installée sur un diffractomètre, a été collecté afin de mesurer expérimentalement cet effet. Les expériences montrent qu'effectivement, lorsque la pression de vapeur d'eau dans la cellule augmente, l'intensité de la réflexion (002) diminue.

Ensuite, nous avons étudié la diffusion de l'eau dans les nanotubes par dynamique moléculaire. L'EISF et le déplacement carré moyen simulés montrent tous deux que les molécules adsorbées sur la surface hydrophile du tube diffusent très peu selon l'axe du tube (eau lente), alors que celles qui se trouvent au centre du pore sont capables de diffuser rapidement (eau rapide), avec un coefficient de diffusion similaire à celui de l'eau en volume.

Un échantillon rempli avec 12wt% d'eau a été étudié expérimentalement sur IN6-SHARP. Le fit du signal quasi-élastique à 200, 250 et 300K révèle deux lorentziennes, l'une étroite et l'autre large. Afin de comprendre l'origine de ces deux composantes, le même traitement a été effectué sur le QENS simulé. Les simulations de dynamique moléculaire montrent que l'on peut associer la lorentzienne étroite à la diffusion des molécules d'eau lentes, c'est-à-dire celles piégées près de la paroi, et la lorentzienne large à la diffusion rapide le long de z dans le cylindre central du tube. L'analyse quantitative des données expérimentales confirme que le coefficient de diffusion de cette deuxième catégorie de molécules est comparable à l'eau bulk.

Enfin, la densité d'états de l'eau nanoconfinée a été étudiée expérimentalement et simulée. La densité d'états d'un nanotube hydraté avec 6wt% d'eau – où toutes les molécules d'eau sont en interaction directe avec les hydroxyles internes du nanotube– est caractérisée par un premier pic autour de 14 meV, un second à 35 meV et une double bande plus large à 60 et 70 meV. Le pic à 35 meV est spécifique de l'eau adsorbé perpendiculairement à la paroi du tube (type 2) et correspond à un mouvement librationnel consistant en des oscillations de grandes amplitudes.

Cette deuxième partie de la thèse apporte une compréhension assez poussée des propriétés structurales et dynamiques de l'eau confinée à l'intérieur des nanotubes d'imogolite. Elle fournit de nouveaux outils pour étudier la structuration de l'eau et contribue à clarifier la façon dont la diffusion longue distance a lieu dans les imogolites. En conclusion, cette étude montre qu'un système connu depuis soixante ans peut encore être un terrain de jeu pour des études de physique et elle ouvre la voie à

de futures investigations sur d'autres nanocanaux, et en particulier sur les nanotubes d'imogolite de différents diamètres et différentes affinités de surface où les atomes de silicium sont substitués par des atomes de germanium et les groupements hydroxyle par des groupements méthyle.

General introduction

Despite constituting two-thirds of Earth's surface, water is still poorly understood. Many of its properties are anomalous compared to other liquids, and it is always at the center of some of the most challenging research problems in science[1]. To this day, a comprehensive molecular model of water that reproduces all its properties is still lacking[2]. Moreover in nature, water is confined in geological or biological environments – the size of the confining cavities being in the nanometer range. Some examples are clays in soils or proteins in biological systems[3,4]. In this case, anomalies multiply: the thermodynamic properties change while new geometric configurations and dynamical features appear.

In this perspective, one-dimensional compounds are systems of fundamental interest. They can constitute model structures for other more complex phenomena, or they can allow to investigate exotic properties of the confined species. Some examples of one-dimensional systems are the well-known carbon nanotubes that have attracted a lot of attention for over thirty years. Nevertheless, there are many more confining 1D systems that have emerged in recent years or that remain fairly little-known such as clay nanotubes. Among them, imogolite nanotubes are considered as a unique inorganic analog of carbon nanotubes. Imogolite nanotubes are naturally occurring clay minerals, first discovered in 1962 in Japanese volcanic soils. Their stoichiometry is $SiAl_2O_7H_4$, and they can also be synthesized by soft chemistry. Due to their cylindrical one-dimensional pore – with a diameter in the nanometer scale –, imogolite nanotubes are ideal systems for the study of nanoconfinement of water. Many other applications are foreseen, such as in catalysis, separation or filtration.

If one aims at having a full comprehensive understanding of the dynamics of a confined species, first the dynamics of the "container" has to be known. For this reason, the present work has a double purpose. It focuses both on the dynamics of the tube itself and in the study of the properties of the confined water, two key parameters that remain poorly understood in the case of aluminosilicate imogolite nanotubes. Another important point is the combination of experimental results with atomistic simulations in order to propose the first complete picture of the dynamics of these nanotubes without and after water confinement.

The first chapter will be dedicated to the state of the art on nanotubes. It will start by describing different kinds of nanotubes, with a special focus on imogolite nanotubes, followed by description of their

structure and their applications. Then, previous studies regarding the confinement of water inside both hydrophobic and hydrophilic tubes will be introduced. The chapter will end with a special section concerning previous works on water nanoconfined inside imogolites.

In the second chapter, all the experimental methods will be described. At first, the classical techniques used to characterize the sample will be presented. Then, two conspicuous sections will describe X-ray and neutron scattering, in terms of their formalism and a detailed description of all the instruments used during the experiments carried out for this thesis.

Chapter three will be consecrated to Molecular Dynamics simulations. Here, all the simulation specifics will be described in detail.

Chapter four constitutes the first chapter containing the results of this thesis. It will be devoted to the study of the own dynamics of the tube. This will be done by means of Molecular Dynamics simulations, complemented with neutron scattering data collected on four different spectrometers at the ILL.

Chapter five concerns the study of nanoconfined water inside imogolites. The first part, related to the structure of water, will be investigated by X-ray diffraction and MD simulations. The second part will be dedicated to dynamics, simulations and neutron experiments being compared. We will be able to understand how water molecules organize themselves and how they diffuse inside imogolites.

1. State-of-the-art on structure of imogolite nanotubes and their related water confinement

1.1 General introduction

A material of any kind is also considered as a nanomaterial if at least one of its dimensions is between 1 and 100 nm. This general definition is recognized by the scientific community but also by the international authorities as the European Commission that first adopted this definition in 2011 (Recommendation on the definition of a nanomaterial 2011/696/EU). The emergence of nanomaterials was made with the development of tools allowing to go down to very small scales. It became possible to realize that objects of a few nanometers can occur in nature, be artificially synthesized and designed to present novel properties, or accidentally caused by human activities (e.g., welding fumes).

Nanomaterials can take different shapes[5], such as spheres, tubes/rods, platelets or more complex structures like torus, stars or flowers (Fig. 1.1). A typical example is that of carbon with endofullerenes nanoballs, carbon nanotubes or graphene nanolayers. From a material perspective, going to very small scales offers new perspectives in terms of physical behavior. Indeed, materials reduced to the nanoscale can show different properties compared to what they exhibit on a macroscale, enabling unique applications. Consequently, nanomaterials are of great scientific interest for their potential as nanoconfining systems. Small molecules can be confined in these systems and their nanometric size induces, when compared to the properties at the macroscopic scale, an original behavior on the confined molecules. This is due to the fact that for these nano-objects, the surface-to-volume ratio increases greatly, making surface effects predominant. In the following, we will focus exclusively on nanotubes, the kind of nanomaterials we studied during this thesis.

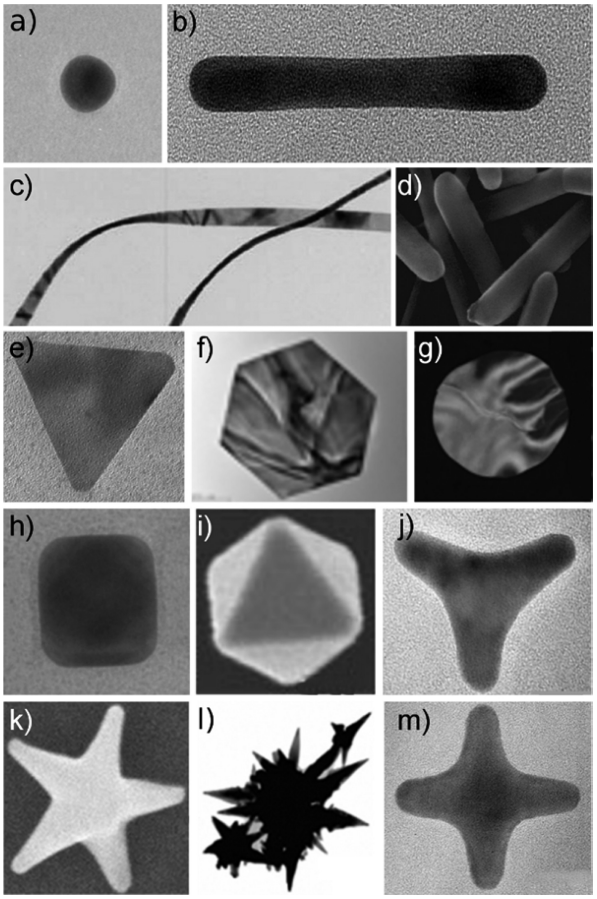

Figure 1.1: Examples of nanomaterials with various morphologies: (*a*) nanosphere, (*b*) nanorod, (*c*) nanobelt, (*d*) nanowires, (*e*) 2D triangle, (*f*) 2D hexagon, (*g*) disc, (*h*) nanocube, (*i*) octahedron, (*j*) tripod, (*k*) nanostar, (*l*) nanothron, (*m*) tetrapod. Adapted from Kinnear et al.[5]

1.2 Nanotubes

Among all nanometric systems, nanotubes represent a unique model system, having a cylindrical pore of the size of a few nanometers, the same order of magnitude as some elementary molecules. This allows them to be considered as potential nanocontainers for the study of molecular confinement and transport, catalysis or for energy applications[6–10].

The most well-known nanotubes are certainly carbon nanotubes (CNT) (Fig. 1.2), formed by one (single-walled nanotubes) or several layers (multi-walled nanotubes) of rolled graphene[11]. Hollow carbon filaments

were discovered in 1952 by Padushkevich et al.[12] while their structure and synthesis procedure were proposed in the seminal work of Iijima in 1991[13].

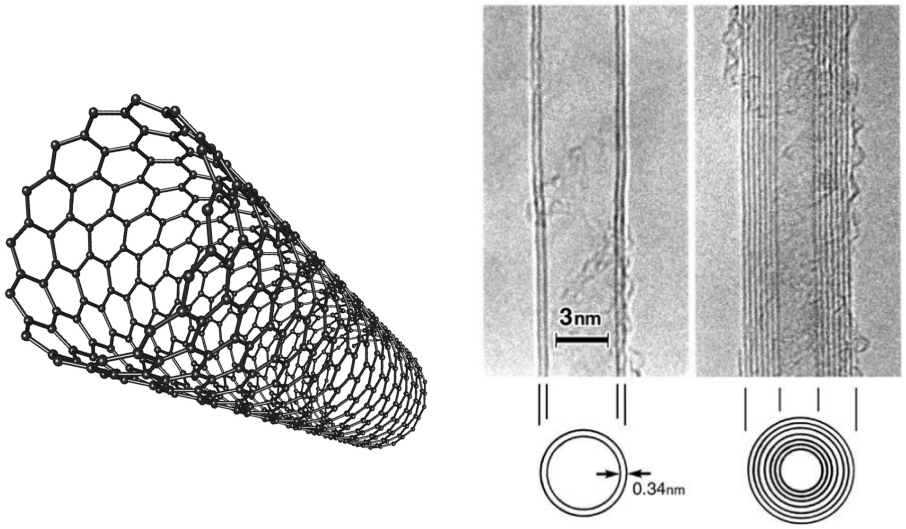

a) *b*)

Figure 1.2: *a*) Atomic organization in the carbon nanotube structure. *b*) Transmission electron microscopy images of multi-walled CNTs from Iijima et al.[13]

Many studies have been devoted to the study of these nano-objects, highlighting their unique mechanical[14], thermal[15], electronic[16] and optical[17] properties, that make them the material of choice for many applications. Indeed, several applications based on CNTs have been reported including functional composite materials[18], electronic nanodevices[19], biosensors[20], transistors[21] or as nanochannels for nanofluidics solutions[7,22].

Despite their success, carbon nanotubes have also to face several constraints. These concerns mainly relate to the manufacturing process of CNTs at high-temperature together with low yield and the lack of control over the tube diameter and chirality[23]. Furthermore, a growing concern about their potential health impacts emerges with proofs of nanotubes internalization in macrophages cells[24] together with the development of pulmonary diseases[25,26].

These issues have motivated research towards inorganic tubes with similar characteristics. Thus, various types of inorganic nanotubes have been synthesized recently[27,28], like chalcogenides (WS_2[29], MoS_2[30] as in Fig. 1.3), oxides (TiO_2[31,32], ZrO_2[31], ZnO[33], SnO_2[34]), hydroxides

($Co(OH)_2$, $Ni(OH)_2$[35]), sulfides (In_2S_3[35], SnS_2 and SnS_2/SnS[36]), nitrides (BN[37], GaN[38]) and many others. Clay minerals, on the other hand, are naturally occurring nanomaterials that present diverse morphologies including also nanotubes. Chrysotile and halloysite (Fig. 1.3) are two examples of this class[39,40]. They consist of the assembly of silica tetrahedrons with magnesium or aluminum hydroxide octahedrons, respectively. Unfortunately, most of these inorganic nanotubes form multiwalled tubes with polydispersed diameters and in most cases with inner cavity larger than 10 nm. However, there are few exceptions such as imogolite clay nanotubes, a system whose diameter is monodisperse while remaining of the order of a few nanometers with one or two walls. This material, which can be considered as an inorganic equivalent of CNTs, will be at the center of this thesis.

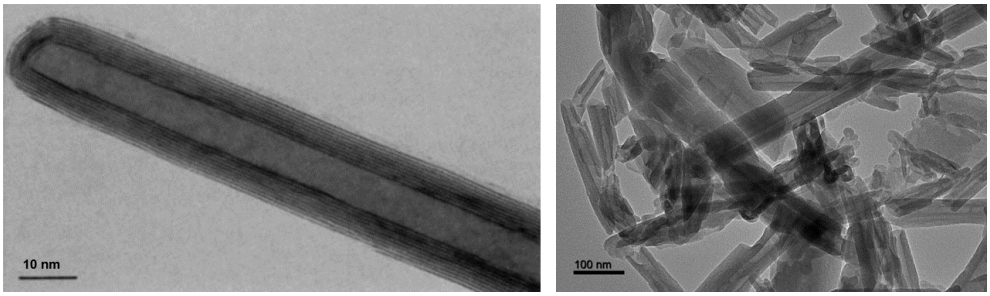

Figure 1.3: (Transmission electron microscopy images of (*left*) a WS_2 nanotube (adapted from Tenne et al.[29]) and (*right*) an halloysite nanotube.

1.3 Imogolite nanotubes: a nanoplatform with unique physical properties

1.3.1 General information

Imogolite nanotubes (INT) are naturally occurring aluminosilicate clay materials. They were discovered in 1962 by Yoshinaga and Aomine[41], in volcanic soils in Japan (Fig. 1.4 a). The name "imogo" (translating to "small potato") originates from the aspect of the parent material, a brownish yellow volcanic ash soil (Fig. 1.4 b, c). Imogolite is common in the clay fraction of soils derived from glassy volcanic ashes or pumice beds all over the world[42–48].

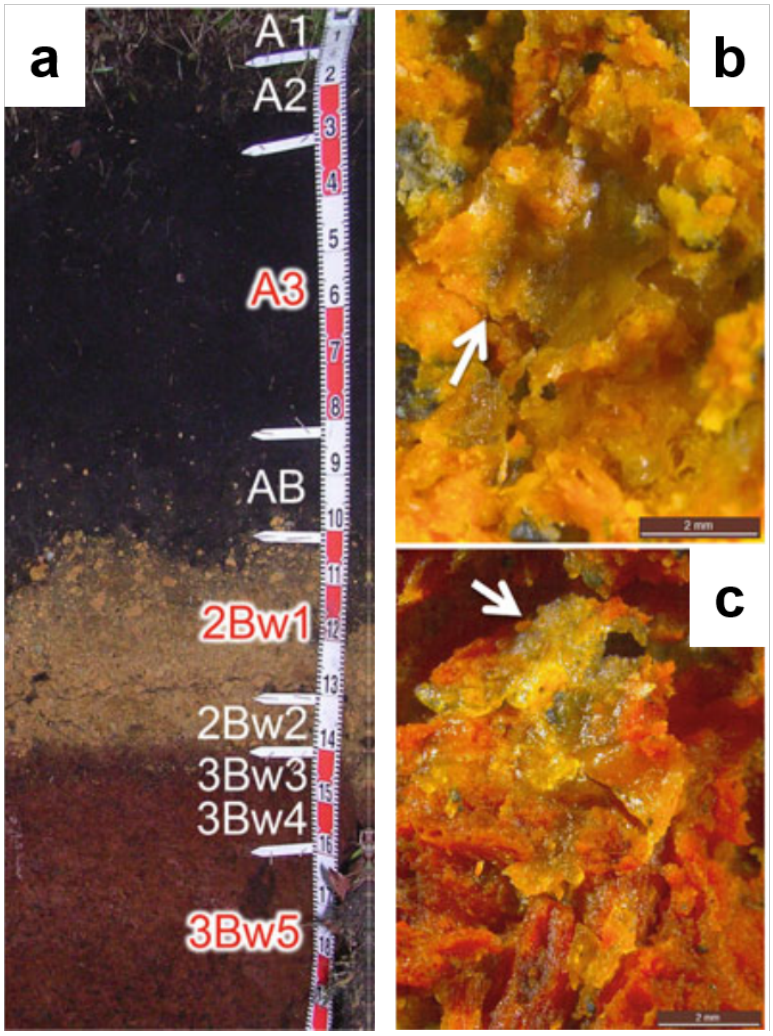

Figure 1.4: (a) Soil profile from Kiwadashima, Tochigi, Japan, $(b-c)$ Optical observations of gel films (white arrows) found respectively in the 2Bw1 and 3Bw5 horizons as shown in panel (a). Adapted from Nanzyo and Kanno[48].

The tubular nature of imogolite took some time to be highlighted. Since their discovery, it was reported, based on transmission electron microscopy (TEM), that these objects formed thread-like structures with fibre units of uniform size (Fig. 1.5a, b)[41,49]. The morphology of imogolite was evidenced a few years later by high-resolution TEM experiments[50]. In this article, the authors revealed that "*the fibre unit is tubular, with a pair of parallel lines representing the walls of the tube*" and which was subsequently confirmed by other groups (Fig. 1.5 c, d)[51,52].

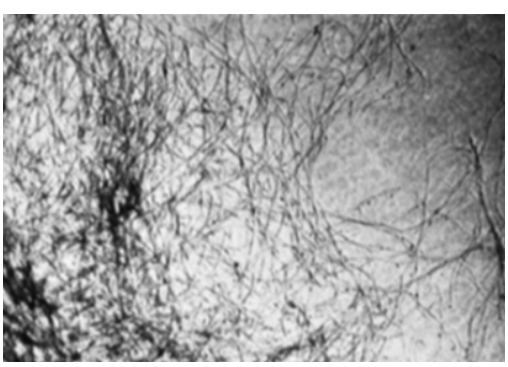

a) Yoshinaga et al.[41]

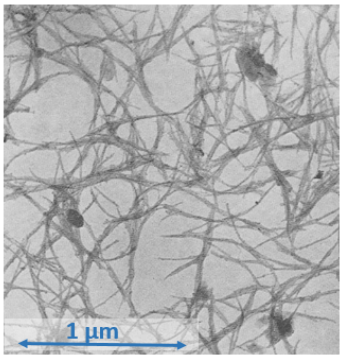

b) Russell et al.[49]

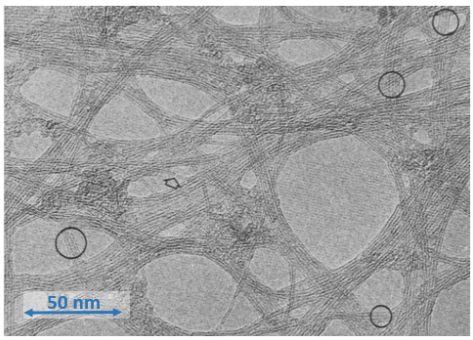

c) Wada et al.[50]

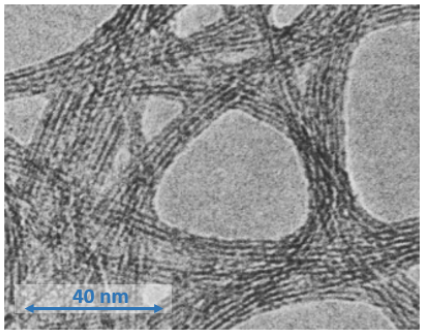

d) Farmer et al.[52]

Figure 1.5: TEM images of imogolites in literature

The first attempt to understand the chemical structure of imogolite was proposed in 1969 by Wada et al.[53]. They hypothesised that these aluminosilicate minerals are made of a one-dimensional chain of octahedral AlO_6 groups laterally bonded to tetrahedral SiO_4 groups. The elementary groups were correct but obviously the overall structure was wrong. It wat not until 1972 that a consensus structure was reached on the community. Fig. 1.6*a* presents the structure proposed by Cradwick et al.[51], which consists of:

- an external di-octahedral gibbsite-like layer, *i.e.* composed by octahedra of aluminium oxide AlO_6
- an internal "layer" of isolated tetrahedra of silicon oxide SiO_4 connected upright to the octahedral vacancy by sharing three mutual oxygen atoms (see Fig. 1.6*b*)

Both octahedra and tetrahedra units have hydroxyl groups, making the tube surface hydrophilic. Its nominal composition is found to be $(HO)_3Al_2O_3SiOH$, which is the sequence of atoms encountered on passing from the outer to

the inner surface. Natural imogolites are single-walled nanotubes with inner and outer diameters of 1 and 2 nm, respectively, while the length can vary from tens of nanometers to several micrometers.

Like any natural material, imogolite nanotubes can be extracted from glassy volcanic ash soils but the samples must be purified to remove any organic and inorganic impurities[54]. These very time consuming steps do not allow to obtain large quantities of samples. Therefore, the reproduction of these tubes synthetically has become an obvious goal. Fifteen years after their discovery, the first synthetic INTs were obtained by Farmer et al.[55].

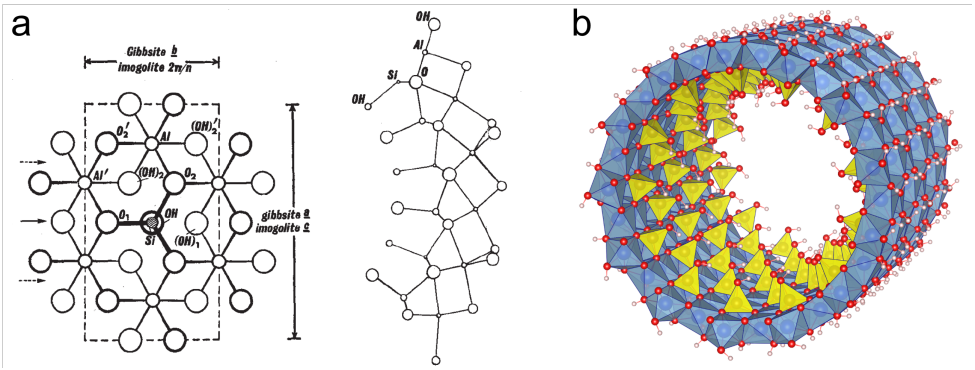

Figure 1.6: (*a*) Structure of imogolite postulated by Cradwick et al.[51]; (*b*) Schematic 3D view of a single-walled imogolite nanotube. Yellow, blue, red and white atoms correspond to Si, Al, O and H atoms, respectively. Adapted from Paineau[56].

The protocol consists in the coprecipitation of silicon and aluminium precursors with NaOH in aqueous solution (Fig. 1.7). In a second step, the pH is adjusted to 4.5 by addition of a mixture of HCl and acetic acid promoting condensation of Al and formation of proto-imogolite structures. The mixture is then aged under hydrothermal conditions either by reflux or in autoclave to allow the growth of nanotubes. After sufficient time, the product is recovered at room temperature and purified by washing against water. Interestingly, the external diameter of synthetic INTs is slightly larger (2.5 nm) than for natural ones.

Several improvements have been proposed to increase the yield of the synthetic product by changing the nature, concentration and stoeichiometric ratios of chemical precursors[57–59], the duration of the ageing[60,61] or the method of heating[62]. In particular, the replacement of Si by Ge atoms, initially explored by Wada et al[63], allows not only the formation of single-waled Ge-analogues with larger inner diameters, but also the formation of double-walled structures depending on the initial con-

ditions[64–67].

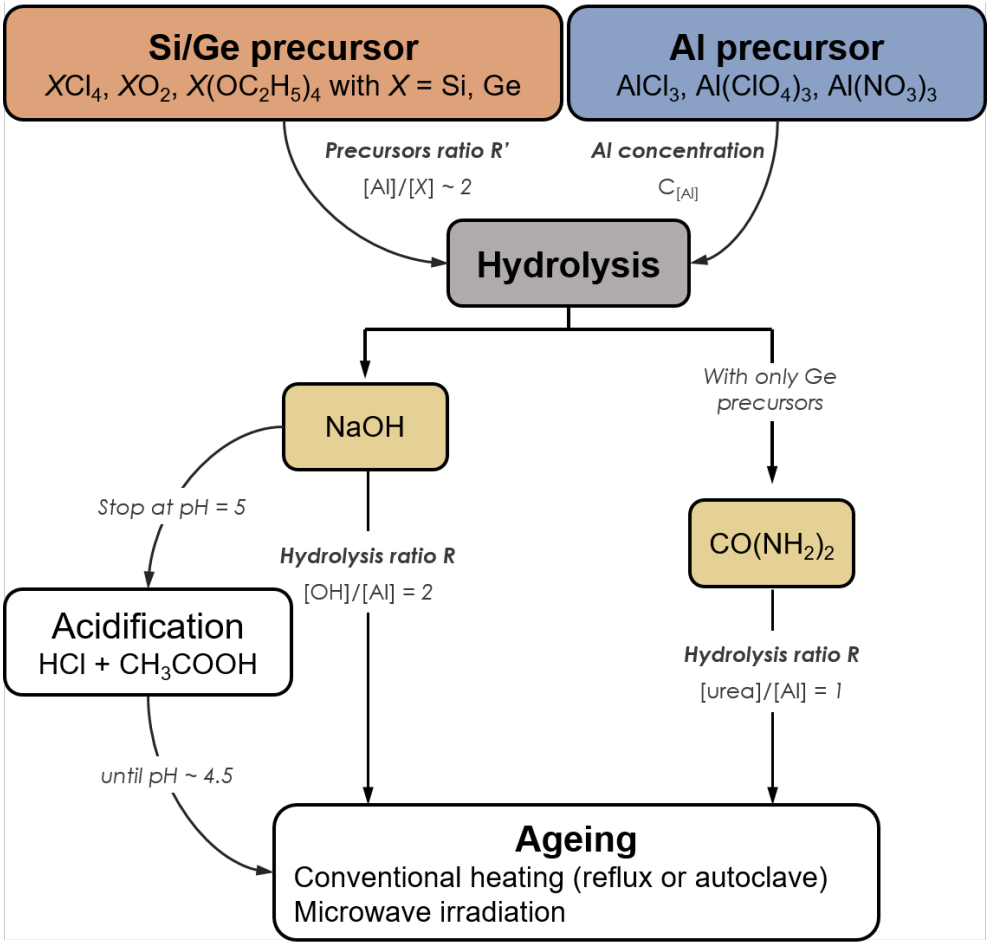

Figure 1.7: Synthetic flowchart for the synthesis of imogolite-like nanotubes. Adapted from Paineau and Launois[66].

Finally, it is possible to substitute the OH groups by other chemical functions in order to modify the chemical affinity of the inner and/or outer wall of the nanotubes[68]. Typically, imogolite nanotubes with a fully methylated inner wall were synthesized, both for Si- and Ge-analogues[69,70]. In summary, the synthesis of imogolite-like structures is a low-temperature process (compared to CNTs) that has been developed and optimized for over 40 years, providing a large variety of nanotubes with monodisperse diameters and adjustable interfaces. In spite of these advances on the production of synthetic imogolite, their structure is still debated.

1.3.2 Atomic structure of imogolite nanotubes

When starting from a gibbsite-like flat surface, there is more than one way to roll the tube. Conceptually, a nanotube can be obtained by cutting a ribbon perpendicularly to a vector joining to equivalent sites on the sides of the ribbon. This vector has indices (N,M) in the hexagonal basis of the gibbsite sheet (Fig. 1.8). It is named 'chiral vector' for carbon nanotubes.

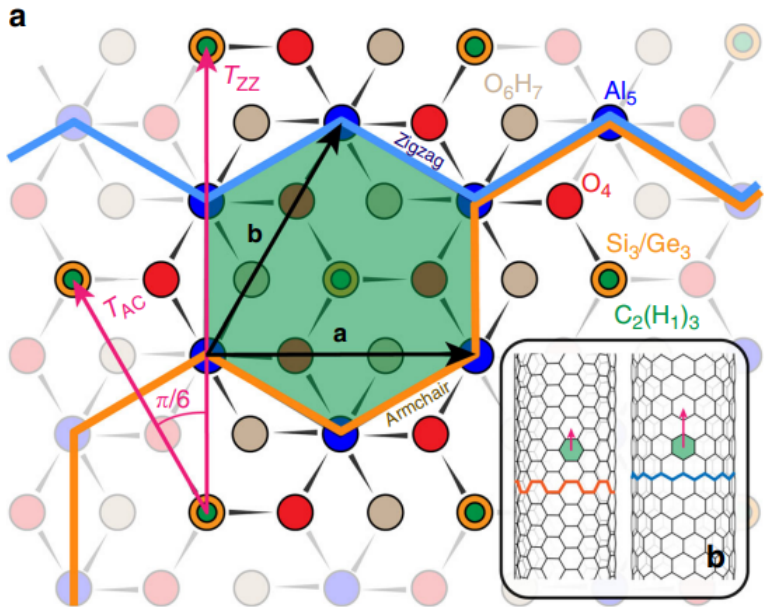

Figure 1.8: *a*) Hexagonal unit cell of the imogolite nanotube (color scheme: green for inner OH, gray for outer OH, blue for Al, red for O, and orange for Si). The (N,M) indices define the 'chiral vector' $\vec{C}_{NM} = N\vec{a} + M\vec{b}$ which joins two equivalent sites, and $(\vec{a}, \vec{b})$ is the lattice basis. The inset *b*) shows an armchair (N,N) (orange) and a zigzag (N,0) (blue) nanotube. Reproduced from Monet et al.[71]

In the seminal work of Cradwick et al.[51], the authors explored three different zigzag structures (N = 10, 11 or 12) and compared their results with electron diffraction patterns. Although the structure for N = 10 provides the best agreement with electron diffraction data, the authors noticed that "*no claim can be made that it is a close approach to the true structure* [of INTs] *than the other two possibilities*[51]. In other words, they cannot define how many unit cells are present around the circumference. According to other experiments, natural imogolite nanotubes seem composed of either N = 10 or N = 12 gibbsite units along the circumference[52,72], while synthetic analogues have N = 12 or N = 14

units[72–75]. Several simulations, using many-body potential or classical force fields suited for imogolites, evidenced that the origin comes from the strain energy per atom depending on the tube radius[76–78]. The strain energy per atom is defined as the difference of the total energies between the tube and the planar layer. Therefore, it represents the energy penalty required for the rolling of the planar sheet onto a cylinder. For all NTs, carbon nanotubes included, this function decreases monotonically. By contrast, the strain energy for imogolite nanotubes presents a minimum according to these simulations. An example is presented in Fig. 1.9, which evidences the minimum in energy found for a (12,0) zigzag and a (8,8) armchair INT. Interestingly, this figure also shows that the "zigzag" configuration is the most stable.

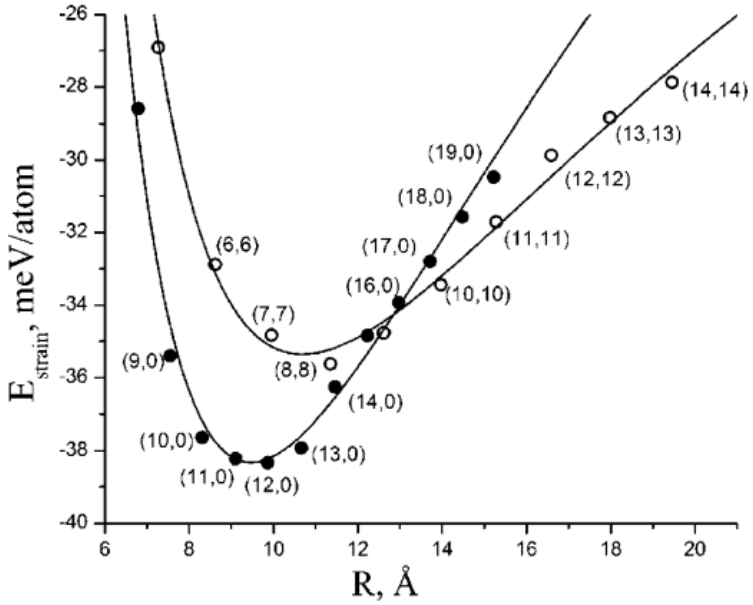

Figure 1.9: Evolution of the calculated strain energy as a function of the nanotube radius for zigzag (filled circles) and armchair (open circles) imogolite nanotubes, according to Guimaraes et al.[78]

It was also proposed by Guimaraes et al.[78] that the difference between carbon and imogolite nanotubes is that the former have the same internal and external surfaces, whereas the inner and outer surfaces of imogolite are different. This induces the appearance of an additional surface tension term in the strain energy which causes the emergence of this minimum. The position of the minimum as well as the chirality of INTs depend on the substitution rate of silicon atoms by germanium

atoms and the functionalization of the inner wall[71,79]. This monodispersity in diameter and chirality is probably the most significant property of imogolite nanotubes.

In this thesis, we will study only synthetic single-walled aluminosilicate imogolites, referred as Si-INTs hereafter. We can define a coordinate system by calling (x, y) the couple of axes generating the plane perpendicular to the tube axis, and z the axis describing the axis along the tube (Fig. 1.10). The atomic structure of Si-INTs is therefore the following. An integer number N of unit cells $(OH)_3Al_2O_3SiOH$ is present along the circumference. From now on, the internal hydroxyls will be indicated as H_{in}, while the external hydroxyls as H_{out}. N is typically between 12 to 14, corresponding to an internal diameter of $\sim$ 1.5 nm (Fig. 1.10). In addition, imogolite nanotubes are periodic along their z axis, the unit cell being T = 8.45 Å as highlighted in orange in Fig. 1.10.

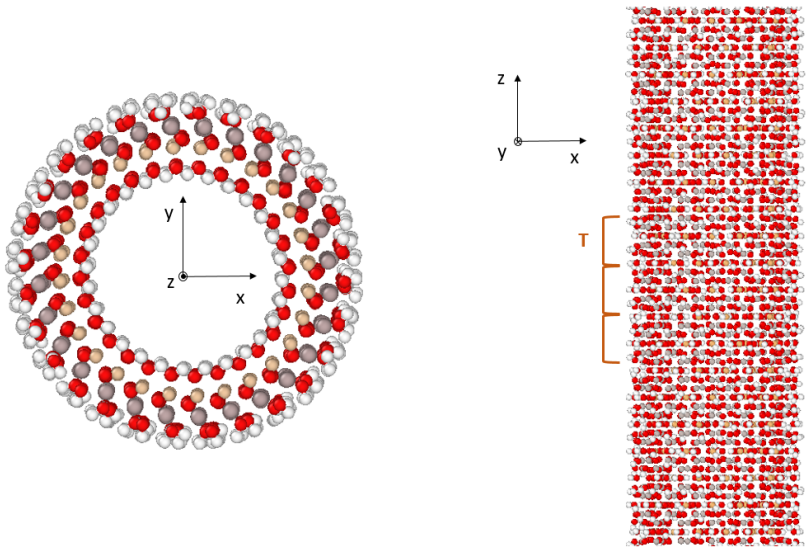

Figure 1.10: Top and lateral view of the structure of a Si-INT with N = 14. White, red, brown and grey atoms correspond to H, O, Si and Al atoms, respectively. T corresponds to the period along the z-axis of the nanotube

For comparison, single-walled aluminogermanate analogues (Ge-INTs) have a zigzag structure with N = 22, which corresponds to inner diameter of $\sim$ 3nm. Indeed, in the case of SW Ge-INTs, the atomic structure was recently been re-determined[71,80], showing that SW hydroxylated Ge-INTs are zigzag with (22,0). On the other hand, methylated Si-INTs and methylated Ge-INTs are armchair with (9,9) and (11,11), respectively. However, for hydroxylated Si-INTs, no study has been carried out and

the precise structure of these nanotubes remains unclear. Nevertheless, a precise knowledge of the structure is crucial for the properties of nanotubes.

1.3.3 Applications of imogolite nanotubes

The monodispersity in diameter is probably the most remarkable structural property of imogolite nanotubes. Moreover, the possibility of controlling during the synthesis both the diameter of these objects and the physico-chemical properties of their surface has led to the consideration of various applications, some examples being illustrated below. For the interested reader, several recent reviews have addressed this topic[81–83].

Because of its unique structure with well-defined porosity and interfaces, it appeared very quickly that imogolite nanotubes could have original properties for the confinement of molecules with applications in the adsorption or separation of pollutants in soils and liquids. For instance, a large number of studies focused on the use of INTs as gas storage with enhanced selectivity behavior for adsorbed molecules such as NH_3, C_6H_6, CO, CO_2 or CH_4[69,84–86]. Several works also demonstrate that fonctionalized INTs, dispersed in a liquid medium, spontaneously confine inside them organic molecules added to the suspension[70,87]. Another possible application is to exploit INTs as nanoreactors. The inner and outer surfaces of INTs present unique acid/base properties as well as polarization behavior, offering different pathways for catalytic reactions, and to a lesser extent photocatalysis[88,89]. Typically, imogolite nanotubes and their derivatives have been applied for catalytic oxidation of aromatic hydrocarbon[90], isomerization of glucose to fructose[91] or degradation of various azo-dyes[92,93].

Imogolite nanotubes present similarities with their carbon counterparts in terms of morphology and aspect ratios, i.e. the ratio between the length and the diameter. However, unlike the latter, INTs are easily dispersed in water, forming stable colloidal suspensions. For anisometric objects such as imogolite nanotubes, a competition should occur between orientational entropy and the packing entropy governed by excluded-volume interactions (see the Onsager theory[94]). Indeed, highly elongated aluminosilicate and aluminogermanate INTs can self-organize spontaneously, forming a rich phase diagram of various liquid-crystalline phases and at very low nanotube concentration (Fig. 1.11a)[67,95]. These mesophases have been used recently for developing novel nanocomposite fibres with enhanced mechanical properties as well as self-healing behavior (Fig. 1.11b)[96]. Another interesting feature of INTs is the high density of hydroxyl groups on their outer surface, that can be used as

binding sites for external surface functionalization. Such modifications facilitate the dispersion of INTs (nanofillers) in various polymer matrix (Fig. 1.11*c*)[56,97].

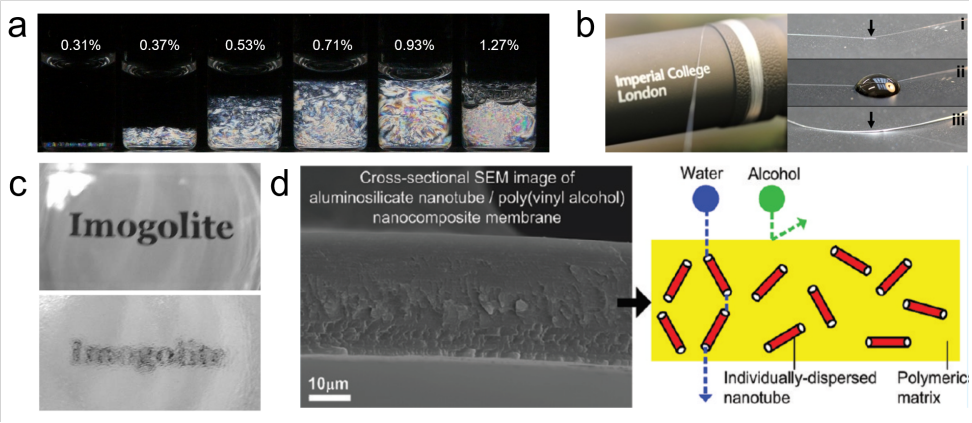

Figure 1.11: Some applications of imogolite nanotubes for (*a*) liquid-crystals, (*b*) highly oriented INT/polymer fibres with self-healing behavior, (*c*) hybrid nanocomposites, (*d*) filtration membranes

Therefore, researchers have explored the possibility to manufacture imogolite-based membranes that start to receive more attention recently. For example, INTs could be incorporated in polymeric membranes for water desalination, working by reverse osmosis[98]. Several studies reported that addition of imogolite nanotubes in water filtration membranes induces a substantial increase of the water flux while achieving significant ion exclusion (Fig. 1.11*d*)[99–102]. However, fundamental researches on water confined in these nanostructures are still in their infancy as we will see below.

1.4 Nanoconfined water

Even though water is ubiquitous on Earth, all its chemical and physical properties are actually extraordinary and anomalous[1,103]. For example, water has higher viscosity, melting point, boiling temperature, dielectric constant and a larger specific heat when compared to other substances.

Water is one of the smallest molecules, formed by two hydrogen atoms covalently bonded to one oxygen atom (Fig. 1.12). The molecule is electrically neutral, but oxygen atoms are more electronegative than hydrogens, inducing a partial negative charge close to the oxygen atoms. This

is why the molecule has a non-zero dipole moment. Polarity is the property of water responsible for the formation of hydrogen bonds[104]. These hydrogen bonds are highly directional and a maximum of four bonds per water molecule can be formed (Fig. 1.12).

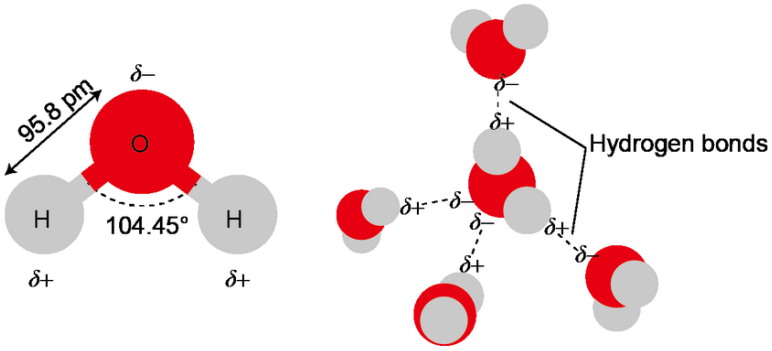

Figure 1.12: Water molecule structure and geometry of hydrogen bonding

Its phase diagram is extremely rich with more than fourteen different crystalline phases of ice (Fig. 1.13)[105]. The ordinary form of ice is called "hexagonal ice" (I_h). Several studies have focused on the structure and thermodynamics of the stable and metastable phases of ice, like "cubic ice" (I_c)[106–109]. This variety of structures is due to the molecule's polarity, its amphoteric character and the flexibility of the hydrogen bond which allows an extraordinary variety of intermolecular interactions and structures[110].

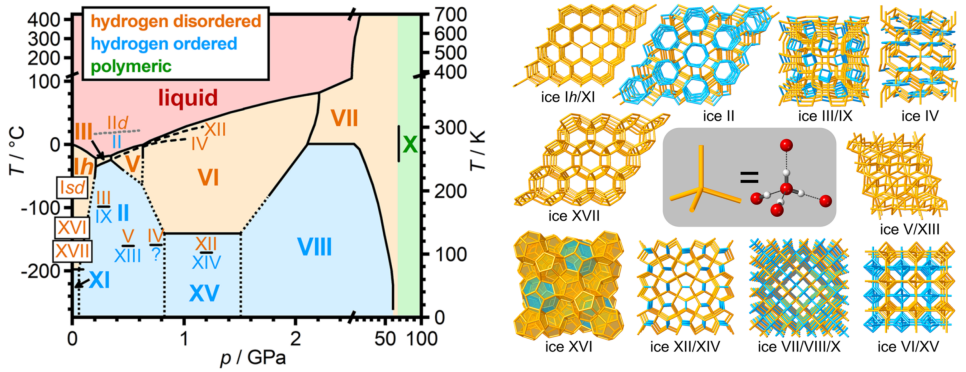

Figure 1.13: (*left*) Pressure-temperature phase diagram of ice and (*right*) the related hydrogen-bonded networks of the various polymorphs of ice. Adapted from Salzmann[105]

These are only the anomalous features for bulk water molecules. If we now look at nanometer scale confinement, water exhibits even more

unexpected behavior than bulk water[111–114]. Its confinement in a 1D geometry of characteristic dimension of the order of 1 nm induces important modifications of its structural, dynamic and thermodynamic properties. A deeper understanding of nanoconfined water is of great interest as in nature there are many cases where water is confined in geometries whose at least one dimension is smaller than 100 nm. This is particularly the case for biological compounds, ranging from proteins to nucleic acids, membranes and tissues. It is well known that the functionality of proteins is activated only when they are surrounded by a layer of hydration layer while their dynamics is strongly correlated with the presence of water[115–121]. Another example is the rapid water transport through aquaporins, a water selective membrane channel protein[3,122,123]. Nanoconfined water is also of prime importance in geological materials such as shales[124], clay minerals[125,126], or other aluminosilicate minerals[127]. In parallel, having porous synthetic systems allows control over the size and nature of the pores. For more than 20 years, many systems have been investigated, like Vycor glass[128], laponite (a synthetic layered clay mineral)[129], carbon nanotubes[130] or silica matrices[131–135]. For example, the phase diagram of water confined in carbon nanotubes was investigated, finding a lower or higher melting point compared to bulk water, depending on the diameter of the tube (Fig. 1.14)[136].

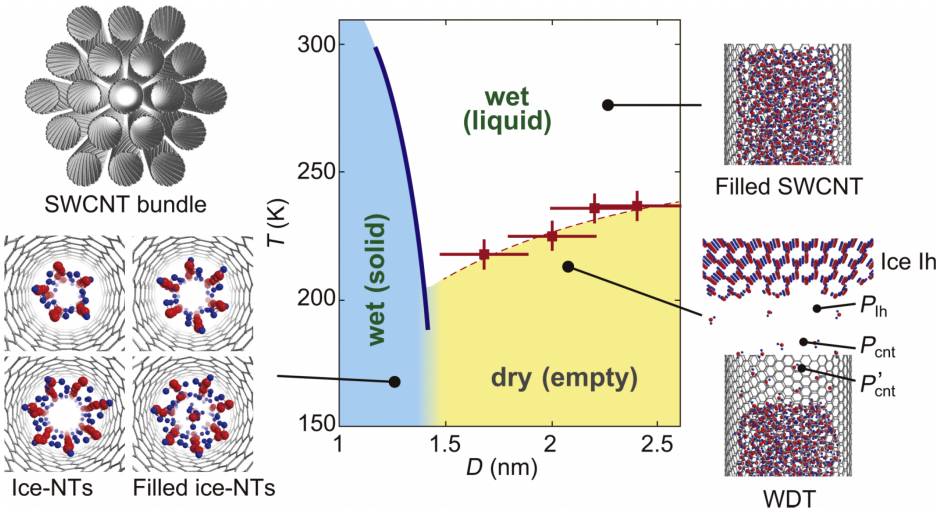

Figure 1.14: Schematic temperature-nanotube diameter phase diagram of single-walled carbon nanotubes. Adapted from Kyakuno et al.[136]

In the next subsections, we will see more in detail the behavior of water inside hydrophobic or hydrophilic nanoconfining systems. Interactions between water molecules and a surface can be of two natures:

electrostatic (including van der Waals interactions) and hydrogen bonds. A system is **hydrophobic** when its surface is non-polar, meaning that the interactions between water and the solid surface are dominated by van der Waals interactions. It implies that interactions are not directional and relatively weak. Therefore, they cannot directly impose water structuring. Nevertheless, the presence of the surface removes water molecules from the neighbors: this induces molecular frustration compared to the bulk phase, that can results in some preferential orientation of molecules near the surface. On the other hand a **hydrophilic** surface is a polar surface that interacts directly – through hydrogen bonds – with the water molecule. These cause a strong water structuring, typically into layers.

The literature on confined water is very broad and cannot be addressed in its entirety. In the following, we will discuss the features of water molecules confined inside two reference systems, namely carbon nanotubes (as hydrophobic pores) and mesoporous silica such as MCM-41 or SBA-15 (as hydrophilic nanochannels).

1.4.1 Water in hydrophobic confining systems

The hydrophobic nanotubes par excellence are certainly single-walled carbon nanotubes.The effects of dimensional restriction on the properties of water can be easily investigated as the diameter of the CNTs can vary from ~ 0.8 up to > 4 nm. This parameter significantly affects the properties of water molecules diffusing inside them. This is due to the hydrophobic nature of the walls, which repels water molecules towards the center of the tube. Water inside CNTs can assume many different configurations depending on the nanotube diameter (Fig. 1.15), each of them having their own distinct characteristics in terms of hydrogen bond network geometry, diffusive properties and freezing temperature.

For very small diameters, *i.e.* $d \sim 1$ nm, a chain of strongly hydrogen bonded molecules is found, having an anomalous single-file diffusion[137,138]. Indeed, the width of the channel is so narrow that the molecules cannot cross each other. For larger diameters, *i.e.* d between 1 and 1.2 nm, water forms concentric n-gonal ice-link rings, whose geometrical structure depends on the thermodynamic parameters, such as temperature or pressure[139–145]. Ice nanotubes disappear in favor of layer-like structures when the diameter goes beyond 1.2 nm. This is particularly true for diameters close to ~ 1.5 nm as illustrated by the radial density profiles derived from Molecular Dynamic simulations[146]. For diameters larger than ~ 4 nm, the confinement effects become less and less pronounced, and water behaves more similarly to bulk water[147].

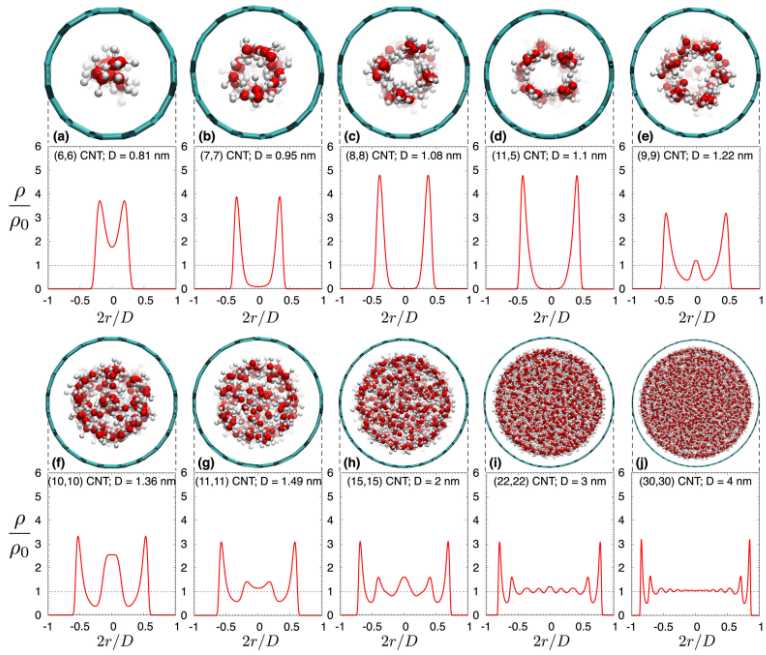

Figure 1.15: Radial density profiles and MD screenshots of the confined water molecules at increasing CNT diameters, reprinted from Borg et al.[146]

It should be noted that most of the studies carried out on confined water in CNTs are theoretical studies using different water models in their calculation. By contrast, the amount of experimental studies is limited, probably by the difficulty to have samples of high purity, very well sorted in size while having advanced tools to measure them.

Several studies have found that confined water molecules present a strongly distorted tetrahedric network[148] and a shift of the liquid-solid transition well below the freezing temperature of bulk water[149,150] as well as the formation of new exotic tubular ice phases having pentagonal, hexagonal or even helix shapes depending on the radius of the tube[145,151]. The paper from Kolesnikov et al.[130] studied the dynamics of water inside CNTs of diameter $\sim$ 1.4 nm, happening to be composed of a square-ice sheet wrapped into the tube and a chain of molecules inside the square-ice shell. The authors highlighted the occurrence of anomalously enhanced thermal motions along the chain direction, with an enhanced diffusive and fluid-like behavior water molecules at temperatures far below the freezing point of hexagonal ice I_h. Water structuring during nanotube filling[152–154] as well as fast water transport[155–157] were reported for both single and multi-walled carbon nanotubes. An example based on X-ray scattering experiments is presented in Fig. 1.16. In this work, the authors evidenced that an homogeneous water filling at

low water content, whereas the water structures into three layers above 5wt% in mass of water[95].

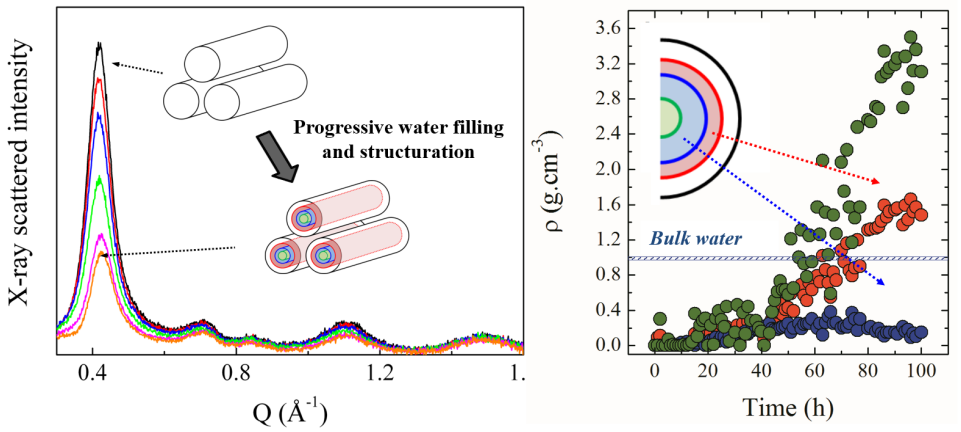

Figure 1.16: (*left*) In situ monitoring of water filling in CNTs using X-ray scattering. (*right*) Evolution as a function of time of the water density in the different layers from the edge of the wall to the center of the tube. Reprinted from Paineau et al.[153]

Many papers reported and attributed the frictionless diffusion of water inside CNTs to the hydrophobic nature of the tube wall[158]. In particular, in some works the exceptional flow was attributed to the smoothness of CNT walls[159,160]. Other studies proposed that the velocity of water increases close to the wall because the presence of the tube wall causes a favorable water orientation and system of hydrogen bonding[161]. Some others suggested that water molecules close to the wall have dangling hydroxyls that make the diffusivity grow by increasing the degrees of freedom of these molecules[147]. In addition, some also attribute this to a bending effect of the tube[162]. Regardless of the mechanism causing the enhanced flow, diffusion cannot be described by the Fick's law, and we can speak about anomalous diffusion. Mathematically, it is defined through the time dependence of the Mean Squared Displacement – which normally depends linearly on time in the case of Brownian diffusion – while has a power-law dependence in the case of anomalous diffusion

$$MSD = At^{\alpha} \tag{1.1}$$

where α>1 in the case of superdiffusion – like in the case of carbon nanotubes. α=2 in the limit of ballistic diffusion[1] (the case α<1 will be introduced in the next section).

[1]More details on the brownian and ballistic diffusion will be given in section 2.6.1.2

Thanks to this superdiffusive behavior, possible applications in nanofluidics have been highlighted[7,163–168].

1.4.2 Water in hydrophilic confining systems

Several studies focused on water inside hydrophilic systems, especially silica matrices. A typical example is MCM-41, a mesoporous silicate material, consisting of an array of uniform hexagonal channels of quite monodispersed size, arranged in a honeycomb-like lattice (Fig. 1.17).

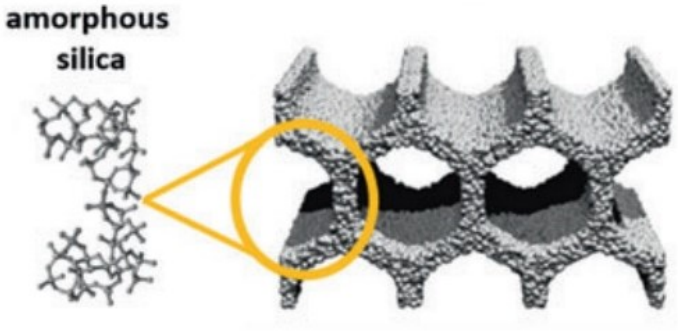

Figure 1.17: MCM-41 honeycomb structure. Reproduced from Schwanke et al.[169]

It has been pointed out that the strong interactions with pore wall cause inhomogeneities in the water density. In other words, the density across the confining volume is not uniform. Oscillatory distributions of both axial and radial densities have been reported[170,171]. Indeed, depending on the degree of ordering in this first layer, an oscillatory density distribution develops, as molecules[2] organize in concentric layers[172–176]. As opposed to hydrophobic pores, water molecules are attracted towards the tube walls, and a layer of denser water wets the silica surface.

Moreover, water in contact with the pore surface forms a first well-defined wetting-layer, that partly screens the hydrophilic interaction to the internal layers of water molecules, so that they act more similarly to bulk water[177] (Fig. 1.18). This wetting-layer of bound water has very peculiar features, of which some are "in common" with water confined in hydrophobic cavities. For instance, water molecules in this wetting-layer have a significantly distorted tetrahedric coordination[170,172,178].

[2]Not only water molecules, but also benzene or glycerol for example.

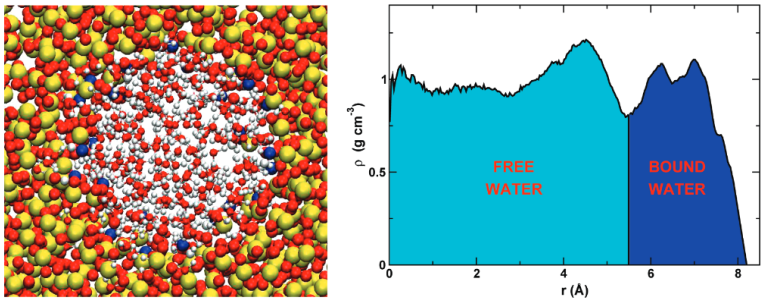

Figure 1.18: MCM-41 pore simulated with MD simulations, and separation in bound water and free water inside its pore, from Gallo et al.[177]

Interestingly, this hydration layer is non-freezable; indeed, since it interacts strongly with the pore wall, it remains amorphous below the freezing point and actually at all the temperatures investigated, since it is unable to assume the regular structure of ice[179–182]. Moreover, its dynamics is significantly slowed down due to the attractive interactions with the wall[131,183–186]. This effect is stronger when the pore diameter decreases as the fraction of molecules in contact with the wall becomes predominant[187]. This is often described as subdiffusive dynamics: the dynamics is slower than the Brownian diffusion taking place in bulk water. Therefore, as for hydrophobic carbon nanotubes, the diffusion is anomalous in these hydrophilic pores, where

$$MSD = At^{\alpha} \tag{1.2}$$

and $\alpha<1$ in the case of subdiffusion[188]. Fig. 1.19 summarizes the three broad types of diffusional behavior.

Overall, in strong hydrophilic confinement, water was found to have a double behavior: the first layers close to a strongly hydrophilic surface are extremely slowed down and show subdiffusive behavior, while the rest of water show a dynamics that is similar to bulk water[172,177,188,189].

The diffusion coefficient of water was previously experimentally measured in MCM-41 or SBA-15[3] in several works, showing an overall slowing down of water compared to bulk water, especially for the smallest pore sizes. The results are summarized in Table 1.1.

[3]Typically the pore diameter is between 2 and 4 nm for MCM-41 and around 6 nm fo SBA-15.

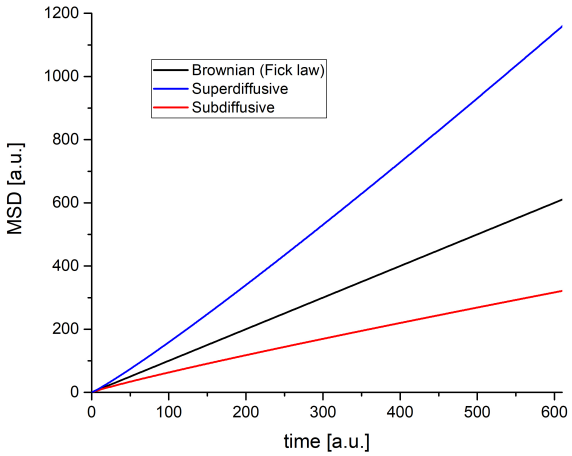

Figure 1.19: Typical time dependence of the MSD for brownian, superdiffusive (blue) and subdiffusive (red) behavior.

confining system	Diffusion coefficient $[cm^2 s^{-1}]$
Exp. bulk water[190–193]	$2.3 \cdot 10^{-5}$
MCM-41 (Takahara[131])	$0.9 - 1.7 \cdot 10^{-5}$
MCM-41 (Takahara[194])	$(1.20 \pm 0.03) - (1.8 \pm 0.1) \cdot 10^{-5}$
MCM-41 (Jani[195])	$1.98 \cdot 10^{-5}$
MCM-41 (Baum[196])	$(1.2 - 1.5) \cdot 10^{-5}$
SBA-15 (Baum[196])	$2 \cdot 10^{-5}$

Table 1.1: Table summarizing the translational diffusion coefficients found in literature for confined water in MCM-41 at room temperature, compared to bulk water.

1.4.3 Water in imogolites

The question of water in imogolites appeared very early because of their specific 1D morphology compared to other clay minerals. As early as 1969, Wada and Yoshinaga[53] reported an important adsorption of water into natural imogolites, which is "*greater even than that of montmorillonite*", a swelling clay known for its strong propensity to adsorb water. The authors attributed this effect to the presence of micropores although the real structure of imogolite nanotubes was not well resolved at this time (see section 1.3.2). An important parameter is therefore the packing pattern that nanotubes can adopt. When an imogolite suspension is

dried, tubes tend to assemble in bundles, whose form has long been debated. Several studies, both experimental and simulated, now consider that imogolites assemble in bundles with a two-dimensional hexagonal lattice (Fig. 1.20a)[57,72,74,197–200]. As a consequence, three different types of pores are proposed for powder samples of imogolite nanotubes (Fig. 1.20b)[74,201]. Pores of type A correspond the cavity of the tube. Pore of type B is the inter-tube cavity between tubes assembled together into a bundle while the last type is the mesoporosity between bundles of nanotubes. In principle, the three types of pores can be hydrated. We will see in section 5.2.2.2 that all of them contribute to the variation of the diffraction pattern of imogolites.

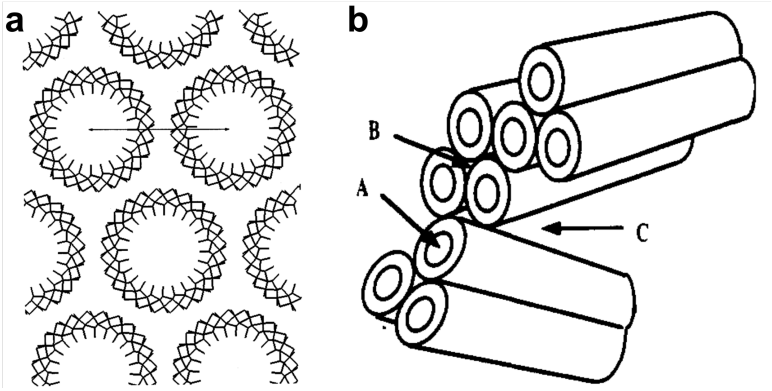

Figure 1.20: (*a*) Section view of imogolite nanotubes in hexagonal close packing according to Pohl et al.[72]. (*b*) Scheme of the different pore types in powder of INTs. Reprinted from Ackermann et al.[201]

From a geometric point of view, a single imogolite nanotube presents two surfaces available for adsorption process, covered by hydroxyl groups, which are supposed to provide a hydrophilic behavior to the nanotubes. Based on electrostatic and atomistic calculations, it has been suggested that the internal surface is strongly hydrophilic whereas the curvature of the nanotube alters the arrangement of surface H-bonds, making the external surface more hydrophobic[78,202,203]. Moreover, the problem is further complicated by the fact that adsorption inside the inner cavity (pore type A) is independent of bundling, whereas adsorption on the outer surface is highly dependent on the specific bundling conditions of a certain sample, depending on its preparation. In addition, as we mentioned before, the exact structure of Si-INTs (N value in the circumference) has not yet been solved contrary to other INT analogues.

Previous works investigated the behavior of adsorbed water in imogolite nanotubes. Two questions arise in confinement at the nano sclae: (*i*)

how water structures itself? (*ii*) what is its dynamics? In the case of imogolite nanotubes, these two issues have been addressed but in most cases either from an experimental point of view[80,204] or using only an atomistic approach (MD simulations, Monte-Carlo and Density Functional Theory simulations)[197,205–208].

In the following, we will review three important papers that will be a reference and source of comparison for this PhD work. The first one is the article by Monet et al.[80] in 2020, where the adsorption of a single layer of water inside single-walled Ge-INTs was studied, by means of DFT calculations and neutron spectroscopy. From DFT trajectories, a density map is obtained by projecting, as a function of time, all the atomic positions on a flat surface, which is equivalent to unrolling the nanotube (Fig. 1.21*a*).

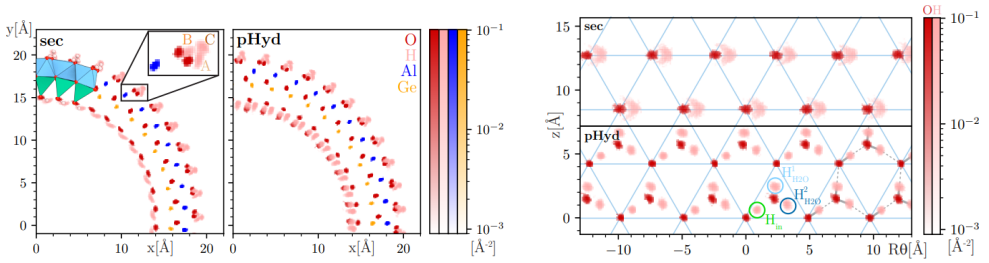

a) *b*)

Figure 1.21: Density maps for a Ge-INT, dry and hydrated tube (oxygen in red, hydrogen in pink, aluminium in blue, germanium in yellow). In *a*), a projection in the (x, y) plane; the left half pictures the dry nanotube, while the right half also contains a layer of water molecules adsorbed on the surface. In *b*), projection in the (Rθ,z) plane of the same system, viewed from the interior of the tube. The oxygens in the inner wall of the tube are located on a triangular network indicated by blue lines. The upper figure shows the hydroxyls of the dry tube, while the bottom half shows also the pattern of the adsorbed water molecules, filling one triangular site every two.

It was shown that the hydration layer adsorbed at the inner surface of a Ge-INT has a unique two-dimensional organization, *i.e.* a layer of water molecules adsorbed into the wall individually – as each molecule forms exclusively three hydrogen bonds with the germanol groups of the Ge-INT inner surface. This configuration was found to be highly ordered, stable and harmonic up to room temperature. Only one site over two is occupied. It is important to underline that this configuration is possible only because in Ge-INTs, the diameter makes the triangular sites

commensurate with the dimension of a water molecule. Therefore, the same ordering is probably not possible inside Si-INTs, as their diameter is much smaller. The adsorption geometry in the case of Si-INTs will be investigated in this thesis in section 5.2. The authors also compared the experimental Generalised Density of States (GDOS[4]) with calculated values, evidencing specific vibrational modes of the water molecule trapped into the nanotube walls[80].

More recently, LeCaer et al.[204] investigated water diffusion inside Si-INT for three different hydration states by neutron spectroscopy. The corresponding experimental GDOS are reported in Fig. 1.22*a*. Independently of the water content, the three GDOS spectra show the same main features at 14, 32 and 60 meV. In particular, the peak located at 32 meV was attributed to a stretching-like translational mode of water molecules bonded to the internal surface.

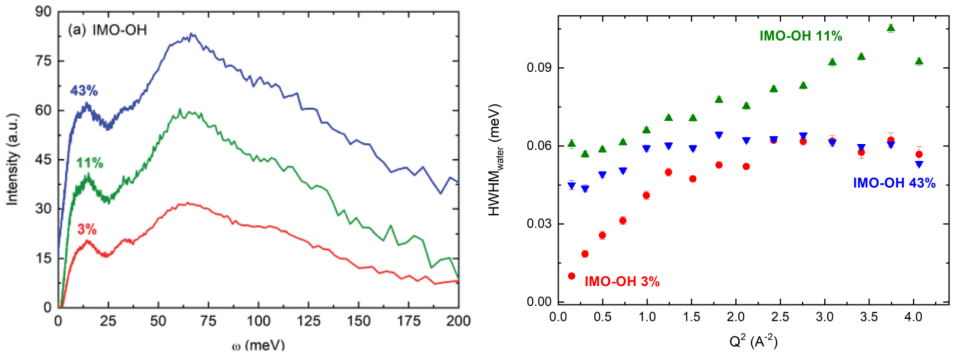

a) *b)*

Figure 1.22: Curves from LeCaer et al.[204] *a*) GDOS for the three samples *b*) HWHM[5]of the Lorentzian associated to water as a function of the square of the momentum transfer

According to their interpretation (1.22*b*), the three hydration levels have the following diffusional features:

- if the tube is hydrated with a single monolayer of water, there is translational long-range diffusion along the NT axis.
- when the tube is full, the hydrogen bond network is stronger, making diffusion difficult over long distances.
- when trying to fill further the tubes, only local motions are possible, because the hydrogen bond network is rigid and locks the diffusive motions.

[4]The GDOS will be introduced in details in Chapter 2
[5]Similarly to the GDOS, the HWHM will be introduced in Chapter 2

It is important to note that the conclusions are only supported by experimental data without any atomistic simulation. In addition, the authors mentioned that they could not obtain a dry sample to be used as a reference in the interpretation of the GDOS.

On the theoretical point of view, one of the most complete work on Si-INTs was proposed by Scalfi et al[207] in 2018. The authors studied, by means of Molecular Dynamics simulations, the water structure into a Si-INT tube having N = 12. The tube was fully hydrated, and they observed two different populations of water molecules: the first hydration layer, adsorbed next to the inner surface, and more disordered water filling up the center of the nanotube. Looking along the tube axis, it was found that water molecules sit mainly in the furrows situated in between two rings of silanol groups. The existence of these furrows and their relevance in the subsequent pattern of water adsorption will be discussed in detail in section 5.2. Six possible adsorption patterns were highlighted. The two more probable are illustrated in Fig. 1.23. The first one (Fig. 1.23*a*) consists in having a molecule lying flat on the surface.

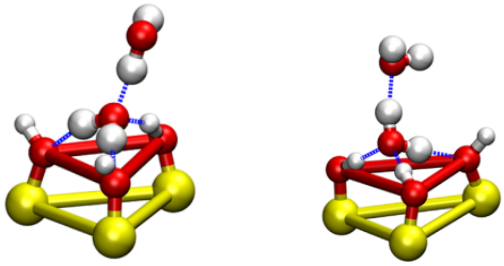

a) *b*)

Figure 1.23: In *a*), pattern having a molecule lying flat on the tube surface, while in *b*) a molecule perpendicular to the surface responsible for the organization in concentric layers

Making a comparison between these patterns and the results presented from Monet et al.[80], we immediately recognize that this is the one and only possible pattern found for Ge-INTs. On the other hand, the second pattern – an "upright" water molecule oriented in a plane bisecting the triangular adsorption site (Fig. 1.23*b*) – is the most common for Si-INTs with N = 12, suggesting that the tube diameter and the adsorption sites dimension should have an impact on the adsorption geometry. Indeed, compared to Ge-INTs, the triangular sites in Si-INTs are much smaller.

Concerning diffusion, in a tube fully hydrated, water crossing the silanol rings was not observed, suggesting that surface diffusion of water molecules takes place only in the (x, y) plane.

The lack of a common vision between experiments and simulations for Si-INTs confirms us in the idea to better understand the structure and dynamics of water in this nanoconfined system. A fundamental point before tackling these issues is to solve the atomic structure of dry Si-INTs. This is of utmost importance in order to simulate accurately the effect of water in these nanotubes and to compare the data with neutron scattering experiments. As shown in the follwing, one of the originalities of our work is having supported our experimental results by a complete investigation with MD simulations, allowing us to reconsider the hypotheses presented in the previous studies. Therefore, frequent comparisons between our results and what found by other authors will be made. To conclude, this brief review of the literature shows that these nanotubes constitute a particularly rich and interesting system for the study of water confined in one-dimensional pores.

2. Experimental methods and formalism

In this chapter, we present the different experimental approaches used during this thesis. As mentioned previously, we focus on synthetic silicon imogolites, kindly provided by Patrick Davidson at Laboratoire de Physique des Solides (LPS). The original Si-INT liquid solution was dried in the oven at 60°C to obtain a thin film. The film was removed from the oven, milled in agate mortar and sieved with a 100 μm sieve in order to obtain a fine powder. The density of the sample was found to be around $\rho = 0.2\frac{g}{cm^3}$. In this chapter, transmission electron microscopy (TEM) and Fourier-transform Infrared Spectroscopy (FTIR) are first employed to evaluate the average length of the nanotubes, to determinate their composition and to characterise their vibrational states. A comparison with previous literature was made in order to verify that the sample does not contain any impurities.

As the purpose of this work is the study of water behavior inside imogolites, a detailed knowledge of their hydration process is necessary. This is investigated with a thermogravimetric analysis (TGA) and adsorption isotherms, which allow defining the best conditions for the preparation of dry and hydrated samples in a controlled manner.

Finally, this chapter ends with a detailed description of X-ray and neutron scattering formalism and experiments that are at the core of this thesis.

2.1 Transmission electron microscopy

Imogolite nanotubes have an average diameter of about 2 nm. The tubular aspect of these objects is not observable by conventional optical microscopy and requires the use of transmission electron microscopy (TEM). TEM osbervations were made in collaboration with Claire Goldmann by using a JEOL1400 microscope from Imagerie-Gif core facility, operated at 120 kV. This microscope is composed of a lanthanum hexaboride single crystal source, connected to a high voltage source, allowing the emission of electrons. The electrons are focused by a Wehnelt cylinder and are accelerated by the positive potential of the anode, the microscope chamber being under vacuum. This beam of electrons passes through different electromagnetic lenses fed by a stabilized current. Following the

electron gun, two condensers have the role of changing respectively the electron current density on the sample and the beam aperture under which a point of the sample is illuminated. The objective, the main part of the microscope, ensures the focus of the image of the sample. Finally, the projection system, composed of several lenses (diffraction, and final projection), ensures the transfer and the magnification of the image given by the lens on the screen. In our case, the samples were imaged with a magnification of x10000 and were collected with a RIO 9 camera with a 3Kx3K resolution (Gatan Inc.). For TEM experiments, highly dilute dispersions of imogolite nanotubes were prepared at 1 $mg.mL^{-1}$ in ethanol and then a drop was laid on a carbon-coated copper grid. The length distribution was determined from the analysis of >300 nanotubes using the Fiji software[209].

2.2 Infrared spectroscopy

Infrared (IR) spectroscopy is based on the absorption of electromagnetic radiation in the IR range by the material[210]. When the frequency of the radiation is close to that of one of the fundamental modes of vibration of a given group of the molecule, the latter resonates and absorbs part of the energy of the radiation. Thus, the variations of length or angle of the bonds induce respectively characteristic vibrations of elongation and deformation. As these frequencies are dependent on the mass of the atoms bonded and on the strength of those bonds, an infrared spectrum is helpful to study the chemical structure of a sample. The transmitted intensity of the beam transmitted through the sample is measured on a detector giving rise to an interferogram, and its Fourier transform gives the infrared absorption spectrum of the sample.

IR spectroscopy is a classical technique to identify and/or characterize imogolite nanotubes since the seminal work of Yoshinaga and Aomine[41]. For IR measurements, 1.5 mg of Si-INT, previously heated at 200^{o}C, was mixed with 150 mg of KBr, milled together and pressed at 8 tons of pressure into a transparent disk. IR spectra were collected with a Nicolet iS50 FTIR spectrometer at room temperature in transmission mode by averaging 64 scans at a resolution of 4 cm^{-1} between 4000-400 cm^{-1}.

2.3 Thermogravimetric analysis

Thermogravimetric analysis (TGA) is a thermal analysis technique that consists of measuring the variation of mass of a sample as a function of temperature. This technique is commonly employed in determining

the composition of samples and predicting their thermal stability. In our case, it allows to identify easily the characteristic temperatures of mass loss of the sample and to quantify the proportion of water contained in the imogolite nanotubes from differential curve (see Chapter 4).

The present TGA measurements were carried out with the help of Maguy Jaber (Laboratoire d'Archéologie Moléculaire et Structurale, Sorbonne Université) on a Q600 STD (TA Instruments). Si-INT powder (around 20 mg), placed in an alumina crucible, was heated under nitrogen gas from room temperature to 500°C at a rate of 5°C/min. The mass loss percentages given in this manuscript are normalized to the mass of the dry powder, before dehydroxylation of imogolite nanotubes, corresponding to the mass of the sample taken at temperature T = 200°C (the results are shown in section 4.1.2).

2.4 Adsorption isotherms

Gas adsorption is a powerful technique for the characterisation of porous materials. It consists in measuring the quantity of a certain gas adsorbing on the surface of a sample according to the pressure. The sample system, whose surface is exposed to gas molecules (referred as adsorbates), is called adsorbent.

Adsorption is a consequence of surface energy. Atoms on the surface of a solid are incompletely surrounded by others atoms, allowing attractions with adsorbates. This is a spontaneous process as it reduces the free energy of the system. In case of physisorption, adsorbates are bounded by weak van der Waals forces while in chemisorption, the process involves a chemical reaction with the adsorbent surface, modifying the chemical bonding structure. Physisorption occurs before chemisorption. For example, it corresponds to the typical adsorption of nitrogen N_2 molecules in porous media as we will see later.

An adsorption isotherm is obtained by measuring the quantity of adsorbates captured by the surface of the adsorbent of known mass or volume, as a function of the relative adsorbate pressure (P/P_0), and for a given temperature, P_0 being the saturating vapor pressure of the gas at the temperature of the experiment. In the case of water, the ratio P/P_0 is also referred to as Relative Humidity ratio (RH). During an adsorption isotherm, the gas molecules condense first in the pores with the smallest dimensions (a micropore is a pore with diameter lower than 2 nm, for N_2 as probe molecule, while mesopores extend from tenths of nanometers to micrometers). With increasing the pressure, molecules cover meso- and macroporosity. According to the final shape of the adsorption isotherm, one can deduce many information about the system, including the size

and shape of the pores, their distribution as well as the specific surface area of the samples.

The appearance of the isotherms is indicative of the textural characteristics of the material. Figure 2.1 illustrates the different physisorption isotherms, according to the nomenclature of the International Union of Pure and Applied Chemistry (IUPAC)[211].

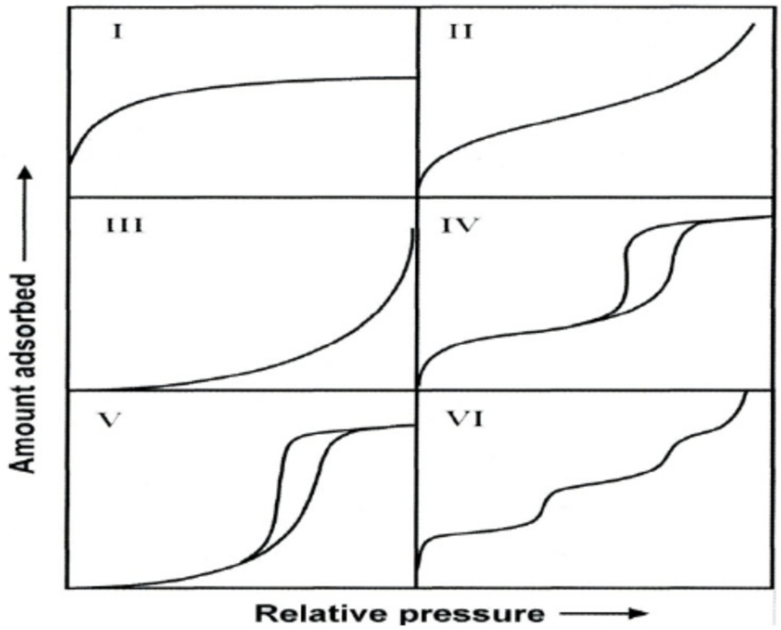

Figure 2.1: IUPAC classification of adsorption isotherms, from Alothman et al[212]

For example, microporous materials, having pore diameters up to 2mm, display adsorption isotherms of type I. There are several types of probes depending on the properties to be investigated. N_2 is used extensively for determining the pore size distribution, microporous volume and specific surface area (SSA). Complementary probes, such as Ar, CO_2 or H_2, are also employed to assess extreme porosity[213]. Moreover, adsorption isotherms with H_2O allow to master the hydration process of a certain sample, by knowing the quantity of water adsorbed by the system as a function of the relative humidity. These experiments are essential for the preparation of hydrated samples as we will see during this work.

Like for other porous systems, gas adsorption isotherms have been widely employed to characterize microporosity of hydrophilic[201,214] and hydrophobic[68,85] imogolite nanotubes. For the present thesis, N_2 and H_2O were performed at ISTerre by Valérie Magnin. Around 200 mg of sample were held into a glass capillary specially made for isotherm measurements (Fig. 2.2).

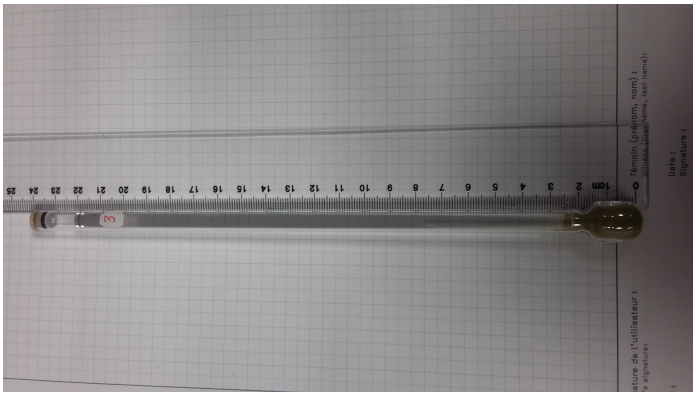

Figure 2.2: Sample holder used for adsorption isotherms

Samples were outgassed prior to measurements because pore volume and area increase with greater outgassing temperature. Indeed, while large pores are opened to adsorbing gas after the removal of water at relatively low temperature, the smaller pores are only accessible after outassing at higher temperatures. In our case, INT samples were outgassed at 200°C during 12h under secondary vacuum. N_2 isotherm was performed at 77.3K (*i.e.* the boiling temperature of N_2) on a BELSORP'MAX (Bel, Japan) while the H_2O isotherm was carried out at room temperature by using an ASAP2020Plus apparatus (Micrometrics).

2.5 X-ray diffraction

X-rays are transverse electromagnetic radiations with a wavelength between 10 nm and 0.001 nm, corresponding to energies ranging from a hundred eV to MeV.

As their wavelength is of the order of magnitude of inter-atomic distances, when studying a material by X-ray scattering, interference effects occur, which provide information on the structure of the system at an atomic scale. This is the reason why, together with the relative facility to produce X-rays, it is traditionally the probe mostly used to investigate the atomic structure of systems. X-rays interact with the electron cloud around the nucleus. This leads to two major conclusions: first of all, the relevant interaction is a long-range electromagnetic interaction and secondly, heavy elements have larger X-ray cross sections than light elements. These two points strongly differ from neutron scattering, that we will see in the Section 2.6.1.

In the next subsections, a quick review about the theory of X-ray scattering and about the experimental setups will be presented. As only the

essential quantities that are necessary for the understanding of the thesis will be mentioned, the particularly interested reader can read reference textbooks on X-ray scattering, such as the one written by Guinier[215].

2.5.1 Scattering theory

X-ray scattering can be either elastic (Thomson scattering) or inelastic (Compton scattering). In this thesis, we will only consider elastic scattering, where scattered waves interfere with each other. The scattering wave-vector is

$$\vec{Q} = \vec{k'} - \vec{k} \tag{2.1}$$

and the energy conservation condition is

$$\|\vec{k'}\| = \|\vec{k}\| \tag{2.2}$$

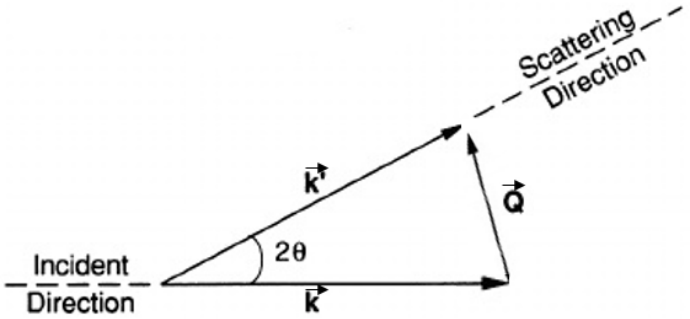

Figure 2.3: Scattering triangle depicted in the case of elastic scattering, illustrating the relationship between the scattering wave-vector $\vec{Q}$ and the scattering angle 2θ

Fig. 2.3 shows the scattering triangle, where 2θ is the scattering angle between the incident and scattered wave.

The norm Q is given by by the Bragg law:

$$Q = \frac{4\pi}{\lambda} sin\theta \tag{2.3}$$

where λ the incident wavelength and 2θ the scattering angle.

Experimentally, the quantity measured is the scattered intensity, which is proportional to the square of the amplitude of the scattered wave:

$$I(\vec{Q}) \propto |A(\vec{Q})|^2 \tag{2.4}$$

The scattered amplitude is:

$$A(\vec{Q}) = \sum_{j=0}^{N} f_j(Q) e^{-i\vec{Q}\cdot\vec{r_j}} \tag{2.5}$$

where the sum runs over all the atoms of the scattering object and $f_j(Q)$ is the atomic scattering factor of the j-th atom. $f_j(Q)$ is the Fourier transform of the electronic density of the atom and it depends only on the modulus Q of the wave-vector $\vec{Q}$.

In the case of X-rays, the atomic scattering factor:

- decreases with the scattering angle θ.
- has the same sign for all elements.
- is proportional to the atomic number Z (and it coincides with the atomic number Z at Q=0).

Fig. 2.4 shows the atomic form factors as a function of Q for the atomic species composing imogolite nanotubes.

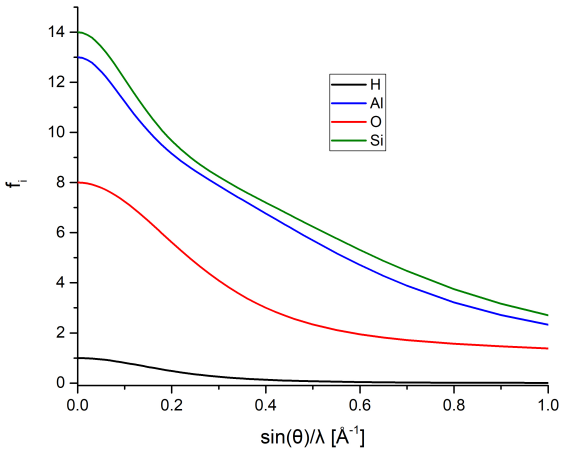

Figure 2.4: Atomic form factors for the elements of imogolite nanotubes (from the International Tables for Crystallography http://it.iucr.org/Cb/ch6o1v0001/)

Interference effects, and therefore diffraction, can take place when X-rays scatter with a material that has a periodic arrangement of electron

clouds. In that case, the scattered amplitude can be seen intuitively as the weighted Fourier transform of the positions of the atoms. Such a system repeating periodically in space is a crystal. Its smallest repeating unit is called unit cell, that can be defined by a triplet of vectors $(\vec{a}, \vec{b}, \vec{c})$. The direct lattice is generated from nodes positioned at integer values n_1, n_2, n_3 in terms of three basis vectors: $\vec{R}_n = n_1\vec{a} + n_2\vec{b} + n_3\vec{c}$. A crystal can therefore be described as the convolution of its unit cell and the direct lattice positions. As the Fourier transform of the convolution of two functions is the direct product of their Fourier transforms, it follows that the scattered amplitude is the product of a form factor, the weighted Fourier transform of the unit cell, and the Fourier transform of the direct lattice. The intensity is the product of the square of the modulus of the form factor $F(\vec{(}Q)$ by a structure factor $S(\vec{Q})$:

$$I(\vec{Q}) \propto |F(\vec{Q})|^2 \cdot S(\vec{Q}) \tag{2.6}$$

For a perfect and infinite crystal, the structure factor consists in a sum of delta distributions located at the Bragg peaks of the reciprocal lattice, its intensity given by:

$$I(\vec{Q}) \propto \left| \sum_{j\ in\ the\ cell}^{N} f_j(Q) e^{-i\vec{Q}\cdot\vec{r_j}} \right|^2 \cdot \sum_{hkl} \delta(\vec{Q} - \vec{Q}_{h,k,l}) \tag{2.7}$$

with $\vec{Q}_{hkl} = h\vec{a^*} + k\vec{b^*} + l\vec{c^*}$. The vectors $(\vec{a^*}, \vec{b^*}, \vec{c^*})$ form the basis of the reciprocal lattice — dual basis of the direct lattice basis $(\vec{a}, \vec{b}, \vec{c})$ — and h, k, l are indices are integers, called Miller indices.
If now one considers a crystalline powder, one sums the intensities of the crystallites in every direction in space and one obtains a diffraction diagram where the intensity depends only of the modulus Q of the wave-vector $\vec{Q}$, with sharp peaks at Q_{hkl}.

After this introduction to X-ray scattering, let us present the two complementary methods which will be used in chapters 5 and 6 to analyze the X-ray scattering diagrams of powders of imogolite nanotubes.

2.5.1.1 Calculations within the homogeneous approximation

For sufficiently small wave-vectors, that is below 1 Å^{-1}, a nanotube can be approximated by an homogeneous cylinder with an inner radius R_i and an outer radius R_e [216]. The presence of water inside or around the nanotubes can also be treated in the homogeneous approximation in this Q range, adding cylinders of water inside or around the nanotubes [200]. In this work, a program already available at LPS was used to calculate the

XRS diagrams that will be presented and discussed in Chapters 4 and 5. Here, the formalism of the homogeneous approximation will be illustrated, in the case of very long imogolite nanotubes arranged on a two-dimensional (2D) hexagonal lattice. Such nanotube bundling is indeed often observed in imogolite powders[200]. It is shown in details in ref.[200] that the scattered intensity can be calculated analytically when assuming the nanotube length to be infinite, by the formula:

$$I(Q) \propto \frac{1}{Q}\Big(\rho_{INT} f_{INT}(Q)\Big(\frac{R_e J_1(QR_e)}{Q} - \frac{R_i J_1(QR_i)}{Q}\Big)\Big)^2 \sum_{j,k} J_1(Qd_{jk}) \tag{2.8}$$

J_0 and J_1 are the cylindrical Bessel functions of order zero and one. ρ_{INT} is the mean electronic density of the nanotube. $f_{INT}(Q)$ is a normalized form factor of the aluminosilicate nanotube: $f_{INT}(Q) = \frac{f_{Si}(Q)+2f_{Al}(Q)+7f_O(Q)+4f_H(Q)}{100}$, $f_i(Q)$ being the X-ray form factor of atom i. The indices j and run over the nanotubes in a bundle and d_{jk} is the distance between the centers of the tubes j and k in a plane perpendicular to their long axis.

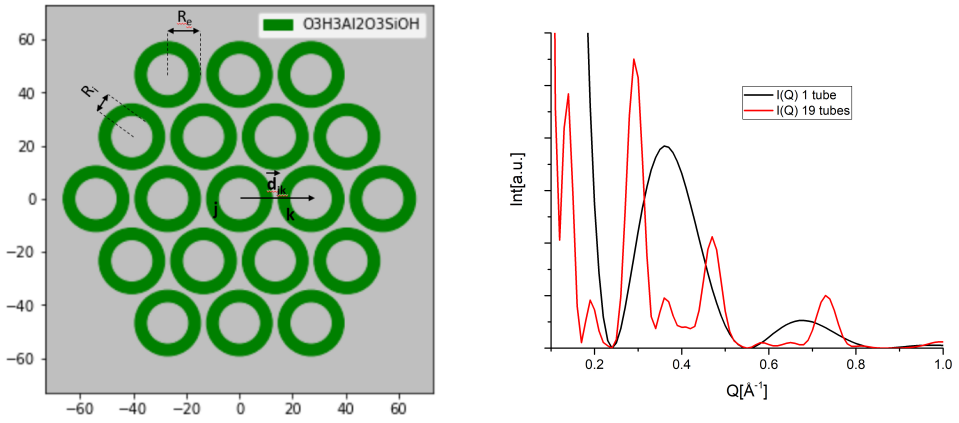

a) *b)*

Figure 2.5: *a)* Organization of tubes in a hexagonal bundle in the homogeneous approximation and *b)* comparison between the XRD diagram for one tube (black) compared to a bundle of 19 tubes (red)

Fig. 2.5 shows the bundle of tubes in the homogeneous approximation as well as the illustrative calculated XRS diagrams for isolated (non-bundled) nanotubes. The broad oscillations in the black curve come from the nanotube form factor while narrower peaks coming from the structure factor contribution are observed for bundles.

2.5.1.2 Calculations from the atomic positions

In order to calculate a diffraction pattern starting from atomic positions, one can use the Debye formula, which allows to calculate the intensity scattered by a powder in terms of the interatomic distances within a constituent of the powder:

$$I(Q) \propto \sum_{j,k} f_j(Q) f_k(Q) \frac{sin(Qd_{jk})}{Qd_{jk}} \tag{2.9}$$

where $f_{j(k)}(Q)$ is the atomic form factor of atom j (k) and d_{jk} is the distance between atoms j and k. Calculations are done using a program written by Neverov et al[217] and a python interface available at LPS. The powder constituent can be a small crystal for a crystalline powder and a nanotube or a bundle of nanotubes for imogolites.
For tubes organized in bundles, two parameters have to be considered: their relative orientations and their phasing along the z axis of the bundle.
At small Q, when the homogeneous approximation applies, the relative orientations or translations along z of the tubes should have no impact on the XRS diagram. We have verified this by performing calculations with tubes all having the same orientation and phasing in z and with nanotubes of random orientations and/or relative positions in z.
At large Q, the orientational coherence and/or z-phasing between the tubes will modify the XRS diagram. In particular, without orientational coherence or z-phasing, the intensity can be calculated by simply considering a powder of isolated tubes, i.e., by taking the coordinates of the atoms of a single tube in Eq. (2.9). If tubes are correlated for their orientations and z positions, their Wide Angle XRS (WAXS) diagram will present narrower modulations than for uncorrelated tubes. From this view point, the WAXS diagram of aluminosilicate nanotubes measured experimentally (shown in chapter 4) presents strong similitudes with those of methylated aluminosilicate and aluminogermanate nanotubes[71] and with the one of hydroxylated aluminogermanate nanotubes[80]. In ref.[71,80], reasonable agreement between experimental and calculated diagrams was found considering isolated nanotubes. It will thus be assumed in this thesis that hydroxylated aluminosilicate nanotubes are not coherent in orientation nor in z-position within a bundle.

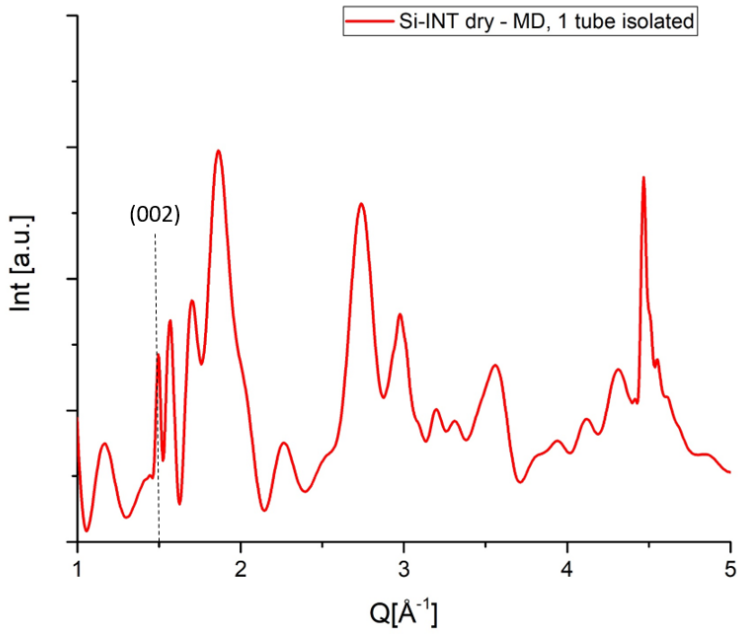

Figure 2.6: Diffraction diagram calculated from the last frame of a MD trajectory, evidencing the positions of the (002) reflection. The length of the tube is 186 Å.

A calculated WAXS diagram is shown in Fig. 2.6. It exhibits broad modulations due to the finite radial size of the nanotube and sawtooth peaks $(00l)$ characteristic of the long range order along the tube axis. The value of the period T along z is determined from the position of the inflexion point of their rising edge[71]. The $(00l)$ reflections are systematically extincted for odd l values because the period of the nanotube structure projected onto its long axis is equal to $\frac{T}{2}$ [71].

The X-ray diffractogram of the dry sample was measured on an extended Q range at the synchrotron SOLEIL. The next section describes the synchrotron and the beamline used. Moreover, an in-situ investigation of the water adsorption process was carried out on a Controlled Humidity Cell (CHC) at Laboratoire de Physique des Solides, by gradually hydrating the sample. The experimental procedure is explained in the last section of the chapter dedicated to X-rays.

2.5.2 Experiments on CRISTAL

Ex-situ measurements on dry imogolites were performed at the beamline CRISTAL of the synchrotron SOLEIL.

A synchrotron is a particle accelerator that accelerates electrons in order to produce synchrotron radiation. The theory of electromagnetic

radiation indeed predicts that when a charged relativistic particle is subjected to centripetal acceleration, it releases part of its energy in form of electromagnetic radiation, emitted at the tangent of its trajectory. The irradiated power is described by the Larmor formula:

$$P = \frac{2}{3} c e^2 \frac{\beta^2 \gamma^2}{r^2} \tag{2.10}$$

where c is the speed of light, e the electron charge, $\beta = \frac{v}{c}$ and $\gamma = \frac{1}{\sqrt{1-\beta^2}}$

This radiation is:

- Intense: the flux of a synchrotron is several orders of magnitude higher than that of X-ray tubes.
- Highly brillant: Brillance is defined as the flux of photons per solid angle of radiation, per area of the source and per bandwidth in energy. A synchrotron source is highly brillant because of its high flux, high collimation (low divergence) and small beam size.
- Polarized: the polarization of the beam can be contolled and set to circular, linear or elliptical.
- Continuous in energy: the beam is polychromatic in energy, so a wide range of energies can be selected with a monochromator. Moreover, experiments needing a "white" beam can be performed.
- Pulsed in time: electrons are grouped together and circulate in the storage ring in packets. An isolated packet emits an isolated pulse of radiation, allowing time-resolved measurements.

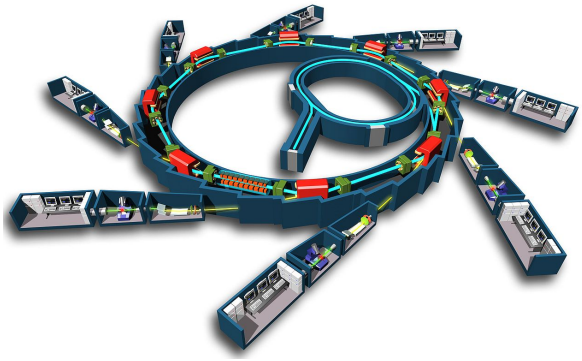

Figure 2.7: Scheme of the synchrotron facility SOLEIL with the linear accelerator and booster in the center. The main circle corresponds to the storage ring with different magnets at the exit of which are located the beamlines.

In SOLEIL (Fig. 2.7), the electron beam is produced by an electron emitter and then accelerated on several steps. It is first accelerated in a 16 meter long linear accelerator, the linac, where the electrons reach energies around 100 MeV. The beam is then directed towards a circular accelerator called Booster where the energy is 2.75 GeV. Only at this point, the beam is injected into the 354 meter circumference storage ring of polygonal shape. Here, magnets (diploles, quadrupoles) maintain the collimation of the electron beam and refocus the trajectory on the angles of the polygon; wigglers or undulators, arranged in the straight sections of the ring, impose a sinusoidal trajectory on the electrons; radio-frequency cavities give it back the energy lost by emitting photons, the so-called synchrotron radiation. The radiation is diverted, selected, and shaped by optic systems in experimental stations called beamlines. Currently, SOLEIL synchrotron has 29 beamlines.

During this thesis, X-ray scattering experiments have been performed on the beamline CRISTAL[218] (Fig. 2.8).

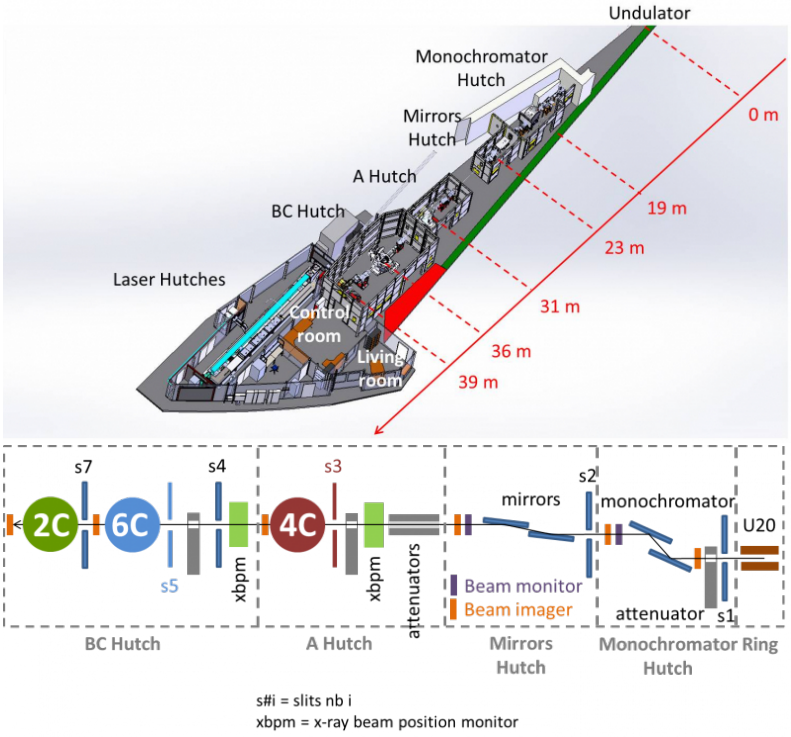

Figure 2.8: 3D view and scheme of the beamline CRISTAL

The source is a U-20 undulator and the energy of the X-ray beam can be adjusted between 4 and 30 keV using a Si(111) double crystal monochromator with an energy resolution of the order of $\Delta E/E\ 10^{-4}$. This

line has three different circle diffractometers for studying monocrystals and polycrystalline compounds: a six-circle diffractometer, a four-circle and a two-circle diffractometer. Powder diffraction is done on the two-circle diffractometer, enabling X-ray diffraction measurements with very high angular resolution. The detection part of the instrument consists of a 21-crystal silicon (Si(111)) analyser followed by a fast YAP(Ce) scintillation detector (Scionix).

Data on the dry nanotubes were collected by Stephan Rouzière and Erik Elkaim. The chosen wavelength was of λ=0.54632 Å, with accessible Q range 0.1 Å^{-1} $< Q <$ 20 Å^{-1}.

The collected curves were only corrected by capillary subtraction. Geometric and polarization corrections – that will be applied in the next section 2.5.3 – are not necessary with synchrotron radiation.

2.5.3 Experiments using a humidity cell chamber

In-situ X-ray scattering experiments were carried out on an in-house X-ray source (MORPHEUS platform of Laboratoire de Physique des Solides) produced by a Cu rotating anode (RU H3R, Rigaku Corp., Japan). A picture of the setup is in Fig. 2.9.

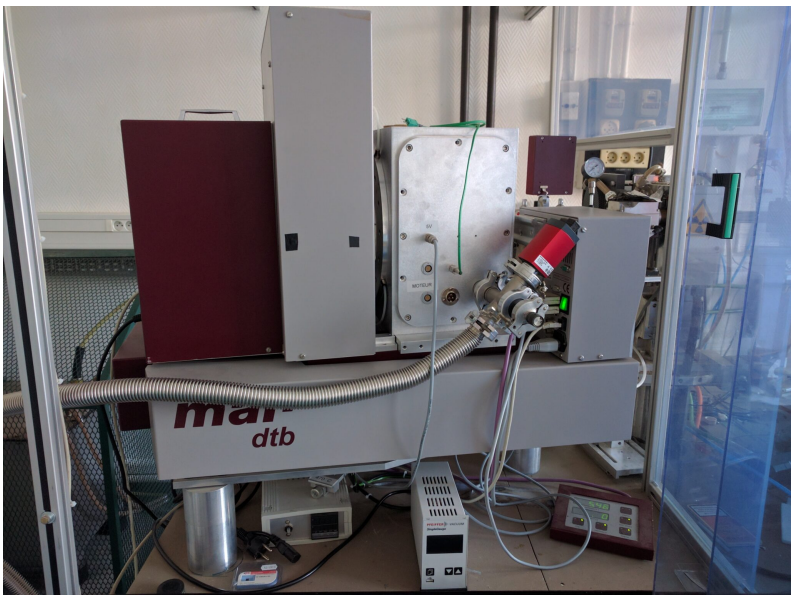

Figure 2.9: Picture of the MarCu diffractometer at LPS

In this setup, X-rays are produced in a sealed-tube source, where electrons, accelerated by a potential difference of up to 40 kV bombard a metal anode inside a vacuum tube. The electrons induce a cascade

of electronic transitions in the atoms of the target material, which emit electromagnetic radiation as they return to the ground state. The anode rotates in order to dissipate the heat produced. The material of the anode must be a good conductor of both electricity and heat, and have a suitably high melting point. One of the most common target elements is Cu. The typical spectrum emitted by a Cu anode is shown in fig. 2.10*a*.

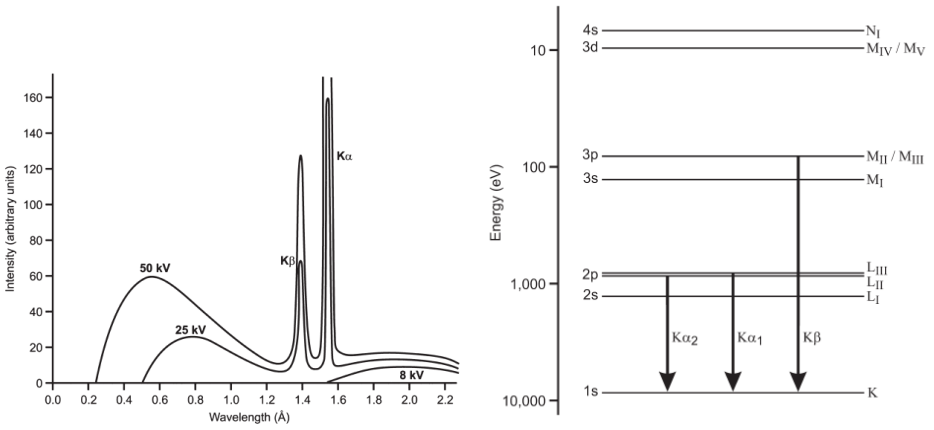

a) *b*)

Figure 2.10: *a*) Typical spectrum emitted from a Cu anode and *b*) energy level diagram for a Cu atom

The continuous part of the spectrum is the bremsstrahlung radiation, due to the deceleration of electrons. On the contrary the discrete peaks, the "characteristic radiation" of the material, are due to the ejection of an electron from one of the inner electron shells of the metal atom and their energy depends solely on the metal used for the target. The energy levels of copper are in Fig. 2.10*b*. The X-ray photon wavelength is characterised by the difference in energy between the two levels. For instance, the K_α line for Cu corresponds to 1.542 Å. During the experiment, the beam was collimated and monochromatized by a multilayered W/Si optic (Osmic), providing a 1 mm^2 wide beam.

X-ray diffraction measurements as a function of relative humidity were performed inside a dedicated Controlled Humidity Cell (CHC) that will be described in details below. The CHC was placed on a mardtb goniostat, equipped with a two-dimensional mar345 image plate detector (0.15 mm pixel size, marXperts GmbH). The sample-detector distance D was determined thanks to quartz calibration. Knowing the lattice distance d and hkl of each diffraction peak for quartz and the pixel position

of the peak in the detector, θ can be calculated and therefore D:

$$\theta = arcsin\Big(\frac{\lambda}{2\, d[\text{Å}]}\Big) \tag{2.11}$$

$$D[mm] = pixel \cdot dim_{pixel} \cdot \frac{1}{tan(2\theta)} \tag{2.12}$$

For these experiments, the sample-detector distance is found to be at D = 188mm. X-ray scattering diagrams were recorded as a function of a certain pressure, that was later converted into relative humidity (RH). A scheme illustrating the functioning of the setup is shown in Fig. 2.11.

The experimental CHC is divided into two devices: one is dedicated to the generation of water vapor pressure from a water tank, while the second is the pressure-regulated chamber, containing the capillary with the sample. Indeed, the sample was filled into a borosilicate glass capillary, with a diameter of 1 mm (WJM-Glas, Müller GmbH, Germany).

At the beginning of the experiments, air molecules were pumped away in both cells. Consequently, the pressure inside the water reservoir corresponds to the saturated vapor pressure P_0 of water. By contrast, the pressure inside the chamber containing the sample is as low as possible. The relative applied pressure is regulated in the chamber thanks to a sensitive pressure gauge connected to a PID (proportional-integral-derivative) controller. When no setpoint is set up, the pressure inside the CHC corresponds to the vapor pressure of water P_0 while by setting a setpoint one obtained an intermediate pressure between 0 and P_0 inside the CHC.

Three valves were present:

- V1: valve between the water reservoir and the pump (behind the PID in the picture). It was needed to pump away the air into the water reservoir. It was done the first time, and then V1 always stayed closed.

- V2: valve between the pump and the humidity chamber (valve in the foreground of the picture). If open, the pump could pump directly into the cell (bypassing the PID). If closed, the pump acted on the PID, which tried to regulate the pressure into the CHC.

- V3: valve that puts the CHC in contact with the PID only (not present in the picture but in the direction of the blue arrow).

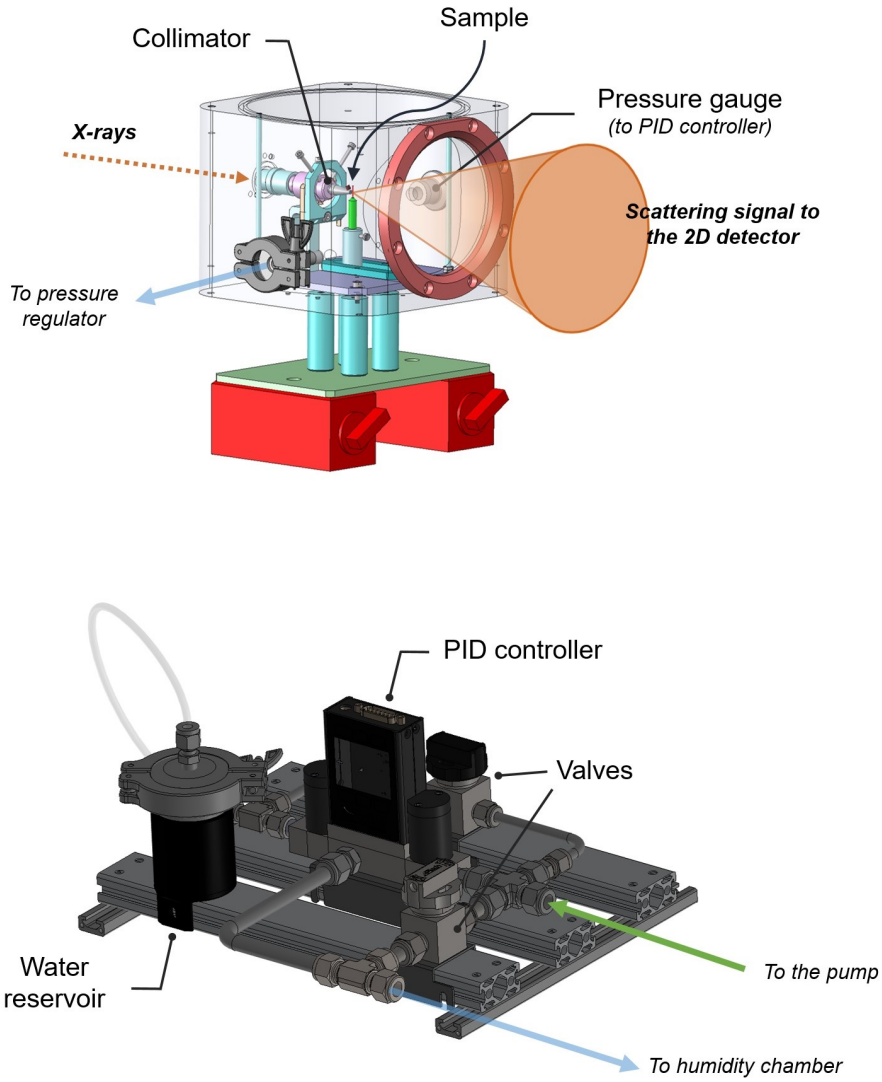

Figure 2.11: Scheme of the CHC setup. *(top)* Pressure-regulated humidity chamber containing the sample placed in the X-ray beam. *(bottom)* Water vapor pressure generating device

A gauge measured the total pressure. The experiments were carried out point by point along the adsorption isotherm. Typically, diffraction patterns were measured continuously for each value of partial pressure P/P_0 until there was no more evolution in the X-ray scattering diagrams. This because the adsorption of water molecules in the sample required a certain waiting time. Then, only the stabilized diffraction patterns were used for the analysis.

The saturated vapor pressure of water is known,[219] and is dependent of the temperature (Table 2.1):

T [^{o}C]	P_0 [mbar]
24	29.85
25	31.69
26	33.62
27	35.67

Table 2.1: Vapor pressure of water for different temperatures. Adapted from Haynes et al.[219]

Therefore a thermocouple was installed on the experimental setup to measure the temperature in order to calculate the proper RH.

As the measured temperature corresponded to 26^o C, the measured pressures and the corresponding RHs were the following:

P [mbar]	RH
0	0.019
3	0.089
6	0.178
9	0.268
12	0.357

Table 2.2: RH values associated to the pressures measured in the CHC

As scattering images were collected on powder samples, the image was isotropic, constituted of concentric circles at constant Q (Fig. 2.12). The image was integrated in order to obtain a one-dimensional diffraction pattern. This was done by finding the picture center and integrating around a certain portion of angle, $(\theta = 0, 142)$ in our case.

Once the one-dimensional curve was obtained, two corrections were later applied in order to convert diffracted radiation intensities to the structure factors:

$$I_{calculated} = I_{measured}(\theta) \cdot \frac{1}{cos^3(2\theta)(\frac{1+cos^2 2\theta}{2})} \tag{2.13}$$

- Geometric correction: necessary because the registered images come from the projection of the Ewald sphere on the flat geometry of the detector. This makes the solid angle covered by a certain pixel change. The correction factor is $cos^3(2\theta)$ for a flat detector.

- Polarization correction: necessary because the X-rays produced by laboratory sources like the anode used here are unpolarized. When

the incoming beam is unpolarized, the diffracted intensity is reduced by the Thompson formula $\frac{1+cos^2 2\theta}{2}$. The equation shows that the scattered beam is stronger in forward or backward directions than in a direction right angle to the incident beam, and it has to be corrected. On the contrary, sources like synchrotrons can polarize the beam and no correction is needed.

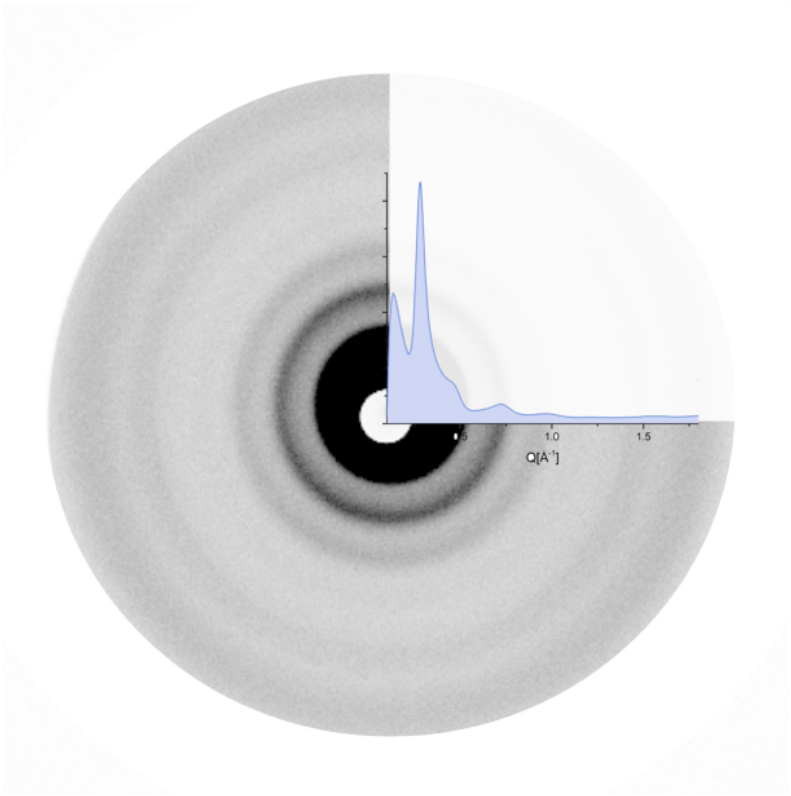

Figure 2.12: Example of a two-dimensional X-ray scattering pattern obtained on a Image Plate MAR detector and one-dimensional diffraction diagram (in light blue) extracted by radial integration from the two-dimensional image

2.6 Neutron scattering

Neutrons are subatomic particles that, due to their main features, are particularly suited to the investigation of condensed matter properties[220].

First of all, similarly to X-rays, their de Broglie wavelength is of the order of magnitude of interatomic distances, so that the structure of systems can be studied at an atomic scale.

Secondly, they are uncharged, and this has several consequences. It gives them the ability to arrive very close to the nuclei, and to be scattered directly by nuclear forces, instead of the electromagnetic ones; since the interaction is not linked to the number of atomic electrons, neutrons can be sensitive to different isotopes; by virtue of their neutrality they are weakly interacting, making the disturbance to the sample small, so that linear-response theory is applicable; furthermore, they investigate bulk properties of the sample, because of their large penetration depth.

Thirdly, even though having the same wavelength as X-rays, neutron energies are much lower, so that they are of the same order of magnitude of many thermal excitations in condensed matter. This means that neutrons also determine the dynamics of atoms. This makes neutrons able to measure energies associated to phenomena inside the sample with a high resolution.

Fourthly, they have magnetic moment so they are an excellent probe for studying the static and dynamical magnetic properties of matter. However, this last point is not relevant to this thesis.

In the next Sections, a quick review about the theory of neutron scattering and about neutron instruments will be presented. As only the essential quantities that are necessary for the understanding of the thesis will be mentioned, the particularly interested reader can read reference textbooks on neutron scattering, such as those written by Lovesey[221], Squires[220] or Bée[222].

2.6.1 Scattering theory

In order to treat a scattering event, a coordinate system must be defined (Fig. 1.1): by placing the sample at the origin, since at a sufficiently large distance the scattered flux will be necessarily radial, the best choice is to use polar spherical coordinates ($\vec{r}$, θ, ϕ). The incident beam direction defines the z axis.

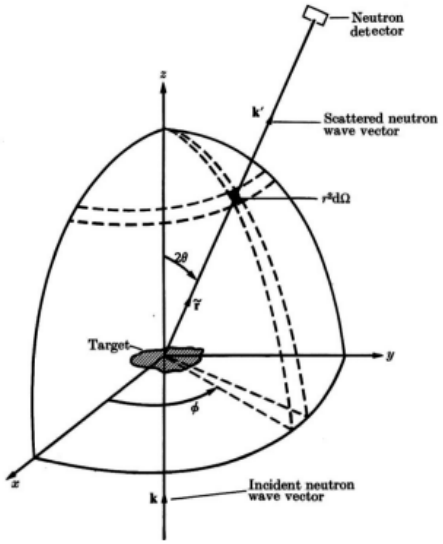

Figure 2.13: Illustration of the scattering experiment geometry

Neutrons having an initial wave-vector $\vec{k}$ and energy E_i are scattered and have final wave-vector $\vec{k'}$ and final energy E_f, in the direction $(2\theta, \phi)$. Two quantities are defined: the exchanged wave-vector $\vec{Q} = \vec{k} - \vec{k'}$ (Fig. 2.14) and the exchanged energy $E_i - E_f = \hbar\omega$.

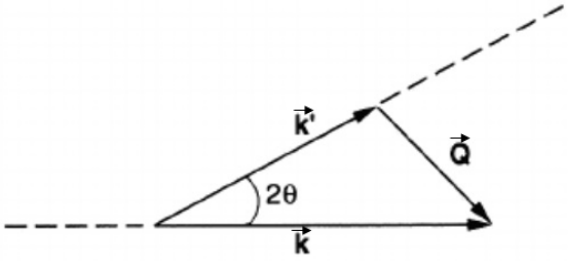

Figure 2.14: Geometrical relationship between initial, final, exchanged wave-vector $\vec{Q}$ and the scattering angle 2θ

In order to relate measured intensities to the properties of the sample, a quantum mechanical formalism is necessary. In the case of neutron scattering, the potential associated with nuclear interactions has a short ranged spatial extension a and the neutron wavelength is $\lambda >> a$. The problem of a particle scattered by a static potential is described by the Schrödinger equation. A theoretical calculation of the neutron cross-section can be obtained in the first Born approximation[221]. Nevertheless,

the Born approximation cannot be used with the true neutron-nucleus potential because, even if very short ranged, it is very strong. To overcome this problem, a Fermi pseudopotential is instead used and defined as:

$$V(\vec{r}) = \frac{2\pi\hbar^2}{m_n} \sum_j b_j \delta(\vec{r} - \vec{r}_j) \tag{2.14}$$

where b_j is the scattering length of the atom j and $\vec{r}_j$ its position.

The solution in the Born approximation with a Fermi pseudopotential is of the form:

$$\psi \propto -\frac{b}{r} e^{-i\vec{k}\cdot\vec{r}} \tag{2.15}$$

Unfortunately, there is no proper nuclear theory to predict the values of b, so they are treated as experimental parameters.

Since a scattering experiment consists in the measurement of the number of neutrons scattered in a given direction and in a certain energy range, the accessible quantity is the double-differential cross-section

$$\frac{d^2\sigma}{d\Omega dE_f} = \frac{1}{\phi} \frac{dN_f}{d\Omega dE} \tag{2.16}$$

where ϕ is the flux of incident neutrons and N_f the number of scattered neutrons.

The corresponding theoretical expression allows us to derive microscopic informations concerning the sample, thanks to the two basic quantities measurable in a scattering experiment, *i.e.* exchanged wave-vector and energy:

$$\frac{d^2\sigma}{d\Omega dE_f} = \frac{k'}{k} \frac{1}{2\pi\hbar} \int_{-\infty}^{\infty} dt\, e^{-i\omega t} \sum_{jj'} \overline{b_j^* b_j'} \, \langle e^{-i\vec{Q}\cdot\vec{r}_j} e^{i\vec{Q}\cdot\vec{r}_{j'}(t)} \rangle \tag{2.17}$$

It indeed contains the correlation of the positions of atoms at different times.

In general,

$$\overline{b_j^* b_{j'}'} = [|\bar{b}|^2 + \delta_{jj'}(\overline{|b|^2} - |\bar{b}|^2)] = \frac{\sigma_c}{4\pi} + \delta_{jj'} \frac{\sigma_i}{4\pi} \tag{2.18}$$

so that the previous expression can be re-written as:

$$\frac{d^2\sigma}{d\Omega dE_f} = N \frac{k'}{k} \frac{\sigma_c}{4\pi} S_c(\vec{Q}, \omega) + N \frac{k'}{k} \frac{\sigma_i}{4\pi} S_i(\vec{Q}, \omega) \tag{2.19}$$

Here $\sigma_c = 4\pi b_{coh}^2$ is called coherent cross-section, while $\sigma_i = 4\pi b_{inc}^2$ the incoherent cross section. The expression

$$S_c(\vec{Q}, \omega) = \frac{1}{2\pi\hbar N} \int_{-\infty}^{\infty} dt\, e^{-i\omega t} \sum_{jj'} \langle e^{-i\vec{Q}\cdot\vec{r}_j} e^{i\vec{Q}\cdot\vec{r}_{j'}(t)} \rangle \tag{2.20}$$

is called coherent structure factor, while

$$S_i(\vec{Q},\omega) = \frac{1}{2\pi\hbar N}\int_{-\infty}^{\infty} dt\, e^{-i\omega t}\sum_j \langle e^{-i\vec{Q}\cdot\vec{r_j}} e^{i\vec{Q}\cdot\vec{r}_j(t)}\rangle \tag{2.21}$$

is known as the incoherent structure factor. Here N denotes the number of atoms in the system.

One can see how:

- **Coherent scattering** depends on the correlation between the positions of the same or of different nuclei at different times. Indeed, it occurs only when strict geometrical conditions are fulfilled, causing interference effects between the waves scattered by each nucleus.
- **Incoherent scattering** depends only on the correlation between the positions of the same nucleus at different times. It depends on the motion of a single particle, so when the position of particles evolves with time, incoherent scattering is a precise measure of their dynamics.

A better understanding of the scattering function can be achieved by noticing that it is the space-temporal Fourier transform of the pair correlation function:

$$S(\vec{q},\omega) = \frac{1}{2\pi\hbar}\int_{-\infty}^{\infty} dt\, e^{-i\omega t}\int d\vec{r}\, e^{i\vec{Q}\cdot\vec{r}} G(\vec{r},t) \tag{2.22}$$

In particular, the coherent dynamic structure factor is the Fourier transform of

$$G(\vec{r},t) = \frac{1}{N}\sum_{jj'}\int d\vec{r}' \,\langle \delta(\vec{r}' + \vec{r} - \hat{r}_j(t))\delta(\vec{r}' - \hat{r}_{j'}(0))\rangle \tag{2.23}$$

while the incoherent dynamic structure factor is the transform of

$$G_s(\vec{r},t) = \frac{1}{N}\sum_{j}\int d\vec{r}' \,\langle \delta(\vec{r}' + \vec{r} - \hat{r}_j(t))\delta(\vec{r}' - \hat{r}_j(0))\rangle \tag{2.24}$$

named self-correlation function. Classically, one would interpret G($\vec{r}$, t) as the probability that, given a particle at the origin at time t = 0, any particle is at position $\vec{r}$ at time t; similarly, $G_s(\vec{r},$ t) would be the probability that, given a particle at the origin at time t = 0, the same particle is at position $\vec{r}$ at time t.

It is interesting to see which kind of scattering – coherent and incoherent – prevails given a certain sample. A chemical compound is composed

of many chemical species, each of them having heir own coherent and incoherent scattering length. The various element contribution will be weighted by the square of their scattering lengths. The scattering lengths are the equivalent of the atomic scattering factors for X-ray scattering, which in that case was θ dependent. For neutrons, it is a constant, and its amplitude is independent of the atomic number Z. One can see in Fig. 2.15 that the values of the scattering lengths vary almost erratically from one nucleus to the other, and the incoherent scattering length of hydrogen prevails on the others.

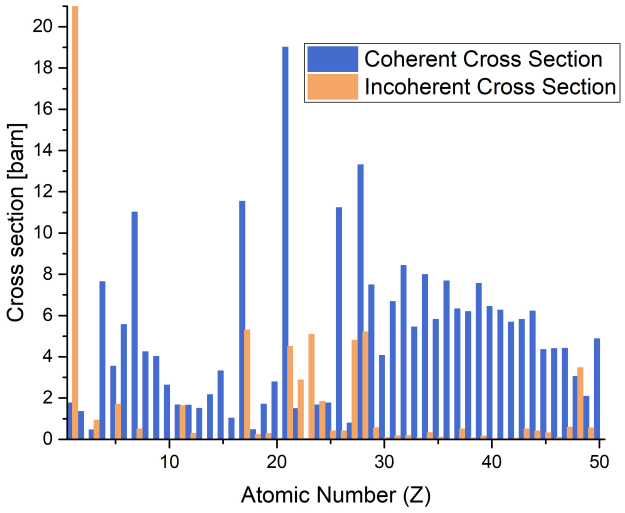

Figure 2.15: Incoherent and Coherent Cross section of elements as a function of their atomic number. In blue the coherent cross section, in orange the incoherent cross section.

That means that neutrons are very sensitive to the self-dynamics of hydrogen nuclei, making all the other contributions negligible. In the case of imogolites, scattering is dominated by hydrogen because of the numerous hydroxyl groups present on the structure. Table 2.3 contains the scattering lengths and cross section of the elements present in a imogolite nanotube. The cross-section of hydrogen is one order of magnitude larger than the other elements.

Element	b_{coh} [fm]	b_{inc} [fm]	σ_{coh} [barn]	σ_{inc} [barn]
H	-3.7406	25.274	1.7568	80.26
O	5.803	0	4.232	0
Si	4.107	0	2.12	0
Al	3.449	0.256	1.495	0.0082

Table 2.3: Coherent and incoherent scattering lengths — b_{coh} and b_{inc} – and coherent and incoherent scattering cross-sections – σ_{coh} and σ_{inc} –, extracted from the NIST website (https://www.ncnr.nist.gov/resources/n-lengths/)

Let's now see more in detail what kind of information can be extracted from a neutron scattering experiment. S($\vec{Q}$,ω) is a two-dimensional map, whose energy axis can be divided in three regions: elastic, quasielastic and inelastic.

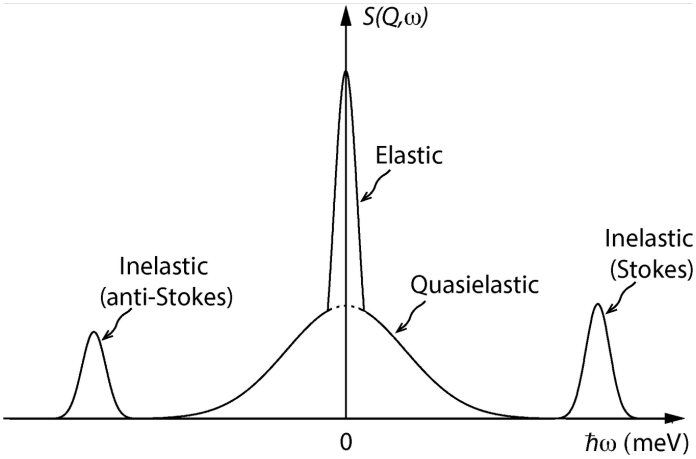

Figure 2.16: Generic S(Q,ω) map, with a schema of the elastic, quasielastic and inelastic features of a spectrum. In particular, in the Stokes side the neutron has lost energy, while in the Anti-Stokes side it has gained energy via its interaction with the sample.

- The **elastic** line corresponds to en exchange of energy equal to zero $\omega = 0$. In practice, every instrument has a finite resolution and all the motions that appear localized in space and therefore "static" in a timescale slower than the timescale associated to the instrument resolution, contribute to the elastic line.

- If atoms diffuse within a time frame to which the instrument is

sensitive, a broadening around the elastic line appears, giving rise to **quasi-elastic** scattering. These kinds of motions are not quantized, giving rise to a continuous distribution of energies around the elastic peak, extending typically up to 1 meV.

- For energies superior to 1 meV, every characteristic periodical vibrations of the system gives rise to a peak at the corresponding frequency in the **inelastic** region. These vibrations are quantized and can be investigated by Inelastic Neutron Scattering (INS).

At low temperature, the elastic and inelastic intensities prevail as diffusional motions are prevented by potential barriers.

In the following section we will see more in detail all the observable of interest in the different regions of the map.

2.6.1.1 Observables of interest in the elastic region

Elastic scattering is related to correlations that are non-zero after an infinite time: the more the motion is confined, the stronger the elastic scattering will be.

The incoherent elastic cross-section for equivalent hydrogens, in the harmonic approximation, is

$$\left(\frac{d^2\sigma}{d\Omega dE_f}\right)_{inc}^{el} = N\frac{\sigma}{4\pi}e^{-2W(Q)}\delta(\hbar\omega) \tag{2.25}$$

The term that contains all the microscopic information is $e^{-2W(\vec{Q})}$, the so-called Debye-Waller factor. For example, if the harmonic approximation holds, for an isotropic system of vibrating equivalent atoms, the Debye-Waller factor is

$$e^{-2W(Q)} = e^{-\frac{1}{3}Q^2\langle u^2\rangle} \tag{2.26}$$

where $\langle u^2\rangle$ is the mean square displacement (MSD) in 1D. The factor $1/3$ takes into account for a diffusion in 3 dimensions.

The Debye-Waller factor reflects the fact that atoms are not fixed but moving because of their thermal motions around their equilibrium position. For a harmonic solid, in the high-temperature region it can be expanded as[221]:

$$W(Q) = \frac{\hbar Q^2}{2m_N}k_BT(\overline{(\hbar\omega)^{-2}} + \frac{1}{12(k_BT)^2} - ...) \tag{2.27}$$

This shows that, for a harmonic solid, the elastic intensity is proportional to a gaussian, and W(Q) shows a linear dependence on temperature. A deviation from linearity at a certain temperature is characteristic

of the appearance of dynamical modes different from the harmonic ones: typically a phase transition or diffusional dynamics.

In conclusion, the aim of an elastic scattering experiment is to investigate a potential depart from linearity at a certain temperature. If present, the drop in the elastic intensity is often counterbalanced by a $QENS$ broadening in the quasielastic region.

2.6.1.2 Observables of interest in the quasielastic region

A diffusional process is a relaxation mechanism, where a system changes irreversibly from a physical state to another. In order to study these processes, it is useful to introduce the Intermediate Scattering Functions.

It was mentioned earlier that the Coherent and Incoherent Structure Factors are the space-time Fourier transforms of the pair Correlation functions. Nevertheless, if one only does the Fourier Transform in time, one obtains the Incoherent Scattering Functions:

$$F_{coh}(\vec{Q},t) = \frac{1}{N}\sum_{jj'} \langle e^{-i\vec{Q}\cdot\vec{r}_{j'}(0)} e^{i\vec{Q}\cdot\vec{r}_j(t)} \rangle \tag{2.28}$$

$$F_{inc}(\vec{Q},t) = \frac{1}{N}\sum_{j} \langle e^{-i\vec{Q}\cdot\vec{r}_j(0)} e^{i\vec{Q}\cdot\vec{r}_j(t)} \rangle \tag{2.29}$$

which correlate the state of a system at two different times.

These are quantities of primary importance in this work, as they are what is experimentally accessible by Neutron Spin Echo experiments. Being the Fourier Transform of the Scattering Factors, they obviously contain the same information. Let's consider for example a system whose relaxation function is a single exponential decay:

$$F(\vec{Q},t) = Ae^{-\frac{t}{\tau}} = Ae^{-\Gamma\cdot t} \tag{2.30}$$

where τ is the characteristic time of the decay. Its Fourier transform gives its theoretical expression in the S(ω) space:

$$S(\omega) \propto \frac{1}{\Gamma^2 + \omega^2} \tag{2.31}$$

which is a Lorentzian whose half-width-half-maximum is Γ. This is indeed the function frequently used to fit $QENS$ data in order to extract the value of Γ. Neutron Spin Echo and quasielastic experiments therefore contain the same information, but in a different space (time *vs* energy) and usually, in a different timescale span — as we will see later, Spin Echo experiments manage to sample longer timescales than classical $QENS$ experiments, meaning the two experiments are complementary.

Although theoretically simple, in certain cases, especially if the quasielastic broadening is small, the first thing to do is to find out whether there is $QENS$ or not in the data-set of study. A straightforward way to comprehend this is to look at the susceptibility. Indeed generally, samples show an harmonic behavior at low temperature, while diffusion appears above a certain transition temperature. Since the $QENS$ broadening can possibly overlap with the inelastic region, the latter evolving with temperature due to an increased phonon population (as explained more in detail in the next subsection), $QENS$ can be conveniently investigated in terms of the imaginary part of the susceptibility divided by the energy:

$$\frac{\chi^{''}(\omega)}{\omega} = \pi \frac{S(\omega)}{\omega}\left(1 - e^{\frac{\hbar\omega}{k_B T}}\right) \tag{2.32}$$

which corresponds to $S(\omega)$ divided by the Bose-Einstein population factor $n(\omega) = \frac{1}{(1-e^{\frac{\hbar\omega}{k_B T}})}$. By dividing by the Bose-Einstein factor allows to cancel the phonon contribution in the quasielastic area.

The main parameter that one wants to get from fitting a $QENS$ profile is the width Γ, or Full Width Half Maximum ($FWHM$). Nevertheless, there are other quantities can contain interesting information about the dynamics of the system. An interesting parameter is for example the Elastic Incoherent Structure Factor ($EISF$). It is the long time limit of the incoherent intermediate scattering function. It is defined as the ratio of the purely elastic contribution to the sum of the elastic and quasielastic contribution. If one splits the total $S(\vec{Q}, \omega)$ map into the elastic and the quasielastic terms, as in:

$$S(\vec{Q}, \omega) = A_0(\vec{Q})\delta(\omega) + A_1(\vec{Q})L(\omega) \tag{2.33}$$

where the elastic peak has been described by a Delta function and the $QENS$ broadening by a Lorentzian, the $EISF$ is defined as

$$EISF = \frac{A_0(\vec{Q})}{A_0(\vec{Q}) + A_1(\vec{Q})} \tag{2.34}$$

The $EISF$ does not contain information about dynamics, but only about geometry, specifically about the region of space accessible to the scatterer: in its two extreme cases it is equal to $\delta(\vec{Q})$ in case of free-long-range motions, while equal to one for a system completely confined in the space explored. Otherwise, its shape can be fitted and give information about the diffusion geometry. As it is an elastic quantity, it can be extracted from Elastic Incoherent Neutron Scattering and will be treated like an elastic quantity Chapter 4.

In the following two parts some basic diffusion models will be presented. These will help in the Chapters 5 and 6 to interpret the simulated and experimental data. In particular, we will see that one of these modesl for confined diffusion will help in the analysis of the dynamics taking place in the dry sample (Chapter 4), while the long range diffusion models are more suitable for analysing for water diffusion (Chapter 5).

Let us now first see some classical models for long-range diffusion. Long-range diffusion is associated to transport phenomena. Roughly speaking, there are three standard cases for diffusion:

- **brownian diffusion**: continuous diffusion of a particle colliding randomly with other particles in an energy dissipative environment. It is the solution of Fick's law and it assumes that diffusion proceeds by small elementary small jumps. In this case:

$$I_{inc}(\vec{Q},t) = e^{-Q^2 D|t|} \tag{2.35}$$

$$S_{inc}(\vec{Q},\omega) = \frac{1}{\pi}\frac{DQ^2}{\omega^2 + (DQ^2)^2} \tag{2.36}$$

$$\Gamma(\vec{Q}) = \hbar D Q^2 \tag{2.37}$$

- **ballistic diffusion**: when the diffusing particle does not encounter frictional forces to its motion. It models the perfect gas behavior:

$$I_{inc}(\vec{Q},t) = e^{-\frac{Q^2}{2}\frac{k_B T}{m}t^2} \tag{2.38}$$

$$S_{inc}(\vec{Q},\omega) = \frac{1}{\hbar}\sqrt{\frac{m}{\pi K_B T}}\frac{1}{Q}e^{-\frac{m}{2k_B T Q^2}\omega^2} \tag{2.39}$$

$$\Gamma(\vec{Q}) = 2\hbar\sqrt{\frac{2ln2k_B T}{m}}|\vec{Q}| \tag{2.40}$$

- **jump diffusion: Chudley Elliot** The Chudley-Elliot jump diffusion model[1] describes the dynamics of particles of a liquid that are caged by other atoms in equilibrium positions for a time τ where they undergo vibrations and then hop to another position at a jump length l. The jump sites are on a Bravais lattice, therefore discrete and periodic.

$$I_{inc}(\vec{Q},t) = I_{inc}(\vec{Q},0)e^{-\Gamma(Q)t} \tag{2.41}$$

[1]The Chudley Elliot model is only one of the models that describe diffusion by a set of jumps, there are others, having a different Q-dependence of the Γ. For simplicity only one model is listed here.

$$S_{inc}(\vec{Q},\omega) = \frac{1}{\pi}\frac{\Gamma(\vec{Q})}{\Gamma^2(\vec{Q})+\omega^2} \tag{2.42}$$

$$\Gamma(\vec{Q}) = \frac{\hbar}{\tau}\Big(1 - \frac{sin(Ql)}{Ql}\Big) \tag{2.43}$$

The different $\vec{Q}$ dependence of Γ for the different models is shown in Fig. 2.17:

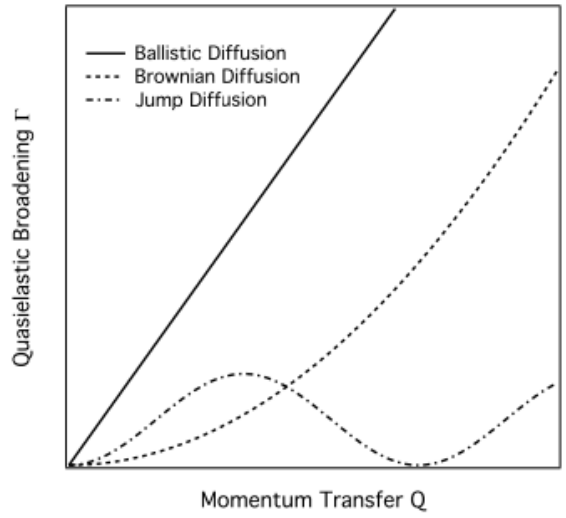

Figure 2.17: Q-dependence of the width Γ for the Brownian, ballistic and jump diffusion models

We'll see that some of these models can be considered or discussed for the analysis of the diffusion of water inside imogolites.

Let's now see some traditional models for confined diffusion[223]. In crystals or solid-like systems, atoms attached to the structure can only have a dynamics that is restricted to reorientation movements around the crystal sites. Continuous diffusion around a centre of symmetry give rise to QENS, that can be modeled with one of the following models:

- **jump between two equivalent sites**: The particle jumps between two sites with average residence time τ. In case of a powder sample:

$$S(Q,\omega) = \frac{(1+j_0(QR))}{2}\delta(\omega) + \frac{1}{\pi}\frac{(1-j_0(QR))}{2}\frac{2\tau}{4+\omega^2\tau^2} \tag{2.44}$$

  where R is the jump distance and j_0 is the 0-th order spherical Bessel function.

- **jump between three equivalent sites**: The particle jumps between three sites with average residence time $\tau_c = \frac{\tau}{3}$. In case of a powder sample:

$$S(Q,\omega) = \frac{(1+2j_0(QR))}{3}\delta(\omega) + \frac{1}{\pi}\frac{2(1-j_0(QR))}{3}\frac{\tau_c}{1+\omega^2\tau_c^2} \quad (2.45)$$

  where j_0 is the 0-th order spherical Bessel function.

- **jump on a circle**: continuous diffusion around a rotation axis gives:

$$I(\vec{Q},t) = \sum_{m=-\infty}^{\infty} J_m^2(Q\cdot R\cdot sin\theta)e^{-D_R m|t|} \quad (2.46)$$

$$S(\vec{Q},\omega) = J_0^2(Q\cdot R\cdot sin\theta)\delta(\omega) + 2\sum_{m=1}^{\infty} J_m^2(Q\cdot R\cdot sin\theta)\frac{1}{\pi}\frac{D_R m^2}{\omega^2 + (D_R m^2)^2} \quad (2.47)$$

  where r is the radius of the circle, θ the polar angle, D_r is the rotational diffusion coefficient and J_m is the m-th cylindrical Bessel function.

Whatever the model, if the diffusion is thermally activated, then it can be described as an Arrhenius process, whose transition rate follows the expression:

$$\frac{1}{\tau} = \frac{1}{\tau_0}exp\Big(-\frac{E_a}{k_B T[K]}\Big) \quad (2.48)$$

where E_a is the temperature-independent activation energy of the process, which is the energy to be given to a system to make it start the chemical or physical process of interest. The activation energy is therefore the amplitude of the potential barrier that prevents a certain diffusive process from occurring if the temperature is too low.

2.6.1.3 Observables of interest in the inelastic region

Vibrations are periodic motions of the atoms of a molecule relative to each other. Some examples are stretching and bending. If they are periodic, the energy of these excitations is quantized, and a quantum of energy is called phonon. A phonon density of states $g(\omega)$ is the number of phonons per energy interval.

When one quantum of vibrational energy is exchanged between the scattered neutron and the system, one can speak about one-phonon scattering. This is of primary interest for studying the lattice dynamics of

a system. Neutrons can also be scattered by more than one phonon, but multi-phonon scattering does not provide useful information and only gives rise to background increasing with $\vec{Q}$. When one phonon is exchanged, the energy exchange can be either positive or negative. If positive, the neutron loses energy and creates a phonon in the system -– phonon emission or Stokes scattering. If negative, it is the case of phonon annihilation, with the neutron gaining energy – Anti-Stokes scattering.

For a Bravais lattice, one can express the incoherent one-phonon cross section as follows:

$$\Big(\frac{d^2\sigma}{d\Omega dE'}\Big) = \frac{\sigma_{inc}}{4\pi}\frac{k'}{k}\frac{3N}{2M}e^{-2W}\frac{\langle(\vec{Q}\cdot\vec{e_s})^2\rangle}{\omega}g(\omega)\Big(coth(\frac{1}{2}\hbar\omega\beta)+1\Big) \quad (2.49)$$

with $\boldsymbol{e_s}$ the solution eigenvector, M the atomic mass, $g(\omega)$ the phonon density of states.

Unfortunately, only in the case of a Bravais lattice $g(\omega)$ has a simple expression directly related to the cross section. For all the other cases, the experiment yields the so-called generalized phonon density of states:

$$G(\omega) = \int_{\vec{Q}} 3\frac{4\pi}{\sigma_{inc}}\frac{2m\omega}{\hbar^2Q^2}\frac{S(\vec{Q},\omega)}{n(\omega)+1}d\vec{Q} \quad (2.50)$$

Phonons obey the Bose-Einstein statistics, and the Bose factor $n(\omega)$ giving the number of phonons with wave-vector $\vec{Q}$ is

$$n(\omega) = \frac{1}{e^{\frac{\hbar\omega}{k_BT}}-1} \quad (2.51)$$

Phonon creation always has a bigger probability than phonon annihilation because at low temperature the Bose factor tends to zero and there are no phonons to be annihilated. That is why a Density of States can be measured at low temperature in the Stokes side, while to measure in the Anti-Stokes side a minimum temperature is required, in order for these states to be populated.

2.6.2 Neutron sources: Institut Laue-Langevin

Neutrons can be produced in a high variety of nuclear reactions, such as fission, spallation and fusion. For scattering experiments, fission and spallation are the most commonly used, the aim being to release as many neutrons as possible in order to achieve a high luminosity. The Institut Laue-Langevin (ILL) is, since 1973, one of the most powerful source of neutrons for scattering experiments using a nuclear reactor. The available flux of neutrons is not a secondary requirement for a scattering experiment, since its quality is primarily determined by the counting rate. ILL

produces a very high flux of neutrons ($1.5 \cdot 10^{15} n \cdot cm^{-2} s^{-1}$) supplying $\sim$ 40 instruments located in the main reactor hall and in two neutron guide halls (Fig. 2.18).

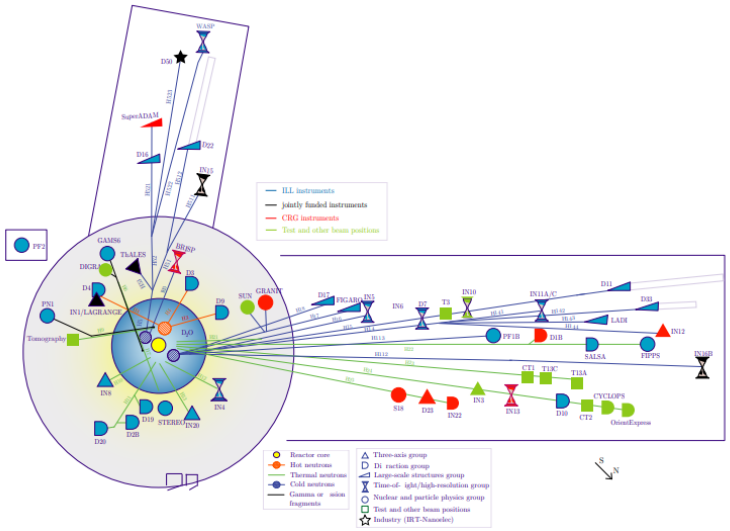

Figure 2.18: Layout of instruments in the main reactor hall and in the two guide halls at Institut Laue-Langevin

The ILL reactor produces neutrons thanks to the fission of Uranium ^{235}U. It produces a continuous flux of neutrons, released with energies in the MeV range. As "slow" neutrons with energy in the meV range are required both for scattering experiments and also to maintain the likelihood of fission high, one has to "cool" them down. This "thermalization" step is achieved by multiple collisions with the atoms of a moderator substance which, in the case of ILL, is heavy water.

Neutrons not involved in the fission process escape the reactor and can be used for scattering experiments. Neutron guides transport them from the source to the instruments without excessive loss in intensity. At the instrument locations, the incident neutrons are "prepared" using optical devices (monochromators, choppers, slits, coils etc...) to best serve the different experiment purposes. After scattering by the samples atoms, they have to be analysed and detected. Since they have little energy and no electric charge, they can only be detected indirectly through induced nuclear reactions with target atoms. The reaction is neutron absorption, which leads to the formation of a compound nucleus that consequently decays. Gas detectors count neutrons by exploiting the avalanche effect produced by the products of the reaction between a neutron and a strongly absorbing isotope *e.g.* ^{3}He, ^{10}B, ^{6}Li, etc...

Neutron instruments can be classified in two categories: The first category does not analyse the neutron energy change after scattering, while the second one does. The first category comprises diffractometers, Small-Angle Neutron Scattering experiments and reflectometers, for which only the change of the neutron direction is analysed. On the other hand, spectrometers measure – in addition – the change of neutron energy after interacting with the sample. One separates *direct geometry spectrometers*, for which the initial energy is defined and the final energy is scanned, from the *inverse geometry spectrometer*, for which the initial energy is varied while the final energy is fixed.

In the present thesis we will use:

- **Diffractometers**: D16
- **Spectrometers**: They differ in the way they measure the energy exchange:
  - **Backscattering spectrometers**: IN13
  - **Spin-echo spectrometers**: WASP
  - **Time-of-flight spectrometers**: PANTHER and IN6-SHARP

The energy resolution at the elastic peak varies with the type of instrument: it is around 1-10 μeV for backscattering, neV for spin echo, from 10 μeV to 1 meV for time-of-flight. The energy resolution defines, by Heisenberg's uncertainty principle $\tau \propto \frac{\hbar}{\Delta E}$, the long-time limit of the observable motions. The spatial extent of the observable motions depend on the accessible Q-range by $\Delta r = \frac{2\pi}{Q}$. The higher the studied Q-value, the smaller the space or distance correlations probed. The features of the instruments – the energy resolution at the elastic peak, the related timescale, and the Q-range accessible – that will be used in this thesis are in Table 2.4 and separately in 2.5 for PANTHER. Clearly PANTHER, and especially the high wavelengths, is not particularly suited for $QENS$ measurements due to the very broad resolution at the elastic. On the other hand, it accesses a very wide Q range that is inaccessible to other instruments.

Instrument	Energy resolution	timescale	Q-range
IN13	8 μeV	150 ps	[0, 4.9] Å^{-1}
IN6-SHARP	70 μeV	20 ps	[0, 2.6] Å^{-1}
WASP	$\sim$ neV	[1, 10^3] ps	[0, 2.2] Å^{-1}

Table 2.4: Energy resolution, time and Q domain explored with the different instruments used (except PANTHER)

PANTHER incident λ [meV]	Energy resolution	timescale	Q-range
19	$\sim$ 1 meV	$\sim$ 1.3 ps	[0, 6] Å^{-1}
30	$\sim$ 1.5 meV	$\sim$ 0.8 ps	[0, 7] Å^{-1}
60	$\sim$ 3 meV	$\sim$ 0.4 ps	[0, 10] Å^{-1}
130	$\sim$ 6.5 meV	$\sim$ 0.2 ps	[0, 14] Å^{-1}

Table 2.5: Energy resolution, time and Q domain explored with PANTHER

During neutron experiments, the sample was held into either a flat aluminium cell – on IN13 and WASP – or a cylindrical vanadium cell – on PANTHER, IN6-SHARP and WASP. A picture of the two is in Fig. 2.19.

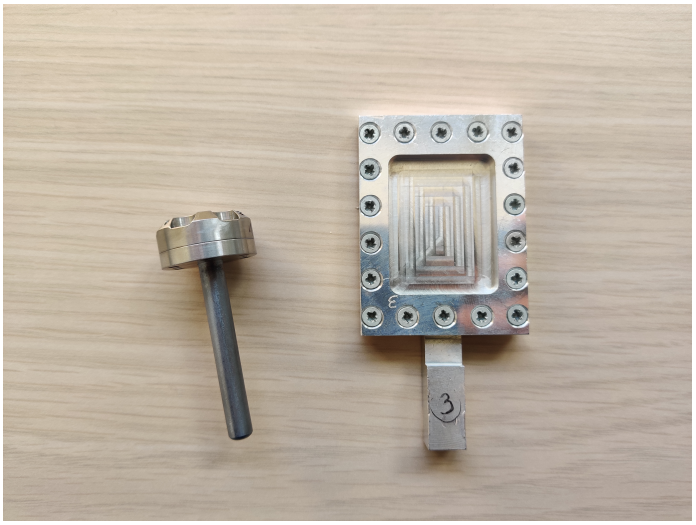

Figure 2.19: Sample cells used for neutron scattering experiments. On the left the cylindrical vanadium cell, while on the right the flat aluminium cell.

2.6.2.1 Backscattering spectrometers: IN13

Backscattering spectrometers are indirect spectrometers, with the final wavelength of the neutrons determined by the crystal analysers (Bragg scattering) and the incident energy varied using either a monochromator (IN13) or a crystal mounted on a doppler machine (IN16B). Backscattering spectrometers have an energy resolution in the μeV range, the highest achievable with spectrometers based on monochromators.

IN13 (Fig. 2.20) is a backscattering spectrometer, installed in the thermal guide H24. Its characteristics are:

- Incident neutron flux at sample equal to $\sim 2 \cdot 10^4\ n\ s^{-1}\ cm^{-2}$
- Incident wavelength λ= 2.23 Å. with energy resolution 8 μeV (Δt $\sim$ 150 ps)
- Accessible Q-range [0.19, 4.9] $Å^{-1}$

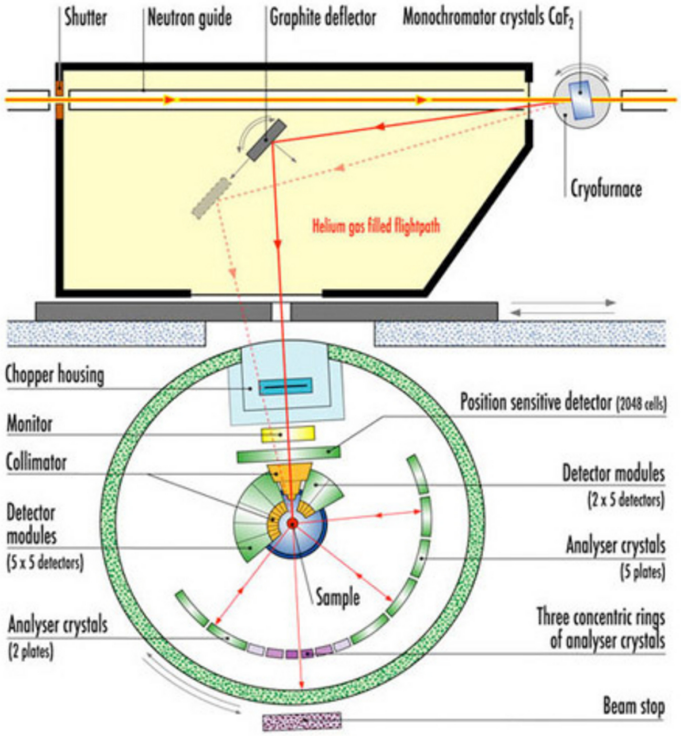

Figure 2.20: Geometry of the backscattering spectrometer IN13

The incident energy is set by Bragg scattering on the CaF_2 monochromator for the (422) reflection. The monochromator is placed inside a cryofurnace and the lattice parameter is slightly varied by thermal expansion, allowing the incident energy of the neutron to be scanned. The backscattering condition is not exactly fulfilled, since θ_M (the Bragg angle) can be varied between 89° and 82°. Monochromatic neutrons are then deflected by a graphite crystal, to re-orientate the beam onto the target. Afterwards, in order to avoid counting neutrons coming from higher orders of reflection and those being scattered directly from the sample to the detectors, neutrons pass through a pair of choppers. A

monitor is placed in front of the sample, to count the incoming neutron flux. Neutrons that crossed the sample without being scattered are absorbed by a beam stop in the forward direction. The final energy is defined by nine spherically curved CaF_2 crystals aligned along the direction (422), kept at room temperature, backscattering neutrons towards seven units of cylindrical ^3He detector tubes, having five tubes each, measuring the scattered intensity.

Raw data were collected by the Nomad software and saved during the experiment. The sample was held into a aluminium flat cell and oriented at 135° with respect to the incoming neutron beam. Data were collected in the temperature range [20, 410] K for the dry sample[2] and [20, 300] K for the hydrated samples [3].

Reduced data were obtained using the LAMP (Large Array Manipulation Program) software[224], by normalizing the raw data to incident flux, correcting them from cell scattering, from self-shielding, and from detector efficiency by measuring a vanadium standard. Since the measured transmission was found to be 98%, multiple scattering was neglected.

2.6.2.2 Spin-echo spectrometers: WASP

The main shortcoming of classical spectrometers is that a good resolution is obtained only at the expense of the incoming flux, as one has to be increasingly selective on the neutrons as a function of their incident (monochromatization) and scattered (analysis) energy. Neutron spin echo (NSE)[225] overcomes this difficulty, managing to probe F($\vec{Q}$,t) in the ns timescale. The trick is to decorrelate the resolution of the measurement from the energy of the neutrons.

NSE uses the precession of a polarized beam of neutrons in a magnetic field to measure the energy exchange. The standard spin-echo experiment works as follows: the neutron beam first passes through a velocity selector that gives around 10% spread in the incident wavelength distribution. A polarizing supermirror then polarizes the beam with polarization parallel to the beam direction. Then a $\frac{\pi}{2}$ spin-turn coil rotates the spins by $\frac{\pi}{2}$. The beam enters a first solenoid. Neutrons with different velocities will perform a different number of precessions, therefore at the exit of the solenoid the spins are "fanned out". The sample is placed at the exit of the first solenoid. After, a π coil rotates the spins by π. This makes the fan of spins entering the second solenoid (having same field strength as

[2]Sample preparation of the dry described in section 4.1.2.

[3]Experiments were done on two different hydrated samples. See section 5.1 for the sample preparation. The same holds for the experiments performed in instruments presented in the following sections, so the same link to the sample preparation will not be mentioned again.

the first one) precess in the inverse way, the ones that were furthest ahead go behind and viceversa. By the end of the second solenoid, the fan closes up. This is the echo effect: if there is no exchange of energy at the sample position, for every spin the precessions in the two solenoids are in same number but opposite direction (clockwise in one, anticlockwise in the other one) so they exit the second solenoid with the exact same spin as when they entered the first solenoid. To measure the actual polarization, a $\frac{\pi}{2}$ spin-turn coil is placed after the second solenoid.
Since the echo condition is independent of the speed of the neutron, the beam can contain a range of wavelengths, which is why spin-echo is considered the ideal technique to access high energy resolutions with large flux.

If there is energy exchange in the sample, the speed of neutrons changes and the number of precessions in the two solenoids don't balance anymore: the initial and final spins differ by a phase angle.

The quantity measured, the polarization along the z axis, gives access to the intermediate scattering function

$$P_z = \frac{I(\vec{Q},t)}{S(Q)} cos\alpha \tag{2.52}$$

where α is a phase parameter that depends on magnetic field intensity. In practice, this is varied by adding a small additional coil that allows to scan over α values.

The output of a spin-echo experiment is the neutron polarization, *i.e.* the real part of the intermediate scattering function F($\vec{Q}$,t)[226]. This gives access to the dynamics of the system, but in the time domain, as opposed to time-of-flight spectrometers.

If the scattering is only elastic, the polarization is fully recovered, therefore F($\vec{Q}$,t) stays at 1 in the whole Q range and time range. If on the contrary, a diffusive process is taking place, only a part of the original polarization is recovered and F($\vec{Q}$,t) departs from unity.

The intermediate scattering function contains both the coherent and incoherent components. If P is the polarization, the fraction of coherent and incoherent scattering is obtained by

$$S_{coh} = \frac{3P+1}{4} \tag{2.53}$$

$$S_{inc} = \frac{3(1-P)}{4} \tag{2.54}$$

WASP (Fig. 2.21) is a spin-echo spectrometer installed in the cold guide H522.

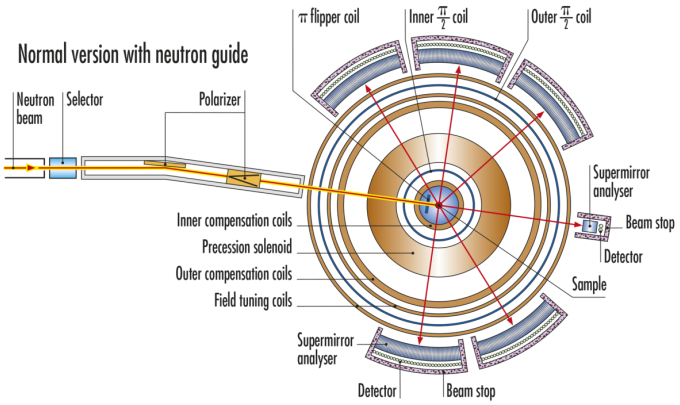

Figure 2.21: Geometry of the spin-echo spectrometer WASP

In the experiment carried out for this thesis, the sample was held into a flat aluminium cell. The incident wavelength was 4 Å, allowing for a a Q range between 0.2 and 2.2 $Å^{-1}$ and an accessible timescale between 1 ps and 1 ns. Data were collected at different temperatures depending on the sample, *i.e.* 2K (to serve as resolution function), 200 K, 250 K, 300 K for the hydrated samples and 300 K, 400 K for the dry sample. Data were acquired and treated with the Igor software.

2.6.2.3 Time-of-flight spectrometers: PANTHER and IN6-SHARP

TOF instruments are based on the particle properties of the neutrons, *i.e.* mass m_n and speed v (as opposed to their wave characteristics symbolized by the de Broglie wavelength λ_n), with kinetic energy given by $E = \frac{1}{2}m_n v^2$. A time-of-flight (TOF) spectrometer measures the velocity of the scattered neutrons in order to determine the energy exchange in the sample.

TOF spectrometers are efficient when one is interested in studying simultaneously a broad range of energies and wave-vectors. They are particularly useful when one does not know in advance which parts of the spectrum are interesting or in case a broad region is of interest. In practice, not all the energy and Q values are accessible experimentally for TOF instruments. For a given $\vec{k}$ and a given $\vec{k'}$ only a restricted region in reciprocal space $(\vec{Q}, \omega)$ is accessible experimentally, called "kinematically allowed region" (Fig. 2.22). By combining the energy and momentum

conservation:

$$\vec{Q} = \vec{k} - \vec{k'} \tag{2.55}$$

$$\hbar\omega = E_i - E_f = \frac{\hbar^2}{2m_n}(k^2 - k'^2) \tag{2.56}$$

in the case of direct geometry, where E_i is fixed, the range of the ($\vec{Q}$, ω) space that can be covered by an experiment is

$$\frac{\hbar Q^2}{2m_n} = 2E_i - \hbar\omega - 2\sqrt{E_i(E_i - \hbar\omega)}cos2\theta \tag{2.57}$$

while for inverse geometry, where E_f is fixed:

$$\frac{\hbar Q^2}{2m_n} = 2E_f + \hbar\omega - 2\sqrt{E_f(E_f + \hbar\omega)}cos2\theta \tag{2.58}$$

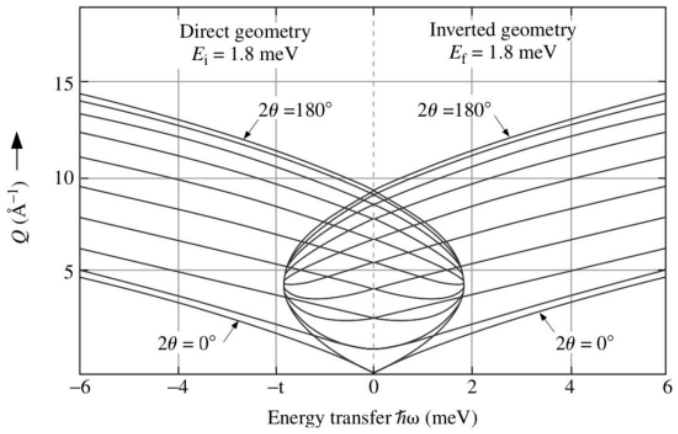

Figure 2.22: Neutron scattering kinematically allowed region for direct and inverse geometry

On direct-geometry instruments the positive side (energy-loss) of the spectrum cannot exceed E_i and the energy resolution at the elastic deteriorates with E_i. Therefore, to study small energy transfers $\hbar\omega$ a small incident energy is chosen, while a large E_i will access high energy transfers, but with the resolution being poor. That's why, for instruments that can cover a broad energy range like PANTHER, usually the map is scanned with several E_i to optimize the resolution in every region and collected data are combined afterwards. The TOF instruments used here will be both in direct-geometry. PANTHER is installed on a thermal guide, allowing for larger incident energy E_i (E_i=19, 30, 60, 130 meV)

but lower resolution around the elastic. IN6-SHARP uses a smaller incident energy (E_i=2 meV), so it samples only the negative side of the spectrum (Anti-Stokes), but with higher resolution around the elastic peak. At the same time, PANTHER resolution is more or less constant on the whole energy range, while IN6-SHARP resolution deteriorates quickly as one moves away from the elastic peak. That's why PANTHER is more suited for inelastic measurements, while IN6-SHARP for quasielastic measurements.

Fig. 2.25 compares the different ($\vec{Q}$, ω) regions accessible for the two instruments.

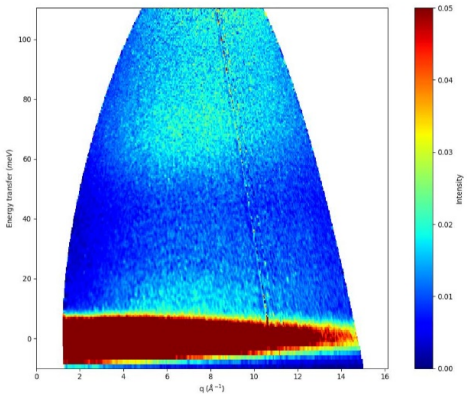

Figure 2.23: *a*)

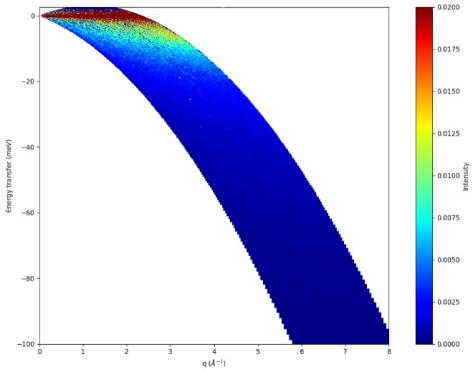

Figure 2.24: *b*)

Figure 2.25: Typical S($\vec{Q}$,ω) maps for *a*) PANTHER at T=10 K — giving access to the Stokes side of the spectrum — and *b*) IN6-SHARP at T=300 K — giving access to the Anti-Stokes side of the spectrum.

PANTHER (2.26) is a time-of-flight spectrometer installed in the nuclear reactor hall of the ILL, in the thermal guide H12. The instrument works as follows: a polychromatic neutron beam coming from the reactor is partially monochromated by two choppers rotating at medium speed. This allows mainly to eliminate the fast neutrons and gamma particles from the neutron beam. Then a monochromator selects the incident energy of neutrons E_i. The monochromator is either a graphite or copper crystal whose orientation allows to select the desired wavelength. The beam emerging from the monochromator then passes through a Fermi chopper rotating at high speed. The neutron beam passes through a monitor and is finally scattered by the sample. The neutron energy gain or loss and the scattering angle are measured by a set of detectors placed around the sample.

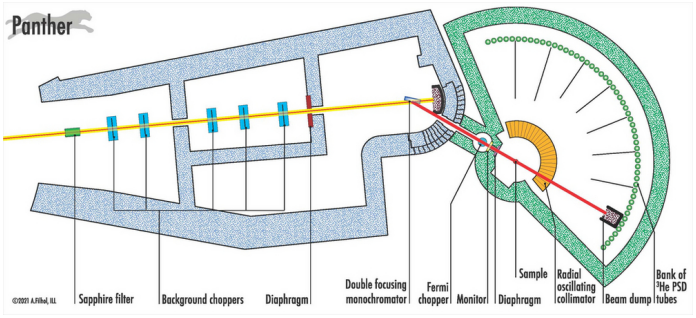

Figure 2.26: Geometry of the time-of-flight spectrometer PANTHER

For the measurements carried out on PANTHER, samples were held into a cylindrical vanadium cell. The density of states was measured at 10 K, with four incident energies, *i.e.* 19, 30, 60 and 130 meV. Data were collected with NOMAD and treated with the software Mantid[227]. They were corrected for incident flux, cell scattering and detector efficiency. Finally, the spectra at 19, 30 and 60 meV and 130 meV were re-scaled and merged, to provide a single spectrum, and converted into the Generalized Density of States.

The characteristics of the instrument are:

- Incident neutron flux at the sample equal to $\sim 10^5\ n\ cm^{-2}s^{-1}$
- several incident wavelengths can be delivered, the resolution at the elastic being around 5% of E_i: 12, 15, 19, 30, 40, 60, 77 or 130 meV
- the Q range accessible depends on E_i and it can reach [0, 14] $Å^{-1}$ at its widest

IN6-SHARP (Fig. 2.27) is a time focussing time-of-flight spectrometer installed in the cold guide H15. Three composite pyrolytic graphite monochromators extract three neutron beams from the guide, which are focused at the sample position. Before that the neutron beam arrives into the sample, it passes trough a beryllium filter that removes the second-order reflection from the monochromators. Then it passes through an anti overlap-chopper that avoids overlap of neutrons from successive bursts, a Fermi chopper, that pulses the beam and compensates for the velocity difference in the three incident beam, and a collimator.

The four wavelengths that can be delivered are 4.1, 4.6, 5.1, and 5.9 Å.

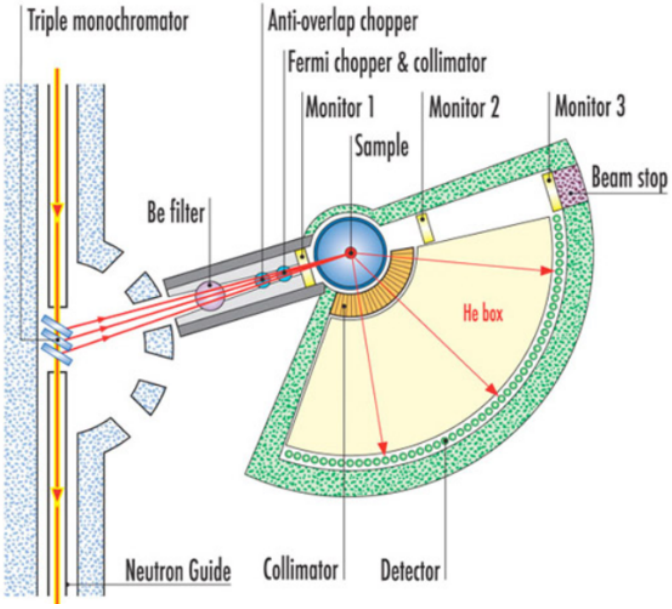

Figure 2.27: Geometry of the time-of-flight spectrometer IN6-SHARP

The characteristics of the instrument are:

- Incident neutron flux (with $\lambda_i = 4.1$ Å) at the sample equal to $\sim 8.9 \cdot 10^4\ cm^{-2}\ s^{-1}$
- four initial wavelengths $\lambda_i = 4.1$, 4.6, 5.1 and 5.9 Å corresponding to 170, 120, 70, 50 μeV for energy resolution
- Q range [0, 2.6] Å^{-1}

Data were collected in IN6-SHARP using a incident wavelength of 5.1 Å. The dry sample was measured at 2, 250, 300, 325, 350, 375, 400, 450 K. The sample hydrated with 12wt%[4] of water was measured at 200, 250 and 300 K. Data were collected with NOMAD and treated with the software Mantid[227]. They were corrected for incident flux, cell scattering and detector efficiency.

2.6.2.4 Diffractometers: D16

For diffraction experiments, there is no analysis of the energy of the scattered neutrons. Therefore the total scattering function $S(\vec{Q})$ only

[4]As opposed to the other experiments, only one of the two hydrated samples was measured on IN6-SHARP. See section 5.1 for the definition of the different hydrated samples.

depends on the scattering vector $\vec{Q}$. For isotropic sample, one can drop the vector notation and only consider the norm Q of the wavevector transfer.

In this thesis, diffraction data were collected at the diffractometer D16 at the ILL. D16 (Fig. 5.2) is a cold-neutron two-circle diffractometer in the beamline H521. The primary white beam is reflected by a focussing pyrolytic graphite monochromator. The monochromator housing has two beam holes at take-off angles of 90° and 115°, corresponding to incoming wavelengths equal to 4.7 Å and 5.6 Å. A collimating slit, obtained with two motorized pairs of slits, when combined to the large, vertically focusing graphite monochromator, provides high neutron flux at the sample position and high resolution in the horizontal plane. The diffracted neutrons are recorded in a high-resolution large area detector, MILAND. The θ range accessible is [–5°, 120°], which is sampled by mounting the detector on a rotation table. The corresponding Q range is [0.01, 2.5] $Å^{-1}$.

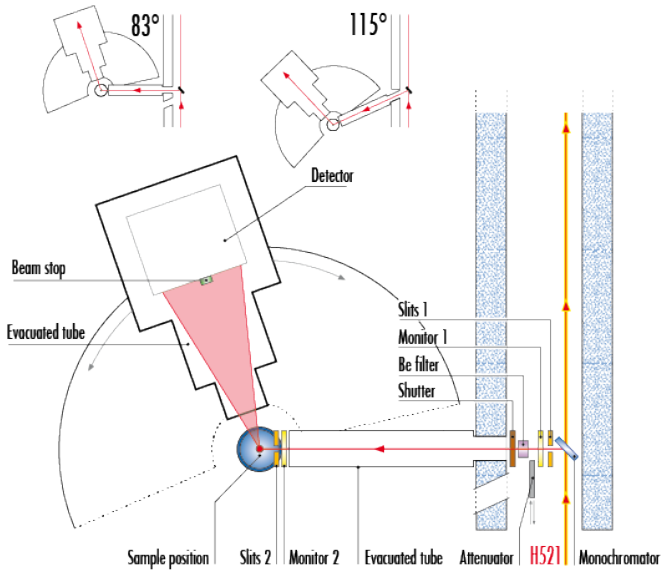

Figure 2.28: Geometry of the diffractometer D16

During the experiment, samples were held into cylindrical vanadium cells. The incident wavelength was 4.461 Å and the data collected at ambient temperature. Data analysis was performed with the Mantid software[227]. Data were normalized to incident flux, and were corrected from cell scattering, ambient room background, by measuring an absorber sample (Cd) and accounting for transmission and thickness of the sample. The two-dimensional scattering intensities were radially integrated to obtain one-dimensional diffraction patterns. The scattering intensities

were normalized to the neutron irradiated mass of the dry nanotubes in the cells.

3. MD simulations

The experimental techniques presented in the previous chapters not always give results that are easy to interpret. Often, one needs to compare the experimental data to their simulated equivalents in order to understand the physics of a certain phenomenon. The tool that helps us understand X-ray and neutron data is Molecular Dynamics (MD). With MD, one can simulate the time-dependent behavior of a system, which is obtained by integrating the equations of motion with adequate boundary conditions.

In order to run a MD simulation, one needs to know the forces between the atoms of the system. This can be done in two ways. The computationally simplest way is to use a force field approximation, *i.e.* define a mathematically simplified expression describing the dependence of the energy of a system on the coordinates of its particles, replacing the true complex potential. This leads to so-called *classical* MD simulations. In this case, the parameters are usually obtained from semi-empirical Quantum Mechanics calculations or by fitting experimental data. Nevertheless, the quality of a force field needs to be confirmed experimentally. Moreover, a force-field cannot describe chemical reactions and is rarely transferable.

An alternative approach is to run an $ab-initio$ (DFT) MD simulations (AIMD), where the Hellman-Feynman forces between atoms are computed from the electronic structure as the simulation proceeds. This first principle method is much more accurate as it does not require any input potential. In addition, this method describes chemical processes. Nevertheless, despite the growing popularity of AIMD simulations, these methods are still computationally expensive. These are good models to extract the structure of a system or its short-time dynamics, but when bigger systems or longer simulations need to be explored, these methods are not convenient anymore.

Therefore, as the main objective of this thesis is to investigate phenomena like transitions and long-range diffusion, where one needs both a large system and a long timescales, a classical force-field was employed. All MD simulations were run with the LAMMPS (Large-Scale Atomic/Molecular Massively Parallel Simulator) software[228] using the CLAYFF and SPC/E force fields, on the cluster of the ILL. Visualization of the trajectories was done with the Ovito (Open Visualization Tool) software[229].

3.1 CLAYFF and SPC/E potentials

The two basic ingredients of all classical MD simulations is the input structure and the definition of the potential describing the interactions between atoms.

In this work, the potential used for the tube is the extended CLAYFF force field[230]. The classical CLAYFF force field was extensively used in literature for clays[231] and specifically for imogolite nanotubes[77,205,206,232–235]. It includes two non-bonded terms, *i.e.* a Coulombic term for electrostatic interactions, and a Lennard-Jones 12-6 term for the van der Waals interactions; it also contains a bonded term, *i.e.* the harmonic bonding term for hydroxyls, that takes into account the OH stretching. The potential used here is an extended form of this potential, including also a second bonded term, *i.e.* the harmonic bending term for the M-O-H angles as proposed in Pouvreau et al[236]. Indeed, by comparison with DFT results, Scalfi et al.[207] validated for Si-INTs having N = 12 the use of the extended CLAYFF force field, claiming its greater suitability for reproducing the properties of the tube, when comparing the results to $ab-initio$ calculations. Here, we use the same extended potential to model a dry nanotube with N = 14. In summary, the total energy is given by:

$$E = E_{LJ} + E_{Coulomb} + E_{bonds} + E_{angles} \tag{3.1}$$

The mathematical expressions of its separate terms are the following:

- **Lennard Jones potential**

$$E_{LJ} = 4\epsilon\left[\left(\frac{\sigma}{r}\right)^{12} - \left(\frac{\sigma}{r}\right)^{6}\right] \qquad r < r_c \tag{3.2}$$

  with cutoff distance $r_c = 8.5$ Å. The LJ potential accounts for the van der Waals interactions, having a cutoff distance in order to minimize the computational cost. The latter can be employed for interactions that weaken rapidly with increasing distance, such as the LJ potential.

- **Coulomb potential**

$$E_{Coulomb} = C\frac{q_i q_j}{\epsilon r} \tag{3.3}$$

  which is accounted by assigning partial atomic charges to each nucleus, obtained from $ab-initio$ calculations. In this case, in order to compute the long-range coulombic interactions, a cutoff distance cannot be used because it decrease very slowly as $\propto r^{-1}$. Therefore,

a long range solver is applied. It performs the Ewald summation in the k-space, with accuracy equal to 10^{-5}, in order to ensure proper convergence.

- **Bond stretching harmonic potential**

$$E_{bonds} = K(r - r_0)^2 \tag{3.4}$$

This term controls the length of covalent bonds, non-zero only for the OH bonds, by approximating the bond as a string with force constant K.

- **Angle bending harmonic potential**

$$E_{angles} = K(\theta - \theta_0)^2 \tag{3.5}$$

This last terms corresponds to the width of the angle between three atoms covalently bonded, and it is non-zero only for the Al-O-H and Si-O-H angles in CLAYFF.

The parameters assigned to the non-bonded interactions, according to the CLAYFF force-field are reported in Table 3.1. One main advantage of CLAYFF is that it differentiates an element into different types depending on its structural position. For example, oxygens have different charges and vdW parameters, depending if it is a bridging oxygen or a hydroxyl oxygen.

	Al	Bridging O	Hydroxyl O	Si	H
Charge [e]	1.575	-1.05	-0.95	2.1	0.425
ϵ_i vdW $[\frac{Kcal}{mol}]$	1.3298e-6	0.1554	0.1554	1.8405e-6	0
σ_i vdW [Å]	4.2712	3.1655	3.1655	3.3020	0

Table 3.1: Parameters of non-bonded interactions in the CLAYFF model

The vdW coefficient between unlike atoms are calculated according to the arithmetic/geometric mean rule:

$$\epsilon_{ij} = \sqrt{\epsilon_i \epsilon_j}$$

$$\sigma_{ij} = \frac{1}{2}(\sigma_i + \sigma_j)$$

For the bonded interactions, parameter values are presented in Table 3.2 and 3.3.

	OH bond
r_0 [Å]	1.0
K $[\frac{Kcal}{mol}^2]$	554.1349

Table 3.2: Parameters of bonded interactions in the CLAYFF model

	M-O-H angle
θ_0 [degrees]	109.47
K $[\frac{Kcal}{radian}^2]$	30.0

Table 3.3: Additional parameters introduced in the extended CLAYFF model. Here M is Al in the case of external OH or Si in the case of internal OH.

Several models have been developed to model water, the most commonly used being SPC[237], SPC/E[238], TIP3P[239] and TIP4P2005[240]. These models have slightly different parameter values and reproduce differently some macroscopic features of water. In this work, water molecules were modeled with a flexible SPC/E model, as it was demonstrated in several works that it reproduces well not only bulk water[241,242] properties but also confinement[172,243,244]. The SPC/E model is a 3-sites model, having three interaction points corresponding to the three atoms of the water molecule. Each site has a point charge, and the site corresponding to the oxygen atom also has the Lennard-Jones parameters. The charges and Lennard-Jones parameters are the same as for the CLAYFF force-field. An harmonic stretching and bending term were added to allow flexibility to the molecule.

The SPC/E stretching parameters are in Table 3.4, while the bending parameters in Table 3.5.

	OH bond
r_0 [Å]	1.0
K $[\frac{Kcal}{mol}^2]$	554.1349

Table 3.4: Stretching parameters in the SPC/E model for water molecules

	water H-O-H angle
θ_0 [degrees]	109.47
K $[\frac{Kcal}{radian^2}]$	45.7696

Table 3.5: Bending parameters in the SPC/E model for water molecules

As shown in the Table, the SPC/E model assumes an ideal tetrahedral shape with $\widehat{HOH} = 109.47°$, instead of the observed $\widehat{HOH} = 104.5$ °.

In the MD simulation, water molecules were first disposed at random positions within an insertion region defined beforehand, for example a cylinder inside the pore of the tube. The insertion was only performed if no current atom in the simulation box was already present within a distance of R = 2 Å. Indeed without R, atoms could overlap in position and cause the explosion of the system, in the worst case. Once the deposition ended, the positions of the molecules were relaxed by performing short MD simulations in the (N,V,T) ensemble.

Periodic boundary conditions were applied, in order to avoid simulating the existence of an artificial surface at the borders of the system. Moreover, global movements of the whole system were impeded, in order to insure that the entire collection of atoms does not drift or rotate during the simulation due to random perturbations.

3.2 Ensembles and thermostats

Once the potential is defined, a MD simulation consists in calculating the forces between atoms and solving the equations of motion for each atom i of the system:

$$\dot{\vec{r}}_i = \frac{\partial H}{\partial \vec{p}_i} \tag{3.6}$$

$$\dot{\vec{p}}_i = -\frac{\partial H}{\partial \vec{r}_i} \tag{3.7}$$

where $\vec{p}_i$ and $\vec{r}_i$ are the momentum and position of the i-th atom, respectively, and H the Hamiltonian of the system. It is defined as a function of positions and momenta:

$$H(\vec{p}_i, \vec{r}_i) = \sum_{i=1}^{N} \frac{\vec{p}_i^2}{2m_i} + V(\vec{r}_i) \tag{3.8}$$

The Hamilton equations of motion can be rewritten into Newton's equations of motion:

$$\vec{F}_i = m_i \cdot \dot{\vec{v}}_i = -\frac{\partial V}{\partial \vec{r}} \tag{3.9}$$

$$\dot{\vec{r}}_i = \vec{v}_i \tag{3.10}$$

where m_i is the mass of the atom, $\vec{a}_i$ its velocity and $\vec{F}_i$ the force acting on it due to all the interactions with the other atoms.

As the forces here defined depend on all the positions $\vec{r}_N$, these are 6N coupled differential equations and there is no analytical solution. There are several way integrate numerically these equations, such as using the Verlet algorithm[245]. In LAMMPS, it is by default the velocity-Verlet algorithm that is used[246]. The algorithm re-computes at each time-step the forces acting on every atom so that the positions and velocities of all atoms are updated. It proceeds as follows:

- at the beginning, $\vec{r}(t)$ and $\vec{v}(t)$ are known, and the forces can be computed
- the new positions can be calculated as

$$\vec{r}_i(t+\delta t) = \vec{r}_i(t) + \vec{v}_i(t)\delta t + \frac{\vec{F}_i(t)}{m_i}\frac{\delta t^2}{2} \tag{3.11}$$

- $\vec{F}_i(t+\delta t)$ is computed
- the new velocities are computed as

$$\vec{v}_i(t+\delta t) = \vec{v}_i(t) + \Big(\frac{\vec{F}_i(t) + \vec{F}_i(t+\delta t)}{m_i}\Big)\frac{\delta t}{2} \tag{3.12}$$

The time-step has to be chosen small enough so that discretization errors are avoided. In this case, a time-step of 0.5 fs is taken.

As well known from Quantum Mechanics, a solution of the Hamiltonian conserves the total energy of the system:

$$H(\vec{r}, \vec{p}) = E \tag{3.13}$$

This provides an important connection between molecular dynamics and statistical mechanics. Indeed, solving the Hamilton equations is equivalent to sampling the micro-canonical ensemble, where the number of particles N, the volume V and the energy E are conserved. In this case, the accessible states to the system are those of constant energy E.

Nevertheless, the micro-canonical ensemble does not correspond to the conditions under which most experiments are carried out. Therefore, if one wants to investigate the behavior of a system at a specific temperature, a canonical (N,V,T) ensemble must be sampled. If so, the total system is divided into a heat bath and the system under study. It can be pointed out that the total energy is still conserved, but not the energy

of our sub-system. In order to modulate the temperature of the system, a thermostat is introduced, which ensures that the average temperature is as desired. There are two broad categories of thermostats:

- **Deterministic thermostats**: for these thermostats the temperature adjustments are determined by the initial conditions. The advantages of deterministic algorithms are that the results can be exactly reproduced and that there are well-defined conserved quantities. An example is the Nose-Hoover thermostat.

- **Stochastic thermostats**: in this case, the velocities of the particles are altered randomly. The instantaneous temperature is altered by important stochastic variations and what is sampled is not exactly a canonical ensemble. Some examples are the Andersen or the Langevin thermostats.

Various thermostats were tested, and the final choice fell on the Nose-Hoover thermostat, as it appeared to be extremely efficient in relaxing a system to the target temperature, and it remained stable at the target temperature, as opposed to some stochastic thermostats tested.

The Nose-Hoover thermostat[247,248] considers the heat bath as an integral part of the system by addition of an artificial variable Q. This is done by using the Lagrangian equations of motions – that are equivalent to the Hamiltonian equations of motion –, where the Lagrangian is the difference between the kinetic energy K and the potential V:

$$L = K - V \tag{3.14}$$

The algorithm adds a fictitious additional coordinate s and a mass Q,that determines the coupling between the reservoir and the real system:

$$L = \sum_{i}^{N} \frac{1}{2} m_i s^2 \vec{v}_i^2 - V(\vec{r}_i) + \frac{Q}{2}\dot{s}^2 - \frac{3N}{k_B T} ln(s) \tag{3.15}$$

In LAMMPS, the mass Q of the fictitious degree of freedom is implicitly set through the temperature damping parameter T_{damp}, which determines how rapidly the temperature is relaxed. This values has to be chosen carefully, as the thermostat does not work well for arbitrary values of T_{damp}: if not set properly, it can either make the temperature fluctuate wildly, either make the equilibration take too long. After testing several values and monitoring the temperature evolution with time, a values of T_{damp}=80 fs was chosen.

The Nose-Hoover thermostat samples the canonical ensemble, nevertheless, it can lead to nearly periodic temperature fluctuations due to the

coupling to the heath bath. These can then introduce artificial effects in dynamical quantities when transformed into the energy domain. For this reason, the (N,V,T) trajectories run for stabilizing the temperature were always followed in this work by simulations run in the (N,V,E) ensemble, where the system is at the equilibrium and isolated. All observables were calculated starting from these (N,V,E) trajectories.

To summarize, all MD simulations were run in three steps:

- **Energy minimization**: since the initial configuration is a high energy state, geometry optimization is necessary to relax the system and to bring it to its state of equilibrium. The process consists in slightly moving all atoms in all directions at every step and calculating the energy of the system. The default algorithm in LAMMPS for energy minimization is the Polak-Ribiere version of the conjugate gradient (CG) algorithm. The procedure terminates when one of the stopping criteria is satisfied, *i.e.* either the maximum number of iterations is reached (here a value of maximum 10^6 iterations was considered), either the energy change between successive iterations is less than or equal to the tolerance (energy tolerance chosen equal to 10^{-7}). Hopefully at that point, the system is at its minimum energy state, *i.e.* the arrangement in space of all the atoms where the interatomic forces on each atoms are close to zero and the position of the system on the potential energy surface is a stationary point.

- **Equilibration in the (N,V,T) ensemble**: after minimization, the system is at 0 K, but in order to start dynamics it has to be brought to the temperature of interest T. In a first step, velocities are assigned at a certain T by picking velocities "at random" from a Maxwell-Boltzmann distribution:

$$P(\vec{v};T) = \Big(\frac{m_i}{2\pi k_B T}\Big)^{3/2} exp\Big(-\frac{m_i \vec{v}_i}{2k_B T}\Big) \tag{3.16}$$

  Then, in the phase of equilibration, the temperature of the system is monitored to ensure that at the end of the (N,V,T) run, it has reached a steady state on average. The temperature monitoring is done by calculating it value with the equipartition principle

$$\frac{N_{dof} k_B T}{2} = \frac{1}{2}\sum_i^N m_i \vec{v}_i^2 \tag{3.17}$$

  where N_{dof} is the number of degrees of freedom of the system. Once temperature or energy fluctuates around a constant value with time, the equilibration period has reached its end.

- **Production run in the (N,V,E) ensemble**: it can happen that the (N,V,T) thermostat re-injects energy in the system at a certain frequency, giving an artificial contribution to, for example, the calculated Density of States. So when calculating dynamical properties, it is preferable that a thermostat is not used. Therefore, a final run in (N,V,E) was always used to calculate all the dynamical time-dependent properties, that are measured with neutrons. Two sets of final trajectories were produced with different time-lengths and frame distance, according to the observable that one had to calculate. Indeed, as the neutron observables are measured as a function of energy, when simulating the same quantities by doing the Fourier Transform of the trajectories, the chosen time length and frame distance impact the result: the time length of the simulation is related to the energy resolution of its Fourier transform, while the time resolution the — the time-step between frames — is related to the maximum value reachable in energy. Therefore, in conclusion, the features of the simulation runs are the following:

  - For the inelastic and elastic region: trajectories had a time length of **100 ps** and frame step **dt=20 fs**. Indeed, for a density of states, what is required is a map with relatively low resolution that extends up to high energies ($\sim$ hundreds of meV). Regarding the elastic region, typically observables are summed over time, so the time length is not relevant and simply the trajectory having more time-steps was chosen.
  - For the quasielastic region: trajectories had a time length of **1ns** with frame step **dt=1000 fs**. Indeed, for $QENS$ what is needed is a restricted energy span but with a high energy resolution.

3.3 Simulated system size and configuration

Another parameter to decide when running a MD simulation is the size of the system. Ideally, the bigger the system the better are the results but unfortunately, this would be very expensive computationally and one has to find a compromise size, according to what quantity one plans to calculate after.

Here two different structures were studied:

- **Single isolated nanotube**: most of simulations were run on an isolated tube having N=14 and 11 unit cells on the longitudinal direction, inside a cubic box of size L=92.97 Å (as T=8.45 Å is the

longitudinal period of the tube and $11 \cdot 8.45$ Å $= 92.97$ Å), as in Fig. 3.1. Indeed, certain physical phenomena – phase transitions or long range diffusion – need a big system to be properly investigated. Therefore, 11 cells were chosen as a compromise between a too small system and a too big one in order to be simulated in reasonable times.

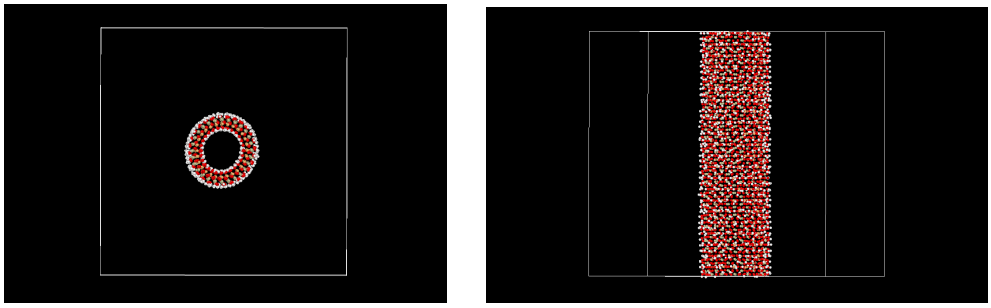

a) *b*)

Figure 3.1: Isolated tube in a cubic box, *a*) top view and *b*) side view

This structure was used to study all the dynamical properties of the dry tube (elastic, quasielastic, inelastic) and of the hydrated states, after adsorbing water molecules inside the tube cavity.

- **Isolated bundle of 19 tubes**: this structure was created uniquely in order to understand the bundling of tubes in the dry sample, in Section 4.1.3. This necessitated the whole bundle to be included in the simulation box. Indeed, a less computationally expensive alternative that was considered was to study a single tube inside an hexagonal box – having the same dimensions of the bundle unit cell – with infinite periodic boundary conditions. Nevertheless, this configuration does not allow to 1) deform the unit cell size inhomogeneously around the bundle, so that every tube can deform independently and different from the others, and 2) access the area around the bundle. Therefore, this second possibility was investigated but later discarded. Therefore, two bundles were considered, one with tubes having N=13 and one with N=14 (the consideration of N=13 will be better explained in Section 4.1.3), and after MD the low Q atomic diffraction pattern was calculated in order to compare to the experimental curve. Since 19 tubes were taken, in order to save computational time only one unit cell along the longitudinal axis was considered. Indeed, the choice of a short system along z does not compromise the calculation results, as the diffraction calculations in the low Q region do not depend strongly

on the length of the tube at the atomic level; it is therefore possible to repeat the structure in z after having performed MD. In conclusion, the chosen simulation box had L_x=L_y=216 Å and L_z=8.45 Å – the length of the single unit cell. This is shown in Fig. 3.2.

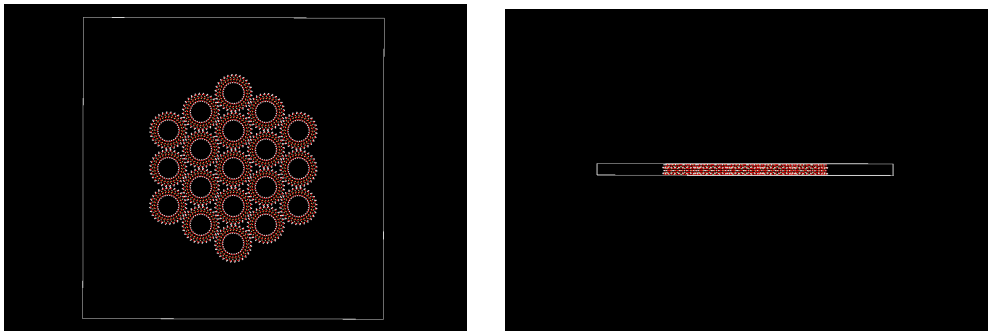

a) *b)*

Figure 3.2: Isolated bundle of 19 tubes, *a)* top view and *b)* side view

3.4 Calculation of neutron and X-ray observables

Neutron observables were then calculated from the trajectories with the MDANSE software[249]. All the quantities were computed in a certain Q-range defined in the software and in the energy span defined by the simulation time resolution. The simulated Q-range always corresponded to the experimental one, depending on the instrument simulated. In particular:

- $EISF$ and MSD were calculated for comparison to IN13 data, therefore in the Q range [0, 5] Å^{-1}. The calculated MSD is defined as:

$$MSD = \frac{1}{N_t}\sum_{j}^{N_t}\frac{1}{N_{atoms}}\sum_{k}^{N_{atoms}}(\vec{r}-\vec{r}(t))^2 \tag{3.18}$$

  where N_t is the number of frames of the simulation. Therefore, the first sum runs over time-frames considered for the calculation and the second one on atoms.

- S($\vec{Q}$,ω) maps were calculated for comparison to the $QENS$ data measured on IN6-SHARP, so the Q range [0, 2] Å^{-1} was chosen.

- F($\vec{Q}$,t) maps were calculated for comparison to WASP data, therefore the Q range [0, 2] Å^{-1} was chosen.

An example of a F($\vec{Q}$,t) map and its Fourier transform S($\vec{Q}$,ω) calculated in MDANSE from a 100 ps long trajectory is in Fig. 3.3:

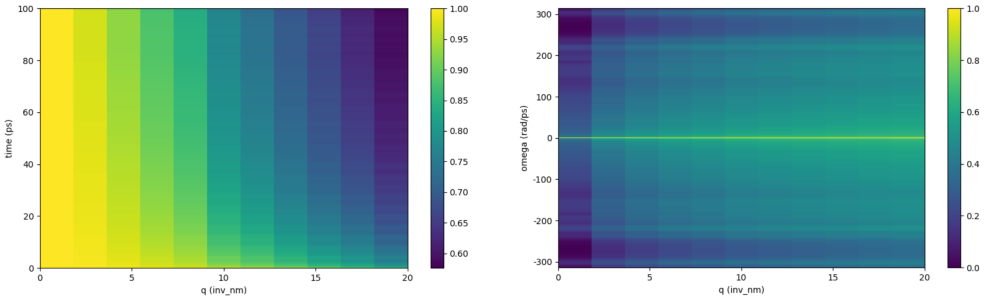

a) *b)*

Figure 3.3: MDANSE *a)* F(Q,t) map and *b)* S(q,ω) for a 100ps long trajectory, with Q range [0, 2] Å^{-1} and step in Q equal to 0.2 Å^{-1}

The Generalized Density of States calculated to reproduce PANTHER's data was calculated with a script developed during Geoffrey Monet's thesis, that considered the multi-phonon contribution and the energy resolution convolution.

Finally, as mentioned before, the atomistic X-ray diffraction patterns (covering the high Q region) were calculated using the XaNSoNS GPU-accelerated simulator[217], from the atomic positions extracted from the last frame of MD trajectories.

4. Investigation of the dry imogolite nanotube: structural analysis and order-disorder transition of the inner hydroxyls groups

This chapter presents all the experimental results obtained on the dry sample of Si-INTs, which are further discussed in the light of molecular dynamics simulations. It is organized as follows: section 4.1.3 presents sample characterization done by TEM, IR and N_2 adsorption isotherms experiments, TGA measurements and the protocol followed to dry the Si-INTs sample, as well as as the study of the structure of the tube structure using X-ray diffraction and MD simulations. A possible deformation of the tubes during the drying process is proposed and its impact on the diffraction pattern is presented. Section 4.2 concerns the evolution of the structure of the dry tube with temperature. A particular focus is put on the occurrence of a transition of the inner hydroxyls sublattice from an ordered configuration to a disordered state predicted to occur with increasing temperature using MD. A rationalization of the problem in terms of a simple Ising model is proposed. An order parameter is therefore defined and its temperature dependence discussed. This is done in parallel with the calculations of a complete set of neutron observables, over a large temperature range. The elastic incoherent structure factor $EISF$, the scattering functions F(Q,t) and S(Q,ω) together with the generalized density of states are extracted from the atomic trajectories recorded at different temperatures, and are directly compared to the experimental ones measured in various neutron instruments.

4.1 Characterization of the aluminosilicate nanotubes and sample preparation

4.1.1 TEM, IR and BET measurements

As mentioned in Chapter 2, the aluminosilicate nanotubes sample used during this thesis comes from a suspension batch that was synthesized via a protocol detailed in the article by Belorizky and co-authors[250]. A first step has been to characterize these nanotubes. Transmission electron microscopy is used to directly image Si-INTs. A characteristic TEM image is presented in Fig. 4.1*a*, highlighting the one-dimensional morphology of imogolite. The associated length distribution results from the analysis of more than 350 particles (Fig. 4.1*b*). The length of Si-INTs displays a log-normal distribution with a mean value around 200 nm.

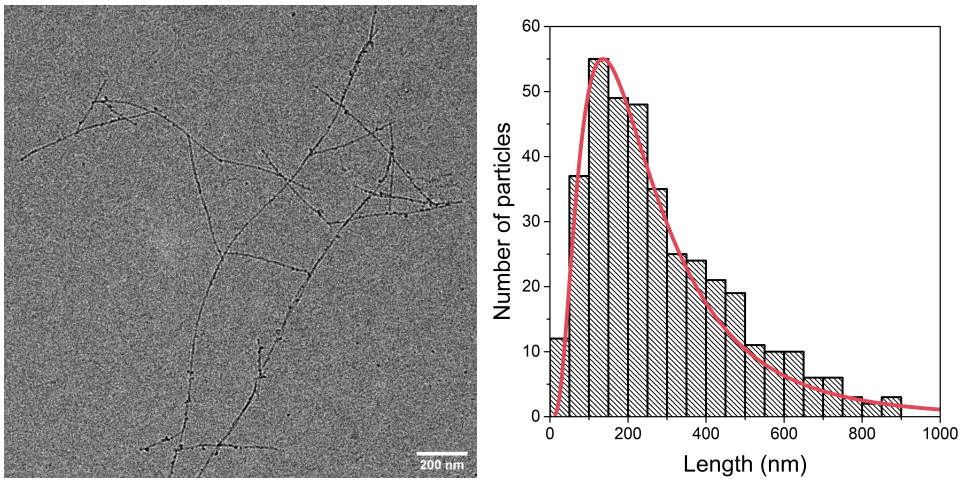

a) *b*)

Figure 4.1: *a*) Representative TEM image of Si-INTs and *b*) corresponding histogram of the length distribution of the tubes

Infrared spectroscopy is a local technique, largely employed to characterize imogolite nanotubes. Fig. 4.2 presents the resulting FTIR spectrum of Si-INTs. For comparison, we also report the IR spectrum obtained in Amara et al[70].

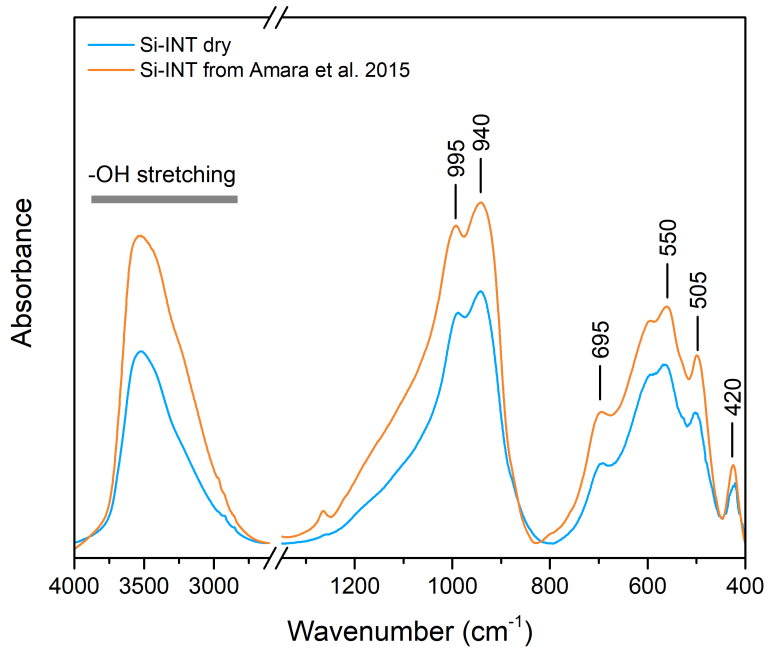

Figure 4.2: Infrared spectrum of a Si-INT powder (blue) compared to the data reported in Amara et al.[70] (orange).

The two spectra are similar, which proves that the sample used in this work is free of impurities. The assignment of vibrations modes, summarized in Table 4.1, is based on the literature[50,70,251].

Frequency [cm^{-1}]	Mode
695, 550, 420	Al-O stretching
505	Al-O-Si bending
995, 940	Si-O-Al, Si-O-Si stretching
(3800-2750)	OH stretching

Table 4.1: Band assignments for spectral features observed for the synthetic Si-INTs

The IR curves present a large absorption band at 3800-2750 cm^{-1}, corresponding to the stretching vibration of structural -OH groups linked to Si and Al atoms. The spectral region below 1200 cm^{-1} is characteristic of the imogolite backbone. In particular, the doublet peak at 995 and 940 cm^{-1} is assigned to Si-O-Al stretching modes while peaks located

at 695, 550 and 420 cm^{-1} correspond to various Al-O stretching modes and OH bending modes. The vibration at 505 cm^{-1} is attributed to a Si-O-Al bending mode.

Finally, nitrogen adsorption isotherm is performed to assess the micropore structure of our synthetic sample. Adsorption-desorption N_2 isotherm is displayed in Fig. 4.3. The obtained adsorption curve shows the characteristics of a IUPAC Type I isotherm[211], typical of microporous materials with pores diameter lower than 2 nm. This is in agreement with previous reports on synthetic aluminosilicate imogolite nanotubes[201,214,252].

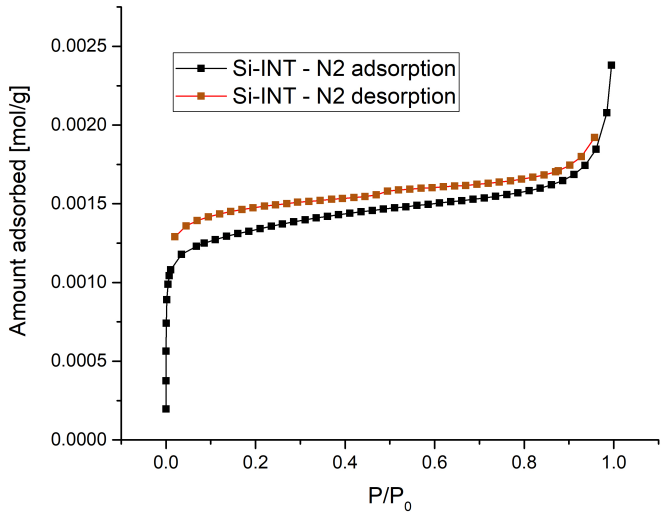

Figure 4.3: Nitrogen isotherm on Si-INTs powder, initially outgassed at 200°C during 12h under secondary vacuum. Adsorption and desorption branches are reported in black and brown, respectively.

From the N_2 isotherm, we can determine the specific surface area (SSA) using the so-called Brunauer–Emmett–Teller (BET) theory[253]. This method allows to determine the number of molecules X_m necessary to cover the surface of a sample with a monolayer of N_2 molecules. The BET equation is given as:

$$\frac{\frac{P}{P_0}}{X(1-\frac{P}{P_0})} = \frac{1}{X_m C} + \left(\frac{C-1}{C}\right)\left(\frac{P}{P_0}\right) \tag{4.1}$$

where X is the number of N_2 molecules adsorbed at $\frac{P}{P_0}$, C is the

BET constant related to the adsorption energy of the first N_2 layer E_1, the liquefaction energy of the gas E_L, the temperature T and the gas constant R according to the following relation:

$$C = exp\Big(\frac{E_1 - E_L}{RT}\Big) \tag{4.2}$$

The calculated SSA of Si-INTs is equal to 113 m^2/g, which is somewhat lower than previously reported values[201,214]. However, several authors have emphasised the effect of the pre-treatment temperature on the resulting isotherm[201,252,254]. In the case of a microporous solid, the surface determined by the BET method corresponds to an equivalent surface. In this case, we can determine the surface fraction of micropores by using the t-plot method[255]. This approach is based on the comparison of the thickness of the adsorbed layer at a given relative equilibrium pressure, between a non-porous reference solid and the solid under study. In our case, we found a micropore area of 94 m^2/g, which is again in good agreement with the value reported for Si-INTs pre-treated at 200°C[201].

In brief, TEM, IR and BET measurements are consistent with what has already been reported in the literature indicating that our Si-INT sample does not present impurities.

4.1.2 Preparation of the dry sample

As mentioned in Chapter 2, thermogravimetric analysis will allow to determine the characteristic temperatures of mass loss of our sample, and more specifically, to know at what temperature to dry the sample without damaging it. The TGA curve of a Si-INT powder is presented in Fig. 4.4a.

For Si-INTs, it is well known that TGA measurements give two steps of mass loss[41,199,252,256,257]. This is even more pronounced when we look at the TGA differential curve (Fig. 4.4b). The two main contributions are:

- an endothermic pic below 200°C, corresponding to the dehydration of the sample

- an endothermic pic between 300°C and 500° C, related to the deshydroxilation of the nanotubes

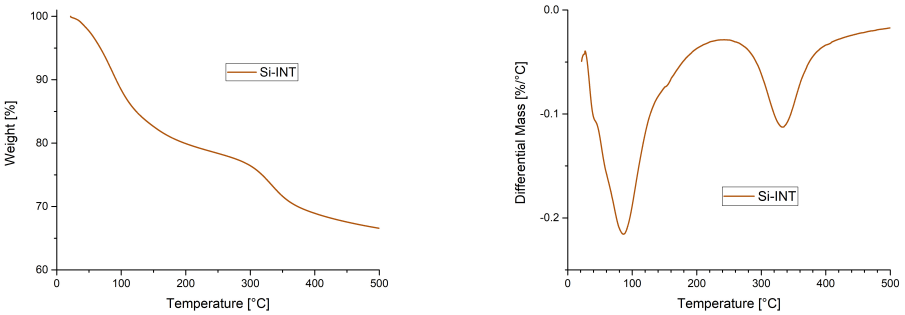

a) *b)*

Figure 4.4: *a)* TGA and *b)* TGA differential curves of a Si-INTs powder, with a temperature ramp of 5°/min under N_2 atmosphere.

Based on the TGA curve, we identify that the temperature at which one can dry the sample safely and completely is 200°C. A dry sample was therefore prepared by placing some Si-INT powder into a borosilicate capillary (for X-ray scattering measurements) or either in aluminium or vanadium cell (for neutron scattering experiments). The powder was then heated at 200°C for 2 hours, and by later quickly sealing the sample holder. Structural features of dry imogolite nanotubes will be presented in the next section.

4.1.3 The structure of dry imogolite nanotube by X-ray scattering at ambient conditions

The dry Si-INT structure has been characterized by synchrotron X-ray diffraction, measured at CRISTAL beamline on a powder sample. As mentioned in Chapter 2.5, the diagram can be divided in two regions in Q. The structure of the scattered particles can be deduced by reproducing the experimental curve with simulations of the scattering diagram.

The high Q part (Q>1 Å^{-1}) contains information about the structure of the tube at the atomic level. The simulation of that Q region can be easily done, once one has chosen the number of unit cells around the circumference N of the simulated tube. In Section 1.3.2, it was mentioned that previous works always found for synthetic Si-INTs either N = 12 or N = 14. Here, a first selection of N values was done by using a python script that uses a semi-empirical potential to perform a simple geometry optimization of the structure, as described in Geoffrey Monet's thesis. The potential is not related to CLAYFF and will only be used here to do a first rough selection of the N values that fit well the data. The

method consists[71] in minimizing the structure by keeping fixed internal and external radii R_i and R_e[1]. The results are summarized in Fig. 4.5*a*. They evidence that the values of N that best reproduce the experimental curve are N = 13 and N = 14. Using either N = 12 or N = 15 results in discrepancies between the experimental and calculated curves. Finally, a tube having N = 14 has been chosen in the following for Molecular Dynamics simulations.

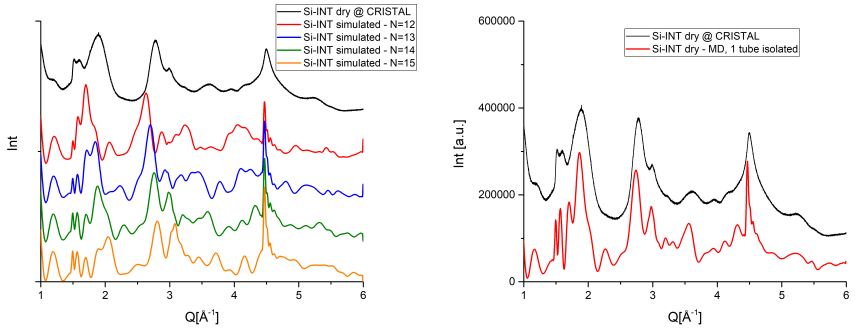

a) *b*)

Figure 4.5: Comparison of measured X-rays diffraction patterns obtained at CRISTAL (black) and *a*) different simulated structures, having N = 12 (red), N = 13 (blue), N = 14 (green) and N = 15 (orange); in *b*), the comparison is made with the calculated diffractogram (red) obtained from a MD simulation run at 300 K with N = 14.

With N chosen, the calculation of that region of the diffractogram can be done easily for an isolated nanotube, in three steps: (*i*) find the minimum energy of the structure by doing a geometry optimization of the model; (*ii*) from this relaxed configuration, perform a MD simulation (using the CLAYFF potential) at 300 K and (*iii*) from the final structure, calculate the diffraction pattern with Eq. 2.9. As discussed in section 2.5.1.2 the large Q part of the diffractogram can be calculated from a powder of isolated nanotubes, even though they are organized in bundles. The resulting simulated curve, shown in Fig. 4.5*b* in red, appears to be in good agreement with the experimental curve. This demonstrates that the atomic positions extracted from the MD simulation are close to the real structure of Si-INTs.

[1]The R_i and R_e values were chosen case by case to obtain the best agreement with the experimental curve. N=12: R_i=7 Å, R_e=11 Å; N=13: R_i=7.9 Å, R_e=11.8 Å; N=14: R_i=8.3 Å, R_e=12.4 Å; N=15: R_i=8.5 Å, R_e=13 Å.

Once the atomic structure is validated, we can investigate also the low Q region (Q<1 Å^{-1}), *i.e.* the 2D organization of nanotubes in bundles.

It was shown previously [76,197,216] that dry nanotubes organized in bundles can be deformed. In order to investigate this point and its effect on the low-Q diffraction diagram, the following procedure was followed:

- The first structure built was the **minimum energy structure** in Fig. 4.6*a*. It is a bundle of 19 "round" tubes organized on a 2D hexagonal lattice with parameter d = 27 Å[2], obtained by (*i*) minimizing the tubes individually (the detailed procedure of minimization is explained in the future section 4.2.1), then (*ii*) packing them on the 2D lattice to finally (*iii*) re-minimizing the entire bundle. We chose bundles constituted of 19 tubes as the simulated and experimental linewidth of the diffraction features match quite well for a bundle of this size.

- In order to provoke a deformation, a layer of water (4.5wt% in mass) was deposited outside the bundle and then a 10 ps (N,V,T) Molecular Dynamics simulation was performed at 500 K.The corresponding bundle is shown in Fig. 4.6*b*.

The resulting diffraction patterns associated to the two structures are calculated using Eq. 2.9 and they are compared to the experimental curve in Fig. 4.6*c*. When comparing the two simulated curves, one can see how the tube deformation smooths some oscillations which become more similar to the experimental shape.

As the experimental diffractogram is still not reproduced very well in this Q region, another try was done by applying the same procedure to a bundle of tubes N = 13, the other value that was reproducing well the curve of Fig. 4.5*a*. In this case, the lattice parameter was d = 26.5 Å[3].

[2]The value of d equal to 27 Å as it is the value that better reproduces the experimental (hk) peak positions (when considering a bundle composed of 19 tubes).

[3]Here the value of d was adjusted in order to find the same peak position while having a slighly different form factor with N=13.

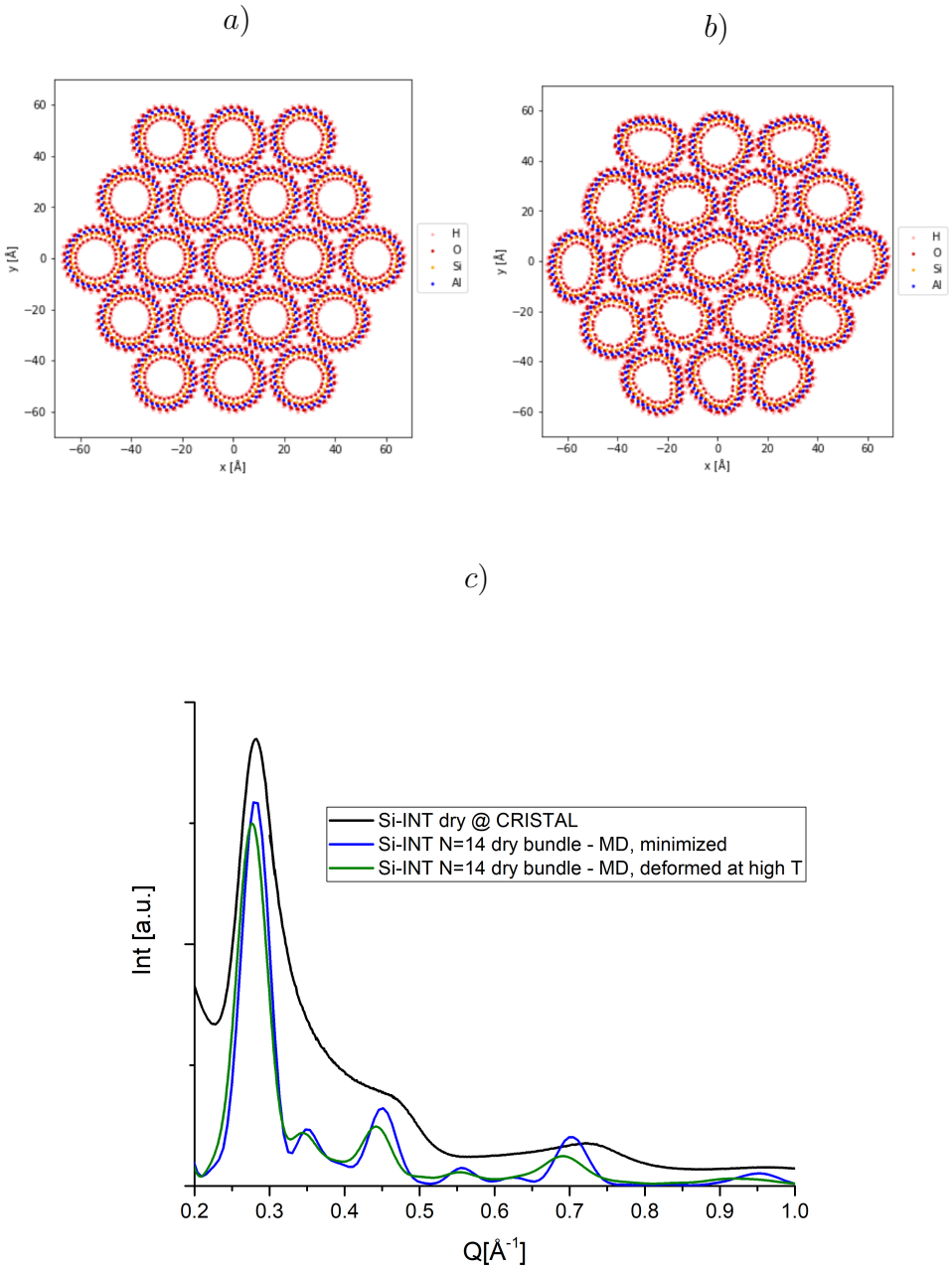

Figure 4.6: Effect of nanotubes deformation, calculated for N = 14: *a*) bundle after energy minimization and *b*) the same after deposition and removal of water molecules at 500 K; *c*) Comparison of the resulting diffraction patterns (blue and green line respectively) with the experimental curve in black.

The results are presented in Fig. 4.7. The maps in Fig. 4.7*a* and 4.7*b* illustrate the structure of the bundles before and after deformation.

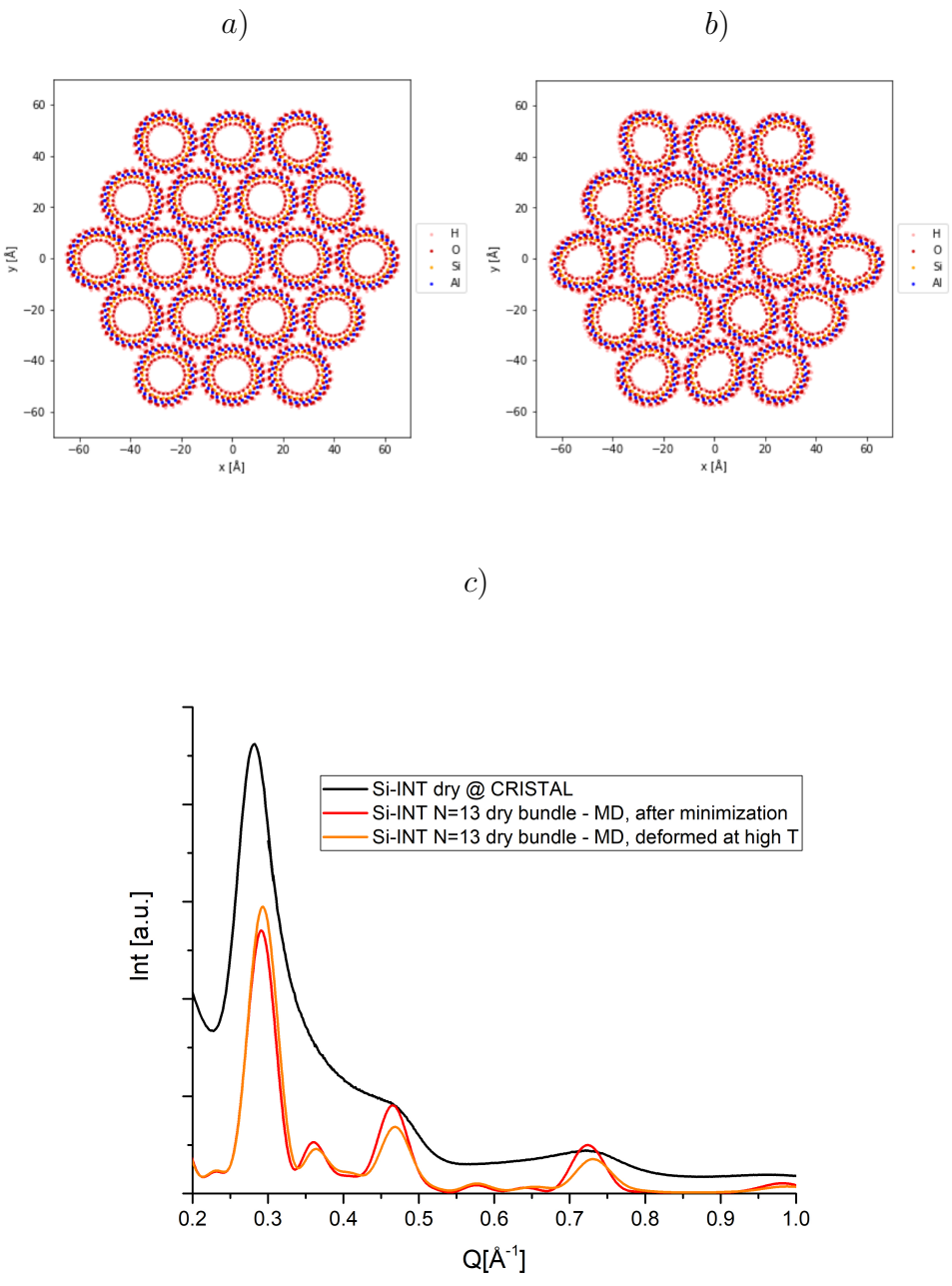

Figure 4.7: Effect of nanotubes deformation, calculated for N = 13: *a*) bundle after energy minimization and *b*) the same after deposition and removal of water molecules at 500 K; in *c*), comparison of the resulting diffraction patterns (red and orange line respectively) with the experimental curve in black.

When comparing figs.4.6*c* and 4.7*c*, we see that neither of them reproduces exactly the diffraction pattern. For N = 14, the relative intensities

are well reproduced, but not the exact peak positions. On the other hand, it is the opposite for N = 13 since the peak positions are better reproduced, especially after taking into account the tube deformation but the various peak intensities do not reflect the experimental ones.

Following on the high Q investigations, as both candidates N = 13 and N = 14 gave similar agreement with the data, we attempted a weighted mixture of these two systems.

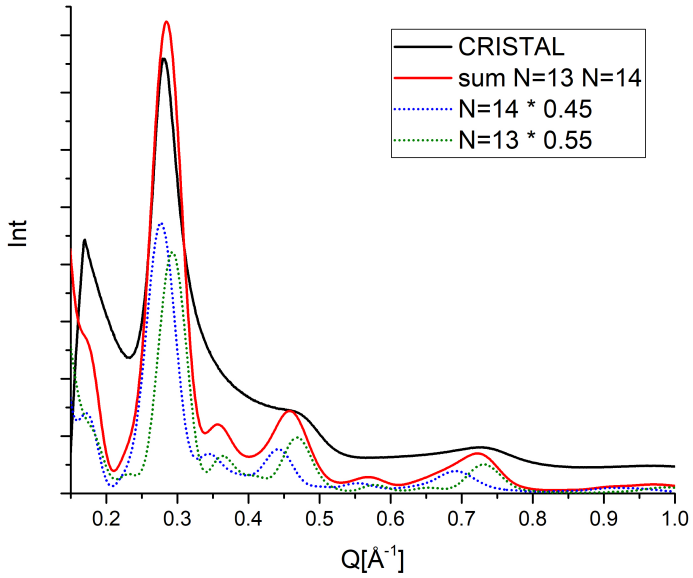

Figure 4.8: Experimental data (black) compared to the average (red) between the N = 14 (dotted line in blue) and N = 13 (dotted in green) curves.

In Fig. 4.8, the dotted blue curve shows the pattern for N = 14, while in green for N = 13. They are both multiplied by a weighting factor – 0.45 for N = 14 and 0.55 for N = 13 – and the weighted sum of the two is displayed in red. The picture indicates that the diffraction diagram obtained for the mixture better reproduces the experimental data: the peak positions, width and intensity are more accurately reproduced, in particular for the asymmetric feature at $Q = 0.75\text{Å}^{-1}$, but the agreement is still far to be perfect. The possible mixing of N=13 and N=14 tubes in the same bundles could be investigated at this point, but it is beyond the frame of this thesis. For simplicity, in the following we restricted our simulations to bundles of undeformed tubes with N = 14.

4.2 Some evidence of an order-disorder transition (ODT) of the inner hydroxyl sublattice

This section is dedicated to the characterization of the minimum energy structure of the inner hydroxyl chains and to its evolution with increasing temperature. Molecular dynamics simulations predict an order-disorder transition at a temperature $T_c \sim 300$ K , which we rationalize using a simple Ising model. In the last part of this chapter, we focus on the neutron scattering experiments aiming at bringing evidence of the reality of this transition.

4.2.1 Insight into the minimum energy configuration of the inner hydroxyl chains

The N = 14 atomic structure resulting from the geometry optimization described in section 3.2 and which was found to well reproduce the diffraction features at large Q is shown in Fig. 4.9 in the form of a density map, *i.e.* a map illustrating the probability of presence of the atomic species during the time of the simulation.

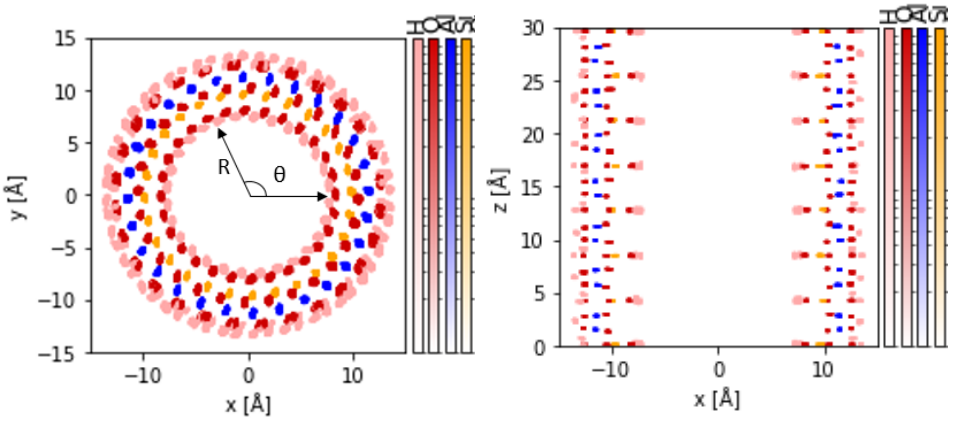

a) *b)*

Figure 4.9: Density map of the minimized structure at T = 50 K, *a)* projection in the (x, y) plan (and definition of R and θ) and *b)* vertical section (only the atoms belonging to the slice of width ±2.5 Å in the y direction are shown).

It is very similar to the one obtained by Scalfi et al[207] for N=12. It can

be noted that we had to perform a simulated annealing of the structure to obtain the same atomic configuration for the external hydroxyls OH_{out} as in ref.[207][4].

The OH_{in} and OH_{out} are shown in Fig. 4.10*a* and *c* in density maps where the horizontal axis is the curvilinear coordinate Rθ and the vertical one, the z axis. It has been obtained after "unrolling" the tube, done by choosing a radius R of reference – equal to the radial coordinate averaged over time – and by defining a curvilinear coordinate Rθ where θ is the polar angle of cylindrical coordinates.

The external OH_{out} (Fig. 4.10*c*) present a variety of different orientations, showing no ordering. They will not be our center of focus in this work. By contrast, the OH_{in} are all aligned along the same (unrolled) "direction" as shown on Fig. 4.10*a*, with the bond lying along a plane perpendicular to the tube axis. In the projected unrolled tube representation, the O and H sublattices form triangular or hexagonal-like closed packed meshes shifted by a constant (curvilinear) vector $\vec{\xi}$[5]. The H and O atoms belong to two different cylinders (having different R: R_O and R_H), which have been rotated by an angle $\psi = -\frac{\xi}{R_H}$.

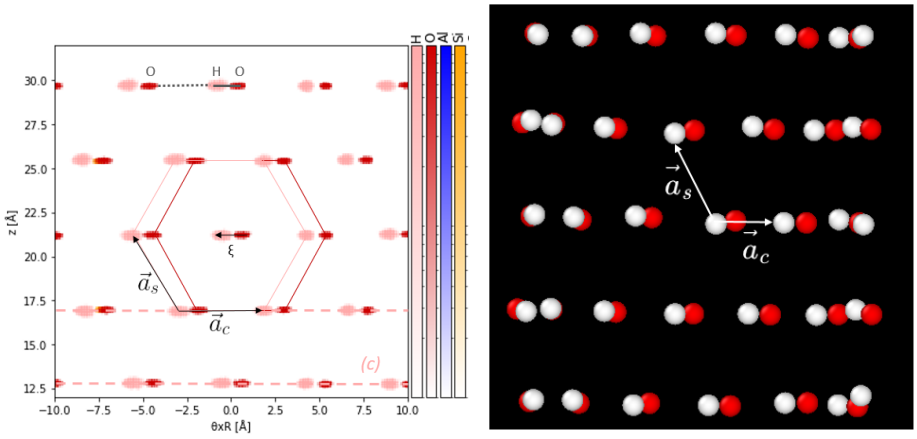

a) H_{in} in flat configuration *b*) H_{in} in rolled configuration

[4]The structure was heated at 600 K for 10 ps, slowly cooled down to 500 K, then another 10 ps long simulation was run, and these two steps were repeated at 400 K, 300 K, 200 K and finally 100 K, to reach the temperature of 50 K. Then, another minimization was performed.

[5]One could also discuss the lattice as an hexagonal-like mesh with a motif composed of an hydroxyl group OH_{in} with the OH bond being represented by the vector $\vec{\xi}$

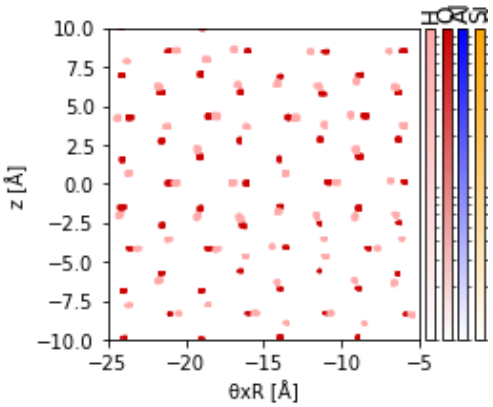

c) H_{out}

Figure 4.10: Density maps showing the configuration of *a*) internal and *c*) external OHs at 50 K. Dashed pink lines in *a*) highlight horizontal or (*c*) chains, which correspond to hydroxyl coronas in 3D, in planes perpendicular to the tube axis. *b*) shows the unrolled view of the internal hydroxyls.

This minimum energy configuration is revealing the chiral nature of the nanotube: aluminium, oxygen and silicon coronas are achiral on their own but they cannot be in phase one with the other because of their different radii. Therefore, their individual mirror planes do not superimpose and the total structure is chiral.

The horizontal lines in Fig. 4.10*a* correspond to corona in 3D – which we will refer to as lines (*c*) – with interatomic distance $a_c \sim 3.7$ Å. On the other side, the distance between closest O atoms of two adjacent chains in z is $a_s \sim 4.5$ Å, a distance significantly larger than a_c. This might explain why the hydrogen bonds $O - H \cdots O$ (with $O \cdots H$ bond length $d_{hb} \sim$ 2.7-2.8 Å) are aligned preferentially along the $\vec{a_c}$ direction. One can also remark that the H atoms have a positional distribution elongated along the horizontal direction, which corresponds to small in-plane rotations of the -OH bond, the out-of-plane rotation being responsible of the width of the distribution along z. If ordering of the -OH bond along $\vec{\xi}$ inside a single (*c*) chain is easily obtained by simple minimization of the structure, the configuration with no chain disorder from one chain to another is obtained only if one proceeds to a very progressive simulated annealing, for which the tube is cooled down progressively, by stopping at every temperature step and giving it time to relax the entire structure at that temperature. On the contrary, if one does the annealing more radically, the result is significantly different and one simulates an operation which is closer to a simulated quenching of the model. The simulated

quenching was done by starting with the model thermalized at 600 K and setting a target temperature of 50 K directly, without intermediate steps. When quenching the system, it was found that, if the -OH bonds are all oriented along the same direction in a chain, different chains had no correlated -OH orientations, showing orientation corresponding either to $+\vec{\xi}$ or $-\vec{\xi}$, disposed at random along the tube axis, *i.e.* suggesting a weak interchain coupling. One could even observe in rare cases (c) chains having half hydroxyls oriented in one direction and half hydroxyls in the other. In other words, when one quenches the system, several domains form and the hydroxyl sublattice is locked in a metastable state. In the following we will not study the metastable cases with simulations, even though the existence of domains cannot be excluded for the real system. The ordering of the alignment of the OH_{in} was already predicted by pre-existent theoretical studies: in a previous computational study, Lourenco et al.[79] calculated the minimum energy state of imogolite nanotubes using a self-consistent charge density-functional tight-binding (SCC-DFTB) method. They proposed that the minimum energy state consists in having all the inner hydroxyls aligned perpendicularly to the tube axis, tangentially to the tube wall – exactly as found in our study using the CLAYFF force field. This ordered configuration was found to be the minimum energy state in several other computational studies[78,258,259]. It was also suggested[260] that the hydrogen bond network between the aligned hydroxyls is responsible for the rolling and the monodispersity in diameter of these nanotubes. Until now, no experimental evidence of the real occurrence of this ordered state has been reported. In the next section, the evolution with temperature of the configuration of the hydroxyls OH_{in} will be investigated.

4.2.2 Order-disorder transition: MD simulations investigations

The temperature dependence of the OH_{in} configuration was investigated by performing 100 ps long MD simulations in the (N,V,E) ensemble at 50, 100, 200, 300, 400, 500, 600 and 700 K. The density map of a representative areas of the inner layer of hydroxyls OH_{in} is shown in Fig. 4.11 at each of these temperatures.
From 50 to 300 K, all the hydroxyls are "ordered", meaning that the -OH bonds are all oriented in average along the same $+\vec{\xi}$ direction. We will referred to this state as the *oriented state* or the *low T phase* in the following. The distribution of the hydrogens positions in this ordered state is represented as clouds characterised by ellipsoid-like shapes, elongated along the curvilinear direction $R\theta$. When increasing temperature from

50 K to 300 K, one observes that the horizontal and vertical dimensions of these clouds significantly increase –especially in the vertical direction– highlighting the large temperature induced (rotations) fluctuations of the -OH bonds direction. Some -OH flips, *i.e.* change of orientation of the -OH bonds from the $+\vec{\xi}$ to the $-\vec{\xi}$ direction, start to be observed in the density map at T = 400 K in some horizontal (c) chains. At this temperature, about half of the total number of hydroxyls have flipped their orientation on the timescale of the simulation. Moreover, these -OH are grouped inside the same chains, so that about half of the chains have not seen any flip. This suggests that, once a -OH is flipped in a chain, the flip is propagated along the chain. It evidences interactions between -OH orientations inside the same (c) chain. At 500 K, most of the hydroxyls in the model have experienced one or several flip on the simulation timescale. The density profile of each hydroxyl now features very wide motions on a surface approximated by two half-circumference the intensity of which represents the probability of this orientation. If the intensity distribution is clearly not symmetric at 500 K, revealing the majority of $+\vec{\xi}$ orientations, the distribution tends to equilibrate when temperatures increases, to reach a very symmetric configuration that we define as the *disordered state* or *high T phase*. Fig. 4.12 show a comparison of the transverse section of the tube in the low T (T=50 K) and high T (T=600 K) phase. The disordered nature of the OH_{in} orientation is revealed by the homogeneous ring figuring the inner H density in the high T phase.

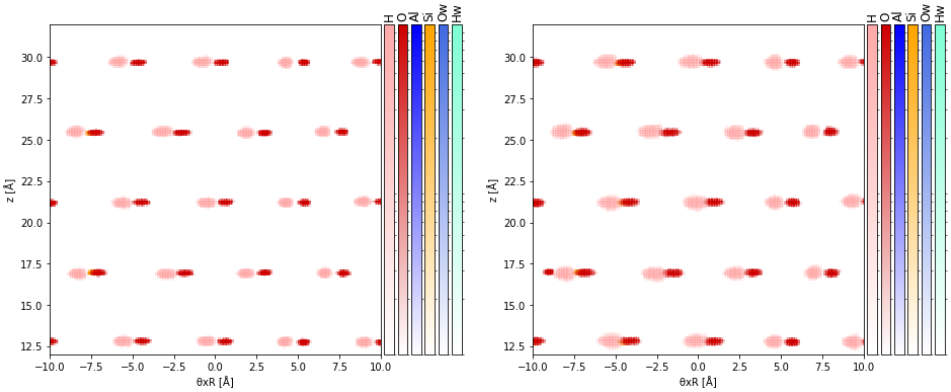

a) T=50 K *b*) T=100 K

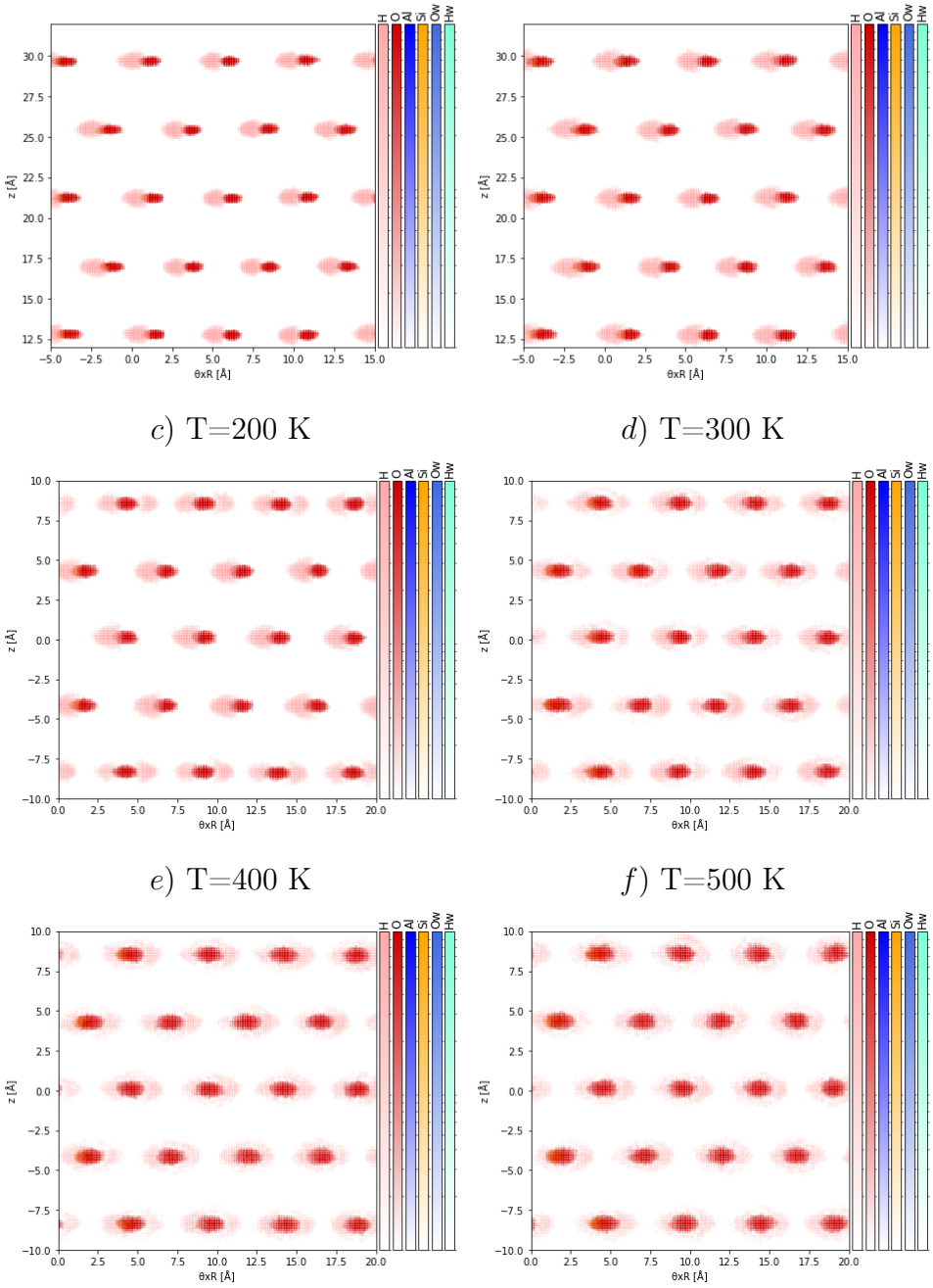

c) T=200 K *d*) T=300 K

e) T=400 K *f*) T=500 K

g) T=600 K *h*) T=700 K

Figure 4.11: Density maps of the internal hydroxyls as a function of T: *a*) T=50 K *b*) T=100 K *c*) T=200 K *d*) T=300 K *e*) T=400 K *f*) T=500 K *g*) T=600 K *h*) T=700 K.The first temperature showing flips on a chain is 400 K (*e*)), and after that temperature, every H visibly flips from the left to the right of the oxygen atom of the hydroxyl group.

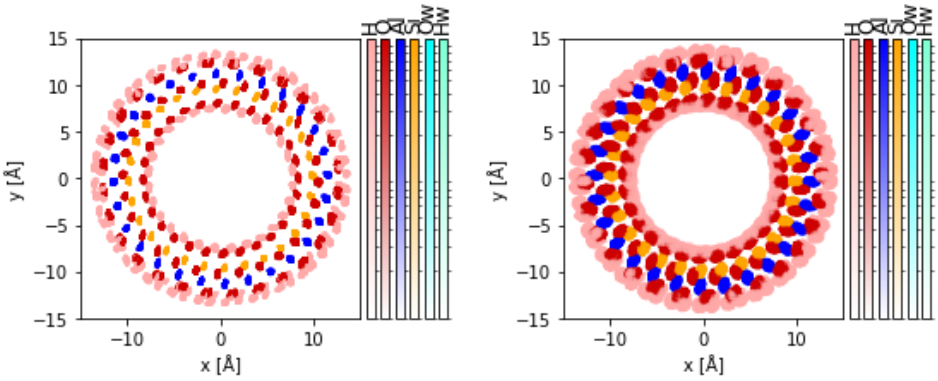

a) T=50K *b*) T=600K

Figure 4.12: Density map in the (x, y) plane *a*) before transition (T=50 K) and *b*) after transition (T=600 K)

As discussed above, flips appear correlated along each horizontal chain. An example of the propagation of flips is illustrated in Fig. 4.13. It represents the time dependence of the complete reversal of all the -OH bonds in a chain from $+\vec{\xi}$ to $-\vec{\xi}$. Here, every image of the picture is a screenshot taken at 400 K and separated by 20 fs. White lines indicate where the domain walls are a given time frame. The complete set of screenshots shows that the full reversal of the chain can take place in a time span of around 100 fs, at 400 K, *i.e.* at the start of the transition. Between one image and the other, the flip of three to five hydroxyls occur, meaning that the propagation of the flip is very fast (when one hydroxyl flips, the neighboring one follows after 4-7 fs). The phenomenon can be seen as a defect propagation, or a domain wall propagating along the chain. If the creation of a flip is done at the expense of energy – creating two walls in the chains – the diffusion of these walls along the chain, and further leading to their relaxation, is at zero energy cost. These diffusional modes, driven by entropy, are called solitons[261].

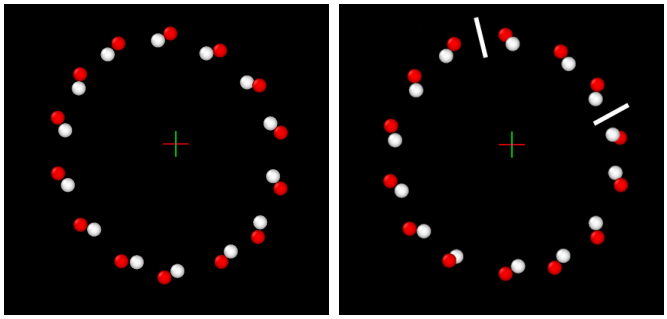

a) *b*)

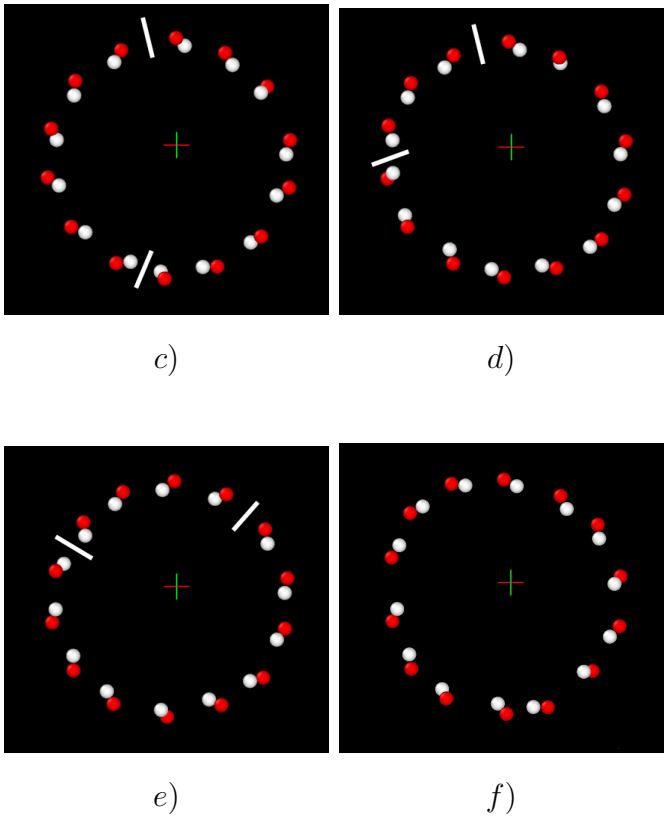

c) *d)*

e) *f)*

Figure 4.13: Screenshots of the reversal on a chosen chain at 400 K. White lines indicate to the domain walls.

The onset of dynamics can be seen quantitatively in the plot of the mean squared displacement (MSD) of the inner H atoms (H_{in}) as a function of temperature, as shown in Fig. 4.14. The MSD shows a first linear harmonic behavior up to 300 K followed by an important increase between 300 K and 500 K, above which a saturation is reached and another harmonic-like linear regime is observed. The transition discussed in the previous paragraphs is therefore seen in the MSD by a large step from 0.5 Å^2 in the low T phase to around 2.2 Å^2 in the high T phase. The slopes of the linear dependence for T $\leq$ 300 K and T $\geq$ 500 K are observed to be very similar, revealing that the vibrational dynamics of the H_{in} are not strongly affected by the transition. The situation resembles the case of a particle trapped in a double well potential, performing local harmonic like vibration in the bottom of the wells and jumping from one well to another with a frequency much lower than the typical vibration frequency. For such a model, the $MSD = \langle u^2 \rangle + R^2$, R being the jump distance and $\langle u^2 \rangle$ the vibrational contribution to the MSD.

According to this image, one can extract a value of $R \sim 1.3$ Å. The H_{in} MSD is observed to be in strong contrast with that calculated for

the H_{out}: if a *transition* is also observed for the H_{out} as revealed by the change of slope at a temperature $\sim$ 400 K, it doesn't feature a step-like increase but an evolution which suggests the appearance of strongly anharmonic fluctuations.

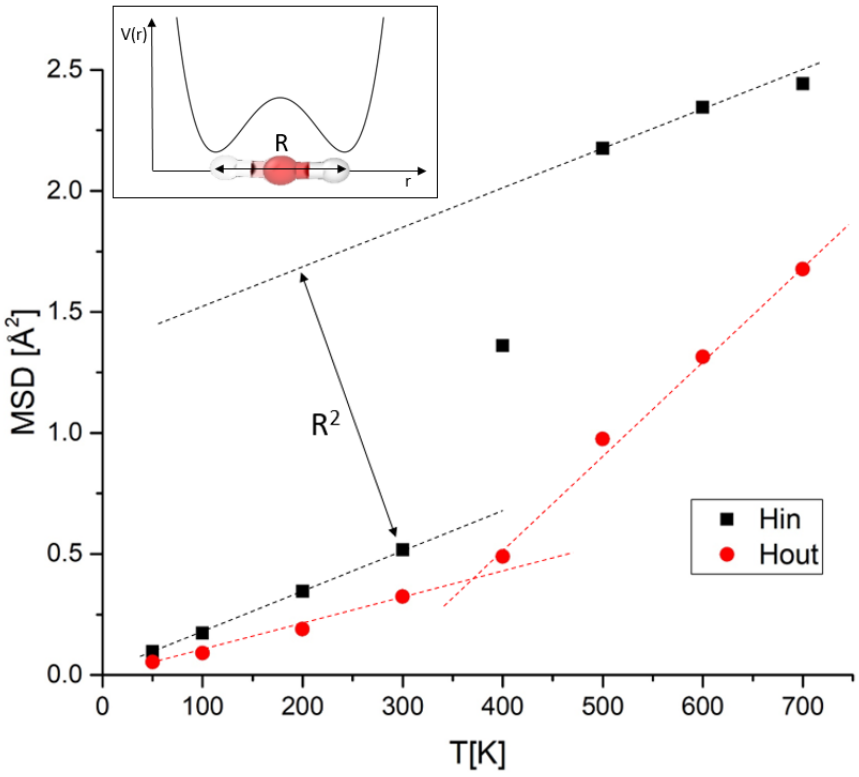

Figure 4.14: Evolution of the mean square displacement (MSD) of H_{in} (black) and H_{out} (red) as a function of the temperature.

The Elastic Incoherent Structure Factor ($EISF$), as already introduced in the chapter devoted to neutron scattering (Chapter 2) is an important neutron scattering observable. It allows one to understand the geometry of the relaxation process at the origin of a local diffusive movement. As such, the onset of local -OH flips with temperature leads to significant modification of the elastic neutron scattering and serves as a fingerprint of the occurence of the ODT. The $EISF$ of the H_{in} as a function of Q, for temperatures between 50 and 700 K, are shown in Fig. 4.15. They were extracted from the trajectories using the MDANSE software. The first three temperatures (T=50, 100 and 200 K) can be reproduced perfectly by using a simple gaussian model, corresponding to a constant elastic intensity, simply modulated by the Debye-Waller factor accounting for thermal vibrations:

$$EISF(Q) = e^{-\frac{1}{6}Q^2 \cdot \langle u^2 \rangle} \tag{4.3}$$

Table 4.2 contains the $\langle u^2 \rangle$ values found from the fit of the $EISF$ in the low T phase. The values obtained from the fit are in complete agreement with the first three values of the $\langle u^2 \rangle$ of the H_{in} plotted on Fig. 4.14.

T [K]	$\langle u^2 \rangle$ [Å^2]
50	0.092 ± 0.001
100	0.171 ± 0.001
200	0.320 ± 0.001

Table 4.2: $\langle u^2 \rangle$ values extracted from the gaussian fit at T=50, 100 and 200 K

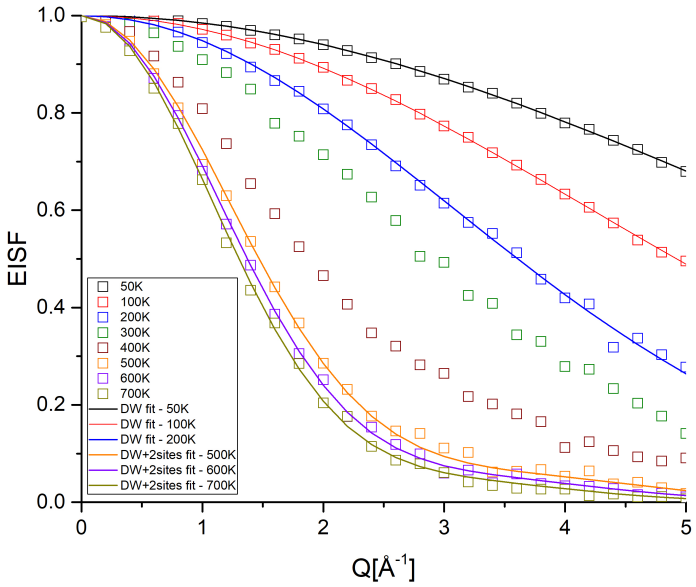

Figure 4.15: $EISF(Q)$ fitted with the Debye-Waller (DW) factor at T=50,100,200 K and by the product between the Debye Waller factor and a two-sites jump model at 500 K, 600 K, 700 K (the fits are illustrated with solid lines)

In the high T phase (T=500, 600 and 700 K), the $EISF$ was fitted to a jump diffusion model between two equivalent sites[6], modulated by a Debye-Waller (DW) factor:

[6]The model is introduced in section 2.6.1.2 when presenting different models describing confined diffusion.

$$EISF(Q) = e^{-\frac{1}{6}Q^2 \cdot \langle u^2 \rangle} \frac{(1 + j_0(RQ))}{2} \tag{4.4}$$

where R is the jump distance and j_0 is the spherical Bessel function. The DW part is therefore constrained in order to account only for the vibrational part of the MSD. The MSD values are taken from Fig. 4.14.

The jump distance between the two sites, extracted from the fits at 500, 600 and 700 K are reported in Table 4.3.

T[K]	R [Å]
500 K	1.25 ± 0.01
600 K	1.32 ± 0.01
700 K	1.36 ± 0.01

Table 4.3: Calculated jump distances between the two sites for the temperatures above the ODT transition temperature

The R values found here correspond to the jump distance between the sites in the density maps (after considering the curvature of the tube wall). They correspond well with the jump distance $R = 1.3$ Å that we estimated from the MSD, using Fig. 4.14.

While a large wealth of geometrical information is contained in the $EISF$, one has to analyze the energy or time domain of the dynamical structure factor S(Q, ω) (or intermediate scattering function F(Q, t)) to extract information on the different relaxation times or typical energies at stake in the ODT. In particular, the flips appearing in the disordered state are responsible for the appearance of a quasi-elastic scattering with clear signature of the jump diffusion model used to discuss the $EISF$. The MD trajectories were analyzed in the energy domain by simulating the $QENS$ broadening of the S(ω) maps using the MDANSE software. The incoherent dynamical structure factor (See Eq. 2.21) was calculated in the Q-range [0, 2] Å^{-1}, with a resolution of FWHM=0.07 meV before being integrated in Q[7]. The results for T=100, 200, 300, 400, 500 and 600 K are shown on Fig. 4.16 for the H_{in} and H_{out}. The curves for both species feature a collections of sharp inelastic features with a rather weak T dependence. These features are also present in the spectra when one considers the dynamical response of the sole oxygen atoms (see black dotted line on Fig. 4.16). Having a closer look one can see that these peaks appear in the S(Q,ω) spectra of all atomic species, indicating that

[7]Which correspond to the experimental conditions on IN6-SHARP, whose data will be presented later in the chapter.

they are due to low energy vibrations of the entire tube. As the H atoms follow these modes adiabatically, these peaks are also present in the H spectra.

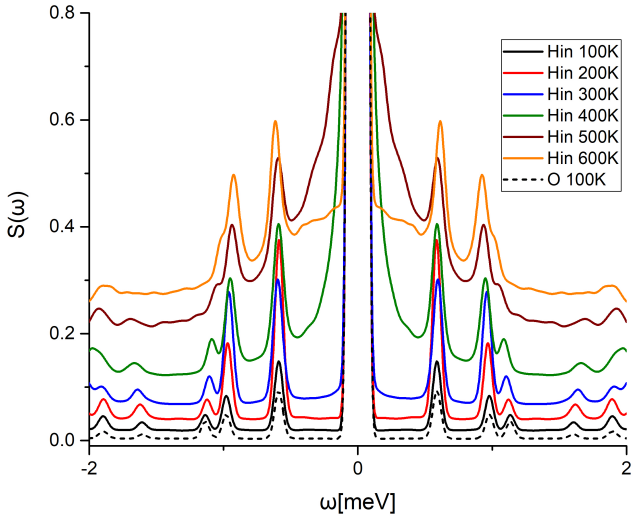

a) H_{in}

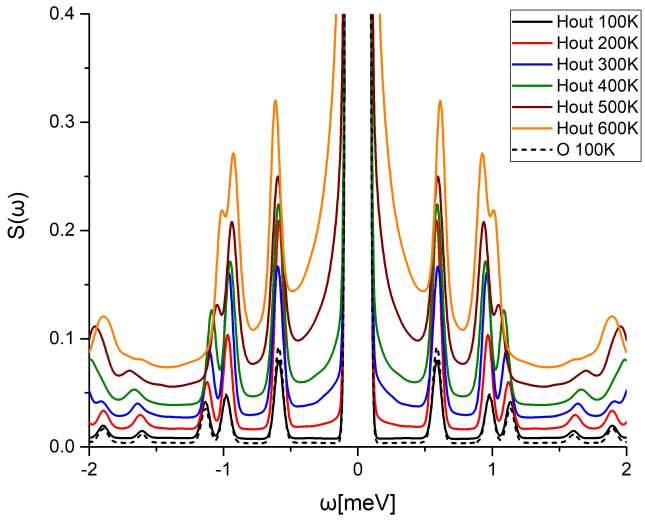

b) H_{out}

Figure 4.16: *QENS* broadening of *a*) H_{in} and *b*) H_{out} for temperatures going from 100 K to 600 K. The dotted line is shown as a comparison, and corresponds to the oxygens' S(Q,ω).

Above 300 K, a clear broadening of the elastic peak is observed in the spectra of H_{in}. This $QENS$ signal gains in intensity for T = 500 K before becoming significantly broader upon further heating. A $QENS$ signal is also observed to appear in the H_{out} spectra for T above 500 K, but presenting a broadening significantly less important than for the H_{in}. The spectra, before being analysed as described in the following, were corrected from the sharp inelastic peaks by subtracting the oxygen contribution after doing a proper scaling. The fits – the results are presented in Fig. 4.17 – were done separately for H_{in} and H_{out} and by using three components in both cases:

- A flat background to account for low frequency density of states.
- A Gaussian lineshape of fixed width to account for an instrumental resolution (FWHM=0.07 meV) and elastic processes.
- A Lorentzian lineshape to account for the local diffusion of the hydrogen atoms.

T[K]	HWHM H_{in} [meV]	HWHM H_{out} [meV]
400	0.055 ± 0.001	-
500	0.31 ± 0.001	0.057 ± 0.002
600	0.90 ± 0.01	0.056 ± 0.001

Table 4.4: HWHM resulted from the fit on simulated $QENS$ for H_{in} and H_{out}, at different temperatures

The half width at half maximum ($HWHM$) are listed in Table 4.4. One can note that while the $HWHM$ of the H_{in} atomes increases significantly with temperature, the $HWHM$ of the $QENS$ associated to the H_{out} movements seems to be T independent, suggesting a non-activated origin of this dynamics. From the temperature evolution of the HWHM of H_{in} one can extract an activation energy (Fig. 4.18a, by using Eq. 2.48), equal to E_a = 0.28 ± 0.1 eV (3250 K). If one associates this activation energy to the barrier separating the two wells of the double well potential representation shown in Fig. 4.14, its rather large value explains why, when disorder builts in, the H always stay localised in one of the local minima at all the temperatures investigated in this thesis.

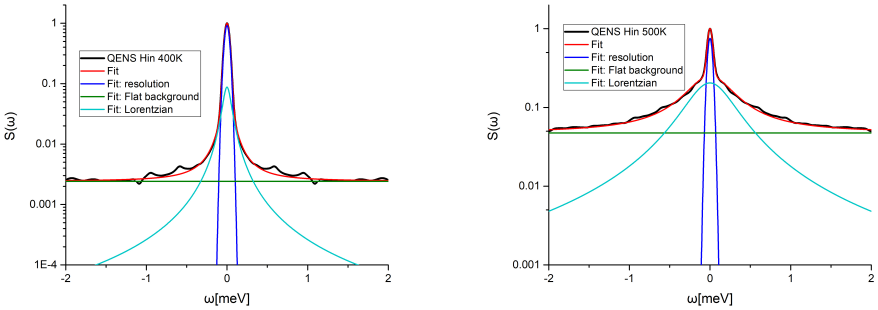

a)

b)

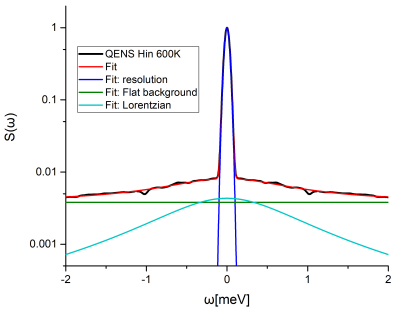

c)

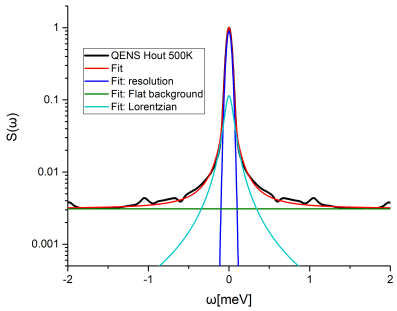

d)

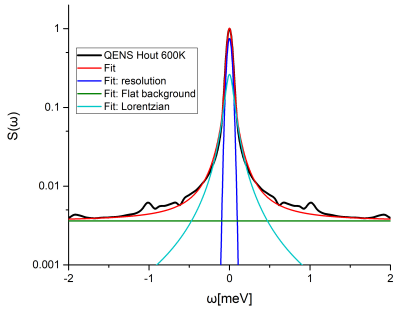

e)

Figure 4.17: Fit of the simulated $QENS$ for H_{in} at *a)* T=400 K, *b)* T=500 K, *c)* T=600 K and for H_{out} at *d)* T=500 K and *e)* T=600 K

The amplitude is constant (Fig. 4.18*b*), as expected from a constant number of hydroxyls participating to the dynamics. The Q-dependence

of the simulated signal was studied at 600 K (Fig. 4.18c and d). The several Q values were analyzed independently one by one. The HWHM is independent of Q, as expected from a confined diffusion (Fig. 4.18d). The amplitude shows an increase with Q that can be fitted with a jump model between two sites (red line in Fig. 4.18c). This confirms further that the simulated system can be modeled as a diffusion between two sites.

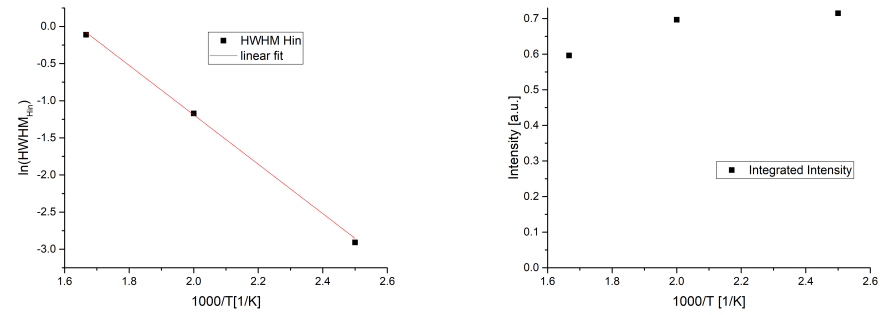

a)

b)

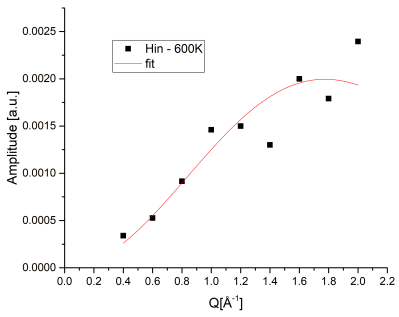

c)

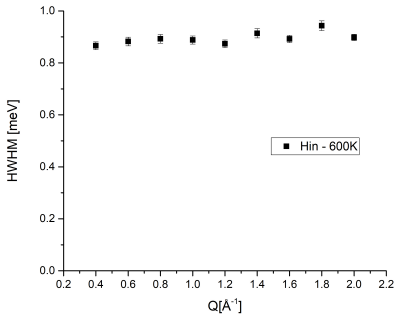

d)

Figure 4.18: a) Arrhenius fit of the HWHM for internal hydroxyls on the last three temperatures (T=400, 500 and 600 K); b) T dependence of the integrated intensity of the Lorentzian; fit on the $QENS$ of the Hin at 600 K: c) Q-dependence of the amplitude and fit with a two-sites jump model (red line); d) Q-dependence of the HWHM.

4.2.3 Rationalisation as a simplified Ising description:

order parameter definition and (static) correlations

The previous section has made clear that the ordered phase of the OH_{in} at low temperature is destroyed progressively by rising the temperature above 300 K, where the -OH bonds of the chains can flip to adopt another – energetically close – orientation that allows to make an hydrogen bond with another O in the chain. The use of molecular dynamics allowed us to derive the jump distance and the activation energy of this local diffusion. In order to extract quantities from the trajectories that are better suited in the context of phase transitions, and in the constant goal of simplifying the physical description of our system, we have introduced the following order parameters (OP_i, OP_c, OP) in order to quantify the overall degree of order as a function of temperature in the model:

$$OP_i(t) = \frac{(\overrightarrow{OH_i}(t) \wedge \overrightarrow{OC_i}(t))_z}{\|\overrightarrow{OH_i}(t) \wedge \overrightarrow{OC_i}(t)\|} \tag{4.5}$$

$$OP_i = \frac{1}{N_t} \sum_{t}^{N_t} OP_i(t) \tag{4.6}$$

$$OP_c = \frac{1}{N_{OH \in c}} \sum_{i}^{N_{OH \in c}} OP_i \tag{4.7}$$

$$OP = \frac{1}{N_{OH}} \sum_{i}^{N_{OH}} OP_i \tag{4.8}$$

$OP_i(t)$ is defined as the component along the tube axis (Oz) of the cross product between the two vectors $\overrightarrow{OC}$ and $\overrightarrow{OH}$ related to the -OH bond i (as illustrated in Fig. 4.19), normalized to the length of the resulting vector. As such, it has a value $+1$ or -1 depending if the -OH bond is oriented respectively along the $+\vec{\xi}$ or $-\vec{\xi}$ orientation. It is calculated at each step t of the trajectory of length N_t and can be further averaged over all the time configurations of the trajectory to give OP_i. This quantity – by not being a curvilinear coordinate anymore – is much easier to manipulate.

If the orientation of the -OH bond is random over the trajectory, it will be averaged to a value equal to zero. Further averaging inside a given chain (c) gives OP_c. Averaging OP_i over the whole system gives OP. The notation $N_{OH \in c}$ refers to the number of OH_{in} per chain in our model which is equal to 14. It has to be precised also that 22 (c) chains are considered in our model. Fig. 4.19*b* shows the evolution of OP with temperature. The order parameter is found to be almost constant until

300 K above which it progressively decreases to zero. This proves that the onset of jumps, already observed in the calculated EISF, $QENS$ and MSD above 300 K, are well translated in terms of disorder by the OP defined here.

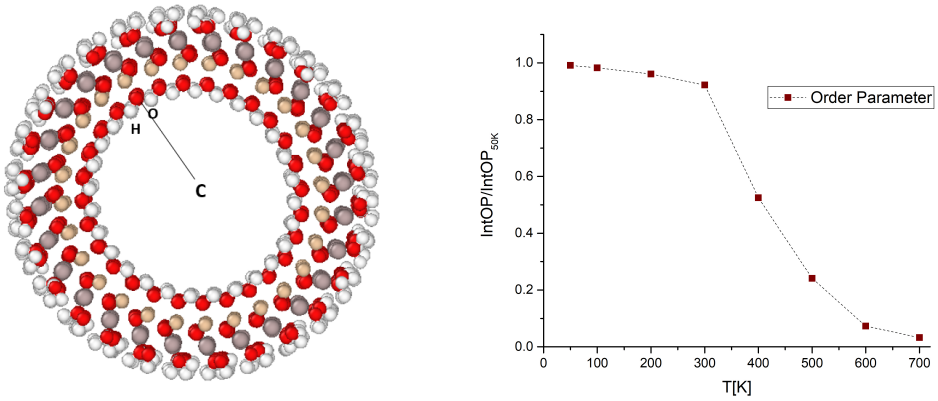

a) *b*)

Figure 4.19: *a*) Geometry of the order parameter cross-product (C=center of the tube, O=oxygen, H=hydrogen) and *b*) order parameter as a function of temperature

To get a more precise idea on the nature of the transition, we represent on Fig. 4.20 the $OP_i(t)$ calculated at each step of the trajectories, for all OH_{in} at the different temperatures, in the form of an histogram. This represents the distribution of $OP_i(t)$ obtained during the trajectories.

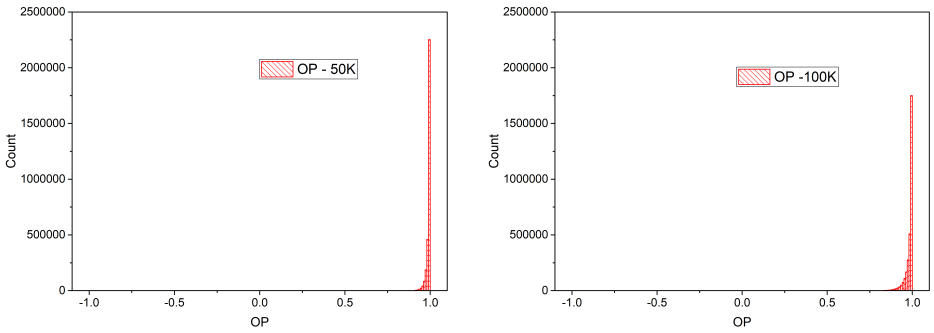

a) T=50 K *b*) T=100 K

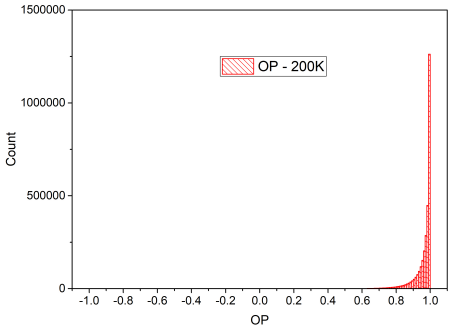

c) T=200 K

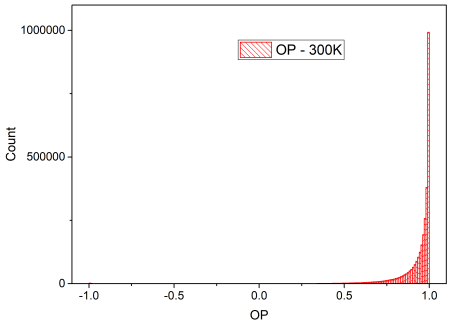

d) T=300 K

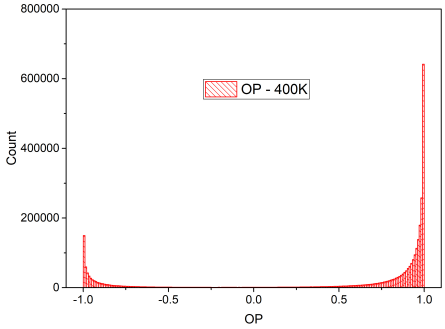

e) T=400 K

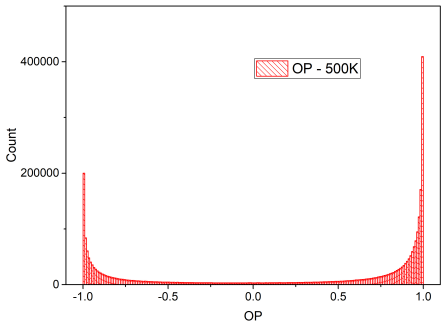

f) T=500 K

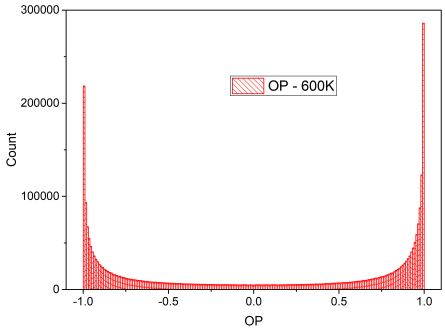

g) T=600 K

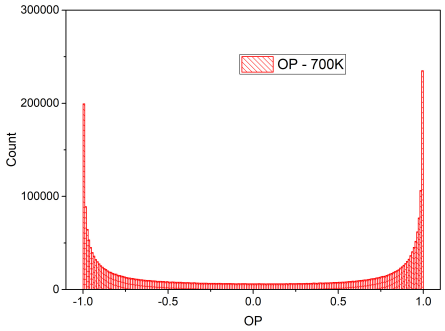

h) T=700 K

Figure 4.20: Histograms of OP_i(t) at *a*) T=50 K *b*) T=100 K *c*) T=200 K *d*) T=300 K *e*) T=400 K *f*) T=500 K *g*) T=600 K *h*) T=700 K.

It can be seen that at very low temperature, in the low T phase, the

distribution is centered at the value $OP_i = +1$ with a sharp distribution, revealing the ordering of the -OH along the same curvilinear direction. As the temperature rises, the distribution widens, until at 400 K the observation of the appearance of a small peak around the value $OP = -1$. The high temperature state corresponds to having both the $+1$ and -1 states equally populated, meaning that the two have the same probability of being occupied. It is important to observe that the high T phase is still characterised, at the highest temperature investigated, by a binary value of the order parameter ($+1$ and -1 equally populated), *i.e.* without distribution of intensity at other values in the range $[-1, +1]$ (*e.g.* the histograms never become flat). This behaviour of the OP is typical of a pseudo-Ising model with pseudo-spin $S_i(t) = OP_i(t)$.

Fig. 4.21 represents the pseudo spin-spin correlation function in a chain defined as:

$$\langle S_i S_{i+n} \rangle = \frac{1}{N_c} \frac{1}{N_t} \frac{1}{14} \sum S_i(t) S_{i+n}(t) \tag{4.9}$$

where N_c is the number of chains in the tube, and N_t the number of configurations saved during the trajectory. The same correlation function

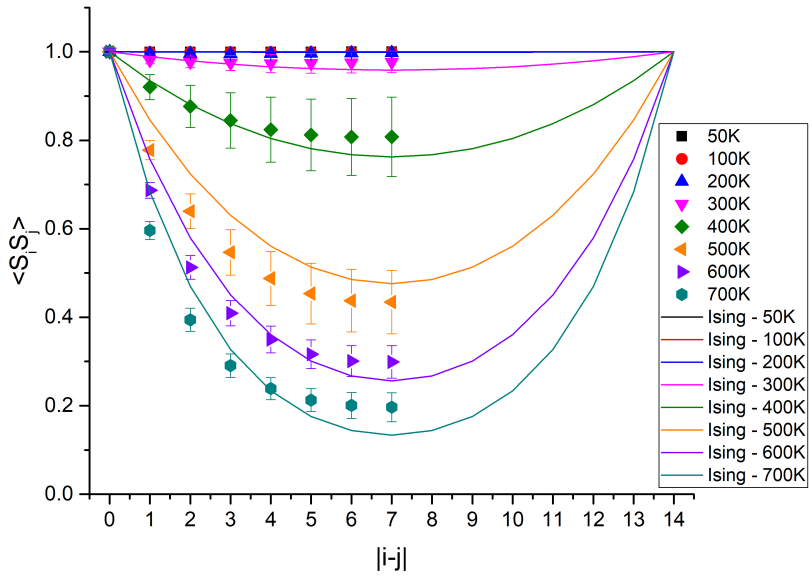

Figure 4.21: Correlation function of the Order Parameter for lines of type (c), MD calculation (with errorbar) and analytical Ising model calculation (continuous line).

was calculated for a finite 1D Ising model for which the Hamiltonian, in

the absence of an external field, writes[262]:

$$H = -J \sum_{ij}^{N-1} S_i \cdot S_j \tag{4.10}$$

where J is the coupling constant and S_i the pseudo-spin variable, that can take values $S_i = +1$ or $S_i = -1$. For a periodic, finite chain of N=14 spins (i.e. with periodic boundary conditions ($S_{14} = S_0$)), the analytical form of the correlation function is known to be[263]:

$$\langle S_i S_j \rangle = \frac{(2cosh(K))^{N-(j-i)}(2sinh(K))^{j-i} + (2sinh(K))^{N-(j-i)}(2cosh(K))^{j-i}}{(2cosh(K))^N + (2sinh(K))^N} \tag{4.11}$$

where $K = \frac{J}{k_B T}$. The comparison between the MD simulation curves and the Ising model analytical solution calculated using a coupling constant $J \sim 50$ meV is shown on Fig. 4.21. The correlation functions for the MD simulations and those calculated using the Ising model show the same trends. They both decay with increasing distance $|i - j|$, and with increasing temperature. For an infinite chain, the spin-spin correlation is exponentially decreasing with the distance $|i-j|$. For a finite chain however, the local constraints imposed by the periodic boundary conditions prevent $\langle S_i S_j \rangle$ to go to zero and the spins (in reality the -OH orientations) keep a non vanishing degree of correlation even at the highest temperatures.

In the preceding section, the study of the quasielastic scattering broadening with temperature allowed us to estimate that an energy barrier with height $E_a \sim 280$ meV separates the positions of the H_{in} atoms described by the pseudo-spins values and separated by $R \sim 1.3$ Å. In this section, we highlight the rather strong bond between the -OH orientations, and using the 1D Ising model we have evaluated the energy of this bond to $J \sim 50$ meV. Combining these two views, a rather reasonable sketch of the (c) chains in our model is illustrated in Fig. 4.22, showing a one-dimensional chain of ordered -OH located in the minima of double-well potentials (with minima separated by an activation energy E_a), and bonded by springs of coupling constant $C = \frac{4J}{R^2}$, with R the distance between the minima. As described by Aubry[264], the fact that J « E_a is typical of an order-disorder transition (as opposed to displacive transitions) and the resulting Hamiltonian of the chain is composed of a pure kinetic term added to a 1D Ising type term (see Eq. (3.2) in[264]). It is this latter term that is responsible for the appearance of disorder inside the chain. This explains why the simple Ising model proposed in this section correctly describes the ODT as observed in our MD simulations. However, it must be precised that the theoretical approach followed here is

developed considering isolated (c) chains in the absence of external field nor interchain interactions. Therefore this model cannot account for the global ordering of the OH_{in} bonds orientation as observed in the MD simulations in the low T phase. A small interchain coupling could involve short lived interchain hydrogen bonding. An external "molecular" field resulting from the chiral nature of the tube's symmetry could also results in rendering the local double well potential slightly asymmetric. Those directions have not been investigated in this thesis but are the natural extension of the work presented in this section.

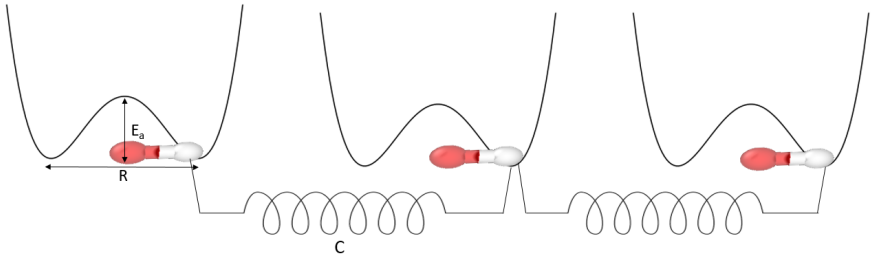

Figure 4.22: Model describing interaction of double-well potentials of activation energy E_a with coupling constant $C = \frac{4J}{R^2}$ (where J « E_a)

4.2.4 Evidence of the ODT from neutron scattering experiments perspectives

The following sections will be dedicated to find, by means of neutron scattering, the experimental proofs of the transition. We first report on the measurements performed on IN13 to follow the T dependence of the elastic scattering. We will then focus on the dynamics of the hydrogens in the sample at different time scale, and report the experiments conducted on the spectrometers WASP and IN6-SHARP.

4.2.4.1 Evolution of the elastic scattering using the IN13 backscattering spectrometer

Using a high resolution spectrometer like IN13 at the ILL, one can measure the elastic scattering, in a $\sim 8\mu eV$ window, as a function of temperature. Any relaxation process with characteristic time smaller than 150 ps will exit the IN13 window and will reduce the scattered signal. The Q-dependence of the intensity can – in principle – lead to the experimental determination of the $EISF$, a quantity we discussed in the

previous sections. With the statistics of the signal we had it was unfortunately indispensable to sum the intensity recorded over all the detectors. However, the T dependence of the signal brings invaluable information on the dynamics: looking at the slope of the evolution of the intensity loss with increasing temperature is a routine method to access the MSD and to detect the onset of fast dynamics. In particular, any ODT generally translates into a step like evolution close to the temperature of the transition.

Fig. 4.23 shows the elastic intensity measured on the dry imogolite nanotube as a function of temperature.

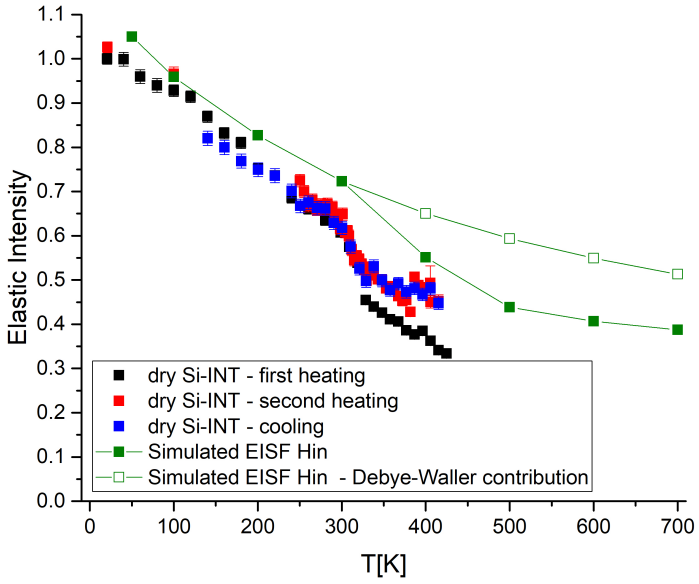

Figure 4.23: (i) Experimental $EISF$(T) measured at IN13, ILL. First heating ramp in black, second heating ramp in red and in blue the cooling ramp from the red. (ii) In green, simulated total EISF(T) for H_{in} as a function of temperature (full squares). The empty squares evidence what the behavior would be with only a harmonic Debye-Waller like behavior. Both experimental and simulated curves where normalized to the lowest temperature (the green curves were later translated slightly to make easier the visualization).

The first heating ramp is in black, the second heating ramp in red and in blue the cooling ramp done at the end of the second heating ramp. On heating from the lowest temperature (black curve), the intensity de-

creases smoothly – almost linearly – until T $\sim$ 300 K where a stronger slope is observed. On further heating, the intensity shows a linear trend again, with a slope similar to the one observed in the low T phase, meaning that the vibrations of the hydrogen atoms are not strongly affected by the transition. The step like decrease, from 300 K to 350 K reveals the onset of a fast dynamics. It corresponds to an intensity loss of $\sim$ 25%. If one assumes that the total intensity is proportional to the number of hydrogen atoms in the sample (*i.e.* that the scattering is purely incoherent), a value of $\frac{1}{4}$ is expected (1 hydrogen over 4 is located on the inner surface of the tube), in very good agreement with our measurement.

After the first ramp was measured, the sample was quickly cooled to room temperature and removed from the cryofurnace. It was let sealed in the aluminum cell for about a week before another measurement was performed on exactly the same conditions. However, due to lack of beamtime, the first cooling ramp (to reach the lowest temperature) was done faster. The transition is observed to appear at the same temperature (see red curve) with a similar behavior as first observed for ramp 1. However, the height of the step is reduced by about half, meaning that 50% less OH_{in} participate to the transition in the second ramp. The similarity of the heating and cooling ramps reveal the reversibility of the transition and the absence of significant hysteresis, when slowly cooling down from 400K. These observations indicate that the thermal history of the sample has an important impact of the proportion of static/blocked H_{in} in the sample, the physical origin of which is not yet understood. Local defects may be invoked to explain this observation[265].

The $EISF$ extracted from the MD trajectories (see Fig. 4.15) of the H_{in} atoms was integrated in the Q range accessible to IN13. It is plotted on the same figure for comparison (full green symbols). If both curves agree qualitatively, even quantitatively if one considers the low T slope of the intensity and the temperature at which the drop appears, a major difference is observed: while the step-like decrease extends from 300 K to 500 K for the simulations, revealing a progressive broadening in energy of the signal, its extension is much reduced in the data. This means that the activation energy calculated in our MD simulations is overestimated, reflecting an imperfect account of the local energy landscape of the OH_{in} and/or that other processes – not accounted in our MD – have to be introduced. In particular, quantum effect are totally absent from our purely classical MD. Considering the low H mass and the small jump length, tunneling or phonon-assisted tunneling could be invoked to help understand this disagreement[266,267].

4.2.4.2 Quasi Elastic neutron scattering analysis in the disordered phase: spin echo and time of flight investigations using the WASP and IN6-SHARP spectrometers

In the MD simulations, the order-disorder transition is accompanied by the appearance of a $QENS$ signal in the scattering, which translates as a decay of the Intermediate Scattering Function (Eq. 2.29) in the time domain. In order to investigate the dynamics of the H_{in} in the high T phase, data were collected on the spin-echo spectrometer WASP with a wavelength of λ=4 Å giving access to the time window [1, 1000] ps and the Q domain between [0.2, 2.2] Å^{-1}. The polarization analysis is shown in Appendix A.

The first measured temperature was 300 K, which is the edge of the transition according to IN13 data. At 300 K, WASP data show the absence of dynamics (Fig. 4.24a), as the echo remains constant and close to a value equal to one over the whole Q range. At 400 K by contrast, the echo intensity is characterised by a Q dependent plateau with a drop for t longer than 0.1 ns.

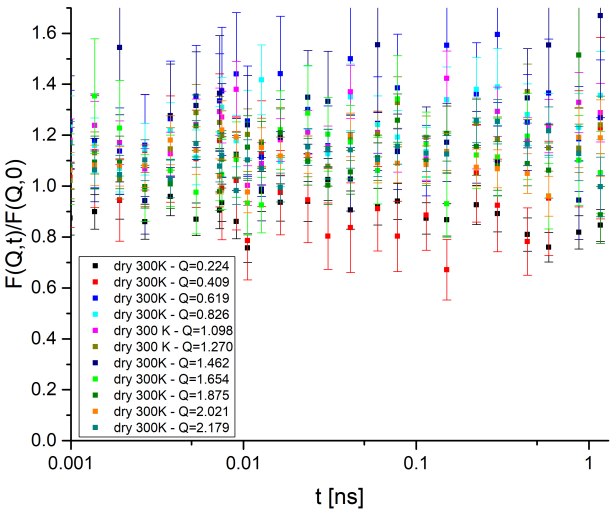

a) T=300 K

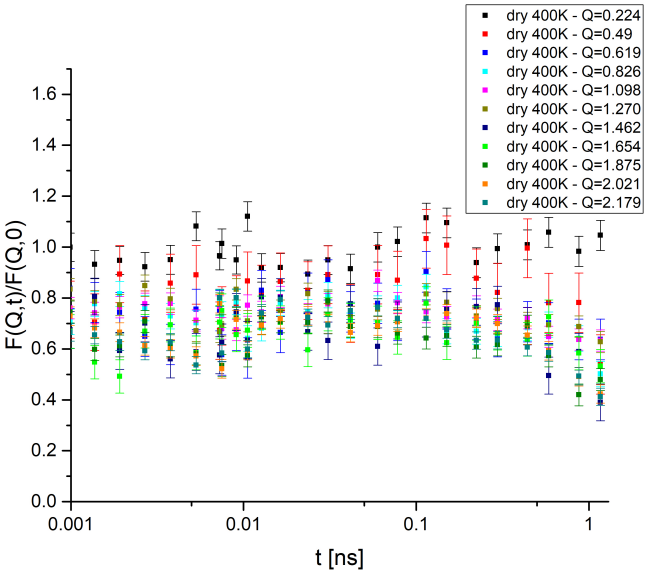

b) T=400 K

Figure 4.24: Echo signal measured at WASP of the dry Si-INT powder at *a*) 300 K and *b*) 400 K. Code of colors: Q=0.224 Å^{-1}: black; Q=0.409 Å^{-1}: red; Q=0.619 Å^{-1}: blue; Q=0.826 Å^{-1}: cyan; Q=1.098 Å^{-1}: magenta; Q=1.270 Å^{-1}: dark yellow; Q=1.462 Å^{-1}: navy; Q=1.654 Å^{-1}: light green; Q=1.875 Å^{-1}: dark green; Q=2.021 Å^{-1}: orange; Q=2.179 Å^{-1}: dark cyan.

The plateaus reveal that the echo has dropped significantly from 1 at 300 K to $\sim$ 0.8 in the small t range (see Fig. 4.24*b*), which evidences a fast dynamics with a decay time constant that falls outside the NSE window, *i.e.* with a correlation time faster than 1ps. Another relaxation appears at much longer times and is responsible for the decrease of the echo at the end of the time window probed.

The simulated intermediate scattering function (ISF) F($\vec{Q}$,t) curves were calculated with 1 ns long trajectories, in the same Q range as WASP. Fig. 4.25 shows the plot for 200 K and 500 K. At 200 K there is no decay and the ISF features constant lines closed to one, as expected in the ordered static phase. At higher temperature (500 K) however, the ISF is characterised by a Q dependent plateau followed by a decrease for long correlation times, in qualitative agreement with the curves observed experimentally. The separation of the H_{in} and H_{out} contribution (see 4.26) further indicates that the fast decay involves mostly the H_{in} while the H_{out} are responsible for the decay of the signal at times longer than $\sim$ 0.1 ns.

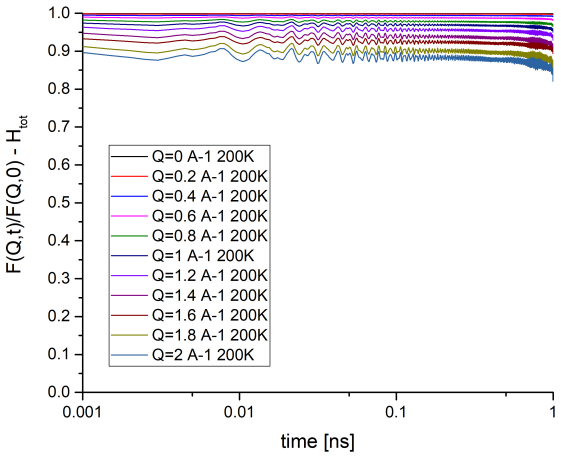

a) H_{tot} T=200 K

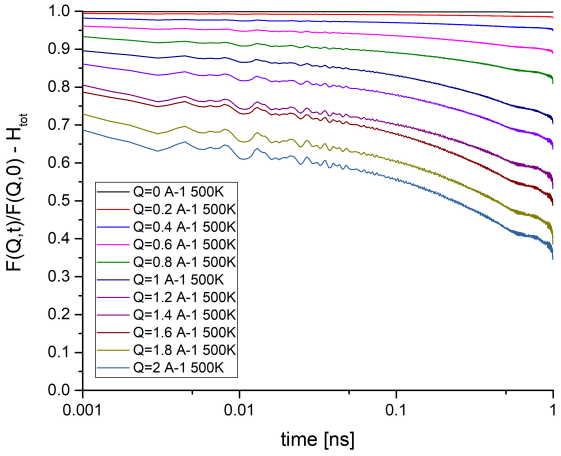

b) H_{tot} T=500 K

Figure 4.25: Simulated F($\vec{Q}$,t) as a function of time for the hydrogen atoms of an imogolite nanotube calculated in the same time and Q range of WASP, at *a*) 200 K and *b*) 500 K

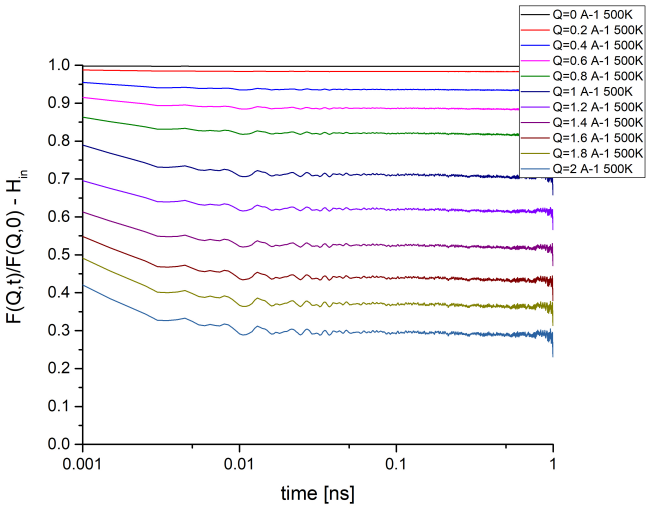

a) H_{in}

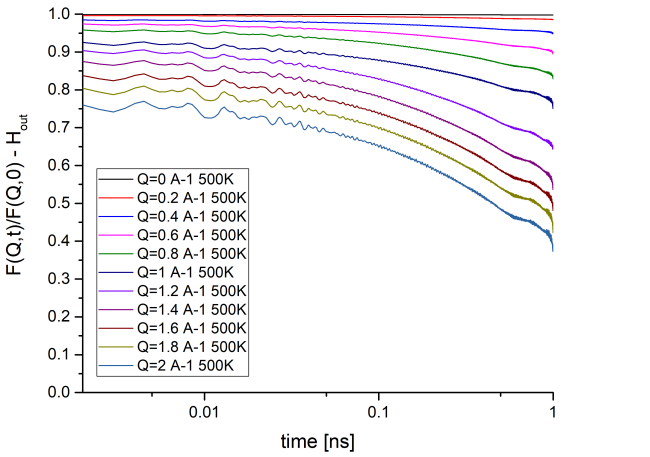

b) H_{out}

Figure 4.26: Simulated F($\vec{Q}$,t) as a function of time for the hydrogen atoms of an imogolite nanotube calculated in the same time and Q range of WASP at 500 K, calculated for *a*) H_{in} and *b*) H_{out} separately

If one considers that the dynamics of the H_{out} is visible only above 0.1 ns, one can attempt to extract the experimental EISF(Q) of the H_{in} from the WASP signal at 400 K in Fig. 4.24, by considering the constant plateau in the echo range between 0.01 and 0.1 ns, *i.e.* in a range where the intensity of the H_{out} signal is equal to 3/4. and Q independent.

We therefore have averaged the time dependence of the echo between 0.01 and 0.1 ns, to which a value of 0.75 was subtracted. The signal is normalized to one in a final step. The resulting curve is shown in Fig. 4.27, and is compared to (i) the one extracted from the simulated EISF using the same procedure, and (ii) to the EISF in the high T phase already shown in Fig. 4.15. The experimental data are characterised by an oscillating behavior, with a maximum located around 1.2 Å^{-1}. Even if the statistic of the data is poor, one clearly observe that the global shape of the curve differs significantly from the simulated EISF, suggesting that the observed dynamics does not correspond to a jump diffusion between two sites.

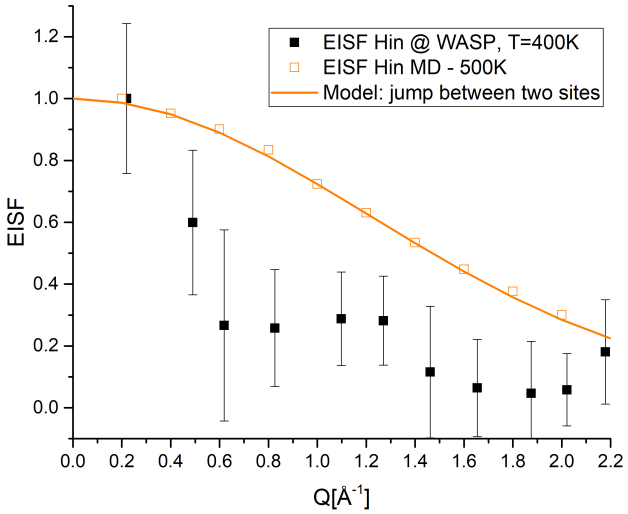

Figure 4.27: Experimental EISF(Q) for the H_{in} calculated from WASP data at 400 K (black), compared to the MD EISF at 500 K (orange open symbols), which was fitted with a model of jump diffusion between two sites (solid orange line)

The dry sample was measured also on IN6-SHARP, at different temperatures (T= 250, 300, 325, 350, 375, 400 and 450 K). The $QENS$ broadenings are reported in Fig. 4.28. Contiguous temperatures were not measured continuously, but on the contrary, three successive ramps were carried out: the first one was measured on heating from 300 K to 450 K. From this point, the temperature was decreased and the points at 350 K, 250 K and 2K were obtained. Another heating ramp was further done and the spectra were measured at 325 K and 375 K (see Table . 4.5).

T ramp 1 (heating) [K]	T ramp 2 (cooling) [K]	T ramp 3 (heating) [K]
300	350	325
400	250	375
450	2	-

Table 4.5: Temperatures sampled in the three temperature ramps performed in IN6-SHARP

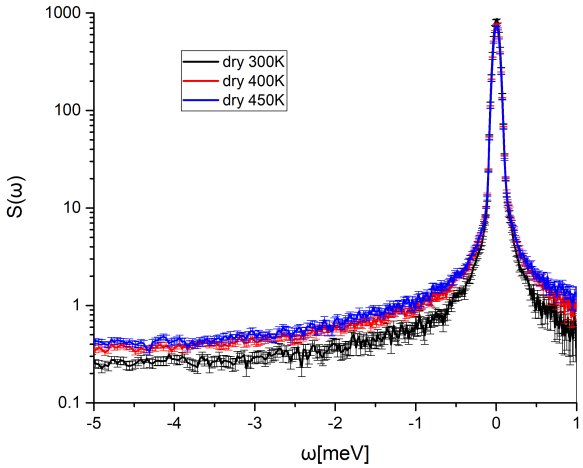

a)

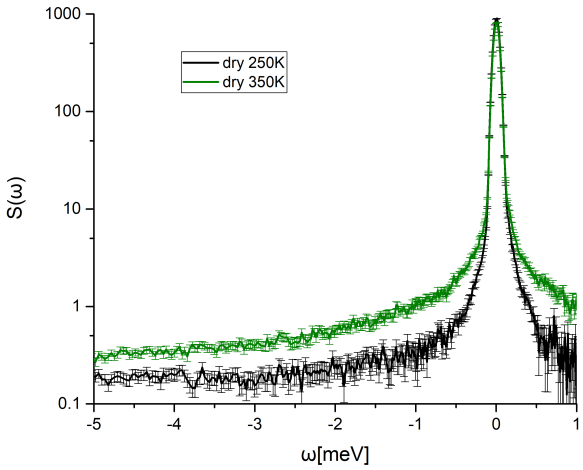

b)

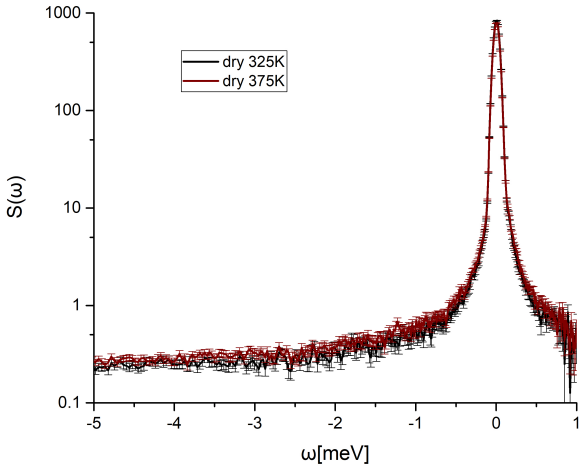

c)

Figure 4.28: $QENS$ broadening *a*) during the first cycle, during *b*) the second cycle and *c*) the third cycle.

On heating the sample from 300 K during the first ramp (see Fig. 4.28*a*)), one sees the appearance of a $QENS$ broadening at 400 K. Further increase of the temperature does not result in a significant increase of the broadening. On cooling to 350 K, the $QENS$ signal is still present but disappears at 250 K (see Fig. 4.28*b*). During the third ramp, after the resolution measurement was performed at 2K, increasing the temperature again at 325 and 375 K doesn't result in any sign of transition as no clear $QENS$ broadening is observed (see Fig. 4.28*c* and 4.29). The lowering of the $QENS$ signal after cycling the temperature is entirely in line with the observations discussed in the section concerning the elastic scattering (see section 4.2.4.1), and suggests that cooling the sample (rapidly?) from the disordered phase has the consequence to block the hydrogens and prevent them to participate to the ODT. One could understand that the onset of a ODT requires *de facto* the ordered state to be the low T phase. If the system is locked in a disordered glass-like phase, the ODT might be strongly affected, if not suppressed and one should probably heat the sample at larger temperatures and cool it down sufficiently slowly to return to the ordered low T state for the OH_{in}.The fact that the transition is systematically seen after the sample has stayed at 300 K (*i.e.* close to the disordered temperature) during a relatively long period might reveal that the relaxation into the ordered state requires a long time.

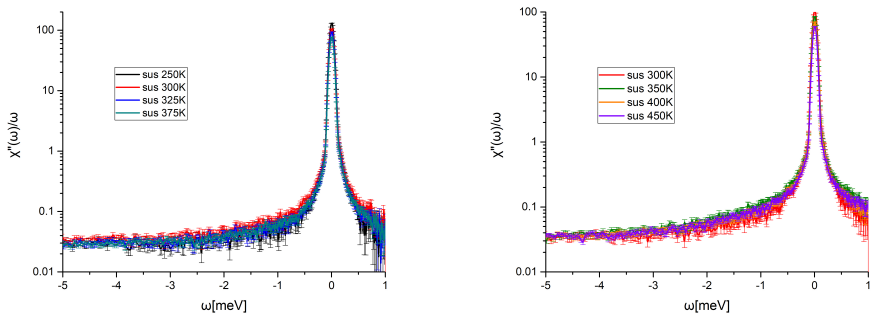

a) *b)*

Figure 4.29: In *a)* susceptibility divided by energy of the curves not having $QENS$ (T=250, 325 and 375K) + T = 300 K for comparison; in *b)* susceptibility divided by energy of the curves having $QENS$ (T = 350, 400 and 450 K) + T = 300 K for comparison. The fact that the susceptibility overlay at all T in *a)* and not in *b)* suggests that the signal is purely of phonon-like origin in *a)*, and that no $QENS$ signal is seen. T = 300 K is the only uncertain temperature. It's reported in both as a comparison, which seems to suggest that there is some small $QENS$ signal at 300 K as well.

The four temperatures that present a $QENS$ signal, *i.e.* 300, 350, 400 and 450 K, were fitted with:

- A flat background to account for low frequency density of states.
- For the elastic peak, a convolution between the experimental resolution (given by the sample at 2K) and a Delta function.
- Two Lorentzians to account for the diffusion of the hydrogen atoms (in principle, both H_{in} and H_{out}). They were convoluted to the experimental resolution.

The fits were done on the Q integrated signal and are shown on Fig. 4.30.

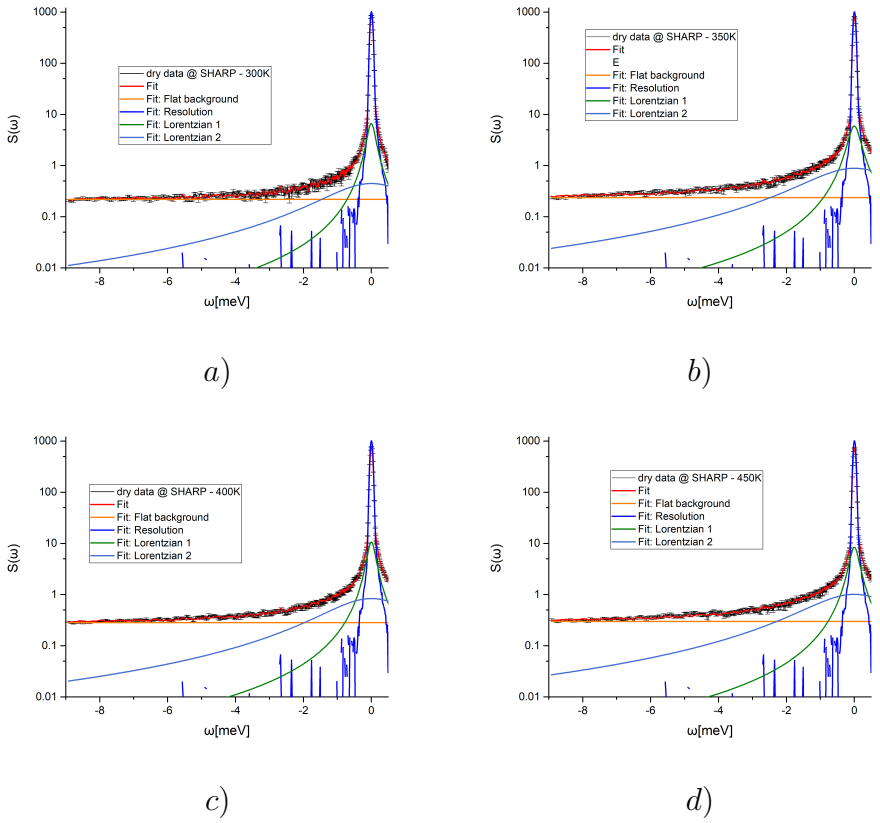

Figure 4.30: Fit components of IN6-SHARP data at *a*) T=300 K, *b*) T=350 K, *c*) T=400 K and *d*) T=450 K.

The HWHMs and the intensity of the lorentzians obtained from the fit are reported in Table 4.6. The data are well reproduced by accounting for a fast and a slow contribution, the widths of which differ by an order of magnitude. In the light of what we found from simulations (See Fig. 4.16 and Tab. 4.4), we would be tempted to associate the narrow Lorentzian to the H_{out} and the broad one to the H_{in}. In the simulations, the ratio between the width associated to each category was in acceptable agreement with the one found here. However, this large ratio is the only one parameter that seems to be reproduced quite satisfactorily by the simulations. In complete disagreement is the striking result that the widths of the slow and fast lorentzians are observed to be almost constant with temperature, the intensity of the signal being the only parameter sensitive to temperature. As already discussed, if one still adopts the image of $QENS$ as resulting from local thermally activated jumps (as was found for the simulations) this suggests that the energy barrier to cross is zero. This is in complete contradiction with the value $E_a \sim 0.28$ eV found in the simulations.

-	$HWHM_1$ [meV]	$Ampl_1$ [a.u.]	$HWHM_2$ [meV]	$Ampl_2$ [a.u.]
300 K	0.13 ± 0.01	2.74 ± 0.08	1.43 ± 0.11	2.01 ± 0.08
350 K	0.19 ± 0.01	3.46 ± 0.09	1.50 ± 0.07	4.16 ± 0.1
400 K	0.13 ± 0.01	4.31 ± 0.07	1.41 ± 0.06	3.71 ± 0.07
450 K	0.15 ± 0.01	3.93 ± 0.08	1.48 ± 0.06	4.70 ± 0.09

Table 4.6: HWHM and amplitudes resulting from the fit on IN6-SHARP data

Finally, the density of states of the dry sample was calculated and measured on PANTHER. As they do not add more to the present discussion, the results are presented and discussed in Appendix B.

4.2.5 Conclusion

At the time of writing, the fine understanding of the dynamics of the dry imogolite sample is lacking. The simulations predict the onset of disorder to be detectable at T $\sim$ 300 K. This ODT is well rationalized by a simple Ising chain with periodic boundary conditions, involving a double well local potential with minima separated by a $E_a \sim 0.28$ eV barrier, the H_{in} being coupled by springs corresponding to an energy of $J \sim 50$ meV. While a transition is actually observed by a singularity at 300 K in the elastic scan measured on a dry imogolite sample, with an intensity drop that clearly is in good agreement with an origin involving H_{in} atoms, the characteristic of the dynamical process deduced from the time of flight and spin echo measurements are not in line with those extracted from the molecular dynamics trajectories. In particular the absence of any T dependence of the width of the $QENS$ spectra suggest that the movement of the H_{in} atoms are almost free. Soliton-like propagations of the domain walls, inherent to any critical phenomenon, might have to be invoked to shed further light into the data.

4.3 Summary

The main conclusions and take-away messages of this chapter dedicated to the study of dry imogolite nanotubes are:

- The structure of the Si-INT powder sample was resolved by

comparing simulation and experimental data. A good agreement was found between synchrotron data and a simulated curve computed from the MD structure at 300 K of a tube having N = 14 (or N=13).

- The minimum energy structure was studied by means of MD simulations, revealing the orientation of the internal hydroxyls, all aligning in the same direction at low temperature.
- Above T=300 K, a jump diffusion mechanism between two equivalent sites – which correspond to the two possible orientations of the hydroxyls – takes place in MD simulations. Simulations evidence strong correlations between hydroxyls belonging to the same horizontal chain, and the diffusion of domain walls.
- An order parameter allows us to model the hydroxyls as a pseudo-Ising system displaying an order-disorder transition.
- The occurrence of the transition is confirmed by experiments using the backscattering spectrometer IN13.
- Nevertheless, IN13, WASP and IN6-SHARP data seem to question the nature of the diffusive dynamics. A diffusion between two sites is not observed.

5. Structure and dynamics of water in imogolite nanotubes

After studying the specific structural properties of Si-INTs, we will now focus on the behavior of water confined in these nanoporous structures. This chapter is organized as follows. In section 5.1, we will present the results of adsorption isotherms, which will allow us to define the preparation of hydrated samples with different water content. In section 5.2, Molecular Dynamics simulations on hydrated Si-INTs will be introduced, with a focus on the resulting structuring of adsorbed water, both in the radial and longitudinal direction. Based on these results, we performed an in-situ X-ray study to investigate how water molecules are organized as a function of water filling. Sections 5.3 and 5.4 will be focused on neutron scattering experiments, containing MD simulations coupled with data measured on various spectrometers at ILL, namely D16, IN13, IN6-SHARP and PANTHER. In particular, the diffusion mechanism of water inside imogolites will be characterized in detail, as well as a particular peak appearing in the density of states, specific to water attached to the tube wall of a certain diameter.

5.1 Preparation of hydrated samples

A H_2O isotherm is first performed to determine the water uptake by dry Si-INTs. This should intend to give reference points for preparing hydrated samples in order to study nanoconfined water in Si-INTs. The evolution of the amount of adsorbed H_2O molecules as a function of P/P_0 is presented in Fig. 5.1.

Water adsorption occurs for the lowest P/P_0 values. It shows a rapid rise and then the trend changes to a flat plateau. This suggests a steep water uptake into the nanopores at very low pressure, while the plateau is related to multilayer adsorption and finally pore condensation, for the highest P/P_0. This experimental finding is in good agreement with previous water adsorption isotherms[204].

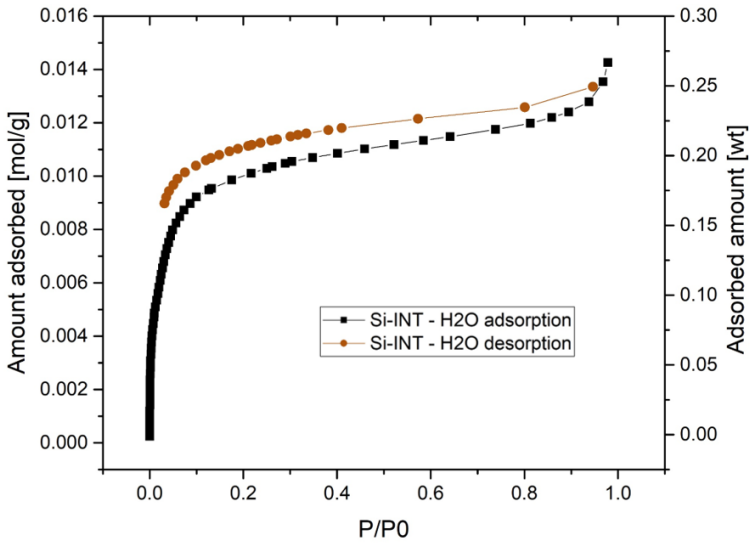

Figure 5.1: Water isotherm on Si-INTs powder: adsorption branch (black squares) and desorption branch (brown circles). The axis on the left is in [mol/g] while the right axis gives the quantity of water adsorbed in wt.

Once the water isotherm is known, we can prepare different hydrated samples by looking into the curve and calculating what $RH = \frac{P}{P_0}$ is associated to the desired water mass. In this work, we are interested in the structure and dynamics of the water molecules confined in the tube, in particular for low water uptake where the molecules would form only a single layer. As shown from water adsorption isotherm, the filling of the nanotubes occurs for RH values smaller than 10%, which corresponds to water uptakes lower than 15 wt%. In practice, the RH can be controlled by preparing saturated salt solutions[219]. Indeed, different salts give access to a range of RH inside an experimental environment like a desiccator. Values of RH of selected saturated salt solutions are given in Table 5.1. The solutions with the lowest possible RH are CsF or $LiBr$.

Salt	$RH[\%]$
Cesium Fluoride	3.39 ± 0.94
Lithium Bromide	6.37 ± 0.52
Zinc Bromide	7.75 ± 0.39
Potassium Hydroxyde	8.23 ± 0.72
Sodium Hydroxyde	8.24 ± 2.1

Table 5.1: Value of RH associated to different salt solutions at T=25°. Values taken from Greenspan et al[268]

By putting both the sample and the saturated salt solution in the desiccator, pumping and then isolating it, we can impose a fixed water vapor pressure. The mass gain is measured by weighting the sample before adsorption and several times during water adsorption, until the desired mass is reached. The mass of water is extracted by calculating the extra weight gained by the sample.

$$mass\ fraction\,[wt\%] = \frac{m_{H_2O+Si-INT} - m_{Si-INT}}{m_{Si-INT}} \tag{5.1}$$

In our case, a first sample with 6wt% of water uptake was obtained by keeping for a few days the Si-INT powder inside a desiccator humidified with a saturated CsF salt solution, while a second sample hydrated at 12wt% was prepared by using a $LiBr$ saturated solution. It is worth noting that the water uptakes are lower than expected from the isotherm. This is rather surprising but both masses – 6wt% and 12wt% – seemed to be stable in time, meaning that the weight gain measured has reached an equilibrium. Therefore, it allows us to have a unique opportunity to study partially filled nanotubes.

In order to confirm the quantity of water adsorbed in the two hydrated samples, diffraction scans on the diffractometer D16 were performed. The diffraction pattern of the dry and the two hydrated samples are reported in Fig. 5.2. In the case of neutron diffraction, the intensity of the (10) reflection is not supposed to change much because the hydrogen that one adds with an hydrated sample – compared to the dry – scatters mainly incoherently while diffraction is a coherent phenomenon. However, the incoherent background varies, as it is proportional to the number of hydrogens in the sample. Therefore, the amount of constant background allows us to measure the quantity of water in the sample.

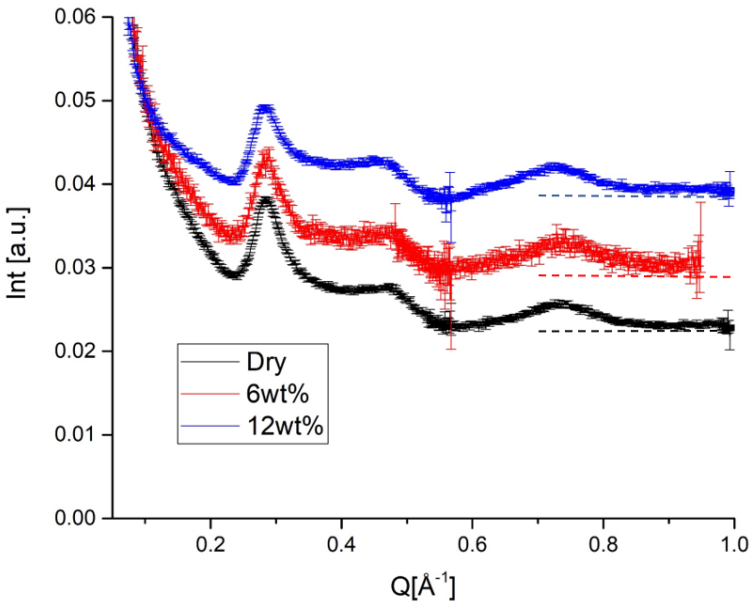

Figure 5.2: Diffraction pattern measured at room temperature with D16 for the dry sample (black), 6wt% (red) and 12wt% (blue). The incoherent background is highlighted with a dotted line.

Table 5.2 shows the agreement between the masses measured when preparing the sample and the masses deduced from the D16 measurement.

-	Sample 1	Sample 2
Measure of mass	6wt%	12wt%
Incoherent background D16	5.7wt%	11.5 wt%

Table 5.2: Comparison between the water mass calculated from a measurement of mass and the incoherent level on D16

5.2 Water periodic structuring by MD and in-situ X-ray diffraction

5.2.1 Structure and radial density profiles

The hydration of Si-INTs was first studied by means of Molecular Dynamics by filling the internal cavity with a growing quantity of water. Four hydration states were studied, corresponding to 3wt%, 6wt%, 12wt% and

15wt% of water in mass. The 100 ps long trajectories were employed here. Density maps in the (x, y) plane corresponding to these mass fractions are displayed in Fig. 5.3.

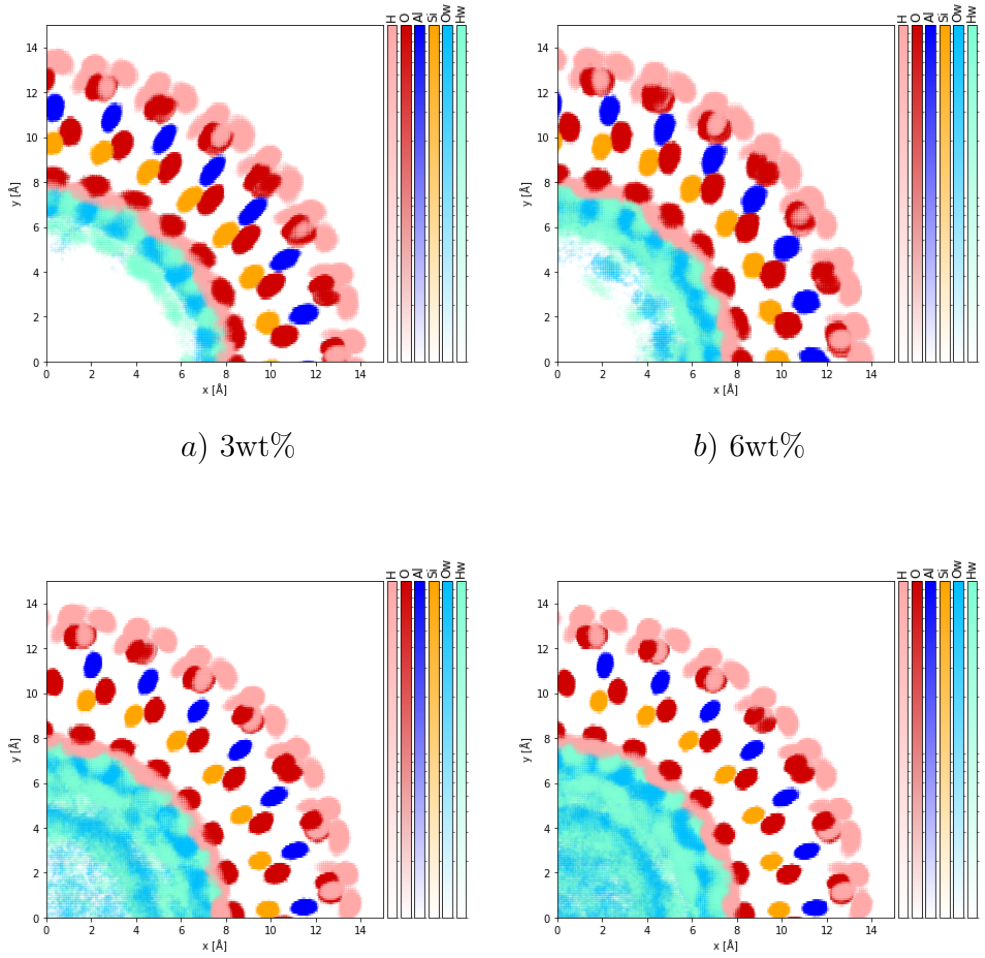

a) 3wt% *b*) 6wt%

c) 12wt% *d*) 15wt%

Figure 5.3: (x,y) Section of the nanotube (T=300 K) filled with (*a*) 3wt%, (*b*) 6wt%, (*c*) 12wt% and (*d*) 15wt% of water. The colors correspond to the different atoms of the Si-INT structure: pink = H, red = O, blue = Al, yellow = Si. Oxygen and hydrogen from water molecules are represented in cyan = Ow and aquamarine = Hw.

These maps allow to evidence how water confined inside Si-INTs structures itself in concentric layers, as already seen in several cylindrical confining systems, as mentioned in section 1.4.2. The 3wt% state corresponds to the presence of a first water monolayer partially filled; at 6wt% of water, the first layer is almost complete while the second one

starts to form. Before this layer fills completely, water molecules start to occupy positions closer to the pore center, showing that the configuration where all the available adsorption sites are occupied is not energetically favorable; at 12wt%, we distinguish clearly a first adsorption layer of water, followed by a second layer, and a less populated internal cylinder. Moreover, at 12wt% the first layer is more populated, showing that water molecules first need to explore the whole cavity before completing the first adsorption layer. Moreover, a non-zero intensity between the three different layers suggest the presence of molecules diffusing between them; 15wt% corresponds to the full nanotube, where also the internal cylinder is loaded at its maximum.

This structuring into three layers can be seen in the density of water oxygens (O_w) projected into the radial direction, summed in time and normalized to the number of Si atoms, as shown in Figs. 5.4.

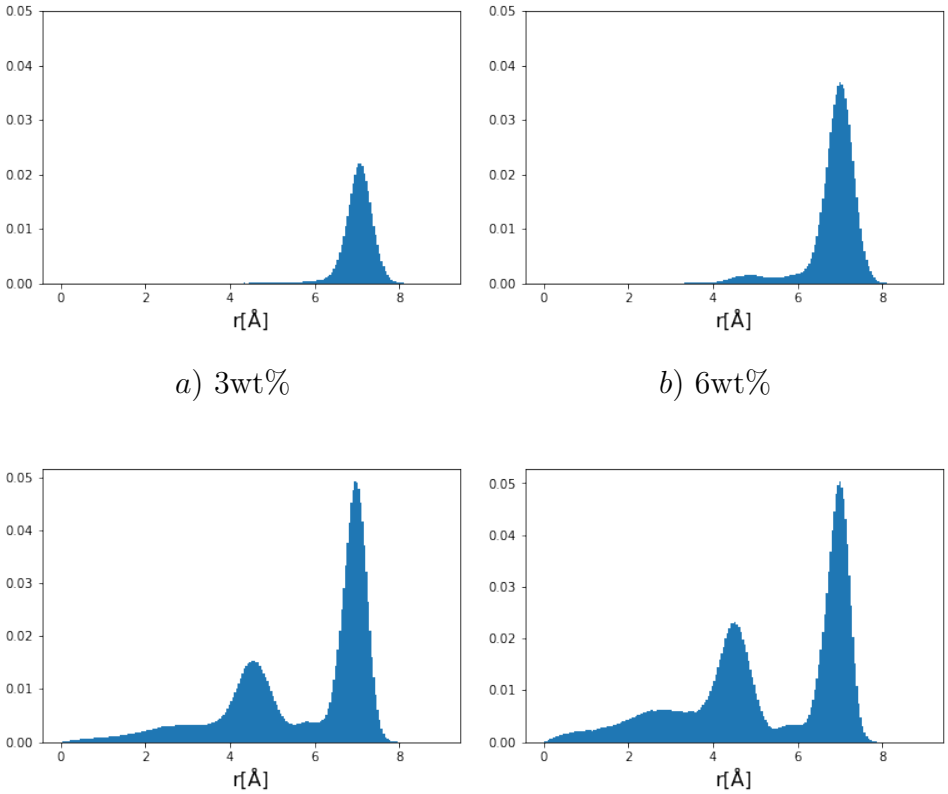

a) 3wt% *b*) 6wt%

c) 12wt% *d*) 15wt%

Figure 5.4: Radial density of O_w for (*a*) 3wt%, (*b*) 6wt%, (*c*) 12wt% and (*d*) 15wt% of water at T = 300 K

According to the geometry, the water molecules can be classified in three different populations:

- **first adsorption layer**: water molecules directly adsorbed onto the tube wall, with average distance from the tube center equal to $\sim$ 7 Å.
- **second adsorption layer**: molecules forming hydrogen bonds with the first layer of water, with distance to the center $\sim$ 4.5 Å.
- **central cylinder**: water molecules into a cylinder with radius 4 Å.

It is interesting to look closer at the first adsorption layer and investigate which adsorption patterns occurs. This can be evidenced from a density map like the one presented in Fig. 5.5 for a Si-INT filled with 6wt% of water. In this map, triangular adsorption sites delimited by three adjacent O_3SiOH tetrahedrons are evidenced with red lines.

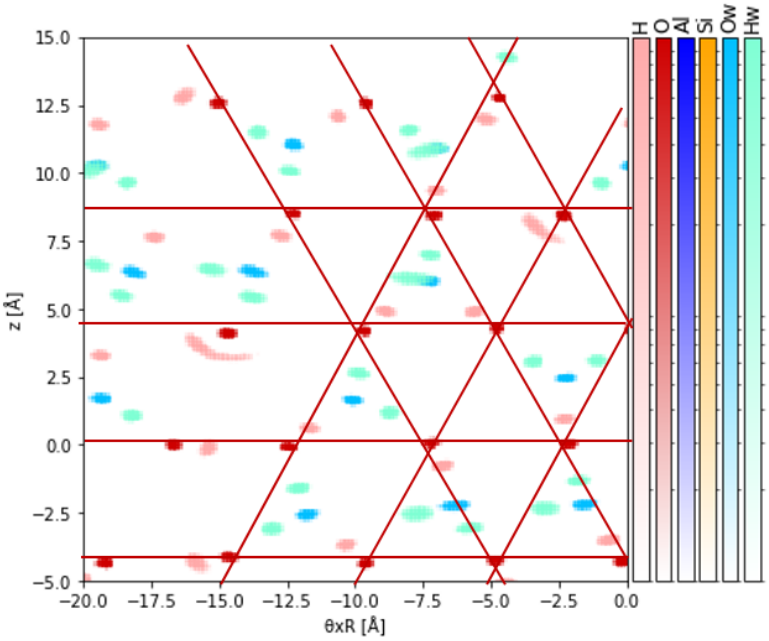

Figure 5.5: Unrolled view of the density profile over time of the nanotube filled with 6wt% of water at T=50 K. Internal triangular adsorption sites are delimited with red lines.

Five types of adsorption patterns are identified:

- Type 1: water molecules adsorbed parallel to the surface, forming three hydrogen bonds with the wall of the nanotube, of which two bonds $H_w \cdots O_{OH-NT}$ and one bond $O_w \cdots H_{OH-NT}$ (Fig. 5.6)

Figure 5.6: First adsorption pattern: molecule adsorbed parallel to the wall.

- Type 2: water molecules adsorbed perpendicularly to the surface, forming three hydrogen bonds with the wall of the nanotube: two bonds $O_w \cdots H_{OH-NT}$, one bond $H_w \cdots O_{OH-NT}$ and having the second H_w freely dangling and pointing towards the center of the nanotube (Fig. 5.7)

Figure 5.7: Second adsorption pattern: molecule adsorbed perpendicularly to the wall (the O_w is not visible because behind one H_w atom which is exactly superposed to it)

- Type 3: intermediary configuration between 1 and 2, where the molecule forms one bond $H_w \cdots O_{OH-NT}$, one bond $O_w \cdots H_{OH-NT}$. The angle formed with the nanotube wall is intermediary between type 1 and 2. That kind of configuration can appear when molecule place one close to the other in "rows", and compared to type 1, they are not anymore at the center of the triangle formed by three OH.

Figure 5.8: Third type of adsorption pattern

- Type 4: the oxygen of the molecule is adsorbed to the wall, forming two bonds $O_w \cdots H_{OH-NT}$. The two hydroxyl groups of the water molecule are both pointing towards the center of the nanotube.

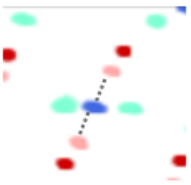

Figure 5.9: Fourth type of adsorption pattern

- Type 5: opposite of the previous configuration, here the two hydroxyls of the water molecule are bound to the surface (two bonds $H_w \cdots O_{OH-NT}$) and the oxygen is pointing towards the center.

Figure 5.10: Fifth type of adsorption pattern

Table 5.3 summarizes the different types of adsorption patterns and the number of hydrogen bonds with the nanotube wall.

Adsorption pattern	No. of $H_w \cdots O_{OH-NT}$	No. of $O_w \cdots H_{OH-NT}$
Type 1	2	1
Type 2	1	2
Type 3	1	1
Type 4	0	2
Type 5	2	0

Table 5.3: Classification of the different adsorption patterns and the related hydrogen bonds formed with the hydroxyls of the tube wall

It is interesting to note that for Ge-INTs, where N = 22, the first adsorption pattern of Fig. 5.6 is the only possible, as the adsorption site is bigger and a single monolayer of isolated molecules can form. Here, we demonstrate that for a Si-INT with N = 14, due to the smaller diameter in contrast to Ge-INTs, it is not possible to have an ordered monolayer. Consequently, different adsorption patterns necessarily occur. Scalfi et al. have proposed that type 2 adsorption pattern is the most abundant configuration but for a Si-INT with N = 12[207]. However, we

demonstrated that the real structure of Si-INTs is for N = 14, which explains why type 1 prevails according to our simulations.

Moreover, already Scalfi proposed that, in these hydrophilic systems, it is thanks to the dangling molecule type 2 if water is structured also beyond the first adsorption layer, and that is why there is a second layer of water having a precise equilibrium distance for the oxygen density. On the contrary molecules of type 1 are less constraining on the second layer and contribute to the fraction of molecules that are less structured. On the other hand, types 3-5 are too few to have a noticeable effect.

5.2.2 Periodic structuring along the nanotube axis

Water also structures along the z direction (Fig. 5.11) due to a "periodically rough" internal surface. Indeed, imogolite nanotubes present a long-range periodic order along the nanotube axis, whose period is equal to T = 8.45 Å. Hence, the internal surface of imogolites is periodically divided into furrows between one silanol group and the other. It is in these furrows that water is preferentially adsorbed. Such periodic layering of water in z would not occur to the same degree with an amorphous tube – like MCM-41 – or a particularly smooth tube – like carbon nanotubes.

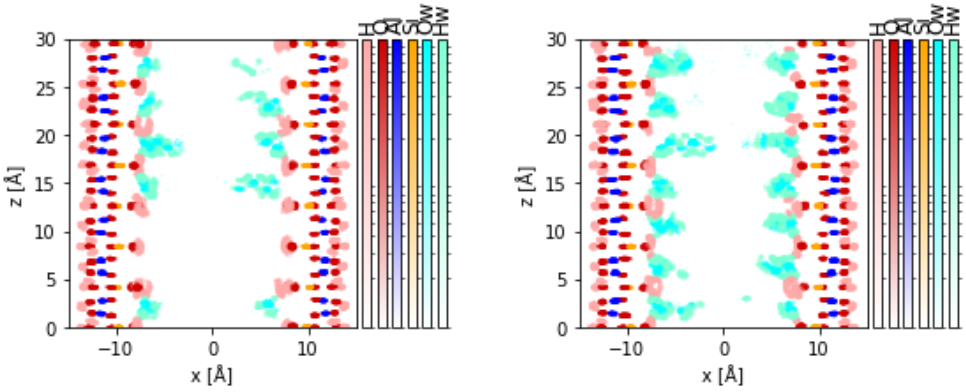

a) 3 wt% *b*) 6 wt%

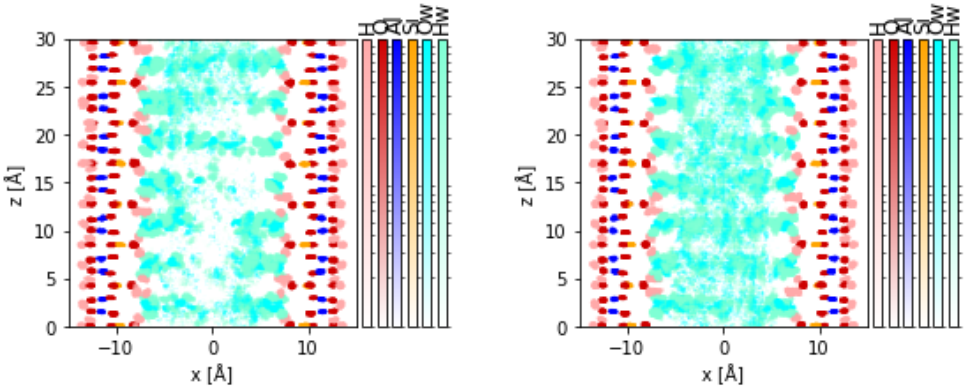

c) 12 wt% *d*) 15 wt%

Figure 5.11: Density maps along the z section of the nanotube (T=300 K) filled with 3wt% (*a*), 6wt% (*b*), 12wt% (*c*) and 15wt% (*d*) of water

Fig. 5.12 shows histograms obtained by summing the water oxygen O_w density of all the unit cells along z inside the same unit cell and by normalizing to the number of Si atoms. The red lines correspond to the average position of Si atoms.

These plots evidence that at low hydration – from 0wt% to 6wt%– water molecules tend to fill the furrows between the silanol groups, and avoid to overlap with the position of Si atoms, as there are no oxygens overlapping with the red lines.

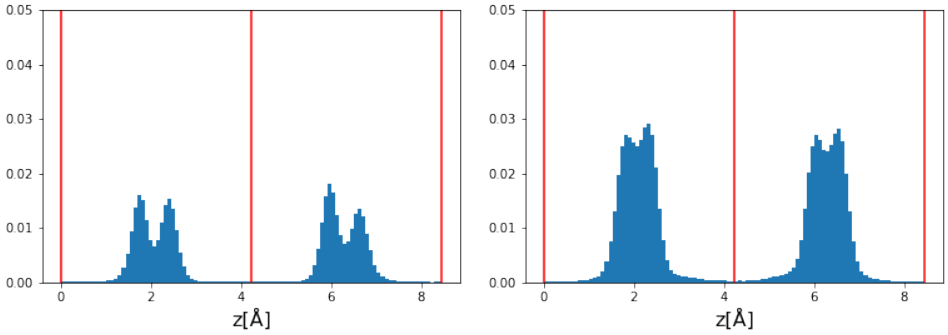

a) 3wt% *b*) 6wt%

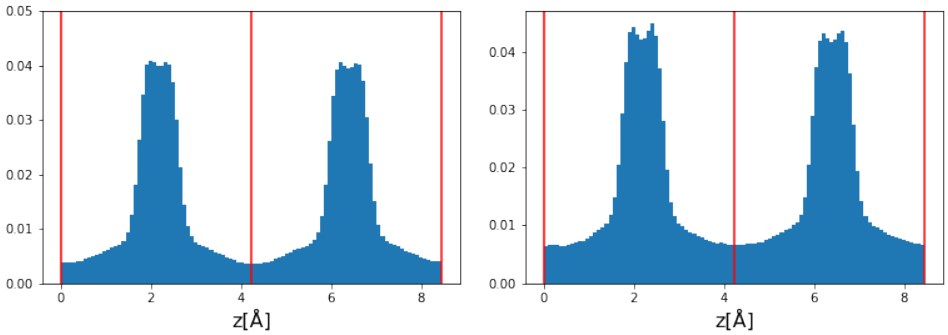

c) 12wt% *d*) 15wt%

Figure 5.12: Longitudinal distribution density profiles of O_w for 3wt% (*a*), 6wt% (*b*), 12wt% (*c*) and 15wt% (*d*) in blue, while the red lines correspond to the average Si atoms position

At 3wt%, a double-peak shape can be seen in the O_w density. Molecules of type 1 (Fig. 5.6) are responsible for this double peak, as it corresponds to the two orientations that they can have in the z direction, depending if they are adsorbed with the oxygen towards the positive side of the z axis or pointing towards the negative side of the axis. At 6wt%, the density profiles indicate that only the furrows are populated and the structuring remains partially in the second hydration layer. When the tube is filled with 12wt%, water molecules are also present in the central part of the nanotubes. They occupy all the positions available in z because the distance to the wall is sufficiently large to not induce periodic structuring of the molecules in the center of the nanotube. This contributes to the constant background of low intensity around the peaks in Fig. 5.12*c*. This fraction of molecules at the center continues to rise with increasing the water content up to 15wt%, while the structured fraction of water molecules close to the walls has reached an equilibrium and is saturated at 0.04 in intensity.

Similar longitudinal density profiles were reported by Konduri et al. in 2008 for Si-INTs with N = 12 and by using the CLAYFF potential[205]. The authors proposed that the structure of water along the axial direction is induced by the water-nanotube interactions due to the periodic silanol groups. Our MD results confirm that the unique structure of the inner surface of Si-INTs drives the water organization for low water content but also influences the orientation of the molecules within these adsorption sites.

5.2.2.1 Evidence of periodic water structuring by means of X-ray scattering

Despite being already proposed previously by simulations, this periodic structuring in z was never proved experimentally. It was therefore investigated in this work by X-ray diffraction.

As described in section 2.5.1, since nanotubes assemble in bundles, the XRD diagram consists in the product between the form factor of a single nanotube and the structure factor of the bundle, the latter involving peaks at the (hk) positions of the reciprocal 2D lattice.Their exact position and width depend on the number of tubes in every bundle[200]. The first reflection, the (10) peak, appears at $Q = 0.27$ Å^{-1} for a bundle of Si-INTs. Moreover – as mentioned in section 2.5.1.2 – the diffraction by a powder of nanotubes of period T along their z axis gives peaks at $Q = (0, 0, l\frac{2\pi}{T})$ positions, where l is an even integer. These peaks are smoothed and asymmetric due to the finite length of the nanotubes. The first asymmetric peak corresponds to the (002) and is located at around 1.5 Å^{-1}.

Interestingly, water structuring has a strong effect on the intensity of the (002) reflection that has not been previously highlighted to the best of our knowledge. The simulated diffraction pattern in the Q-range between 1 and 2 Å^{-1} is in Fig. 5.13*a*. Here the (002) is intense for the dry nanotube and progressively disappears as the water content increases.

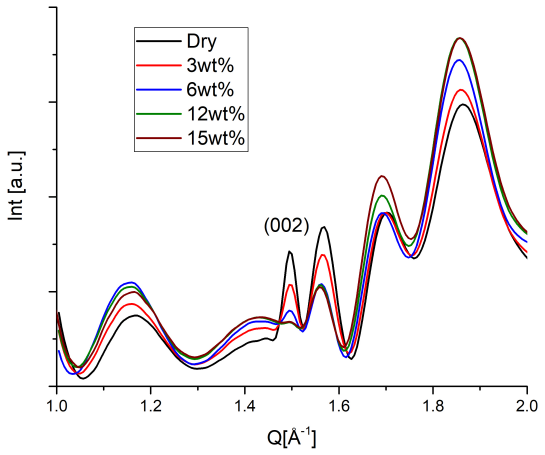

a)

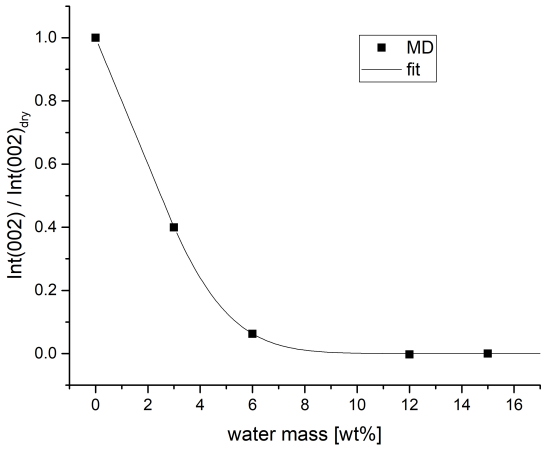

b)

Figure 5.13: *a*) Zoom of the diffraction pattern in the Q-range between 1 and 2 Å^{-1} and evolution of the (002), according to MD simulations, with growing water filling and *b*) its integrated intensity evolution as a function of the filling.

The (002) is a reflection that uniquely depends on the periodicity of the nanotube along z at an atomic level. If the water distribution inside the nanotube cavity is homogeneous in z, the (002) intensity is not supposed to change. On the contrary, if water structures in z, its intensity should be modified. Therefore, the (002) characterizes the portion of water adsorbed directly into the inner wall of the tube, and it cannot contain any information about the water molecules being unstructured in the central cylinder of the pore.

The integration of the (002) allows us to propose a quantitative link between the intensity of this reflection and the water content in the nanotubes. This is done as follows: as the last curve — 15wt% – corresponds to the maximum water filling, we assume that the structured water is at its maximum and the (002) cannot decrease further. Therefore, the last curve corresponds to the state of water confinement at saturation and can be subtracted from all the other curves. Then, the remaining intensity is integrated between 1.45 and 1.62 Å^{-1}, which corresponds to the part of the diffractogram that varies with structured water filling. The resulting intensity drop for the simulated data is shown in Fig. 5.13*b*, whose evolution has been fitted with an exponential curve. This demonstrates that the first hydration layer is complete for a filling of $\sim$ 7wt% in mass, for which the intensity of the (002) peak is completely suppressed

without any further evolution.

A set of data was collected in order to measure experimentally this effect. It consists of in-situ measurements, *i.e.* collected as a function of the water pressure inside the humidity cell described in Section 2.5.3. Here, the diffraction pattern of a powder sample is measured as the water pressure is increased externally. The related experimental curves are shown in Fig. 5.14*a* with an emphasis on the region between 1 and 2 $Å^{-1}$.

The curves are presented as a function of pressure, from which one can deduce a Relative Humidity. Experimental curves show that, as the water pressure increases, the (002) decreases gradually. In order to quantify the amount of water adsorbed onto the tube wall, the same data treatment done to simulations was applied to experimental data. The 12 mbar data-point was considered at saturation since the difference between 9 mbar and 12 mbar is very limited. This curve was subtracted from the others, and the remaining intensity was integrated between 1.45 and 1.62 $Å^{-1}$. Then, the experimental intensity drop was reported in Fig. 5.13*b* in order to extract the water mass. This is shown in Fig. 5.14*b*[1].

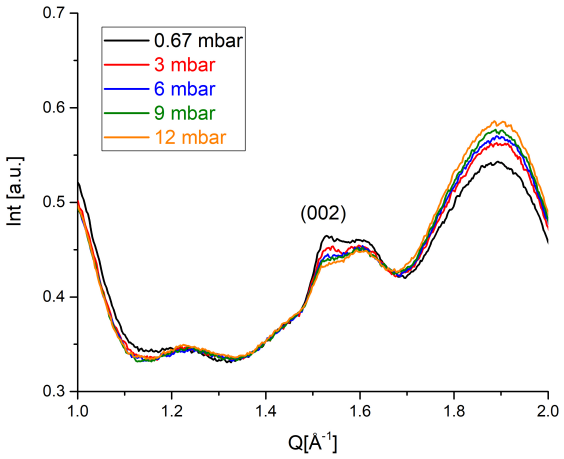

a)

[1]As a simple integration does not give an error bar, errors are assigned by extracting the masses with two other methods – fitting the area with two or three Gaussians – and by calculating the standard deviation of the values obtained with the three methods. One can clearly see how the error that one does in placing the "reference" point (in orange) is quite large as above 6wt% the reference curve is basically flat and the point could be placed anywhere in that flat section.

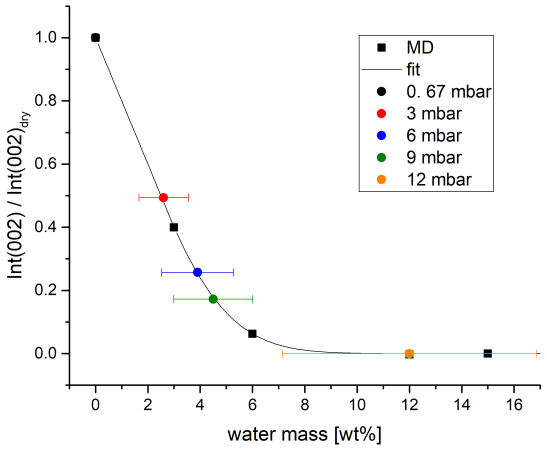

b)

Figure 5.14: In-situ experiments during the hydration of Si-INTs in the CHC setup. *a*) Zoom of the diffraction pattern in the Q-range between 1 and 2 $Å^{-1}$, for the evolution of the (002); *b*) Evolution of the integrated intensity of the (002) peak as a function of the water mass. The colored points correspond to the experimental (CHC) integrated intensity, in the same color scheme. Symbols in black correspond to the values obtained from MD simulation in Fig. 5.13.

With this method, we obtain the water masses that have been reported in Table 5.4.

P [mbar]	*RH*	structured mass	total mass predicted by isotherms
0.67	0%	0 wt%	0 wt%
3	10%	2.6 ± 0.9 wt%	14 wt%
6	20%	3.9 ± 1.37 wt%	15 wt%
9	30%	4.5 ± 1.5 wt%	16 wt%
12	40%	(reference)	17.5 wt%

Table 5.4: *RH* associated to the measured pressures and structured water mass calculated with the plot in fig 5.14*b*.

The Table shows that masses of structured water calculated with this method may seem to disagree with the water adsorption isotherm in Fig. 5.1. Indeed, considering the total mass predicted by the isotherm and assuming that water first fills the inner core of the nanotube – since the

internal surface of the nanotube is supposed to be more hydrophilic than the outer one[78,202] – we would expect all the curves of Fig. 5.14 to show a (002) at saturation. In other words, the four RH values equivalent to the imposed pressures should not give a significant variation around the (002) reflection. Nevertheless, a gradual decrease is observed. This can lead to two possible explanations. A first scenario, assuming that water first enters inside the nanotube, leads to water contents smaller than what is predicted from the isotherm. The second scenario, taking the water content deduced from the isotherm, implies that part of the water molecules are adsorbed around the tubes.

The two scenarios will be now discussed by using the information contained in the (10) reflection.

5.2.2.2 The total amount of water in nanotube bundles

Before going to the two scenarios, we will first present the evolution of the (10) peak as a function of the water contents by means of MD simulations for the four hydration states studied.

Fig. 5.15*a* displays X-ray scattering pattern of a powder of isolated nanotubes, calculated at different water filling contents. We evidence a decrease of the first oscillation related to the form factor of the nanotubes with increasing the water filling. When nanotubes are arranged in bundles with a 2D hexagonal lattice, the product between form factor and structure factor causes the peak (10) to decrease (fig 5.15*b*), making this reflection an evidence of the increasing water content inside the tube. The reduction of the (10) was already evidenced for Si-INTs by Kang et al, and more generally, the same effect was observed for carbon nanotubes as well[136,140,142,152,153].

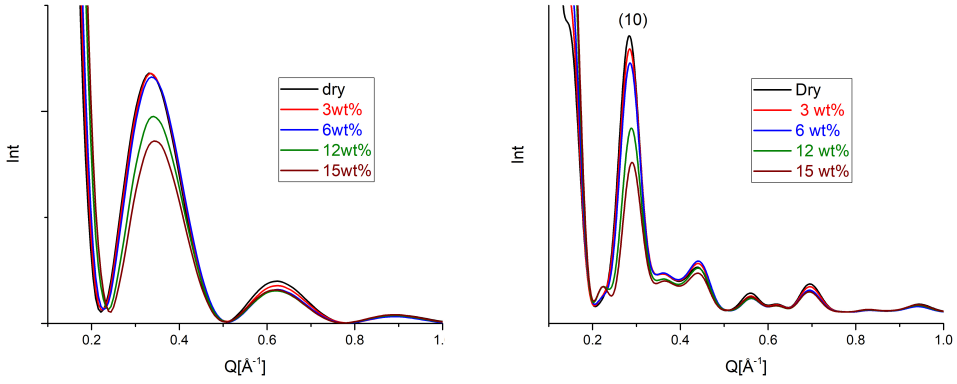

a) *b)*

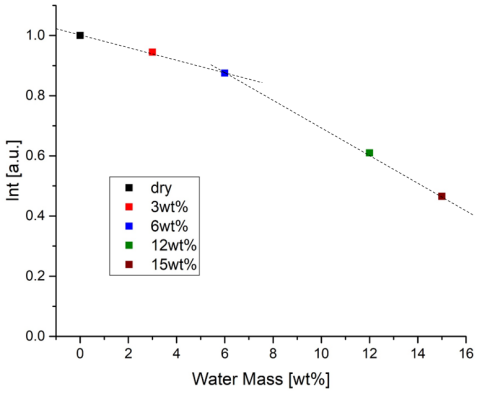

c)

Figure 5.15: *a*) Evolution of the simulated X-ray scattering diagram of a powder of *a*) isolated nanotubes and *b*) bundled nanotubes with 13 tubes per bundle (2D hexagonal arrangement, $a = 27$ Å); in *c*), integrated intensity of the (10) peak in *b*.

Fig. 5.15*c* shows the (10) integrated area between 0.23 $Å^{-1}$ and 0.33 $Å^{-1}$. The figure highlights that the decrease is small and approximately linear as long as the nanotube is hydrated with only a layer of water (between 0 and around 6wt%, as shown by Fig. 5.4*a* and 5.4*b*). Above 12wt%, the curve departs from linearity. This can be easily explained considering from 6wt% to 12wt% the second layer and the central pore are populated, so that the form factor of water goes from being that of a hollow cylinder to that of a full cylinder (as shown in figs. 5.4*b* and 5.4*c*). This conclusion departs from what Kang et al.[252] stated, who found a single linear behavior in the whole mass range. This disagreement can possibly be explained by the use of a different potential (simple CLAYFF instead of the extended CLAYFF force field).

In literature, the experimental intensity of the (10) peak has been widely used to calculate the water mass adsorbed in a tube. Nevertheless, in the following section we will show how the same (10) evolution – measured in the CHC – can be reproduced by several different sets of configurations, making this peak not fully reliable when doing this kind of calculation. The experimental curve up to 1 $Å^{-1}$ is in Fig. 5.16.

To reproduce the curves, we employed the homogeneous approximation, as simulating a bundle in MD is quite computationally expensive. On the other hand, the (10) peak is located in a low Q region, where the nanotube can be approximated as an homogeneous cylinder with internal and external radii R_i and R_e.

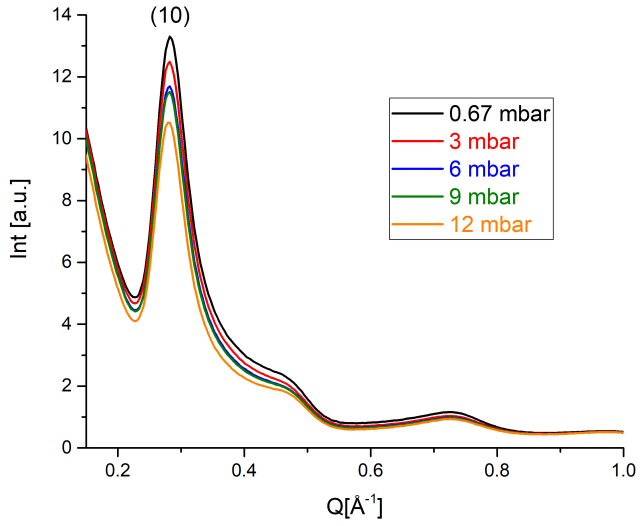

Figure 5.16: CHC data: Zoom of the diffraction pattern between 0 and 1 $Å^{-1}$ and evolution of the (10) with growing water filling

Tubes and water molecules were therefore modeled by homogeneous cylindrical layers whose diffraction pattern can be described by an analytical formula as explained in section 2.5.1.1.

In order to use the homogeneous approximation, the main parameter that we have to choose is the internal and external radii of the tube R_i and R_e, as it defines the minima of the form factor. The values of R_i and R_e were calculated starting from the MD tube (considering both N=13 and 14), by following this procedure:

- the experimental form factor of an isolated tube — measured by X-ray diffraction on a Si-INT liquid suspension, where tubes are isolated — was plotted together (Fig. 5.17*a*) with the form factor of a MD tube with N=13. The values of $R_{i,e}$ were extracted by finding the values that allowed to have the same minima as in MD. This is shown by the blue curve in the plot, obtained by an homogeneous cylinder of R_i =7.7 Å and R_e=12.7 Å.

- The same was done for N = 14, as in Fig. 5.17*b*, obtaining R_e=8.4 Å and R_e=13.4 Å.

- Since the experimental curve seems to be exactly between the two simulated N = 13 and N = 14, an artificial N = 13.5 tube was taken into account, having R_i=8.05 Å and R_e=13.05 Å. This is shown

in Fig. 5.17*c*. This seems to reproduce well the diffractogram suspension, and it also goes in the same direction of what was mentioned in Section 4.1.3, where the diffractogram of the bundle was better reproduced by an average between N = 13 and N = 14.

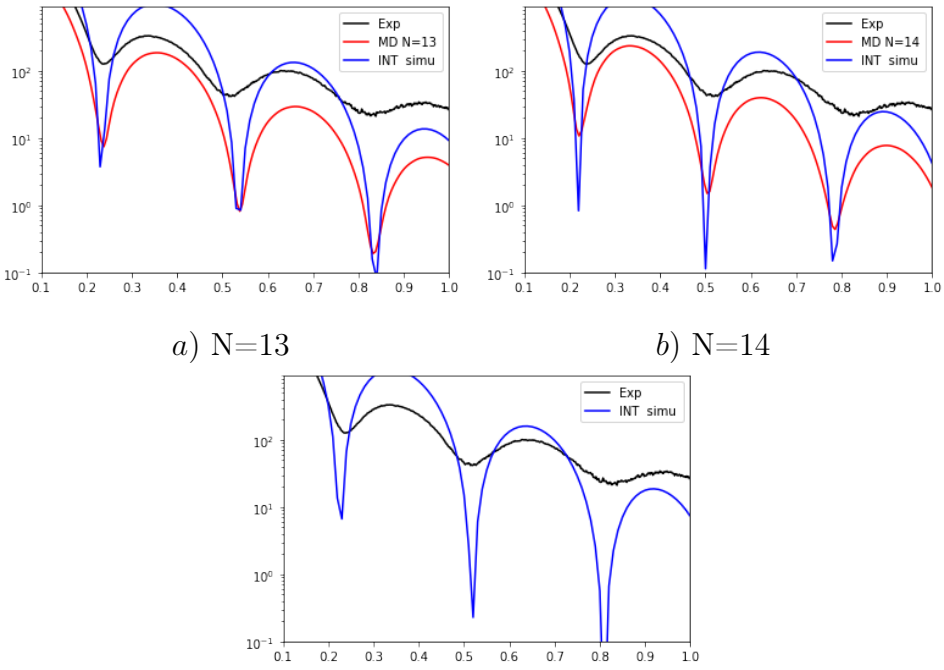

a) N=13 *b*) N=14

c) N=13.5

Figure 5.17: *a*) Comparison between experimental data obtained on a suspension of Si-INTs (black), the simulated curve on a tube having N = 13 using MD (red) and the calculated curve within the homogeneous approximation (blue) by using the same internal and external radii as the MD simulation. Same in *b*), but for a tube having N = 14. In *c*), the blue curve is obtained with the homogeneous approximation, with internal and external radii corresponding to N = 13.5

Once the radius of the tube found, the structure of water was modeled. In order to explore all the adsorption possibilities — tube hydrated with a single monolayer, tube fully hydrated, tube with an external layer of water — water was divided in three possible layers: a first internal adsorption layer, an internal cylinder and an external layer, having the dimensions presented in Table 5.5.

Layer	R_{in} [Å]	R_{ext} [Å]
Nanotube	8.05	13.05
first internal layer	5.55	7.55
internal cylinder	0	7.55
external layer	13.55	15.59

Table 5.5: Values of the internal and external radii for all the layers considered in the homogeneous approximation[2].

The good value for the water mass inside the different layers was found by taking as a reference the electronic density of bulk water, equal to $\rho_{water} = 0.334$ e$^-$.Å^{-3}, and by multiplying it by a scaling factor.

A bundle of 19 tubes was built, with hexagonal arrangement and lattice parameter $a = b$ =27 Å. The final result can be seen in figs. 5.18 and 5.19. The two scenarios proposed at the end of the previous Section were explored by two sets of configurations. The first one privileges the adsorption of water inside the tube, but disregards the mass predicted by the isotherm. The second set privileges the total mass to be close to the isotherm one, but allows a big quantity of water to be adsorbed on the external surface of the tubes.

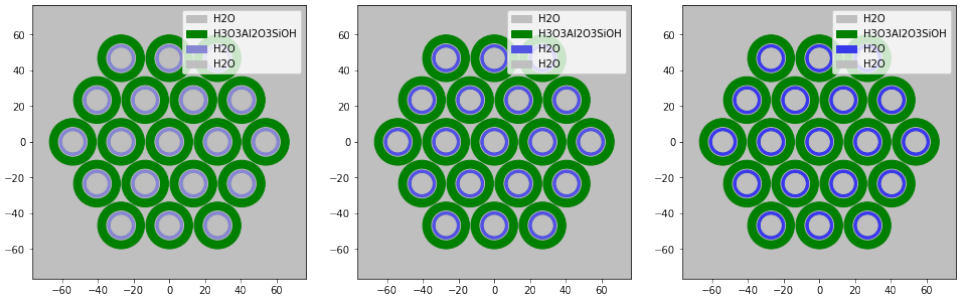

a) 3 mbar *b*) 6 mbar *c*) 9 mbar

Figure 5.18: 1st scenario of simulations: water adsorbed only in a single internal adsorption layer

[2]The value of 15.59 for R_{ext} of the external water comes from the maximum value possible in order to follow the formalism in Paineau et al.[200]

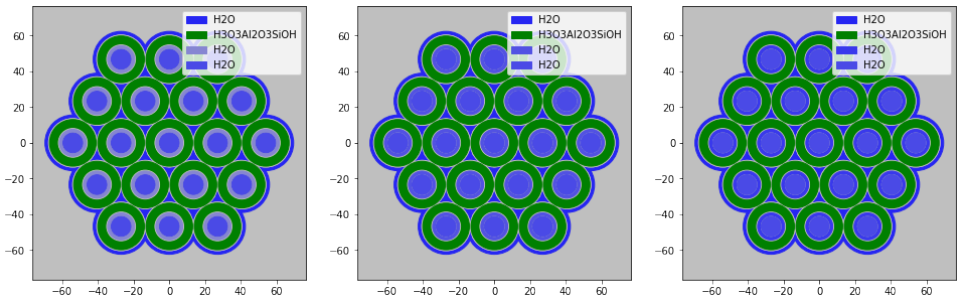

a) 3 mbar *b*) 6 mbar *c*) 9 mbar

Figure 5.19: 2nd scenario of simulations: water populating the three possible layers of water: internal first layer, internal cylinder and external layer

These two sets of structures, were shown to produce equivalent diffraction patterns (Fig. 5.20*b* and *c*), both reproducing the (10) evolution of the data collected in the CHC of Fig. 5.16. The confinement of water inside the nanotubes induces a decrease of the (10) peak while the reverse occurs if water is located outside. In the case of the second set, the contribution of water in the internal cylinder and in the external layer balances themselves, leading to the same evolution of the scattering intensity as for set one (illustrated in Fig. 5.20*a*).

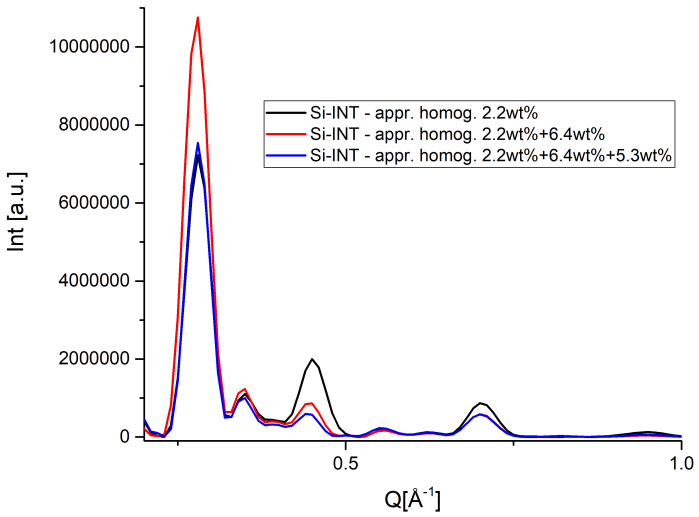

a)

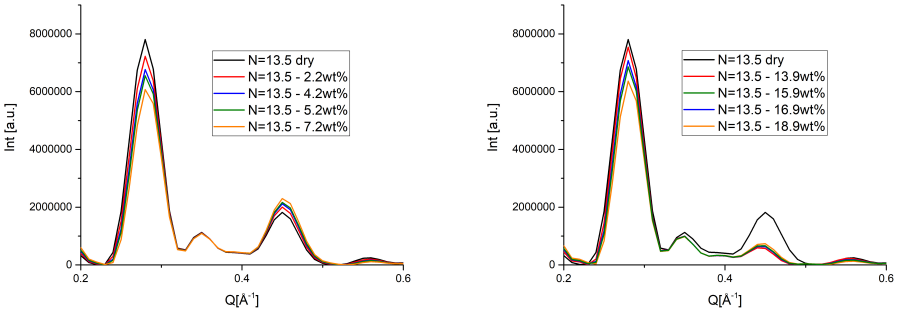

b) *c*)

Figure 5.20: In *a*, the effect of adding an external layer of water on the (10). In particular 2.2wt% is in the first layer, 6.4wt% in the inner cylinder and 5.3wt% outside the pore. 1st (*b*) 2nd (*c*) scenario of simulation of the (10) evolution in homogeneous approximation

Nevertheless, the total mass content in the two sets strongly differs. Tables 5.6 and 5.7 contains the water masses put in the three layers, together with the total mass, as a function of the experimental curve that is reproduced with that combination of masses.

Pressure [mbar]	$m_{first\ layer}$	$m_{inner\ cylinder}$	$m_{external}$	m_{total}
0	0 wt%	0 wt%	0 wt%	0 wt%
3	2.2 wt%	0 wt%	0 wt%	2.2 wt%
6	4.2 wt%	0 wt%	0 wt%	4.2 wt%
9	5.2 wt%	0 wt%	0 wt%	5.2 wt%
12	7.2 wt%	0 wt%	0 wt%	7.2 wt%

Table 5.6: Mass distribution for the first scenario

Pressure [mbar]	$m_{first\ layer}$	$m_{inner\ cylinder}$	$m_{external}$	m_{total}
0	0 wt%	0 wt%	0 wt%	0 wt%
3	2.2 wt%	5.3 wt%	6.4 wt%	13.9 wt%
6	4.2 wt%	5.3 wt%	6.4 wt%	15.9 wt%
9	5.2 wt%	5.3 wt%	6.4 wt%	16.9 wt%
12	7.2 wt%	5.3 wt%	6.4 wt%	18.9 wt%

Table 5.7: Mass distribution for the second scenario

One should also notice that the oscillation around 0.45 $Å^{-1}$ is strongly diminished in the scenario 2, hinting that the presence of water at the exterior of the tube can be inferred from the intensity of that peak, compared to the dry sample.

In summary, these results evidence how the information enclosed in the (10) is not univocal, and the present data do not allow us to conclude on the most probable scenario. Nevertheless, a few considerations can be done.

The second scenario agrees with what we know about adsorption isotherms, but assumes that an important portion of water goes outside of the tubes when hydrating a sample. On the other hand, the first scenario only needs an internal layer of water to have a coherent value of water intake between the information given by the (10) and the (002). The first scenario also goes in the direction of a tube more hydrophilic in the internal cavity than in the outside, as suggested in literature. To explain the discrepancy with the isotherm, one could suggest that in the CHC, the *RH* inside the sample capillary was lower than the measured *RH* in the rest of the cell, so that the water uptake was lower than expected. Moreover, the first scenario would go in the same direction of the issue encountered with the preparation of samples (section 5.1), where a lower mass of water was found to be adsorbed compared to what expected from the isotherm – mass confirmed by D16 data. In that case, both the atmosphere in the CHC and in the desiccator was different to what measured in the isotherm, even though it is not clear why. The additional data from D16 may argue in favour of scenario 1 but it is not sufficient to completely rule out the second scenario.

The experimental sections that will follow will include neutron data collected on the two samples prepared with a saturated salt solution, having mass of 6wt% and 12wt%, complemented by MD simulations. MD simulations are carried out considering that water is only inside the tube, *i.e.* in scenario 1.

5.3 Water diffusion inside imogolite nanotubes

Diffusion was first characterized by means of MD simulations. Calculations for the four simulated hydration states – 3wt%, 6wt%, 12wt% and 15wt% — were run at 50 and 300 K. The 50 K trajectory will be mainly used to simulate the inelastic region, as the density of states is better investigated at low temperature where only vibrational motions take place. On the contrary, the 300 K trajectory will be employed to

investigate the quasielastic, where diffusion occurs.

As shown in Chapter 2 in Eq. 2.34, an elastic quantity that can be extracted is the $EISF(Q)$ of water hydrogens as a function of the water content (Fig. 5.21). At 300 K, it can illustrate the geometry of water diffusion.

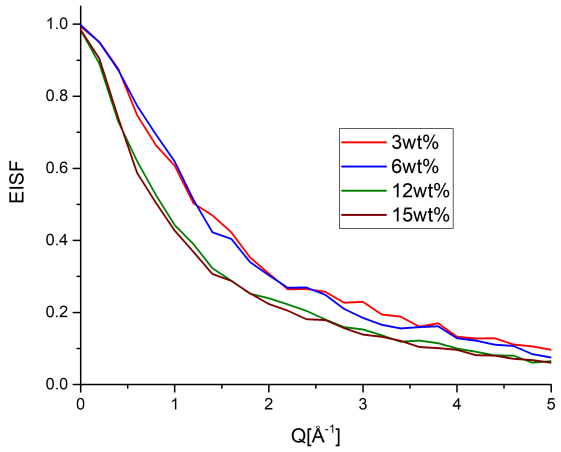

Figure 5.21: Calculated $EISF(Q)$ of all the water hydrogens at 300 K, at different hydration levels. The trajectory employed is the one 100 ps long.

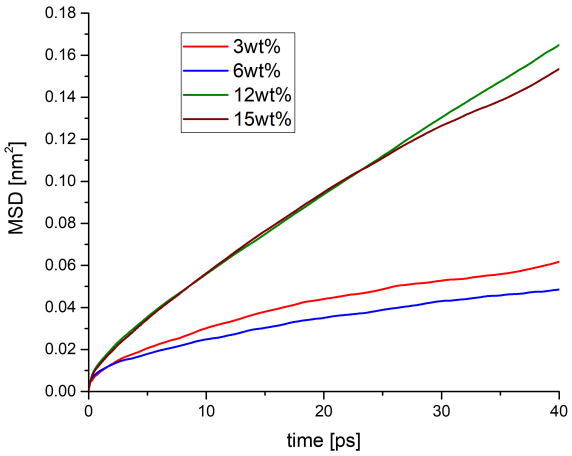

Figure 5.22: Simulated MSD for all the water hydrogens at 300 K, at different hydration levels

The plot evidences that both 3wt% and 6wt% states present the same geometry. A similar conclusion can be drawn for samples with 12wt% and 15wt% water filling. This is not particularly surprising, as the first two display monolayer water configuration, while the two others allow water molecules to access the central cylinder and therefore larger spaces.

When investigating diffusion, the MSD – as defined in Eq. 3.18 but without integrating in time – is a meaningful quantity to look at. The simulated MSD for water hydrogens at different water hydration levels is represented in Fig. 5.22, as a function of time. Like for the $EISF$, two separate groups are evidenced with on one side the 3 and 6wt% states and a second group with 12 and 15wt% samples. The diffusion is clearly enhanced in the 12wt% nanotube compared to 6wt%.

Knowing that only 6wt% and 12 wt% hydration levels have been explored experimentally, we will only focus on these two hydration levels in the following section.

Overall, the MSD can be fitted by a law of the type $MSD \propto t^{\alpha}$, typical of the subdiffusive regime, with $\alpha = 0.65$ for 6wt% and $\alpha = 0.8$ for 12wt%. This is not surprising as imogolite nanotubes are hydrophilic, as mentioned in section 1.4.2[3]. From an energetic point of view, each triangular adsorption site acts like an attractive potential wall that traps a water molecule for long timescales.

5.3.1 Dynamics of confined water molecules: slow vs. fast water diffusion

The restrained diffusion of molecules attached to the wall can be seen easily by projecting in the z direction the trajectories of water molecules, as shown in Fig. 5.23 for three selected water oxygens. Fig. 5.23*a* shows the Si-INT hydrated at 6wt% of water: all water molecules are attached to the surface due to the attractive interactions with the hydroxyls of the wall, which prevent water molecules to diffuse freely along z. Jumps from one furrow to the other in the z direction are possible, but seem to be rare.

On the other hand, with 12wt% (Fig. 5.23*b*) of water in the nanotube, there is also inhomogeneity in water populations: molecules attached to the surface diffuse very little (trace in green in Fig. 5.23*b*), while those at the center of the pore are able to diffuse quickly in the longitudinal direction (dark blue trace in Fig. 5.23*b*).

[3]Actually, also in carbon nanotubes, for D<1.5nm the behavior is subdiffusive (α<1) due to confinement effects[147]. Ballistic diffusion near the surface of the CNT is expected only for larger diameters (2.4 nm <D < 4 nm).

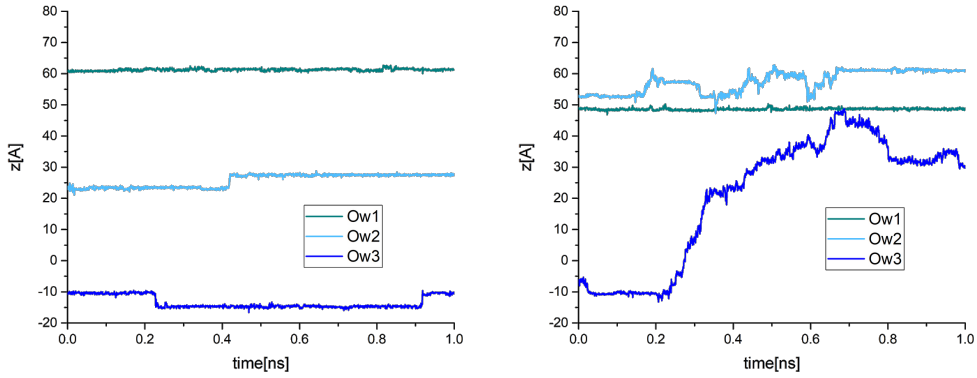

a) *b)*

Figure 5.23: z projection of the trajectory as a function of time of (a) three oxygens of a Si-INT filled at 6wt% and (b) three water oxygens of different kind (slow in green, intermediate in light blue, fast in blue) for a Si-INT filled at 12wt%

Therefore, from a dynamical point of view, we can attempt to replace the classification in the first and second layers as well as in the center of the inner cavity of the nanotube that was done previously in Section 5.2, with a classification based on dynamic of confined water molecules:

- **slow water**: water molecules stuck inside a potential well on the tube wall. This constitutes the totality of water molecules when the hydration level is low — up to $\sim$ 7wt%.
- **fast water**: water molecules that manage to access the central area of the pore and to diffuse quickly and long range in the longitudinal direction. This is possible only if the hydration level exceeds a certain threshold (at least above $\sim$ 7 wt%). For example the tube with 12wt% of water has a set of molecules that are attached to the surface and remain trapped during the whole simulations, and others that diffuse more.

Due to its potential for long range diffusion, special interest will be dedicated to the 12wt% state. In order to better understand the dynamical results given by the simulations at this hydration level, two subsets of water hydrogens were selected: ten "slow" hydrogens, that belong to the first hydration layer and that during the whole simulation are bonded to the surface, and ten "fast" hydrogens, that are observed diffusing long range along the tube axis. Fig. 5.24 represents the trajectory of the ten slow and fast atoms as a blue cloud over time, both in the (x, y) and z

directions. Fig. 5.24e and 5.24f also display the separate trajectories of single fast atoms (which are part of the 10 chosen), to highlight that the main direction of diffusion occurs along z.

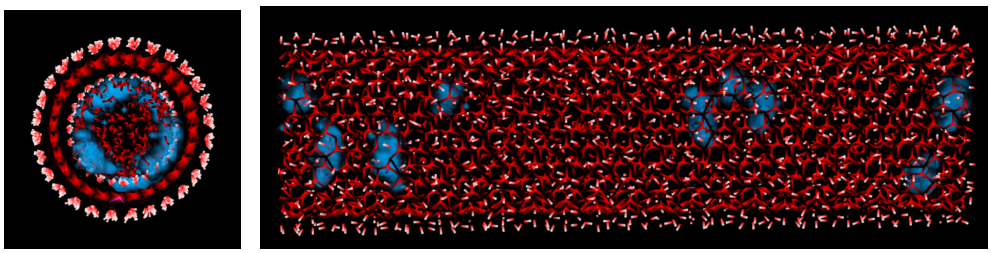

a) b)

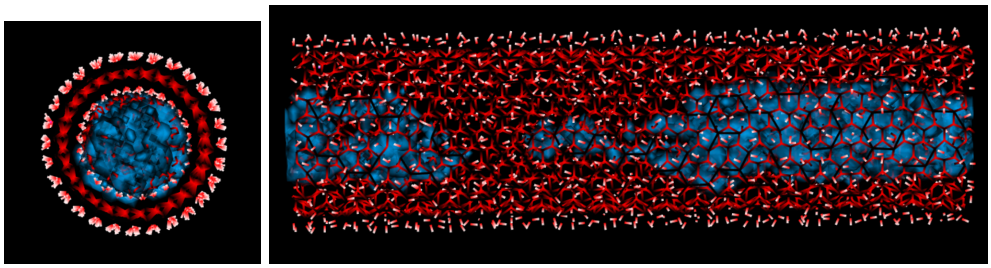

c) d)

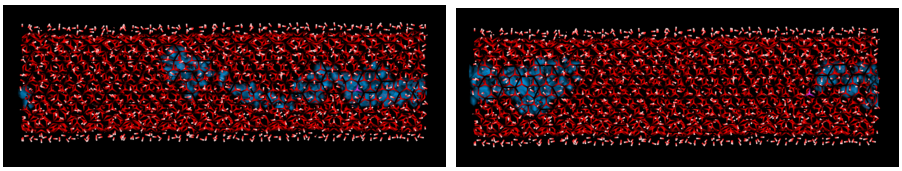

e) f)

Figure 5.24: a) (x, y) and b) z projection of the cloud trajectory (in blue) of the 10 slow atoms. c) (x, y) and d) z projection of the cloud trajectory of the 10 fast atoms. e) and f) show the trajectories of two specific fast atoms of the 10 selected.

These cloud maps suggest that the first type of molecules remains always in contact with the tube wall with a limited diffusion. Diffusion only takes place on the tube wall, *i.e.* in the (x, y) plane. By contrast, the second type of water molecules explores the entire pore of the tube, and while being in the central part of it, diffuses over long-distance along the longitudinal axis.

Their strong dynamical differences can be evidenced easily by plotting their MSD as a function of time (Fig. 5.25).

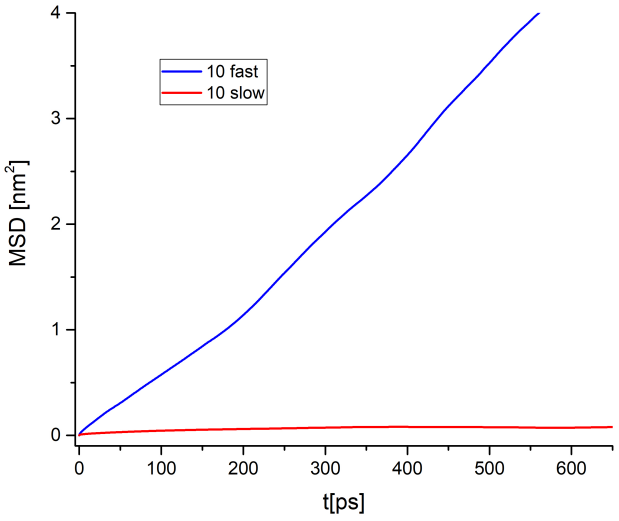

Figure 5.25: MSD of 10 slow and 10 fast water hydrogens as a function of time

While the MSD of slow atoms is – as expected – extremely weak (blue trace in Fig. 5.25), the one related to the 10 fast atoms increases linearly with a much larger slope. This suggests that fast water molecules follow a Fickian-like diffusion along the tube (following the Einstein law, $MSD \sim 2Dt$ for a 1D diffusion). As the diffusion is predominantly along z, the slope of the MSD was fitted with a line[4] and divided by 2, determining a diffusion coefficient which appears to be equal to $(3.2 \pm 0.1) \cdot 10^{-5} cm^2 s^{-1}$ – which is slightly larger than the diffusion coefficient of bulk water in SPC/E, equal to $2.9 \cdot 10^{-5} cm^2 s^{-1}$ [241,269]. This division into populations – of which one is slower than the other – is not new: also in carbon nanotubes having a diameter between 2.4 and 4 nm, ballistic diffusion is expected only near the surface, while water at the centre of the pore has Fickian-like diffusion [147]. Obviously, being the surface hydrophobic in that case, the faster component is the one closer to the wall, as opposed to imogolites, where closer water slows down.

More dynamical quantities for these subsets of atoms will be presented later on in this chapter in order to better interpret the experimental data.

[4]The slope varies according to where one fits the curve. The fit was repeated by taking different time ranges, the average was considered and the errorbar was taken as the standard deviation.

5.3.2 Diffusional behavior sampled by neutron scattering experiments

5.3.2.1 Evolution of the elastic scattering using the IN13 backscattering spectrometer

We first performed an elastic scan in order to determine at what temperature the hydrated samples depart from the dry. This should allow us to discriminate in broad terms the dynamics of the three samples. Elastic scans were carried out on IN13 on heating, and present a change of slope around 200 K (Fig. 5.26) for the two hydrated samples, showing the onset of anharmonic dynamics. The slope above 200 K is slightly larger for the sample hydrated with 12wt% of water, than the one with 6wt% of water.

The lack of a sharp drop in intensity at 273 K confirms that water is nanoconfined inside the tubes, therefore excluding the presence of bulk water outside the pore – that by contrast would exhibit a structural phase transition at the temperature of melting of ice.

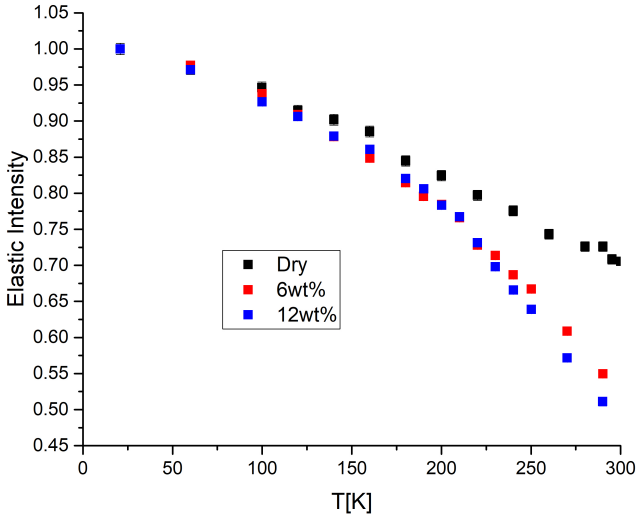

Figure 5.26: Elastic intensity measured in IN13 for the dry, 6wt% and 12wt% sample, in the temperature range between 20 and 300 K

Diffusion was then studied experimentally on IN6-SHARP, at the temperatures where diffusion is expected from IN13 data – *i.e.* above 200 K.

5.3.2.2 Quantitative characterization of confined water: diffusion coefficient

The sample hydrated with 12wt% of water was studied at the IN6-SHARP spectrometer at T=200 K, 250 K and 300 K. Fig. 5.27 shows the S(ω) curve for the three temperatures and the corresponding susceptibilities (defined as in Eq. 2.32), also compared to the susceptibility of the dry sample at 300 K. The susceptibility plot evidences at 200 K and 250 K the coexistence of vibrational motions and diffusive behavior, as a vibrational peak is present at -7 meV (that will be interpreted in section 5.4), as well a small $QENS$ broadening around the elastic peak. At 300 K, the diffusive $QENS$ component is dominating.

The same $QENS$ was measured and analysed by LeCaer et al.[204]. They did not report the measurement on a reference dry sample, but stated that the fast component appearing in the $QENS$ of all the hydrated samples is due to a fast rotation of the the hydroxyls of the tube. The plot in 5.27 evidences that the $QENS$ at 300 K, and especially the large component, cannot be due to the hydroxyls of the tube as stated by LeCaer. As shown in dark red, the $QENS$ associated to the dry tube at the same temperature is very narrow and weak. Moreover, the dynamics of the hydroxyls in presence of water is expected to slow down even more, as the activation of the dynamics evidenced in the previous chapter (section 4.2.2) cannot occur.

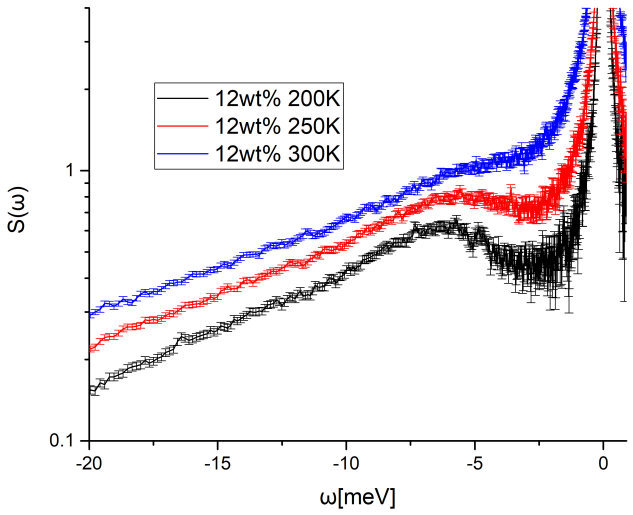

a)

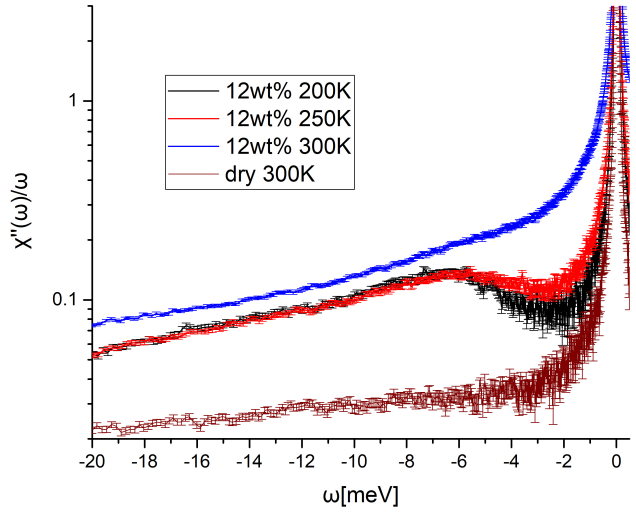

b)

Figure 5.27: *a*) S(ω) for the 12wt% state at T=200 K, 250 K and 300 K and *b*) their susceptibility divided by the exchanged energy. The susceptibility of the dry sample at 300 K is also shown as a comparison in dark red.

The curves of Fig. 5.27 were fitted in order to extract the parameters associated to their dynamics. The fit was done in the energy range $[-10, 1]$ meV, by including several components:

- a Delta function convoluted to the experimental resolution for the elastic peak, where the resolution curve is given by the sample at 2K.
- a flat background to account for low frequency density of states.
- a Damped Harmonic Oscillator for the peak at -7 meV, of the form

$$Int^{DHO} = \frac{A}{(c \cdot \omega)^2 + (\omega^2 - \omega_0^2)^2} \tag{5.2}$$

  to account for the non flat part of the density of states appearing around -7 meV.
- two Lorentzians depending on the temperature studied – only one at 200 K, two at 250 K and 300 K – for the $QENS$ broadening due to water diffusion.

The total fits and their components are reported in Fig. 5.28 while Table 5.8 contains the HWHMs of the two Lorentzians deduced from the fit.

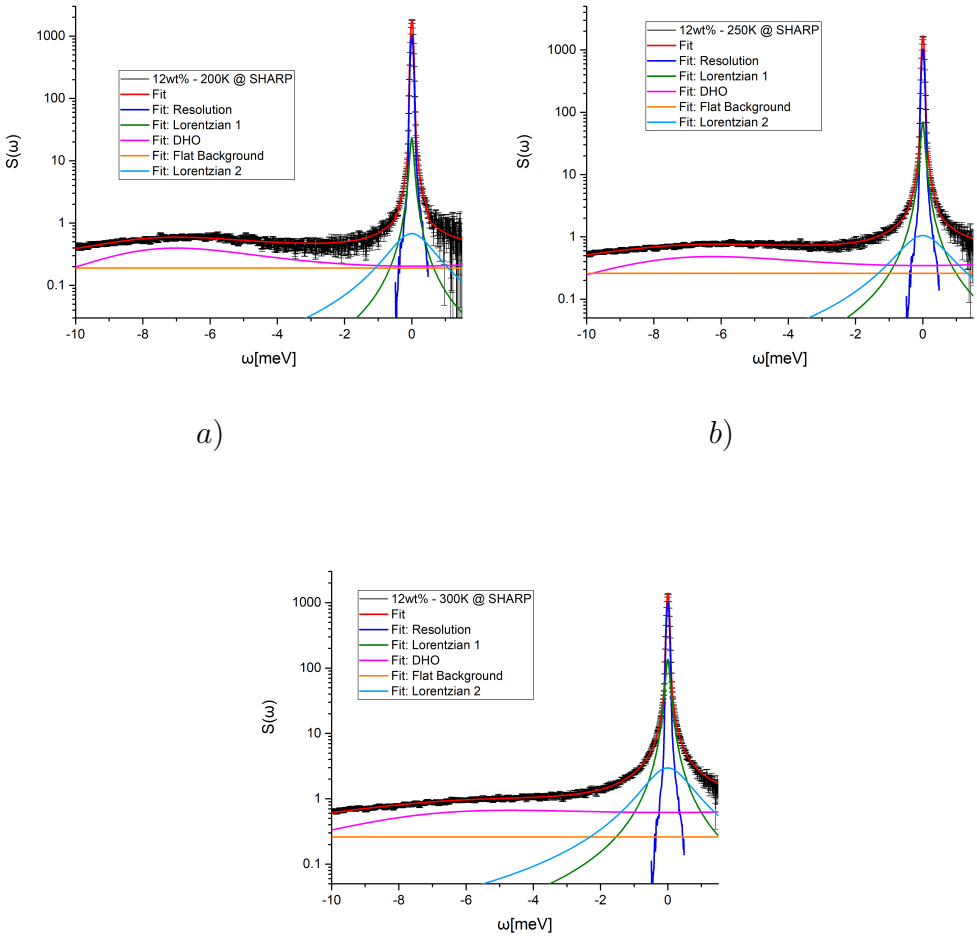

Figure 5.28: Fit components of the data collected in IN6-SHARP for the sample hydrated at 12wt% in mass, at *a*) T=200 K *b*) T=250 K *c*) T=300 K

-	$HWHM_1$ [meV]	Ampl. 1	$HWHM_2$ [meV]	Ampl. 2
200 K	0.059 ± 0.012	4.3 ± 0.6	0.67 ± 0.08	1.44 ± 0.1
250 K	0.060 ± 0.004	13.3 ± 0.6	0.75 ± 0.05	2.5 ± 0..1
300 K	0.067 ± 0.003	28.6 ± 0.6	0.68 ± 0.03	6.5 ± 0.2

Table 5.8: HWHM resulting from the fit on IN6-SHARP data

In summary, experimentally water diffusion is composed of two Lorentzians: a narrow component present at all the temperatures, and a large Lorentzian appearing at 250 K. The narrow component must be associated to some slow diffusion, while the large one to some fast diffusion. In order to correlate these two components to different diffusion mechanisms, the same analysis was made on MD simulations. For 12wt% and T=300 K, the simulated $QENS$ of all water molecules and hydroxyl groups in the presence of water is shown in Fig. 5.29. The calculation confirms how the broadening due to the tube is negligible compared to water.

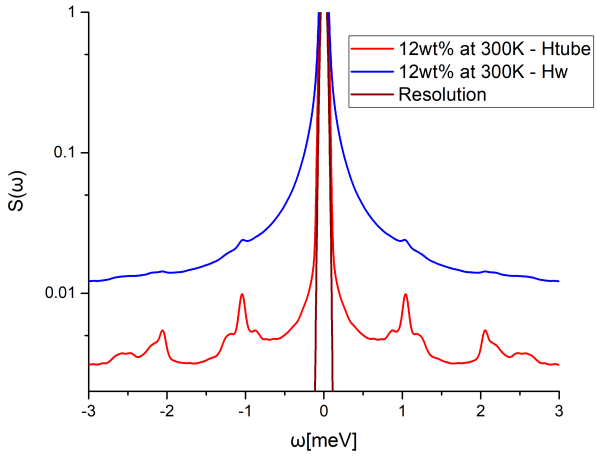

Figure 5.29: Comparison between the simulated $QENS$ for the water molecules of the 12wt% state (blue) with the tube $QENS$ (red) and the resolution (dark red).

A detailed analysis of the simulated $QENS$ was done by selecting the same 10 slow and 10 fast atoms as used previously in this chapter. Their $QENS$ was calculated separately – with an elastic resolution of FWHM=0.07 meV and in the Q range [0, 2] $Å^{-1}$ – and fitted similarly to experimental data (Fig. 5.30). The results of the fit are summarized in Table 5.9. For the slow atoms, the S(ω) can be fitted with a Gaussian, a constant background and a Lorentzian having $HWHM$=0.057 $\pm$ 0.001 meV. On the other hand, the fast atoms need a second broader Lorentzian to fit well the global shape, with a $HWHM_2$=0.88 $\pm$ 0.04 meV. One should also notice that the second type of molecules needs the presence of the first lorentzian as well, corresponding to their diffusion during the periods of time where they go close the wall and are adsorbed into it (indeed, there are no molecules only diffusing along the tube, they all are

adsorbed onto the wall at some point).

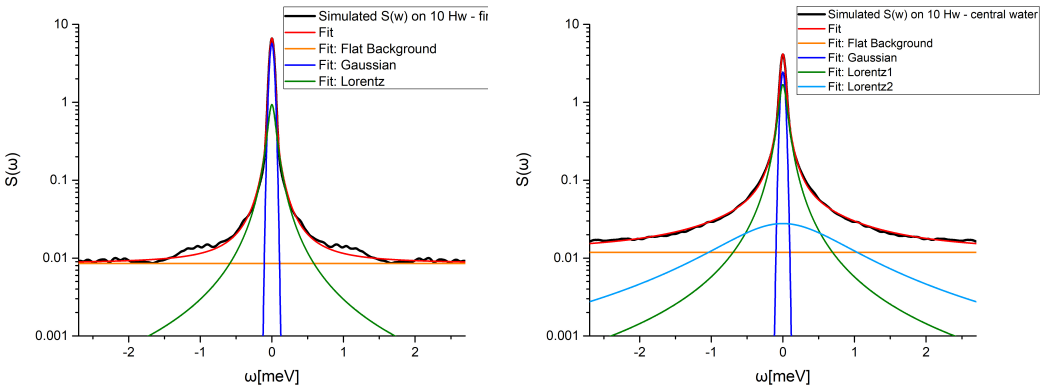

a) *a*)

Figure 5.30: Fit components of the simulated $QENS$ broadening obtained by selecting *a*) 10 slow atoms and *b*) 10 fast atoms

-	$HWHM_1$ [meV]	$HWHM_2$ [meV]
slow atoms	0.057 ± 0.001	-
fast atoms	0.080 ± 0.001	0.88 ± 0.04

Table 5.9: HWHM resulting from the fit on simulations at 300 K

Being these values close to the experimental ones, one can propose to associate the narrow Lorentzian with the diffusion of slow water molecules, *i.e.* those trapped close to the wall, while the broad Lorentzian with fast diffusion along z in the central cylinder of the tube, which occurs by jumps. LeCaer et al. showed the same experimental results but associated the broad Lorentzian to the fast rotation of the hydroxyls of the tube and the narrow one to water[204]. Nevertheless, MD simulations confirm that not only the $QENS$ of the hydroxyls is very weak and further slows down by water, but also that the fast component is actually the most interesting, being associated to long-range diffusion along the tube. We also believe, as opposed to these authors, that the sample where long range diffusion is facilitated the most is not the monolayer, but the 12wt% state where the tube is fully hydrated because long range diffusion can only take place in the very central pore. By contrast, the monolayer state is quite stable.

The $QENS$ Q-dependence was analysed at 300 K for both simulations and experimental data. Fig. 5.31*a* shows the simulated Q-dependence

of the $QENS$ for the 10 slow atoms (green symbols) and the 10 fast atoms, represented in black and red for their two components. The slow component is similar between the two populations of water and equal to $HWHM_1$=0.056 meV while the large component is typical of fast water only. The latter stabilizes at the highest Q values around $HWHM_2$=0.6 meV. For the fast component, unfortunately the fit was not achieved in the whole Q-range, being particularly difficult for the Q values below 1 $Å^{-1}$.

Experimentally, the Q-dependence analysis was done by performing a first sequential fit with free parameters, starting from the highest Q values – where the fit is stable –, to the lowest Q values – where the fit is more difficult. As the $HWHM_1$ showed a constant behavior but with some random oscillations, a second sequential fit was performed by fixing $HWHM_1$ equal to its average value, *i.e.* 0.07 meV. The resulting Q-dependence of the fast component is in Fig. 5.31*b*.

$HWHM_2$ shows an initial growing behavior, which then stabilizes around 0.7 meV. This tendency evidences that the second component is not confined, but on the contrary associated to fast long-range diffusion. A linear fit as a function of Q^2 at low Q allowed to calculated the experimental diffusion coefficient, which happens to be equal to $(2.6 \pm 0.3) \cdot 10^{-5} cm^2 s^{-1}$.

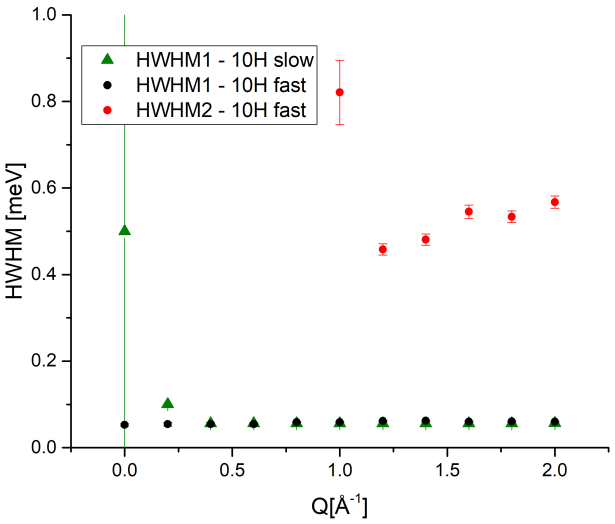

a)

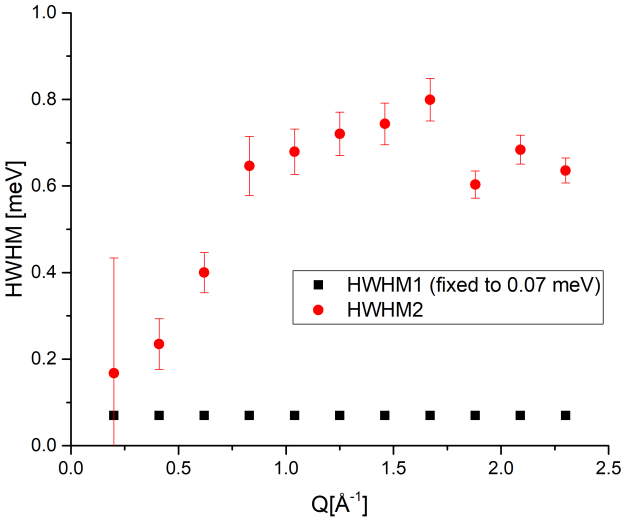

b)

Figure 5.31: *a*) Q-dependence for simulated data. The $QENS$ obtained from the 10 slow atoms can be fitted with only one component (in green), while the 10 fast atoms have two components, in black and red, where the narrow seems to be the same as for the 10 slow atoms. In *b*), the experimental Q dependence of the fit done on IN6-SHARP data[5].

The present diffusion coefficient can be compared to the diffusion coefficient of bulk water –both simulated and experimental –, and also to the diffusion coefficient computed for the "fast" molecules from the slope of the MSD in Fig. 5.25. The comparison is illustrated in Table 5.10. First of all, the SPC/E model overestimates the diffusion coefficient of bulk water.

Moreover, the diffusion coefficients found for fast water – both experimental and simulated – are comparable to the values for bulk water, and even slightly larger. The diffusion coefficient reported in literature are listed in the last three rows of the Table, varying depending on the water loading of the tube.

[5]The present Q-dependence can be fitted with one of the models for long-range diffusion mentioned in section 2.6.1.2, especially a model describing jump diffusion (Chudley-Elliot or Hall-Ross[270], etc). It was not done in this thesis but it is a natural continuation of the present analysis.

system	Diffusion coefficient $[cm^2 s^{-1}]$
Exp. bulk water [190–193]	$2.3 \cdot 10^{-5}$
Bulk water for SPC/E (rigid) [241,269]	$2.9 \cdot 10^{-5}$
exp. fast water @ IN6-SHARP	$(2.6 \pm 0.3) \cdot 10^{-5}$
fast water (flexible) @ MD	$(3.2 \pm 0.1) \cdot 10^{-5}$
Si-INTs @ MD (Scalfi) [207]	$3.5 \cdot 10^{-6}$
Si-INTs @ MD (Konduri) [205]	$1 - 3 \cdot 10^{-5}$
Si-INTs @ MD (Zang) [206]	$1 - 6 \cdot 10^{-5}$

Table 5.10: Table summarizing the diffusion coefficients found, compared to bulk water.

Our results suggest that at room temperature, water inside imogolite nanotubes splits into two populations, one slower than bulk water and one comparable to bulk water. This agrees with previous studies on MCM-41 and listed in section 1.4.2 [177,195], that highlight the presence of two distinct populations of water, one subdiffusive and one closer to bulk water. Nevertheless, when comparing the measured diffusion coefficient with the values reported for MCM-41 (Table 1.1), diffusion seems to be greater inside imogolites by a factor 1.5-2, even if the diameter is more or less twice smaller[6]. Moreover, in MCM-41, the diffusion coefficient decreases with decreasing diameter [131]. Imogolites do not seem to follow this tendency, as a small diameter does not correspond to a small diffusion coefficient. This is probably due to the structuring of water in the first adsorption layer – impossible in MCM-41 due to their amorphous surface –, that leaves more freedom to the water inside the pore to diffuse.

5.4 Density of States of confined water molecules

Finally, the DOS introduced in Eq. 2.49 as $g(\omega)$ was calculated at 50 K and 300 K for water hydrogens and for the four different water fillings –3wt%, 6wt%, 12wt% and 15wt%– introduced at the beginning of this chapter concerning water. The curves are presented in Fig. 5.32. As evidenced previously with the MSD and $EISF$ (in figs. 5.22 et 5.21 respectively), also in the inelastic region of the spectrum, the 3wt% and 6wt% states seem quite equivalent, as well as 12wt% and 15wt%.

[6]Pore diameter of MCM-41 investigated in literature between $\sim$ 2 and 4 nm, while equal to 1.5 nm for imogolites.

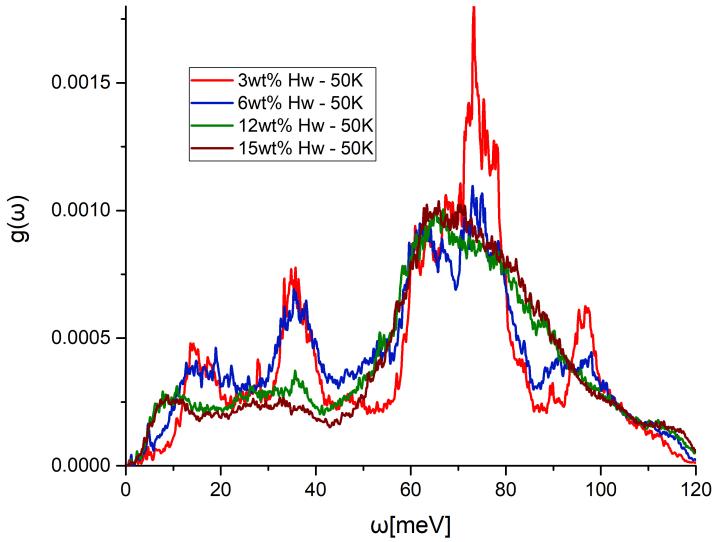
3wt% Hw - 50K
6wt% Hw - 50K
12wt% Hw - 50K
15wt% Hw - 50K
g(ω)
0.0015
0.0010
0.0005
0.0000
0
20
40
60
80
100
120
ω[meV]

a)

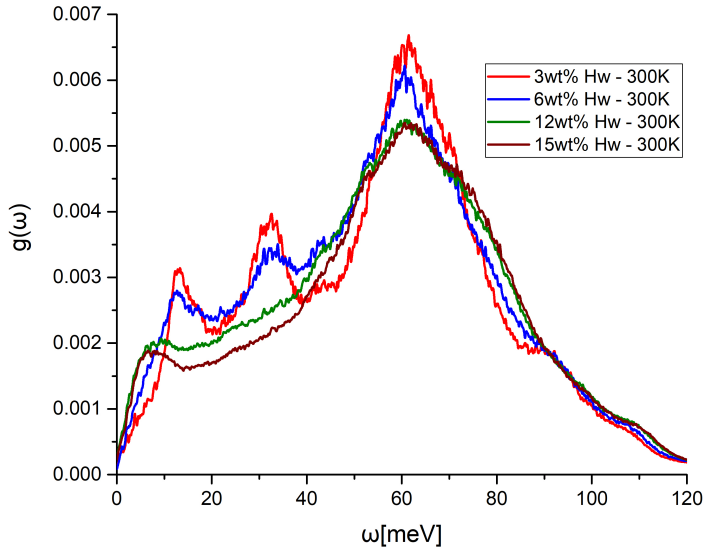
3wt% Hw - 300K
6wt% Hw - 300K
12wt% Hw - 300K
15wt% Hw - 300K
g(ω)
0.007
0.006
0.005
0.004
0.003
0.002
0.001
0.000
0
20
40
60
80
100
120
ω[meV]

b)

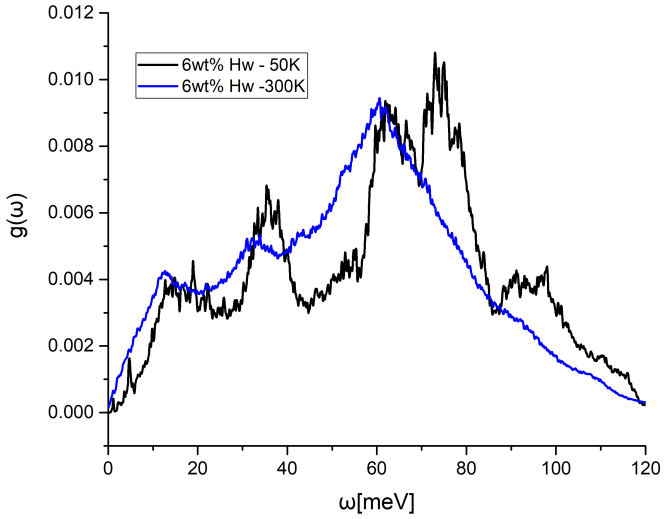

c)

Figure 5.32: Simulated DOS of H_w at *a*) 50 K, *b*) 300 K for different water contents and *c*) comparison of the 6wt% at 50 K and 300 K (after normalization to 1)

The first two states, *i.e.* 3wt% and 6wt%, where all the water molecules are in direct interaction with the inner hydroxyls of the nanotube, display a first peak around 14 meV, a second one at 35 meV and a wider double band located at around 60 and 70 meV. On the contrary, the 12wt% and 15wt% states (presenting also water molecules in the center of the nanotube), show intensity starting at 8 meV, followed by a large band starting at 50 meV and peaking at 60 meV. The DOS for a fully filled tube quite resembles what was found for a carbon nanotube with comparable diameter by Kolesnikov et al.[130]. At 300 K, the main features of the DOS remain slightly similar. The peak positions slightly move at lower frequencies, *i.e.* the 14 meV moves at 13 meV, the 35 one at 32 meV, and the peak of the libration band moves from 67 to 61 meV.

When compared to Ge-INTs, where the experimental GDOS of the single water layer showed absolute no dependence on temperature, here when superimposing the (calculated) DOS of the 6wt% at 50 K and 300 K (Fig. 5.32*c*), we can see that at room temperature water is not strictly solid-like anymore. This may suggest that molecules are more loosely bound to the surface, and are allowed to detach themselves from the surface and have a more liquid-like behavior.

In the following two sections, the most interesting features of the DOS

of the 6wt% and 12wt% states will be interpreted.

5.4.1 Peak attribution for 6wt% of water

6wt% of water corresponds to have a monolayer of adsorbed water. Therefore, in order to understand the meaning of the different peaks of the DOS of the 6wt% hydration state, we employed the classification introduced in 5.2.1, where 5 different adsorption patterns were introduced. The two most probable populations were found to be: (*i*) type 1: molecules attached to the wall, and (*ii*) type 2: those dangling out the wall. In order to understand if different populations produce different features in the DOS, the DOS of 10 hydrogens belonging to water molecules of the type 1 and of 10 hydrogens belonging to molecules of type 2 were computed and compared to the total DOS. This is shown in Fig. 5.33.

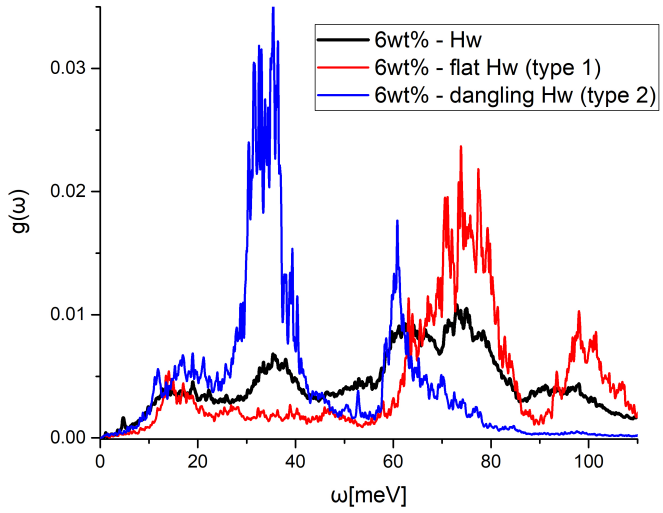

Figure 5.33: DOS for different species for the single wetting layer of water (6wt% in mass): in red, molecules completely attached to the wall (type 1), in blue molecules adsorbed perpendicularly to the wall (type 2)

It is clear that the peak at 14-16 meV is present for both types of H_w. On the other hand, the peak at 35 meV is specific to type 2, water molecules adsorbed perpendicularly to the surface and dangling out.

An interesting comparison can be made with the simulated and measured GDOS for a monolayer of water in Ge-INTs, reported recently by

Monet et al.[80]. The GDOS of this layer of structural water has peaks at 15, 70, 200 and 430 meV. The modes at 70, 200 and 430 meV are attributed to librations, bending and stretching vibrations, respectively. The mode at 15 meV was associated to local translational motions of the whole water molecule trapped into a triangular germanol site, specific to structural water. Interestingly, same modes are found for Si-INTs, except for the one at 35 meV.

In order to find out to which movement it is associated, we filtered the trajectory around specific frequencies, and looked at the trajectory after filtering, evidenced by a black trace[7]. Here the size of the trace was multiplied by a factor s chosen case by case in order to highlight small magnitude motions. Filtering between 30 and 43 meV evidences that the peak at 35 meV corresponds to a librational motion consisting in large amplitude oscillations around the axis formed by the other OH of the water molecule that is strongly bound to the nanotube surface (Fig. 5.34*a*). The amplitude of displacement associated to this libration mode is around 0.15 Å at 50 K. This vibration is specific to Si-INTs and corresponds to water molecules adsorbed perpendicularly to the wall, a configuration not present in Ge-INTs. For the same reason, this peak at 35 meV is expected to be present also for N = 12 Si-INTs, since the water adsorption pattern associated to it, the type 2, is even more common than for N = 14.

It is worth mentioning that this configuration of water – a dangling water molecules towards the center of the tube – was also recently found inside MCM-41 by Malfait et al[135], which in the paper was associated experimentally to specific bands in the Raman spectrum, being around 3700 cm^{-1}. Our result is complementary to what found by the authors, as we characterize the libration (at 35 meV) belonging to the same kind of molecule having its stretching band at 3700 cm^{-1} ($\sim$ 459 meV)

Going back to the DOS of water molecules of type 2, we also investigated the asymmetric peak around 60 meV. Indeed normally, for water molecules, there is a librational band around 60 meV. Filtering between 55 and 70 meV for a hydrogen of type 2 reveals that the peak at 60 meV does not correspond to librations but to bendings perpendicular to the movement responsible of the peak at 35 meV (Fig. 5.34*b*).

[7]Band-pass filtering consists in setting to zero the components of the Fourier transform of the trajectory that do not lie inside the chosen interval $[E_{min}, E_{max}]$. The interval is chosen case by case so that it only includes the selected vibrational mode.

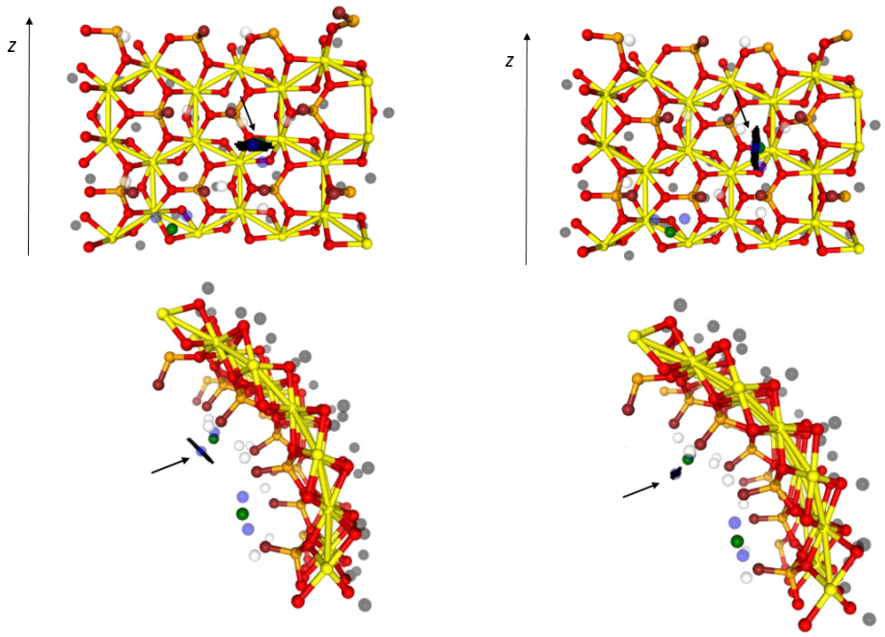

a) *b*)

Figure 5.34: Section of the nanotube hydrated with 6wt% of water and trace (in black) illustrating the movement selected by filtering the water trajectory between *a*) 30 and 43 meV (trace amplitude amplified by a factor s=3) and *b*) 55 and 70 meV (trace amplitude amplified by a factor s=10). Code scheme: Hin in white, Hout in black, Obr and Oout in red, Oin in brown, Si in orange, Al in yellow, Ow in green, Hw in blue.

5.4.2 Peak attribution for 12wt% of water

To interpret the DOS of the 12wt% state, we used the structural broad division into three water populations introduced earlier in section 5.2.1, *i.e.* first adsorption layer, second adsorption layer and water in the central cylinder.

The DOS for these different populations of H_2O molecules is shown in Fig. 5.35. First of all, here each type of H atom has a "proper" libration band. The other main characteristic is the position of translational peak at low frequency. As highlighted by the arrows, it is found to be at 14 meV for the first layer of water (red), at 10 meV for the second layer (blue) and at 6 meV (green) – as for bulk water and as observed in IN6-SHARP, Fig. 5.27 – for the water at the center showing that going from the inner wall to the center, water is less and less constrained and tends to behave like bulk water. This is in agreement with the diffusion

coefficient found in the previous chapter, which is compatible with the bulk water diffusion coefficient.

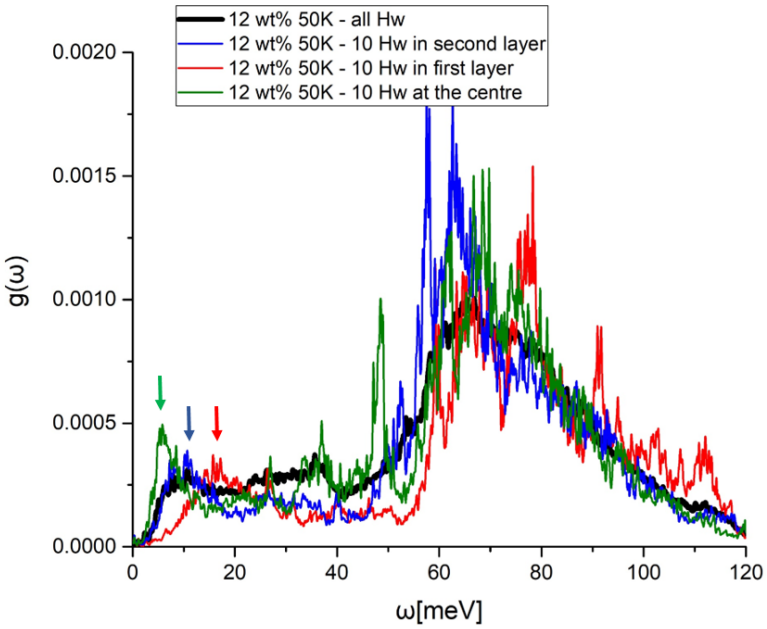

Figure 5.35: Simulated DOS for different species of water molecules at 12wt%: in black the total DOS, in red molecules belonging to the first hydration layer, in blue to the second hydration layer and in green molecules being at the center of the tube pore.

Moreover, the peak at 35 meV nearly disappears when the nanotube has more than a single layer of water. This is due to the fact that the H_w atoms that were free to dangle in the 6wt% hydration state, at 12wt% start interacting with the additional water molecules, forming hydrogen bonds and loosing their ability to have large amplitude oscillations. Therefore, the appearance of a peak at 35 meV is truly specific to a Si-INT hydrated with a single layer of water.

5.4.3 Experimental Density of States

The GDOS – as defined by Eq. 2.50 – was measured experimentally at 10 K with the time-of-flight spectrometer PANTHER (Fig. 5.36). The measured GDOS was compared to the simulated one calculated from all the hydrogens of the system – H_{in}, H_{out} and H_w — by taking an energy resolution of 3.5 meV everywhere and by adding the multi-phonon contribution.

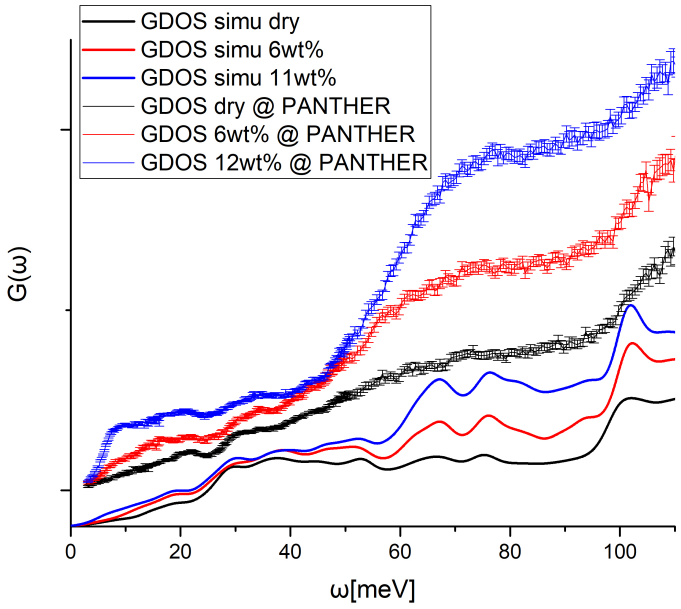

Figure 5.36: GDOS measured with PANTHER at 10 K compared to the total simulated GDOS at 50 K for all the hydrogens of the tube (dry in black, 6wt% in red, 12wt% in blue).

The simulated curve seems to reproduce well the experimental one, validating the features found in the simulated DOS, especially the existence of the peak at 35 meV that otherwise is not easily visible in experimental data. When looking at the experimental curves of Fig. 5.36, one can see a little additional intensity at 35 meV in the red curve (6wt%) when comparing to the black curve (dry). This little shift is probably due to the intensity at 35 meV in the DOS of water, but it is difficult to go further. In order to extract the density of states of water, a subtraction was attempted, by making the difference between the GDOS of the hydrated samples and the GDOS of the dry sample. Nevertheless, we found out that a simple subtraction does not allow us to recover the density of states of water, as the dry tube contribution is different from the tube contribution in interaction with water. This was found to be true also for the calculated curves.

The GDOS of the dry sample and of the sample with 12wt% of water was measured also in IN6-SHARP (Fig. 5.37).

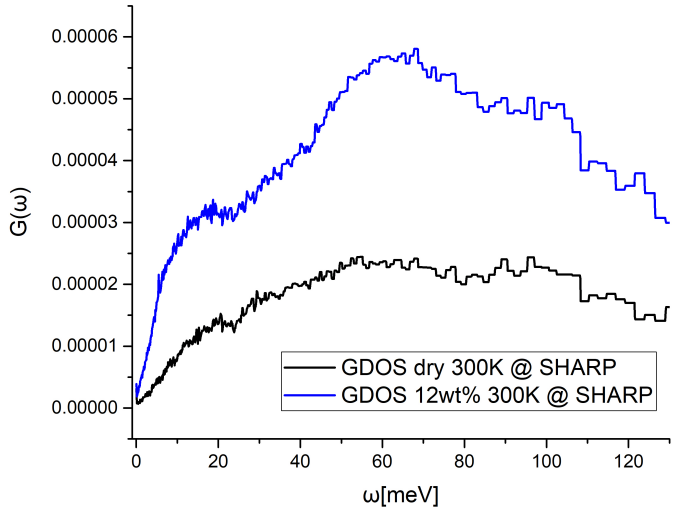

Figure 5.37: GDOS measured with IN6-SHARP at room temperature for the dry sample (blue) and the 12wt% (red).

The figure shows how the dry differs from the hydrated sample: for the hydrated sample, the intensity starts at lower energy – due to water translations starting to appear around 6-8 meV – and has more intensity around 60 meV due to water librations. On the other hand, the intensity peak around 100 meV is present in both the dry and hydrated samples, and can be associated to the peaks of H_{out}, according to our simulated curves (see Appendix B). This also means that, as opposed to some conclusions in LeCaer et al.[204], our measurement is not the water density of states directly, but the density of states of all the hydrogens constituting the system. This questions the interpretation made previously in LeCaer to the peak at 32 meV, attributed to a stretching-like translational mode of water molecules bonded to the internal surface. Although the peak is present in the DOS of water as shown by our simulations (for 6wt% of water), such peak is, first of all, not related to some stretching but to large amplitude oscillations of a very specific type of water – type 2; secondly, the bump that one can see in the GDOS is probably not only due to that peak of water, but to many other contributions given by also H_{in} and H_{out}, that also have some peaks around that frequencies. The bump at 32 meV probably appears as a single peak only because there are too many contributions to be distinguished, and the presence of the bump at 100 meV proves that the contribution of the tube cannot be neglected.

5.4.4 Conclusion

To conclude the chapter, a final visual summary of all the findings of this part, in particular with a comparison of the two hydration states studied, is presented in Fig. 5.38.

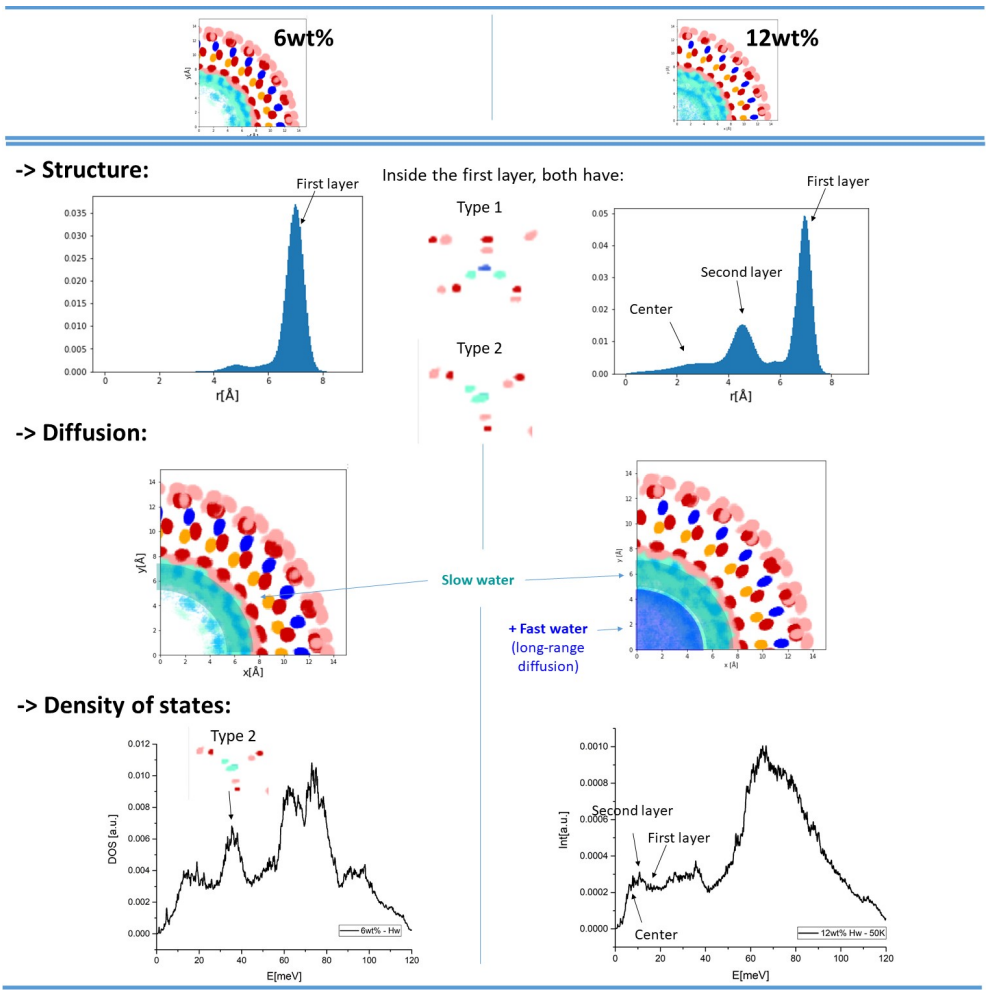

Figure 5.38: Summary of the structural and dynamical properties of the two hydration states studied.

In summary, the combination of MD simulations and experiments leads to a coherent understanding of the structure ad dynamics of water inside imogolites. Water is strongly structured in z along the tube, and this has visible consequences in the diffraction diagram and in the density of states. Moreover, as the internal surface of the tube is hydrophilic, the water molecules in close contact with the wall are strongly slowed down. On the other hand, the water molecules that populate the central fraction of the pore are less constrained and are shown to diffuse along

the tube longitudinal axis, with a comparable diffusion coefficient to that of bulk water.

5.5 Summary

The main conclusions and take-away messages of this second chapter of results are:

- MD simulations show that water inside imogolite nanotubes organizes itself in concentric circles in the (x, y) plane and periodically in z. The periodicity of water adsorption can be proved experimentally by observing the evolution with water filling of the (002) peak of the X-ray diffraction pattern.
- Water molecules in the first adsorption layer can be adsorbed into five possible patterns. The two main patterns are 1) a molecule adsorbed parallel to the tube wall and 2) a molecule perpendicular to the wall. This second type of molecule has a signature peak in the density of states at 35 meV.
- Among all the hydration states that one can investigate, there are two main categories: a tube hydrated with a single layer of water, stable and attached to the wall, and a tube whose pore is fully hydrated, which on the contrary has some molecules quite mobile and free to explore the tube pore.
- Long-range diffusion is allowed inside imogolite nanotubes only if the water filling is above a certain threshold (above $\sim$ 7wt% of water). In this case, the molecules that cross the very central pore of the tube, can diffuse quickly along the tube's longitudinal axis. This kind of water shows a diffusion coefficient similar to bulk water, as opposed to water molecules attached to the wall that are not allowed to diffuse by the attractive potential of the hydrophilic wall.

6. General conclusions and perspectives

This thesis aims at understanding first the physics of dry imogolite nanotubes, and secondly the structuring and dynamics of water confined inside these nanotubes. Compared to previous literature on this system, one of the originalities of this work is to have coupled several experimental approaches (X-ray scattering, complementary neutron spectroscopies) with MD simulations, thanks to which we are able to compare and interpret the experimental observables.

A key point for the use of any nanostructure is to have a very precise idea of its structure. In the case of Si-INTs, we confirm that these nanotubes present a zigzag (N,0) structure with N = 14. Although the minimum energy state was calculated previously, the dynamics of the nanotube has never been a source of interest. This Ph.D work investigates this point by carefully preparing dry samples of Si-INTs. Our results suggest that the inner layer of hydroxyls – consisting of a set of circular chains along the tube – happens to have a dynamics that activates around room temperature. Moreover, the existence of an order-disorder transition taking place in the inner hydroxyl sublattice is proposed here by means of classical MD simulations. We have shown that this transition occurs between an ordered phase – where all the hydroxyls are aligned — to a disordered state — where hydroxyls flip from one orientation to the other. In addition, the flips are shown to be correlated inside a circular chain. We have then characterized the transition by applying an order parameter, which can be treated as a pseudo-spin, helping to draw a parallel with the Ising model. The occurrence of this peculiar transition has been verified experimentally first by elastic neutron scattering and then by neutron spin-echo. The amplitude of the scattering, associated with the observed transition, is in very good agreement with an origin involving internal hydroxyls. However, the detailed analysis of the spin-echo and quasielastic data reveal a disagreement with what was predicted by the simulations. In particular, the signatures of the hydrogen jump diffusion between two equivalent sites, predicted by simulations, are not observed experimentally. In addition, the T dependence of the scattering is not in line with the characteristic energies of the models. Additional ingredients to those already present in the simulations developed in this thesis, have to be introduced. In particular, the validity of

classical simulations is a very questionable aspect when hydrogen jumps are involved, especially when the distance between the jumps is small, and one could argue that quantum effects might play a role in order to promote diffusion which could result in lowering the energy barrier. Phonon assisted quantum jumps could also be involved in the diffusion process, especially if the double well potential introduced in Chap. 4 is asymmetric. One could also evoke that the latter model disregarded interchain correlations, and that the treatment of the neutron observables has systematically ruled out coherent effects. Domain-wall diffusion and classical excitations involved in critical scattering can't therefore be reproduced. The fine interpretation of the dynamics of the inner hydrogens is a final step to the complete understanding of the structure of the tube as a whole, including hydrogen atoms, which is somehow the ground state to the study of water confined in this objects. At the moment, the response to the questions are hidden into the SHARP and WASP data, which require the development of new model (theoretical and simulations), to complete their analysis satisfactorily. This first part of the present thesis work has lead the way to the study of the physics of this system, which never received any attention. Our findings hint that the system (*i*) may constitute a real-life exemplary of the 1D Ising model with periodic conditions (Ising ring) and (*ii*) may display unsuspected quantum phenomena.

Based on the resolution of the structure the nanotube itself, the organization and dynamics of water confined inside Si-INTs is investigated. Few computational and experimental works have tried to reach a full understanding of the behavior of water inside these tubes. In this thesis, an original comprehensive picture of the phenomenon is attempted by coupling MD simulations with elastic, quasielastic and inelastic neutron scattering. First of all, it is found that water molecules in (14,0) Si-INTs present five different adsorption patterns, of which the most relevant are two: a molecule adsorbed flatly into the surface, or a molecule perpendicular to the tube surface. This second type of water molecules is shown to have a particular signature in the inelastic region, with a peak in the density of states at around 35 meV. Moreover, water is strongly structured inside the tube: the molecules organize themselves in concentric rings in the transverse plane, and periodically along the longitudinal axis of the tube due to the presence of furrows in the internal wall of the tube. Unexpectedly, this structuring in z induces strong variations in the intensity of a specific reflection (the (002) peak) that is related to the periodicity of the system. We propose therefore an original approach to quantify the periodic organization of water that has been validated

by performing in-situ X-ray diffraction experiments. Concerning diffusion, the overall behavior of water is subdiffusive, as expected for an hydrophilic tube. Moreover, water appears to be divisible into two main categories: (*i*) water molecules attached to the wall, which are trapped into the adsorption sites of the tube and present a very limited chance of diffusing; this kind of water is referred as "slow" water. (*ii*) The second category – the "fast" water – is composed of water molecules diffusing freely at the center of the pore, similarly to bulk water. The distinction in these two categories is confirmed by quasielastic neutron scattering.
Overall, this second part of this thesis contributes to reach a better understanding of water confinement inside imogolite nanotubes. It provides a new tool, the (002), to detect the occurrence – or not – of periodic structuring of water inside aluminosilicate imogolite nanotubes. It also contributes to clarify how long-range diffusion takes place into imogolites, which up to now is not completely elucidated. To further deepen the understanding of water diffusion, especially at long timescales, one should analyze and interpret the data collected on WASP (not shown in this manuscript as the complete data reduction and analysis is still pending), or perform new neutron experiments with deuterated samples, in order to completely disentangle the contribution of the tube and water in the scattering. Moreover, as opposed to the dry nanotube, for which the classical CLAYFF force field might not be adequate, the results of Chapter 5 suggest that the combination of the CLAYFF and SPC/E models reproduce well the experimental data, and are suitable for studying the hydrated tube. For instance, our study of water dynamics in imogolites could be continued to better understand the influence of the internal wall on the organization of molecules. It would be interesting to apply the methodology used in this work to investigate the water confinement in recently developed hydrophobic (methylated tubes) or amphiphilic (partially functionalized hybrid nanotubes) nanostructures. More generally, this study shows that a system that has been known for more than 60 years can still be used as a playground for fundamental physics studies, paving the way for future investigations.

A. NSE polarization

The polarization of the dry sample is shown in Fig. A.1.

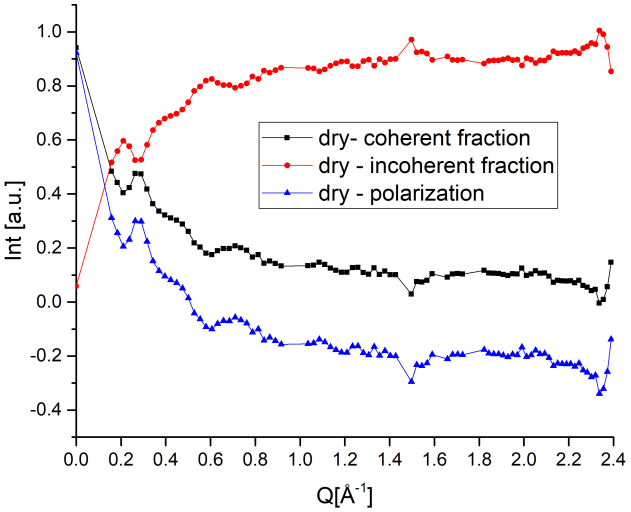

Figure A.1: Polarization measured at WASP, and coherent and incoherent components for the dry sample

One can see that the elastic coherent scattering dominates the NSE signal for Q<0.8 $Å^{-1}$, while the incoherent dynamics of hydrogens becomes predominant at high Q. Therefore, the optimal Q range for incoherent NSE is Q>0.8 $Å^{-1}$.

B. Density of States of the dry nanotube

Chapter 4 was about the order-disorder transition of the dry Si-INT. The present Appendix collects some additional material concerning this phenomenon, in particular in the inelastic region of the spectrum.

In principle, the presence of a transition can also be spotted into the evolution of the Density of States g(ω) calculated for the inner hydroxyls as a function of temperature from Eq. 2.49 (Fig. B.1). The DOS at 50 K is composed of a large band between 2 and 60 meV and centered at 40 meV, and a peak at 140 meV. The density of states is quite similar to what found for Ge-INTs – a large band between 2 and 52 meV and a peak at 123 meV – showing that for Si-INT the same peaks appear at slightly higher frequencies.

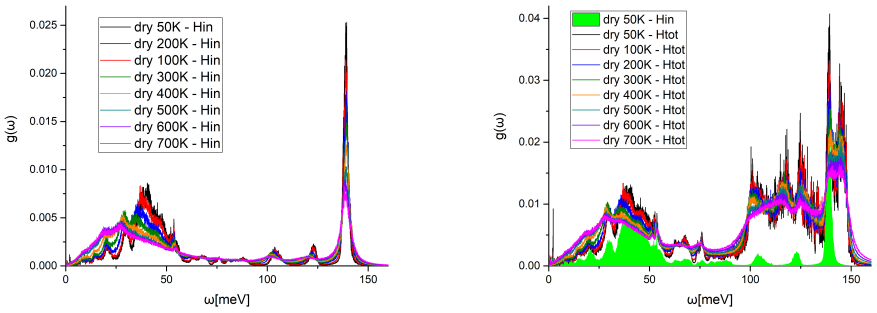

a) *b)*

Figure B.1: Calculated DOS of *a)* inner hydroxyls of the dry nanotube and *b)* total DOS of all hydrogens, for T=50, 100, 200, 300, 400, 500, 600 and 700 K; in pink the H_{in} contribution in the total DOS.

Modes can be associated to some specific motions by filtering the trajectory[80] around a certain peak and by looking at the trajectory of atoms after filtering. Here the size of the trace was multiplied by a factor s chosen case by case in order to highlight small magnitude motions. For example in Fig. B.2, the trace of a selected hydrogen atom is visualized by a black trace, after filtering it around different peaks of the DOS at T=50 K. The band of modes centered at 40 meV is the one associated to the large-amplitude displacements parallel to the NT surface, around the

SiO axis, that are visible in the traces in Fig. B.2*a*. The corresponding mode in the Density of States is very broad. The peak at 140 meV is, on the contrary, very sharp and corresponds to the bending perpendicular to the NT surface (bending on the Si-O-H plane) (Fig. B.2*b*). The same attribution was done for Ge-INTs.

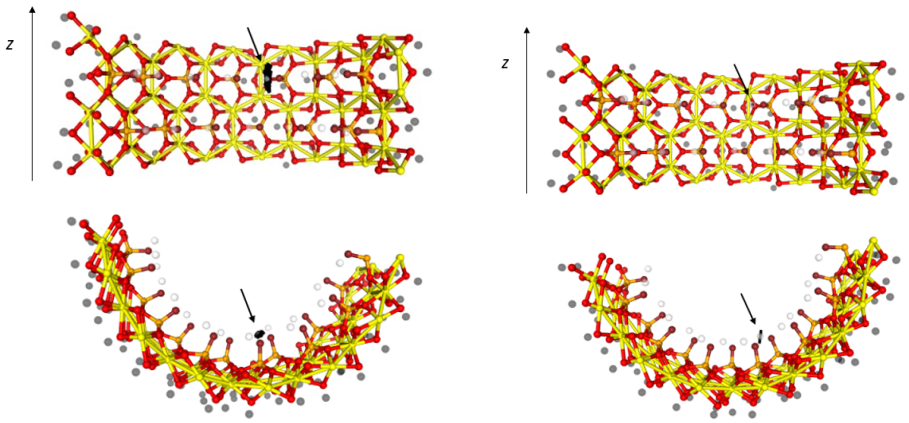

a) *b*)

Figure B.2: Transversal and longitudinal section of the dry nanotube and trace (in black) illustrating the movement selected by filtering the trajectory between *a*) 25 and 60 meV (trace amplitude amplified by a factor s=3) and *b*) 135 and 142 meV (trace amplitude amplified by a factor s=10). Code scheme: Hin in white, Hout in black, Obr and Oout in red, Oin in brown, Si in orange, Al in yellow.

Fig. B.1 highlights that the mode at 40 meV tends to reduce with the transition taking place. This is not surprising, as the mode at 40 meV corresponds to the large-amplitude motions that were evidenced by the density maps of Fig. 4.11 in the pre-transition temperatures.

One has to bear in mind that there are three external hydroxyls for every internal hydroxyl. Therefore, the contribution in the total DOS of external hydroxyls is not negligible, and has to be considered when comparing to experimental data. The total DOS of all hydrogens is in figure B.1*b*. Moreover, in order to compare with the experimental data, one must not only add the H_{out} contribution, but also transform the DOS into the Generalized Density of States G(ω) of Eq. 2.50, the quantity containing also the multi-phonon contribution and accessible by Inelastic Neutron Scattering (INS).

The GDOS was measured experimentally by using the two time-of-flight spectrometers, *i.e.* PANTHER and IN6-SHARP. PANTHER data

were collected at 10 K at different wavelengths. The different spectra were then merged in order to obtain a final GDOS in the energy range between 0 and 120 meV. The comparison between the experimental and simulated GDOS (at 50 K and 300 K) is presented in Fig. B.3*a*. Although the positions are quite well reproduced by the simulation, the relative intensities are less so, since the experimental data show an unstructured growth in intensity at around 60-70 meV which is not present in simulations. This is possibly due to some modes of H_{out} that hardened when going from an isolated tube – in simulations – to a bundle – in the real-life sample. Moreover, when comparing the simulations at 50 and 300 K, one would say that the simulated curve at 300 K reproduces better the area around 40 meV, as the peak is less pronounced. The only difference between the two temperatures is that at 300 K, the inner hydroxyls are slightly more disordered, even if they have not undergone the order-disorder transition yet. This suggests that the experimental sample is more disordered than the simulated tube. The higher level of disorder can be due to the fact that when doing a measure of density of states in PANTHER, the sample is cooled down to 10 K very quickly, not giving the time to the glassy-system to find its full ordered configuration.

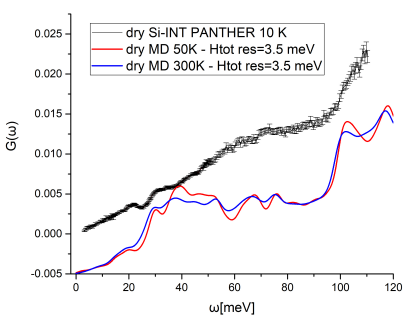

a)

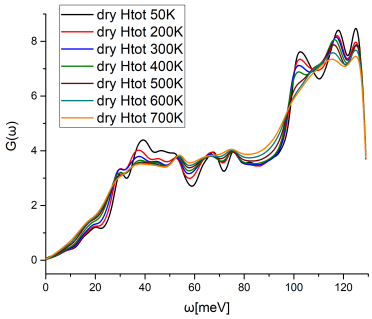

b)

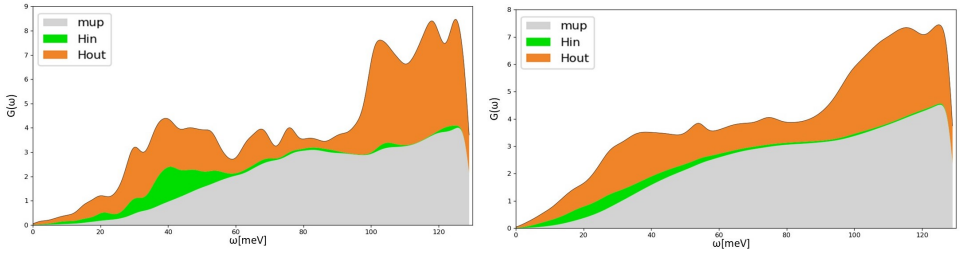

c) *d)*

Figure B.3: *a*) Experimental GDOS of the dry nanotube measured in PANTHER at T=10K (black) and simulated one (red at T=50 K, blue at T=300 K) after convolution with an experimental resolution equal to 3.5 meV everywhere and multi-phonon calculation. *b*) Temperature evolution of the simulated GDOS of the dry nanotube; in *c*), the different contribution in the GDOS at 50 K and *d*) at 700 K (green for H_{in}, orange for H_{out} and grey for multi-phonons

Fig. B.3*b* represents the simulated GDOS convoluted with PANTHER's resolution and calculated in the whole temperature range. The results reveal how the transition can be in principle evidenced by the drop in intensity of the 40 meV mode also in experimental data but also how the effect is expected to be very small. On the other side, the H_{out} are responsible for the peaks centred at 120 meV, which are therefore dumped when their dynamics starts, *i.e.* above 400-500 K (as we saw in Fig. 4.14). Figs. B.3*c* and B.3*d* show what is the entity of multi-phonons. The comparison of the two figures also show that, with this resolution, the group of peaks around 40 meV belonging to the H_{in} (in green in the figure), while clearly present at 50 K, are completely flattened out at 700 K, after the transition.

The GDOS of the dry sample was also measured at IN6-SHARP, as a function of temperature (Fig. B.4). As for the *QENS* measurements, the same three ramps were performed:

T ramp 1 (heating) [K]	T ramp 2 (cooling) [K]	T ramp 3 (heating) [K]
300	350	325
400	250	375
450	2	-

Table B.1: Temperatures sampled in the three temperature ramps performed in IN6-SHARP

Since the measurements seem to depend on the history of the sample,

the three ramps will be treated separately.

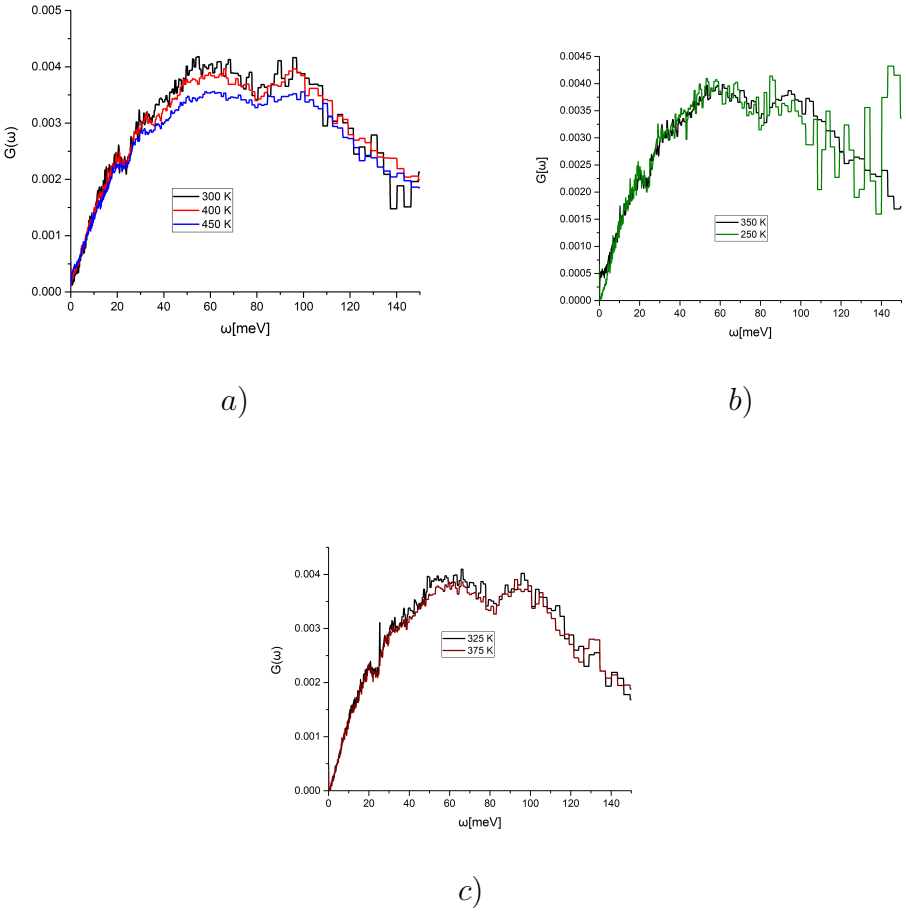

a) *b*)

c)

Figure B.4: Experimental GDOS measured in IN6-SHAPR during *a*) the first ramp, *b*) second ramp and *c*) third ramp

A decrease in the intensity around 50 meV can be seen in the two heating ramps, and also a small decrease of the peak at 100 K can be seen at 450 K. The modifications observed in the two heating ramps seem to indicate that the bending band around 40-50 meV looses intensity with rising temperature, suggesting the activation of the dynamics of the hydroxyls due to the order-disorder transition. The reduction in intensity around 100 K at 450K may probably mean that also the dynamics of the H_{out} is activated at 450 K.

The effect is quite small but simulations already told us that the phenomenon is quite difficult to see in the Density of States.

Nevertheless, the whole interpretation of the phenomenon is not achieved and the fact that the interpretation of the GDOS does not agree fully

with what is observed in the $QENS$ region, further shows how this phenomenon is complex and not fully understood.

Bibliography

[1] P. Ball, Nature, 2008, **452**, 291–292.

[2] O. Mishima and H. E. Stanley, Nature, 1998, **392**, 164–168.

[3] P. Agre, Angewandte Chemie International Edition, 2004, **43**, 4278–4290.

[4] K. Wood, M. Plazanet, F. Gabel, B. Kessler, D. Oesterhelt, D. Tobias, G. Zaccai and M. Weik, Proceedings of the National Academy of Sciences, 2007, **104**, 18049–18054.

[5] C. Kinnear, T. L. Moore, L. Rodriguez-Lorenzo, B. Rothen-Rutishauser and A. Petri-Fink, Chemical reviews, 2017, **117**, 11476–11521.

[6] P. Serp and E. Castillejos, ChemCatChem, 2010, **2**, 41–47.

[7] H. G. Park and Y. Jung, Chemical Society Reviews, 2014, **43**, 565–576.

[8] J. L. Blackburn, ACS Energy Letters, 2017, **2**, 1598–1613.

[9] M. Ge, Q. Li, C. Cao, J. Huang, S. Li, S. Zhang, Z. Chen, K. Zhang, S. S. Al-Deyab and Y. Lai, Advanced Science, 2017, **4**, 1600152.

[10] X. Zhang, H. Liu and L. Jiang, Advanced materials, 2019, **31**, 1804508.

[11] A. Loiseau, P. Launois, P. Petit, S. Roche and J.-P. Salvetat, Lect. Notes Phys, 2006, **677**, 495–543.

[12] L. Radushkevich and V. á. Lukyanovich, Zurn Fisic Chim, 1952, **26**, 88–95.

[13] S. Iijima, nature, 1991, **354**, 56–58.

[14] J.-P. Salvetat, J.-M. Bonard, N. Thomson, A. Kulik, L. Forro, W. Benoit and L. Zuppiroli, Applied Physics A, 1999, **69**, 255–260.

[15] K. Sun, M. A. Stroscio and M. Dutta, Journal of Applied Physics, 2009, **105**, 074316.

[16] T. W. Odom, J.-L. Huang, P. Kim and C. M. Lieber, Structure and electronic properties of carbon nanotubes, 2000.

[17] H. Kataura, Y. Kumazawa, Y. Maniwa, I. Umezu, S. Suzuki, Y. Ohtsuka and Y. Achiba, Synthetic metals, 1999, **103**, 2555–2558.

[18] P. M. Ajayan and J. M. Tour, Nature, 2007, **447**, 1066–1068.

[19] M. Anantram and F. Leonard, Reports on progress in physics, 2006, **69**, 507.

[20] S. Kruss, A. J. Hilmer, J. Zhang, N. F. Reuel, B. Mu and M. S. Strano, Advanced drug delivery reviews, 2013, **65**, 1933–1950.

[21] A. D. Franklin, Nature, 2013, **498**, 443–444.

[22] M. Monthioux, Carbon, 2002, **40**, 1809–1823.

[23] M. Dresselhaus and H. Dai, MRS bulletin, 2004, **29**, 237–243.

[24] C. Bussy, J. Cambedouzou, S. Lanone, E. Leccia, V. Heresanu, M. Pinault, M. Mayne-l'Hermite, N. Brun, C. Mory, M. Cotte et al., Nano Letters, 2008, **8**, 2659–2663.

[25] H. J. Johnston, G. R. Hutchison, F. M. Christensen, S. Peters, S. Hankin, K. Aschberger and V. Stone, Nanotoxicology, 2010, **4**, 207–246.

[26] S. Lanone, P. Andujar, A. Kermanizadeh and J. Boczkowski, Advanced drug delivery reviews, 2013, **65**, 2063–2069.

[27] B. Ni and X. Wang, Chemical Science, 2016, **7**, 3978–3991.

[28] M. Serra, R. Arenal and R. Tenne, Nanoscale, 2019, **11**, 8073–8090.

[29] R. Tenne, L. Margulis, M. e. Genut and G. Hodes, Nature, 1992, **360**, 444–446.

[30] M. Nath, A. Govindaraj and C. N. R. Rao, Advanced Materials, 2001, **13**, 283–286.

[31] H. Shin, D.-K. Jeong, J. Lee, M. M. Sung and J. Kim, Advanced Materials, 2004, **16**, 1197–1200.

[32] Y.-G. Guo, J.-S. Hu, H.-P. Liang, L.-J. Wan and C.-L. Bai, Advanced functional materials, 2005, **15**, 196–202.

[33] X.-P. Shen, A.-H. Yuan, Y.-M. Hu, Y. Jiang, Z. Xu and Z. Hu, Nanotechnology, 2005, **16**, 2039.

[34] Y. Wang, J. Y. Lee and H. C. Zeng, Chemistry of Materials, 2005, **17**, 3899–3903.

[35] B. Ni, H. Liu, P.-p. Wang, J. He and X. Wang, Nature communications, 2015, **6**, 1–8.

[36] G. Radovsky, R. Popovitz-Biro, M. Staiger, K. Gartsman, C. Thomsen, T. Lorenz, G. Seifert and R. Tenne, Angewandte Chemie, 2011, **123**, 12524–12528.

[37] D. Golberg, Y. Bando, Y. Huang, T. Terao, M. Mitome, C. Tang and C. Zhi, ACS nano, 2010, **4**, 2979–2993.

[38] J. Goldberger, R. He, Y. Zhang, S. Lee, H. Yan, H.-J. Choi and P. Yang, Nature, 2003, **422**, 599–602.

[39] P. Yuan, D. Tan and F. Annabi-Bergaya, Applied Clay Science, 2015, **112**, 75–93.

[40] L. W. Wong, C. B. S. Goh, P. Pasbakhsh and J. B. L. Tan, Journal of Science: Advanced Materials and Devices, 2022, 100431.

[41] N. Yoshinaga and S. Aomine, Soil Science and Plant Nutrition, 1962, **8**, 22–29.

[42] N. Miyauchi and S. Aomine, Soil Science and Plant Nutrition, 1966, **12**, 19–22.

[43] N. Yoshinaga and M. Yamaguchi, Soil Science and Plant Nutrition, 1970, **16**, 215–223.

[44] C. Gense, Bulletin du Groupe français des Argiles, 1973, **25**, 79–84.

[45] N. Yoshinaga, J. Tait and R. Soong, Clay Minerals, 1973, **10**, 127–130.

[46] R. Parfitt and W. McHardy, Clays and Clay Minerals, 1974, **22**, 369–371.

[47] P. Violante and J. Tait, Clay Minerals, 1979, **14**, 155–158.

[48] M. Nanzyo and H. Kanno, Inorganic Constituents in Soil, Springer, 2018, pp. 59–95.

[49] J. Russell, W. McHardy and A. Fraser, Clay Minerals, 1969, **8**, 87–99.

[50] K. Wada, N. Yoshinaga, H. Yotsumoto, K. Ibe and S. Aida, Clay Minerals, 1970, **8**, 487–489.

[51] P. Cradwick, V. Farmer, J. Russell, C. Masson, K. Wada and N. Yoshinaga, Nature Physical Science, 1972, **240**, 187–189.

[52] V. C. Farmer and A. Fraser, Developments in Sedimentology, Elsevier, 1979, vol. 27, pp. 547–553.

[53] K. Wada and N. Yoshinaga, American Mineralogist: Journal of Earth and Planetary Materials, 1969, **54**, 50–71.

[54] W. Ma, W. O. Yah, H. Otsuka and A. Takahara, Beilstein journal of nanotechnology, 2012, **3**, 82–100.

[55] V. Farmer, A. Fraser and J. Tait, Journal of the Chemical Society, Clinical Communications, 1977, **12**, year.

[56] E. Paineau, Applied Sciences, 2018, **8**, 1921.

[57] S. M. Barrett, P. M. Budd and C. Price, European polymer journal, 1991, **27**, 609–612.

[58] C. Levard, A. Masion, J. Rose, E. Doelsch, D. Borschneck, C. Dominici, F. Ziarelli and J.-Y. Bottero, Journal of the American Chemical Society, 2009, **131**, 17080–17081.

[59] N. Arancibia-Miranda, M. Escudey, R. Ramírez, R. I. Gonzalez, A. C. Van Duin and M. Kiwi, The Journal of Physical Chemistry C, 2017, **121**, 12658–12668.

[60] H. Yang, C. Wang and Z. Su, Chemistry of Materials, 2008, **20**, 4484–4488.

[61] G. I. Yucelen, D.-Y. Kang, I. Schmidt-Krey, H. W. Beckham and S. Nair, Chemical Engineering Science, 2013, **90**, 200–212.

[62] C. H. Lam, A.-C. Yang, H.-Y. Chi, K.-Y. Chan, C.-C. Hsieh and D.-Y. Kang, ChemistrySelect, 2016, **1**, 6212–6216.

[63] S.-i. Wada and K. Wada, Clays and Clay Minerals, 1982, **30**, 123–128.

[64] P. Maillet, C. Levard, E. Larquet, C. Mariet, O. Spalla, N. Menguy, A. Masion, E. Doelsch, J. Rose and A. Thill, Journal of the American Chemical Society, 2010, **132**, 1208–1209.

[65] M.-S. Amara, E. Paineau, M. Bacia-Verloop, M.-E. M. Krapf, P. Davidson, L. Belloni, C. Levard, J. Rose, P. Launois and A. Thill, Chemical Communications, 2013, **49**, 11284–11286.

[66] E. Paineau and P. Launois, Crystals, 2020, **10**, 1094.

[67] E. Paineau, S. Rouzière, G. Monet, C. C. Diogo, I. Morfin and P. Launois, Journal of Colloid and Interface Science, 2020, **580**, 275–285.

[68] D.-Y. Kang, J. Zang, C. W. Jones and S. Nair, The Journal of Physical Chemistry C, 2011, **115**, 7676–7685.

[69] I. Bottero, B. Bonelli, S. E. Ashbrook, P. A. Wright, W. Zhou, M. Tagliabue, M. Armandi and E. Garrone, Physical Chemistry Chemical Physics, 2011, **13**, 744–750.

[70] M. S. Amara, E. Paineau, S. Rouzière, B. Guiose, M.-E. M. Krapf, O. Taché, P. Launois and A. Thill, Chemistry of Materials, 2015, **27**, 1488–1494.

[71] G. Monet, M. S. Amara, S. Rouzière, E. Paineau, Z. Chai, J. D. Elliott, E. Poli, L.-M. Liu, G. Teobaldi and P. Launois, Nature communications, 2018, **9**, 1–9.

[72] P. I. Pohl, J.-L. Faulon and D. M. Smith, Langmuir, 1996, **12**, 4463–4468.

[73] S. Mukherjee, V. M. Bartlow and S. Nair, Chemistry of Materials, 2005, **17**, 4900–4909.

[74] V. Farmer, M. Adams, A. Fraser and F. Palmieri, clay Minerals, 1983, **18**, 459–472.

[75] S.-i. Wada, Clays and Clay Minerals, 1987, **35**, 379–384.

[76] K. Tamura and K. Kawamura, The Journal of Physical Chemistry B, 2002, **106**, 271–278.

[77] S. Konduri, S. Mukherjee and S. Nair, Physical Review B, 2006, **74**, 033401.

[78] L. Guimarães, A. N. Enyashin, J. Frenzel, T. Heine, H. A. Duarte and G. Seifert, Acs Nano, 2007, **1**, 362–368.

[79] M. P. Lourenco, L. Guimaraes, M. C. Da Silva, C. De Oliveira, T. Heine and H. A. Duarte, The Journal of Physical Chemistry C, 2014, **118**, 5945–5953.

[80] G. Monet, E. Paineau, Z. Chai, M. S. Amara, A. Orecchini, M. Jimenéz-Ruiz, A. Ruiz-Caridad, L. Fine, S. Rouzière, L.-M. Liu et al., Nanoscale Advances, 2020, **2**, 1869–1877.

[81] P. Yuan, A. Thill and F. Bergaya, Nanosized tubular clay minerals: Halloysite and Imogolite, Elsevier, 2016.

[82] E. Paineau and P. Launois, Nanomaterials from Clay Minerals, Elsevier, 2019, pp. 257–284.

[83] J. Govan, N. Arancibia-Miranda, M. Escudey, B. Bonelli and F. Tasca, Materials Chemistry Frontiers, 2021, **5**, 6779–6802.

[84] M. A. Wilson, G. S. Lee and R. C. Taylor, Clays and clay minerals, 2002, **50**, 348–351.

[85] C. Zanzottera, M. Armandi, S. Esposito, E. Garrone and B. Bonelli, The Journal of Physical Chemistry C, 2012, **116**, 20417–20425.

[86] D.-Y. Kang, N. A. Brunelli, G. I. Yucelen, A. Venkatasubramanian, J. Zang, J. Leisen, P. J. Hesketh, C. W. Jones and S. Nair, Nature communications, 2014, **5**, 1–9.

[87] R. Nasi, F. Sannino, P. Picot, A. Thill, O. Oliviero, S. Esposito, M. Armandi and B. Bonelli, Applied Clay Science, 2020, **186**, 105449.

[88] J. D. Elliott, E. Poli, I. Scivetti, L. E. Ratcliff, L. Andrinopoulos, J. Dziedzic, N. D. Hine, A. A. Mostofi, C.-K. Skylaris, P. D. Haynes et al., Advanced Science, 2017, **4**, 1600153.

[89] J. Li, P. Jiménez-Calvo, E. Paineau and M. N. Ghazzal, Catalysts, 2020, **10**, 89.

[90] M. Ookawa, Clay Minerals in Nature: Their Characterization, Modification and Application. Croatia: InTech, 2012, 239–258.

[91] N. Olson, N. Deshpande, S. Gunduz, U. S. Ozkan and N. A. Brunelli, Catalysis Today, 2019, **323**, 69–75.

[92] E. Shafia, S. Esposito, M. Armandi, E. Bahadori, E. Garrone and B. Bonelli, Catalysis Today, 2016, **277**, 89–96.

[93] E. Bahadori, V. Vaiano, S. Esposito, M. Armandi, D. Sannino and B. Bonelli, Catalysis Today, 2018, **304**, 199–207.

[94] L. Onsager, Annals of the New York Academy of Sciences, 1949, **51**, 627–659.

[95] E. Paineau, M.-E. M. Krapf, M.-S. Amara, N. V. Matskova, I. Dozov, S. Rouzière, A. Thill, P. Launois and P. Davidson, Nature communications, 2016, **7**, 1–8.

[96] W. J. Lee, E. Paineau, D. B. Anthony, Y. Gao, H. S. Leese, S. Rouziere, P. Launois and M. S. P. Shaffer, ACS nano, 2020, **14**, 5570–5580.

[97] W. Ma, W. O. Yah, H. Otsuka and A. Takahara, Journal of Materials Chemistry, 2012, **22**, 11887–11892.

[98] K.-H. Liou, D.-Y. Kang and L.-C. Lin, ChemPhysChem, 2017, **18**, 179–183.

[99] D.-Y. Kang, H. M. Tong, J. Zang, R. P. Choudhury, D. S. Sholl, H. W. Beckham, C. W. Jones and S. Nair, ACS Applied Materials & Interfaces, 2012, **4**, 965–976.

[100] G. N. B. Baroña, M. Choi and B. Jung, Journal of colloid and interface science, 2012, **386**, 189–197.

[101] G. N. B. Baroña, J. Lim, M. Choi and B. Jung, Desalination, 2013, **325**, 138–147.

[102] M. Li and J. A. Brant, Journal of membrane science, 2018, **563**, 664–675.

[103] M. Chaplin, Water structure and science, 2011.

[104] X.-F. Pang, Water: molecular structure and properties, World Scientific, 2014.

[105] C. G. Salzmann, The Journal of chemical physics, 2019, **150**, 060901.

[106] D. Eisenberg and W. Kauzmann, 2005.

[107] C. G. Salzmann, P. G. Radaelli, E. Mayer and J. L. Finney, Physical review letters, 2009, **103**, 105701.

[108] C. G. Salzmann, P. G. Radaelli, B. Slater and J. L. Finney, Physical Chemistry Chemical Physics, 2011, **13**, 18468–18480.

[109] P. Geiger, C. Dellago, M. Macher, C. Franchini, G. Kresse, J. Bernard, J. N. Stern and T. Loerting, The Journal of Physical Chemistry C, 2014, **118**, 10989–10997.

[110] A. I. Fisenko and N. P. Malomuzh, Chemical Physics, 2008, **345**, 164–172.

[111] M. F. Chaplin, Adsorption and phase behaviour in nanochannels and nanotubes, Springer, 2010, pp. 241–255.

[112] W. H. Thompson, The Journal of chemical physics, 2018, **149**, 170901.

[113] H. Zhu, Y. Wang, Y. Fan, J. Xu and C. Yang, Advanced Theory and Simulations, 2019, **2**, 1900016.

[114] S. H. Lee and P. J. Rossky, The Journal of chemical physics, 1994, **100**, 3334–3345.

[115] E. Westhof, Annual review of biophysics and biophysical chemistry, 1988, **17**, 125–144.

[116] W. Doster, S. Cusack and W. Petry, Nature, 1989, **337**, 754–756.

[117] C. Arcangeli, A. R. Bizzarri and S. Cannistraro, Chemical physics letters, 1998, **291**, 7–14.

[118] B. Bagchi, Chemical Reviews, 2005, **105**, 3197–3219.

[119] G. Caliskan, R. M. Briber, D. Thirumalai, V. Garcia-Sakai, S. A. Woodson and A. P. Sokolov, Journal of the American Chemical Society, 2006, **128**, 32–33.

[120] J. Roh, R. Briber, A. Damjanovic, D. Thirumalai, S. Woodson and A. Sokolov, Biophysical journal, 2009, **96**, 2755–2762.

[121] G. Schirò and M. Weik, Journal of Physics: Condensed Matter, 2019, **31**, 463002.

[122] K. Murata, K. Mitsuoka, T. Hirai, T. Walz, P. Agre, J. B. Heymann, A. Engel and Y. Fujiyoshi, Nature, 2000, **407**, 599–605.

[123] G. Benga, IUBMB life, 2009, **61**, 112–133.

[124] J. Li, X. Li, K. Wu, D. Feng, T. Zhang and Y. Zhang, International Journal of Coal Geology, 2017, **179**, 253–268.

[125] L. J. Michot, E. Ferrage, M. Jiménez-Ruiz, M. Boehm and A. Delville, The Journal of Physical Chemistry C, 2012, **116**, 16619–16633.

[126] E. Tertre, S. Savoye, F. Hubert, D. Prêt, T. Dabat and E. Ferrage, Environmental science & technology, 2018, **52**, 1899–1907.

[127] A. I. Kolesnikov, G. F. Reiter, N. Choudhury, T. R. Prisk, E. Mamontov, A. Podlesnyak, G. Ehlers, A. G. Seel, D. J. Wesolowski and L. M. Anovitz, Physical review letters, 2016, **116**, 167802.

[128] H. Thompson, A. K. Soper, M. A. Ricci, F. Bruni and N. T. Skipper, The Journal of Physical Chemistry B, 2007, **111**, 5610–5620.

[129] M. Ricci, V. Tudisca, F. Bruni, R. Mancinelli, E. Scoppola, R. Angelini, B. Ruzicka and A. Soper, Journal of Non-Crystalline Solids, 2015, **407**, 418–422.

[130] A. I. Kolesnikov, J.-M. Zanotti, C.-K. Loong, P. Thiyagarajan, A. P. Moravsky, R. O. Loutfy and C. J. Burnham, Physical review letters, 2004, **93**, 035503.

[131] S. Takahara, M. Nakano, S. Kittaka, Y. Kuroda, T. Mori, H. Hamano and T. Yamaguchi, The Journal of Physical Chemistry B, 1999, **103**, 5814–5819.

[132] P. Smirnov, T. Yamaguchi, S. Kittaka, S. Takahara and Y. Kuroda, The Journal of Physical Chemistry B, 2000, **104**, 5498–5504.

[133] A. Galarneau, M. Nader, F. Guenneau, F. Di Renzo and A. Gedeon, The Journal of Physical Chemistry C, 2007, **111**, 8268–8277.

[134] B. Malfait, A. Jani, J. B. Mietner, R. Lefort, P. Huber, M. Froba and D. Morineau, The Journal of Physical Chemistry C, 2021, **125**, 16864–16874.

[135] B. Malfait, A. Moréac, A. Jani, R. Lefort, P. Huber, M. Froba and D. Morineau, The Journal of Physical Chemistry C, 2022, **126**, 3520–3531.

[136] H. Kyakuno, M. Fukasawa, R. Ichimura, K. Matsuda, Y. Nakai, Y. Miyata, T. Saito and Y. Maniwa, The Journal of Chemical Physics, 2016, **145**, 064514.

[137] G. Hummer, J. C. Rasaiah and J. P. Noworyta, nature, 2001, **414**, 188–190.

[138] J. Köfinger, G. Hummer and C. Dellago, Physical Chemistry Chemical Physics, 2011, **13**, 15403–15417.

[139] K. Koga, G. Gao, H. Tanaka and X. C. Zeng, Nature, 2001, **412**, 802–805.

[140] Y. Maniwa, H. Kataura, M. Abe, S. Suzuki, Y. Achiba, H. Kira and K. Matsuda, Journal of the Physical Society of Japan, 2002, **71**, 2863–2866.

[141] J. Bai, C.-R. Su, R. Parra, X. C. Zeng, H. Tanaka, K. Koga and J.-M. Li, The Journal of chemical physics, 2003, **118**, 3913–3916.

[142] Y. Maniwa, H. Kataura, M. Abe, A. Udaka, S. Suzuki, Y. Achiba, H. Kira, K. Matsuda, H. Kadowaki and Y. Okabe, Chemical Physics Letters, 2005, **401**, 534–538.

[143] J. Bai, J. Wang and X. C. Zeng, Proceedings of the National Academy of Sciences, 2006, **103**, 19664–19667.

[144] T. Ohba, Angewandte Chemie, 2014, **126**, 8170–8174.

[145] K. Mochizuki and K. Koga, Proceedings of the National Academy of Sciences, 2015, **112**, 8221–8226.

[146] M. K. Borg, D. A. Lockerby, K. Ritos and J. M. Reese, Journal of membrane science, 2018, **567**, 115–126.

[147] A. Barati Farimani and N. R. Aluru, The Journal of Physical Chemistry B, 2011, **115**, 12145–12149.

[148] O. Byl, J.-C. Liu, Y. Wang, W.-L. Yim, J. K. Johnson and J. T. Yates, Journal of the American Chemical Society, 2006, **128**, 12090–12097.

[149] J. Hassan, G. Diamantopoulos, D. Homouz and G. Papavassiliou, Nanotechnology Reviews, 2016, **5**, 341–354.

[150] W. Sekhaneh, M. Kotecha, U. Dettlaff-Weglikowska and W. S. Veeman, Chemical physics letters, 2006, **428**, 143–147.

[151] D. Takaiwa, I. Hatano, K. Koga and H. Tanaka, Proceedings of the National Academy of Sciences, 2008, **105**, 39–43.

[152] H. Kyakuno, K. Matsuda, H. Yahiro, Y. Inami, T. Fukuoka, Y. Miyata, K. Yanagi, Y. Maniwa, H. Kataura, T. Saito et al., The Journal of chemical physics, 2011, **134**, 244501.

[153] E. Paineau, P.-A. Albouy, S. Rouzière, A. Orecchini, S. Rols and P. Launois, Nano letters, 2013, **13**, 1751–1756.

[154] S. Dalla Bernardina, E. Paineau, J.-B. Brubach, P. Judeinstein, S. Rouzière, P. Launois and P. Roy, Journal of the American Chemical Society, 2016, **138**, 10437–10443.

[155] B. J. Hinds, N. Chopra, T. Rantell, R. Andrews, V. Gavalas and L. G. Bachas, Science, 2004, **303**, 62–65.

[156] J. K. Holt, H. G. Park, Y. Wang, M. Stadermann, A. B. Artyukhin, C. P. Grigoropoulos, A. Noy and O. Bakajin, Science, 2006, **312**, 1034–1037.

[157] M. Majumder, N. Chopra, R. Andrews and B. J. Hinds, Nature, 2005, **438**, 44–44.

[158] S. Supple and N. Quirke, Physical review letters, 2003, **90**, 214501.

[159] M. Whitby and N. Quirke, Nature nanotechnology, 2007, **2**, 87–94.

[160] A. I. Skoulidas, D. M. Ackerman, J. K. Johnson and D. S. Sholl, Physical review letters, 2002, **89**, 185901.

[161] S. Joseph and N. Aluru, Nano letters, 2008, **8**, 452–458.

[162] K. Falk, F. Sedlmeier, L. Joly, R. R. Netz and L. Bocquet, Nano letters, 2010, **10**, 4067–4073.

[163] R. Das, M. E. Ali, S. B. Abd Hamid, S. Ramakrishna and Z. Z. Chowdhury, Desalination, 2014, **336**, 97–109.

[164] L. Liu, C. Yang, K. Zhao, J. Li and H.-C. Wu, Nature communications, 2013, **4**, 1–8.

[165] T. Han, A. Nag, S. C. Mukhopadhyay and Y. Xu, Sensors and Actuators A: Physical, 2019, **291**, 107–143.

[166] S. Arunachalam, A. A. Gupta, R. Izquierdo and F. Nabki, Sensors, 2018, **18**, 1655.

[167] R. Wang, L. Xie, S. Hameed, C. Wang and Y. Ying, Carbon, 2018, **132**, 42–58.

[168] L. Bocquet, Nature materials, 2020, **19**, 254–256.

[169] A. J. Schwanke, R. Balzer and S. Pergher, Handbook of ecomaterials, 2017, 1–22.

[170] A. K. Soper, Chemical Physics Letters, 2013, **590**, 1–15.

[171] R. Mancinelli, F. Bruni and M. Ricci, Journal of Molecular Liquids, 2011, **159**, 42–46.

[172] P. Gallo, M. Rovere and E. Spohr, The Journal of Chemical Physics, 2000, **113**, 11324–11335.

[173] A. Kohlmeyer, C. Hartnig and E. Spohr, Journal of molecular liquids, 1998, **78**, 233–253.

[174] P. Gallo, M. Rapinesi and M. Rovere, The Journal of chemical physics, 2002, **117**, 369–375.

[175] B. Coasne, C. Alba-Simionesco, F. Audonnet, G. Dosseh and K. E. Gubbins, Adsorption, 2007, **13**, 485–490.

[176] R. Busselez, R. Lefort, Q. Ji, F. Affouard and D. Morineau, Physical Chemistry Chemical Physics, 2009, **11**, 11127–11133.

[177] P. Gallo, M. Rovere and S.-H. Chen, The Journal of Physical Chemistry Letters, 2010, **1**, 729–733.

[178] R. Mancinelli, S. Imberti, A. Soper, K. Liu, C. Mou, F. Bruni and M. A. Ricci, The Journal of Physical Chemistry B, 2009, **113**, 16169–16177.

[179] G. H. Findenegg, S. Jähnert, D. Akcakayiran and A. Schreiber, ChemPhysChem, 2008, **9**, 2651–2659.

[180] D. T. Limmer and D. Chandler, The Journal of chemical physics, 2012, **137**, 044509.

[181] M. D. Fayer, N. E. Levinger et al., Annual Review of Analytical Chemistry, 2010, **3**, 89.

[182] S. Jähnert, F. V. Chávez, G. Schaumann, A. Schreiber, M. Schönhoff and G. Findenegg, Physical Chemistry Chemical Physics, 2008, **10**, 6039–6051.

[183] V. Crupi, D. Majolino, P. Migliardo, V. Venuti and M. Bellissent-Funel, Molecular physics, 2003, **101**, 3323–3333.

[184] S.-H. Chen, P. Gallo and M.-C. Bellissent-Funel, Canadian journal of physics, 1995, **73**, 703–709.

[185] P. Gallo and M. Rovere, Journal of Physics: Condensed Matter, 2003, **15**, 7625.

[186] O. V. Bychuk and B. O'Shaughnessy, The Journal of chemical physics, 1994, **101**, 772–780.

[187] T. Takamuku, M. Yamagami, H. Wakita, Y. Masuda and T. Yamaguchi, The Journal of Physical Chemistry B, 1997, **101**, 5730–5739.

[188] P. Gallo, M. Rovere and S. Chen, Journal of Physics: Condensed Matter, 2010, **22**, 284102.

[189] P. Gallo, M. Rovere and E. Spohr, Physical review letters, 2000, **85**, 4317.

[190] K. T. Gillen, D. Douglass and M. Hoch, The Journal of Chemical Physics, 1972, **57**, 5117–5119.

[191] R. Mills, The Journal of Physical Chemistry, 1973, **77**, 685–688.

[192] W. S. Price, H. Ide and Y. Arata, The Journal of Physical Chemistry A, 1999, **103**, 448–450.

[193] J. Teixeira, M.-C. Bellissent-Funel, S.-H. Chen and A.-J. Dianoux, Physical Review A, 1985, **31**, 1913.

[194] S. Takahara, N. Sumiyama, S. Kittaka, T. Yamaguchi and M.-C. Bellissent-Funel, The Journal of Physical Chemistry B, 2005, **109**, 11231–11239.

[195] A. Jani, M. Busch, J. B. Mietner, J. Ollivier, M. Appel, B. Frick, J.-M. Zanotti, A. Ghoufi, P. Huber, M. Fröba et al., The Journal of Chemical Physics, 2021, **154**, 094505.

[196] M. Baum, F. Rieutord, F. Juranyi, C. Rey and D. Rebiscoul, Langmuir, 2019, **35**, 10780–10794.

[197] B. Creton, D. Bougeard, K. S. Smirnov, J. Guilment and O. Poncelet, The Journal of Physical Chemistry C, 2008, **112**, 10013–10020.

[198] J. Zang, S. Nair and D. S. Sholl, The Journal of chemical physics, 2011, **134**, 184103.

[199] C. Zanzottera, A. Vicente, M. Armandi, C. Fernandez, E. Garrone and B. Bonelli, The Journal of Physical Chemistry C, 2012, **116**, 23577–23584.

[200] E. Paineau, M. S. Amara, G. Monet, V. Peyre, S. Rouzière and P. Launois, The Journal of Physical Chemistry C, 2017, **121**, 21740–21749.

[201] W. C. Ackerman, D. M. Smith, J. C. Huling, Y. W. Kim, J. K. Bailey and C. J. Brinker, Langmuir, 1993, **9**, 1051–1057.

[202] J. P. Gustafsson, clays and clay Minerals, 2001, **49**, 73–80.

[203] A. Fernandez-Martinez, J. Tao, A. F. Wallace, I. C. Bourg, M. R. Johnson, J. J. De Yoreo, G. Sposito, G. J. Cuello and L. Charlet, Environmental Science: Nano, 2020, **7**, 2759–2772.

[204] S. Le Caër, M.-C. Pignié, Q. Berrod, V. Grzimek, M. Russina, C. Carteret, A. Thill, J.-M. Zanotti and J. Teixeira, Nanoscale Advances, 2021, **3**, 789–799.

[205] S. Konduri, H. M. Tong, S. Chempath and S. Nair, The Journal of Physical Chemistry C, 2008, **112**, 15367–15374.

[206] J. Zang, S. Konduri, S. Nair and D. S. Sholl, ACS nano, 2009, **3**, 1548–1556.

[207] L. Scalfi, G. Fraux, A. Boutin and F.-X. Coudert, Langmuir, 2018, **34**, 6748–6756.

[208] R. I. González, J. Rojas-Nunez, F. J. Valencia, F. Munoz, S. E. Baltazar, S. Allende, J. Rogan, J. A. Valdivia, M. Kiwi, R. Ramírez et al., Applied Clay Science, 2020, **191**, 105582.

[209] J. Schindelin, I. Arganda-Carreras, E. Frise, V. Kaynig, M. Longair, T. Pietzsch, S. Preibisch, C. Rueden, S. Saalfeld, B. Schmid et al., Nature methods, 2012, **9**, 676–682.

[210] B. H. Stuart, Infrared spectroscopy: fundamentals and applications, John Wiley & Sons, 2004.

[211] K. S. Sing, Pure and applied chemistry, 1985, **57**, 603–619.

[212] Z. A. ALOthman, Materials, 2012, **5**, 2874–2902.

[213] A. Beda, C. Vaulot and C. M. Ghimbeu, Journal of Materials Chemistry A, 2021, **9**, 937–943.

[214] B. Bonelli, I. Bottero, N. Ballarini, S. Passeri, F. Cavani and E. Garrone, Journal of Catalysis, 2009, **264**, 15–30.

[215] A. Guinier, X-ray diffraction in crystals, imperfect crystals, and amorphous bodies, Courier Corporation, 1994.

[216] M. S. Amara, S. Rouziere, E. Paineau, M. Bacia-Verloop, A. Thill and P. Launois, The Journal of Physical Chemistry C, 2014, **118**, 9299–9306.

[217] V. S. Neverov, SoftwareX, 2017, **6**, 63–68.

[218] P. Fertey, F. Berenguer, E. Elkaïm, F. Legrand, C. Laulhé and S. Ravy.

[219] W. M. Haynes, D. R. Lide and T. J. Bruno, CRC handbook of chemistry and physics, CRC press, 2016.

[220] G. L. Squires, Introduction to the theory of thermal neutron scattering, Courier Corporation, 1996.

[221] S. W. Lovesey, 1984.

[222] M. Bée, 1988.

[223] P. Damay and F. Leclercq, Le Journal de Physique IV, 2000, **10**, Pr1–105.

[224] D. Richard, M. Ferrand and G. Kearley, Journal of Neutron Research, 1996, **4**, 33–39.

[225] F. Mezei, Zeitschrift für Physik A Hadrons and nuclei, 1972, **255**, 146–160.

[226] F. Mezei, Neutron spin echo, Springer, 1980, pp. 1–26.

[227] O. Arnold, J.-C. Bilheux, J. Borreguero, A. Buts, S. I. Campbell, L. Chapon, M. Doucet, N. Draper, R. F. Leal, M. Gigg et al., Nuclear Instruments and Methods in Physics Research Section A: Accelerators, Spectrometers, Detectors and Associated Equipment, 2014, **764**, 156–166.

[228] S. Plimpton, Journal of computational physics, 1995, **117**, 1–19.

[229] A. Stukowski, Modelling and simulation in materials science and engineering, 2009, **18**, 015012.

[230] R. T. Cygan, J.-J. Liang and A. G. Kalinichev, The Journal of Physical Chemistry B, 2004, **108**, 1255–1266.

[231] R. T. Cygan, J. A. Greathouse and A. G. Kalinichev, The Journal of Physical Chemistry C, 2021, **125**, 17573–17589.

[232] S. Konduri, S. Mukherjee and S. Nair, ACS nano, 2007, **1**, 393–402.

[233] J. Zang, S. Chempath, S. Konduri, S. Nair and D. S. Sholl, The Journal of Physical Chemistry Letters, 2010, **1**, 1235–1240.

[234] R. I. Gonzalez, R. Ramírez, J. Rogan, J. A. Valdivia, F. Munoz, F. Valencia, M. Ramírez and M. Kiwi, The Journal of Physical Chemistry C, 2014, **118**, 28227–28233.

[235] R. I. Gonzalez, J. Rogan, E. M. Bringa and J. A. Valdivia, The Journal of Physical Chemistry C, 2016, **120**, 14428–14434.

[236] M. Pouvreau, J. A. Greathouse, R. T. Cygan and A. G. Kalinichev, The Journal of Physical Chemistry C, 2017, **121**, 14757–14771.

[237] C. D. Berweger, W. F. van Gunsteren and F. Müller-Plathe, Chemical physics letters, 1995, **232**, 429–436.

[238] H. Berendsen, J. Grigera and T. Straatsma, Journal of Physical Chemistry, 1987, **91**, 6269–6271.

[239] W. L. Jorgensen, J. Chandrasekhar, J. D. Madura, R. W. Impey and M. L. Klein, The Journal of chemical physics, 1983, **79**, 926–935.

[240] J. L. Abascal and C. Vega, The Journal of chemical physics, 2005, **123**, 234505.

[241] P. Mark and L. Nilsson, The Journal of Physical Chemistry A, 2001, **105**, 9954–9960.

[242] J. Qvist, H. Schober and B. Halle, The Journal of chemical physics, 2011, **134**, 144508.

[243] P. Gallo, M. Rovere, M. Ricci, C. Hartnig and E. Spohr, Philosophical Magazine B, 1999, **79**, 1923–1930.

[244] P. Gallo, M. Rovere, M. Ricci, C. Hartnig and E. Spohr, EPL (Europhysics Letters), 2000, **49**, 183.

[245] L. Verlet, Physical review, 1967, **159**, 98.

[246] W. C. Swope, H. C. Andersen, P. H. Berens and K. R. Wilson, The Journal of chemical physics, 1982, **76**, 637–649.

[247] S. Nosé, The Journal of chemical physics, 1984, **81**, 511–519.

[248] W. G. Hoover, Physical review A, 1985, **31**, 1695.

[249] G. Goret, B. Aoun and E. Pellegrini, Journal of chemical information and modeling, 2017, **57**, 1–5.

[250] E. Belorizky, P. H. Fries, A. Guillermo and O. Poncelet, ChemPhysChem, 2010, **11**, 2021–2026.

[251] J. L. Bishop, E. B. Ethbrampe, D. L. Bish, Z. L. Abidin, L. L. Baker, N. Matsue and T. Henmi, Clays and Clay Minerals, 2013, **61**, 57–74.

[252] D.-Y. Kang, J. Zang, E. R. Wright, A. L. McCanna, C. W. Jones and S. Nair, Acs Nano, 2010, **4**, 4897–4907.

[253] S. Brunauer, P. H. Emmett and E. Teller, Journal of the American chemical society, 1938, **60**, 309–319.

[254] K. Egashira and S. Aomine, Clay Science, 1974, **4**, 231–242.

[255] J. De Boer, B. Lippens, B. Linsen, J. Broekhoff, A. Van den Heuvel and T. J. Osinga, Journal of Colloid and Interface Science, 1966, **21**, 405–414.

[256] N. Donkai, T. Miyamoto, T. Kokubo and H. Tanei, Journal of materials science, 1992, **27**, 6193–6196.

[257] Y. Liao, P. Picot, J.-B. Brubach, P. Roy, S. Le Caër and A. Thill, Applied Clay Science, 2018, **164**, 58–67.

[258] G. Teobaldi, N. S. Beglitis, A. J. Fisher, F. Zerbetto and W. A. Hofer, Journal of Physics: Condensed Matter, 2009, **21**, 195301.

[259] M. Zhao, Y. Xia and L. Mei, The Journal of Physical Chemistry C, 2009, **113**, 14834–14837.

[260] S. U. Lee, Y. C. Choi, S. G. Youm and D. Sohn, The Journal of Physical Chemistry C, 2011, **115**, 5226–5231.

[261] S. Coleman, Aspects of Symmetry (Cambridge, 1985.

[262] M. Le Bellac, Des phénomènes critiques aux champs de jauge-Une introduction aux méthodes et aux applications de la théorie quantique des champs, EDP sciences, 2012.

[263] S. R. Salinas, Introduction to Statistical Physics, Springer, 2001, pp. 257–276.

[264] S. Aubry, The Journal of Chemical Physics, 1975, **62**, 3217–3229.

[265] G. I. Yucelen, R. P. Choudhury, J. Leisen, S. Nair and H. W. Beckham, The Journal of Physical Chemistry C, 2012, **116**, 17149–17157.

[266] C. Cavallari, D. Pontiroli, M. Jiménez-Ruiz, M. Johnson, M. Aramini, M. Gaboardi, S. F. Parker, M. Riccó and S. Rols, Physical Chemistry Chemical Physics, 2016, **18**, 24820–24824.

[267] J. Skinner and H. Trommsdorff, The Journal of chemical physics, 1988, **89**, 897–907.

[268] L. Greenspan, Journal of research of the National Bureau of Standards. Section A, Physics and chemistry, 1977, **81**, 89.

[269] S. Tazi, A. Boţan, M. Salanne, V. Marry, P. Turq and B. Rotenberg, Journal of Physics: Condensed Matter, 2012, **24**, 284117.

[270] P. L. Hall and D. Ross, Molecular Physics, 1981, **42**, 673–682.